Active control of heat transfer by an electric field

Antoine Meyer

Normandie Université

THESE

Pour obtenir le diplôme de doctorat

Spécialité PHYSIQUE

Préparée au sein de L'UNIVERSITE DU HAVRE

Active control of heat transfer by an electric field

Présentée par
Antoine MEYER

Thèse soutenue publiquement le 15/12/2017 devant le jury composé de		
Mr Christoph EGBERS	Professeur / Université de Technologie de Bandenburg, Cottbus, Allemagne	Rapporteur
Mr Oleg N. KIRILLOV	Professeur / University of Northumbria, United Kingdom	Rapporteur
Mr Patrice LE GAL	Directeur de Recherche CNRS / IRPHE, Aix Marseille Université	Examinateur
Mr Hassan PEERHOSSAINI	Professeur / Université Paris Diderot	Examinateur
Mme Laurette TUCKERMAN	Directrice de Recherche CNRS / ESPCI Paris	Examinatrice
Mr Harunori N. YOSHIKAWA	Maître de Conférence HdR / Université Nice	Examinateur
Mr Innocent MUTABAZI	Professeur / Université du Havre	Directeur de thèse

Thèse dirigée par Innocent MUTABAZI, Laboratoire Ondes et Milieux Complexes (LOMC)

UNIVERSITÉ LE HAVRE

ED PSIME

LABORATOIRE ONDES et MILIEUX COMPLEXES

Acknowledgement

I consider myself as very lucky to have had the opportunity to work on this subject. Thermal instabilities in fluids have a kind of apparent simplicity, but exhibit a complex physics which has been source of excitation and intellectual stimulations for me. Therefore I would like to address my first thanks to Innocent Mutabazi, my PhD director. He always trusted me and found the perfect balance between criticism and encouragement, so that I never felt discouraged by the work required. I also trusted his competences and his experience, and I hope this is how I managed to learn from his expertise in physics.

Being invited to work with our German partners in Cottbus and to participate in parabolic flight campaigns was also a great opportunity. It allowed me to meet very kind people, who have different points of view on our common subject, and who were always available for discussions. Of course, it also allowed me to experience the unique feeling of weightlessness. In that way, I am very thankful to Christoph Egbers, Martin Meier, Marcel Jongmanns, and their entire team for their multiple invitations.

I would like to thank Harunori Yoshikawa, who was the first to introduce me to the world of scientific research. His rigor in his work will always be an example for me. It has been a pleasure to work with him, and I hope that it will continue in this way.

I thank the referees and the jury of my thesis for the valuable time they have spent to examine my manuscript. I would like to thank all the personnel from Le Havre, from Cottbus and from Novespace, who participated in one way or another in the realization of this project.

I am grateful to the Region Normandie for funding my PhD, and to CNES, DLR, CNRS and LIA, for funding the various research expeditions during these last three years.

Finally, I would like to thank my mum Françoise, my dad Jean-Claude, my brother Jilou, all my family and all my friends (in particular Guillaume, Coralie, Léa, Amélie, Corentin, Marie, Thomas, Théo) for their support during this PhD. Beyond their contribution, that I think they sometimes did not even notice, they reminded me at what point this experience was unique.

Contents

1 Introduction **17**

1.1 Previous work 18

1.1.1 Taylor-Couette instability 18

1.1.2 Thermo-hydrodynamic instability 18

1.1.3 Convection induced by centripetal gravity 19

1.1.4 Thermo-electro-hydrodynamic instability 20

1.2 Thesis organisation 21

2 Problem formulation **25**

2.1 The dielectrophoretic force 26

2.2 Governing equations 28

2.3 Base state 31

2.4 The rotation regimes 33

2.5 Linearised equations 35

2.6 Chebyshev collocation method 38

2.7 Equation for kinetic energy 40

2.8 Complex Ginzburg-Landau equation 42

I Effect of the centrifugal buoyancy on the Couette flow **45**

3 Taylor-Couette instability and centrifugal buoyancy **47**

3.1 The Taylor-Couette instability 47

3.1.1 Inner rotating cylinder ($\mu = 0$) 48

3.1.2 Counter-rotation regimes ($\mu < 0$) 50

3.2 The generalized Rayleigh criterion 53

3.3 1-D model for the heated Taylor-Couette system . . . 53

4 Centrifugal buoyancy in Taylor-Couette flow with fixed outer cylinder 59

4.1 Base pressure . . . 59

4.2 Results . . . 60

4.2.1 Influence of the tenperature difference . . . 61

4.2.2 Influence of Pr . . . 63

4.2.3 Eigenvalues behaviour . . . 65

4.3 Discussion . . . 69

4.3.1 Energy analysis . . . 69

4.3.2 Frequency analysis . . . 71

4.3.3 Comparison with numerical simulations . . . 74

4.4 Conclusion . . . 75

5 Centrifugal buoyancy in Rayleigh stable Taylor-Couette flows 79

5.1 Outer rotating cylinder . . . 79

5.1.1 Critical parameters . . . 80

5.1.2 Eigenfunctions . . . 83

5.2 Keplerian regime . . . 83

5.2.1 Critical parameter . . . 84

5.3 Discussion . . . 84

5.3.1 Energy analysis . . . 84

5.3.2 Small gap approximation . . . 86

5.4 Conclusion . . . 88

6 Centrifugal buoyancy in fluids with solid-body rotation 89

6.1 Flow equation in the rotating frame of reference . . . 89

6.2 Critical parameters . . . 91

6.3 Discussion . . . 95

6.3.1 Centrifugal Rayleigh at the logarithmic radius . . . 95

6.3.2 Nature of the frequency . . . 96

6.3.3 Energy analysis . . . 96

6.3.4 Comparison with numerical simulations . . . 97

6.4 Conclusion 99

II Thermoelectric convection in cylindrical annular geometry 101

7 Thermoelectric convection in stationary cylindrical annulus 103

7.1 Threshold of the thermoelectric convection 103

7.2 Heat transfer 106

8 Thermo-electric convection in a fluid system in solid-body rotation 109

8.1 Effect of the DEP force on the centrifugally-induced thermal convection 109

8.1.1 Influence of the Prandtl number 110

8.1.2 Influence of the thermal parameters 112

8.1.3 Influence of the radius ratio 114

8.2 Effect of the rotation on thermoelectric convection 114

8.2.1 Influence of the Prandtl number 114

8.2.2 Influence of the thermal parameters 118

8.3 Discussion 121

8.3.1 Parabolic behaviour of the threshold 121

8.3.2 Energy analysis 121

8.3.3 Frequency analysis 122

8.3.4 Columnar modes in outward heating 124

8.4 Conclusion 125

9 Thermo-electric convection in a vertical fluid system on the Earth 127

9.1 Dimensionless control parameters 127

9.2 Thermal convection in a stationary annulus due to the Archimedean buoyancy . . 128

9.3 Coupled effect of Archimedean and dielectrophoretic buoyancies 128

9.3.1 Influence of the radius ratio 129

9.3.2 Influence of the Prandtl number 130

9.3.3 Influence of the ratio of the two thermal expansion coefficients 131

9.3.4 Eigenfunctions 132

9.4 Energy analysis 134

9.5 Conclusion 134

10 General conclusions and outlook **137**

A Experiments and simulation of shadowgraph method **141**

A.1 Experimental setup 142

A.2 Parabolic flight campaign 143

A.3 The shadowgraph method 145

A.3.1 Principle 145

A.3.2 Theoretical modeling 146

A.3.3 Weightless environment 148

A.3.4 Earth gravity environment 153

A.4 Experimental results 154

A.4.1 Laboratory experiments 154

A.4.2 Parabolic flight experiments 159

A.5 Discussion 162

A.5.1 Comparison between the simulation of the shadowgraph method and the experimental results 162

A.5.2 Comparison between the linear stability analysis and the experimental results 162

A.6 Conclusion 163

List of Figures

1.1 Diagram of the different chosen values of μ associated with the chapter where they will be studied. 22

2.1 Sketch of the flow configuration. 25

2.2 Skech of the physical mechanism of the different terms of the electrohydrodynamic force. 26

2.3 Direction of the base electric gravity in the (η, γ_e) plane. CP means centripetal and CF means centrifugal. 32

2.4 Radial profiles of (a) the temperature, (b) the axial velocity, (c-d) the electric field and (e-f) the electric gravity. X is given by $X = (r - R_1)/d$. (c) and (e) are obtained for $\gamma_e = 0.01$. (d) and (f) are obtained for $\eta = 0.5$. 34

2.5 Radial profiles of the base azimuthal velocity in the case of (a) the inner cylinder rotation regime, (b) the outer cylinder rotation regime, and (c) the Keplerian regime. X is given by $X = (r - R_1)/d$. 36

3.1 Eigenvalue spectrum as function of the axial wavenumber for $\eta = 0.5$ and for (a) Ta = 68, (b) Ta = 100, (c) Ta = 200, (d) Ta = 300. Black and red curves correspond to stationary and oscillatory modes respectively. 49

3.2 Marginal curves for $\eta = 0.5$. 50

3.3 Azimuthal vorticity in the (r, z) plane and amplitudes of the velocity components for the three first modes at their respective criticality for $\eta = 0.5$. For the first, second and third modes, the values of (k, Ta) are $(3.2, 68.19)$, $(5.4, 228.75)$ and $(7.5, 483.94)$, respectively. 51

3.4 Marginal curves for $\eta = 0.8$, $\mu = -4$ and for different values of n. 52

3.5 Azimuthal vorticity in the (r, z) plane and amplitudes of the velocity components at the criticality for $\eta = 0.8$, $\mu = -4$, $\mathrm{Ta} = 364.4$, $k = 8.76$ and $n = 5$. 52

3.6 Variation of (a) the Taylor number and (b) the frequency at the marginal state for $\eta = 0.8$, and for various μ. At the critical condition, (Ta_c, k_c) is $(48.75, 3.17)$ for $\mu = -0.25$, $(57.37, 3.33)$ for $\mu = -0.5$, and $(76.25, 3.74)$ for $\mu = -0.8$. 54

3.7 Generalised Rayleigh discriminant profile when the outer cylinder is at rest as a function of the dimensionless radial position for different values of γ_a and for $\eta = 0.5$. 55

3.8 Schematic representation of the stability of the flow depending on the value of $\mu - \eta^2$. The condition obtained by the one dimensional model tells that the value $\gamma_a \mathrm{Pr}$ has to be below a certain value $\gamma_a \mathrm{Pr}^*$, which mainly depends on $\mu - \eta^2$. 57

4.1 Base pressure profile (a) and its derivative (b) as function of the dimensionless position for different values of γ_a with $\eta = 0.5$ and $\Pi_0 = 0$. 60

4.2 Marginal stability curves obtained for $\mathrm{Pr} = 10$, $\eta = 0.5$ and $\gamma_a = 0.001$ and for two values of n. The critical state for this set of parameters is located at the marginal curve for $n = 0$. 61

4.3 Variation of the critical parameters with γ_a for different η and and for $\mathrm{Pr} = 50$: (a) normalized Ta, (b) wavenumber and (c) frequency. SA: stationary axisymmetric mode; OA: oscillatory axisymmetric mode; ONA: oscillatory non-axisymmetric mode. 62

4.4 Variation of the critical parameters with Pr for different η and γ_a: (a) normalized Taylor number, (b) wavenuber and (c) frequency. For clarity, q_c (b) was plotted only for $\gamma_a = 0.01$. SA: stationary axisymmetric mode; OA: oscillatory axisymmetric mode; ONA: oscillatory non-axisymmetric mode. 64

4.5 Zones of critical states for (a) $\eta = 0.5$ and for (b) $\eta = 0.99$. 65

4.6 (a) Variation of the growth rate with the wavenumber for $\mathrm{Ta} = 47.4$ and (b) marginal stability curves for $\eta = 0.8$ and $\mathrm{Pr} = 10$ for isothermal case ($\gamma_a = 0$), the inward heating ($\gamma_a = -0.01$) and outward heating ($\gamma_a = 0.01$). Black and red curves correspond to stationary and oscillatory modes respectively. 66

4.7 (a) Variation of the growth rate with the criticality $\epsilon = \mathrm{Ta}/\mathrm{Ta}_c - 1$ and (b) marginal stability curves for $\eta = 0.8$, $\mathrm{Pr} = 50$ and $\gamma_a = -0.01$. Black and red curves correspond to stationary and oscillatory modes respectively. 66

4.8 Variation of the growth rate and of the frequency with the wave number k for $\eta = 0.8$ and Pr = 50 at Ta = Ta_c. The thermal expansion parameter $\gamma_a = 0.001 < {\gamma_a}^*$ in (a) and (b) and $\gamma_a = 0.01 > {\gamma_a}^*$ in (c) and (d). Black and red curves correspond to stationary and oscillatory modes respectively. 67

4.9 Stability analysis for $\eta = 0.8$, Pr = 50, and $\gamma_a = 0.01$: Variation of the growth rate (a) and the frequency (b) with the criticality $\epsilon = \mathrm{Ta}/\mathrm{Ta}_c - 1$, marginal curves of the first two unstable modes (c), variation of the frequency of the oscillatory modes with the wave number, i.e., dispersion relation (d). Black and red curves correspond to stationary and oscillatory modes respectively. 68

4.10 Energy generation terms for $\eta = 0.5$ as functions of (a) the thermal expansion parameter γ_a for $Pr = 50$ and (b) as function of the Prandtl number Pr for $\gamma_a = 0.01$. 69

4.11 Eigenfunctions at critical conditions with $\eta = 0.5$ and $\gamma_a = 0.01$. 70

4.12 Critical frequencies as a function of Brunt-Väisälä frequency. 72

4.13 Critical frequencies in units of $\beta\Omega$ (a) as function of the Prandtl number for $\gamma_a = 0.0004$, (b) as function of γ_a and (c) as function of the Brunt-Väisälä frequency. All these results have been obtained for $\eta = 0.99$. [52] 73

4.14 Total friction coefficient as function of Ta for different values of Pr and γ_a. The solid line corresponds to the isothermal laminar flow. 75

4.15 Variation of the heat transfer coefficients at the inner cylinder with Ta for different values of Pr and γ_a. (a) Pr = 10 and different values of $|\gamma_a|$, (b) Pr = 100 and $|\gamma_a| = 0.001$ and (c) Pr = 100 and $|\gamma_a| = 0.01$. 76

5.1 Marginal stability curves obtained for $\eta = 0.5$, Pr = 1000 and for $\gamma_a = -0.008$. The critical modes are axisymmetric. 80

5.2 Variation of the critical parameters with $-\gamma_a\mathrm{Pr}$ for different η: (a) Taylor number and (b) wavenumber. 81

5.3 Isovalues of the growth rate σ in the (k, Ta) plane for different radius ratio and different $\gamma_a\mathrm{Pr}$. Diagrams (a - c) are obtained for $\eta = 0.2$ and diagrams (d - f) are obtained for $\eta = 0.9$. The values of $-\gamma_a\mathrm{Pr}$ are: (a) 7.5, (b) 8, (c) 10, (d) 3.2, (e) 3.5 and (f) 5. 82

5.4 Eigenfunctions at critical conditions for Pr = 1000 and for different values of η and γ_a. 83

5.5 Variation of the critical parameters with $-\gamma_a \mathrm{Pr}$ for different η: (a) Taylor number and (b) wavenumber. 84

5.6 Power terms of the outer rotation regime (a) as function of $-\gamma_a \mathrm{Pr}$ for $\eta = 0.5$, and (b) as function of η for $\gamma_a \mathrm{Pr} = -10$. 85

5.7 Power terms in the Keplerian regime (a) as function of $-\gamma_a \mathrm{Pr}$ for $\eta = 0.5$, and (b) as function of η for $\gamma_a \mathrm{Pr} = -10$. 86

5.8 Variation of the critical parameters as functions of Pr for $\eta = 0.99$ and $\gamma_a = -0.01$ in the Keplerian regime: (a) Taylor number, (b) wavenumber and (c) frequency. . 87

6.1 Sketch showing the analogy between the rigidly rotating cylindrical annulus with heated outer cylinder and the Rayleigh-Bénard problem. 89

6.2 Variation of the critical parameters as fonctions of the radius ratio for different Pr and different γ_a: (a) Rayleigh number, (b) wavenumber and (c) normalized frequency. 92

6.3 Variation of (a) the critical axial wavenumber, (b) the critical azimuthal mode number and (c) the angle of vortices with respect to the azimuthal direction as function of the radius ratio for $\gamma_a \mathrm{Pr} = -10$. 93

6.4 Zones of critical states. Columnar modes are critical below the solid line, otherwise helical modes are critical. 94

6.5 Perturbation temperature profile and perturbation velocity field at the critical condition (a) in the (r, φ) plane (b) in the (φ, z) plane, and (c) in the (t, φ) plane for $\eta = 0.5$, $\mathrm{Pr} = 10$ and $\gamma_a = -0.01$. 94

6.6 Critical centrifugal Rayleigh number defined at the logarithmic radial position $R_{\ln,c}$ as a function of the radius ratio 95

6.7 (a) Critical normalized frequency ω_c/τ of columnar modes scaled with the parameter $-\gamma_a/\mathrm{Pr}$ as a function of the radius ratio, and (b) azimuthal phase velocity as a function of τ for $\gamma_a \mathrm{Pr} = -10$. 96

6.8 Variation of the power performed by the base centrifugal buoyancy W_{BBu} and of the power performed by the perturbation centrifugal buoyancy W_{PBu} with η for $\mathrm{Pr} = 10$ and $\gamma_a = -0.01$. 97

6.9 Flow and temperature fields in the (r, z) plane for $\eta = 0.5$, $\mathrm{Ra} = 1811$, $\mathrm{Pr} = 1$ and $\gamma_a = -0.01$: (a) velocity fields and pressure, (b) avial vorticity, and (c) temperature. 98

6.10 Variation of the Nusselt number with Ra for $\eta = 0.5$, Ra $= 1811$, Pr $= 1$ and $\gamma_a = -0.01$. 98

7.1 Variation of the critical parameters with the radius ratio: (a) electric Rayleigh number for different γ_e and (b) wavenumber and angle of the vortices with respect to the azimuthal direction for $\gamma_e = 0.01$. [33] 104

7.2 Power given by the base and perturbation electric gravity (W_{BG} and W_{PG} respectively) as function of the radius ratio for different γ_e. [33] 105

7.3 Variation of the Nusselt number with the electric Rayleigh number: (a) for $\eta = 0.1$, $\gamma_e = 0.01$ and for different Pr, (b) for $\eta = 0.5$, $\gamma_e = 0.01$ and for different Pr, (c) for $\eta = 0.3$, Pr $= 10$ and for different γ_e, and (d) for $\eta = 0.7$, Pr $= 100$ and for different γ_e. [42, 43] 106

8.1 Sketch of the directions of the gravity fields with respect to the temperature gradient.110

8.2 Marginal stability curves in the (k, Ra) plane for $\eta = 0.5$, Pr $= 10$, $\gamma_a = \gamma_e = -0.01$, $V_E = 100$ and for different azimuthal mode number. 110

8.3 Variation of the critical values with V_E for $\eta = 0.5$, $\gamma_a = \gamma_e = -0.01$, and for different Prandtl number. (a) centrifugal Rayleigh number, (b) wavenumber, and (c) frequency. 111

8.4 Perturbation temperature and perturbation velocity fields: (a) in the (r, φ) plane (b) in the (φ, z) plane, and (c) in the (t, φ) plane for $\eta = 0.5$, Pr $= 10$ and $\gamma_a = \gamma_e = -0.01$ and $V_E = 600$ at the critical condition ($\mathrm{Ra}_c = -211.6$). 112

8.5 Critical values of (a) the electric Rayleigh number, and (b) the normalised frequency for $\eta = 0.5$ and Pr $= 10$ in inward heating. 113

8.6 Variation of the critical parameters with V_E for Pr $= 10$, $\gamma_a = \gamma_e = -0.01$ and for different η: (a) centrifugal Rayleigh number, (b) wavenumber, and (c) normalised frequency. 115

8.7 Sketch of the directions of the gravity fields with respect to the temperature gradient.116

8.8 Marginal stability diagram in the (k, V_E) plane for $\eta = 0.5$, Pr $= 10$, $\gamma_a = \gamma_e = 0.01$, $\tau = 1.63$ (a) and $\tau = 163.30$ (b) and for different azimuthal mode number. 116

8.9 Variation of the critical electric Rayleigh number with τ for $\eta = 0.5$, $\gamma_a = \gamma_e = 0.01$, and for different Prandtl number. 116

8.10 Variation of the critical values with the centrifugal Rayleigh number for $\eta = 0.5$, $\gamma_a = \gamma_e = 0.01$, and for different Prandtl number: (a) electric Rayleigh number (b) wavenumber and normalized frequency (c) of ONA modes and (d) of OC modes. . 117

8.11 Critical normalised frequency of OC modes as a function of Ra for different Prandtl numbers close to $\omega_c/\tau = 0$. The critical frequency changes its sign at a constant value of Ra. 118

8.12 Perturbation temperature and perturbation velocity fields of an ONA mode (Ra = 5) in (a) the (r, φ) plane, (b) in the (φ, z) plane and (c) in the (t, φ) plane, and of an OC mode (Ra = 4000) in (d) the (r, φ) plane, (e) in the (φ, z) plane and (f) in the (t, φ) plane at the critical condition for $\eta = 0.5$, $\gamma_a = \gamma_e = 0.01$ and Pr = 10. . 119

8.13 Variation of the critical parameters with Ra for $\eta = 0.5$, Pr = 10 and for different γ_a and γ_e: (a) electric Rayleigh number, (b) wavenumber, (c) normalised frequency of ONA modes and (d) normalised frequency of OC modes. 120

8.14 Threshold fitted with a polynomial function of second order for $\eta = 0.5$, Pr = 10: (a) Ra_c against V_E in inward heating with $\gamma_a = \gamma_e = -0.01$ ($P_1^i = 0.0067; P_2^i = 0.0638; P_3^i = 1774.4$) and (b) L_c against τ in outward heating with $\gamma_a = \gamma_e = 0.01$ ($P_1^o = 0.0300; P_2^o = 0.3058; P_3^o = 1527.9$). 121

8.15 Power given by the different mechanisms for $\eta = 0.5$, Pr = 10 (a) in inward heating against V_E with $\gamma_a = \gamma_e = -0.01$ and (b) in outward heating against τ with $\gamma_a = \gamma_e = 0.01$. 122

8.16 Critical normalised frequency scaled with the parameter γ_a/Pr in outward heating for (a) different Pr with $\gamma_a = \gamma_e = -0.01$ and (b) for different γ_a with $\gamma_e = -0.01$ and Pr = 10. 123

8.17 Critical normalised frequency of OC modes scaled with the parameter γ_a/Pr in outward heating for (a) different Pr with $\gamma_a = \gamma_e = 0.01$ and (b) for different γ_a with $\gamma_e = 0.01$ and Pr = 10. 123

8.18 Critical wavenumber in outward heating for (a) different Pr with $\gamma_a = \gamma_e = 0.01$ and (b) for different γ_a with $\gamma_e = 0.01$ and Pr = 10. 124

9.1 Variation of the critical parameters with η for Pr = 0.72 and $V_E = 0$: (a) Grashof number (b) frequency, (c) axial wavenumber and (d) azimuthal mode number. . . 129

9.2 Variation of the critical parameters with V_E for $Pr = 10$, $Ga = 1370$, $\delta = 0.1$ and for different values of η: (a) Grashof number, (b) axial wavenumber, (c) azimuthal mode number, (d) total wavenumber and (e) frequency. 130

9.3 Variation of the critical parameters with V_E for $\eta = 0.5$, $Ga = 1370$, $\delta = 0.1$ and for different values of Pr: (a) Grashof number, (b) axial wavenumber, (c) azimuthal mode number, (d) total wavenumber and (e) frequency. 131

9.4 Variation of the critical parameters with the electric Rayleigh number for Ga = 1370, $\eta = 0.5$, Pr = 10 and for different δ: (a) Grashof number, (b) axial wavenumber, (c) azimuthal mode number, (d) total wavenumber and (e) frequency. 132

9.5 Temperature and velocity fields at the critical condition for Ga = 1370, $\delta = 0.1$, $\eta = 0.5$ and for (a) a hydrodynamic mode (Pr = 0.72, $V_{E,c} = 200$, $\mathrm{Gr}_c = 8342$, $k_c = 2.747$ and $n_c = 0$), (b) a thermal mode (Pr = 10, $V_{E,c} = 113$, $\mathrm{Gr}_c = 3150$, $k_c = 1.604$ and $n_c = 0$), (c) a stationary columnar mode (Pr = 10, $V_{E,c} = 512$, $\mathrm{Gr}_c = 1760$, $k_c = 0$ and $n_c = 5$) and (d) a stationary helical mode (Pr = 10, $V_{E,c} = 4780$, $\mathrm{Gr}_c = 20$, $k_c = 1.674$ and $n_c = 4$). 133

9.6 Variation of the energy generation terms with the dimensionless electric potential V_E. These curves has been obtain for $Ga = 1370$, $\delta = 0.1$, $Pr = 10$ and $\eta = 0.5$. . 134

A.1 Sketch showing the different gravity phases encountered during one parabola. Courtesy of Novespace. 143

A.2 Time variation of the different components of the acceleration during a parabolic flight. The acceleration values are normalized by the earth gravity intensity. . . . 144

A.3 Participants of the parabolic flight campaign of October 2016 in front of the ZERO G aircraft. From the left to the right: R. Stöbel, V. Ruoff, M. Jongmanns, M. Meier, A. Meyer, I. Mutabazi, C. Egbers. 144

A.4 Schematic representation of the light beam trajectories inside the cells. The light beams are refracted due to the inhomogeneity of the fluid optical index n_f which is a function of the temperature. 145

A.5 Schematic representation of the different instability modes that can appear in a cylindrical gap. 146

A.6 Temperature profile (color) and trajectories of a selection of light beams (black) in the (r, z) plan for different ΔT. 149

A.7 Relative intensity as function of the radial position for stable states. 150

A.8 (a): relative intensity as function of the radial position for different ΔT and T_{amp} with $p = 10$ and (b): relative intensity at the mid-gap as function of the axial modes number for different T_{amp}. 151

A.9 (a): relative intensity as function of the azimuthal angle for different shape of modes with $T_{amp} = 0.2K$ and (b): maximum of the relative intensity at as function of the deviation angle of the modes with respect to the azimuthal direction with $T_{amp} = 0.2K$. 152

A.10 Shadowgraph images for (a) axisymmetric mode ($m = 0; p = 10$), (b) spiral mode ($m = 4; p = 5$) and (c) collumnar mode ($m = 5; p = 0$) both for $DT = 1K$ and $T_{amp} = 0.2K$. 152

A.11 Results for the base flow of (a) temperature distribution and trajectories of some light beams shown by the black lines and (b) resulting 1D shadowgraph images. The temperature difference is $DT = 1K$ 154

A.12 (a) Contour, (b) radial distribution and (c) azimuthal distribution of the shadowgraph red level (RL) with $\Delta T = 0$ K and V_{peak})0 kV. 155

A.13 Radial profile of the light intensity for different temperature differences between the two cylinders. 156

A.14 Shadowgraph images obtained for different temperature differences and different applied electric potential. 157

A.15 Comparison between the linear stability diagram obtained for the silicone oil AK5 under earth gravity conditions (black curve) and the experimental results in the dimensional plan ($V_{peak}, \Delta T$). The blue circles correspond to axisymmetric intensity profiles while the red crosses exhibit non-axisymmetric patterns. 158

A.16 Shadowgraph images obtained at the end of the three different gravity phases with $\Delta T \approx 10$K and without applied electric tension. 159

A.17 Shadowgraph images obtained at the end of the normal gravity phase and of the microgravity phase with $\Delta T \approx 10$K and for different applied electric tensions. . . 160

A.18 Time variation of the light intensity measured in the azimuthal direction at $r = 5/7R_2$ during a parabola. The electric potential is always active with $V_0 = 6.36kV$ and $\Delta T \approx 10K$. 161

A.19 Patterns of the light intensity distribution. All images are captured at $V_0 = 6.36kV$ and $\Delta T \approx 10$K. The images (a), (b) and (c) are taken at the end of the $1g$, $1.8g$ and $0g$ phases respectively. 161

List of Tables

2.1 Expressions of the Taylor number and of the base azimuthal velocity depending on the rotation regime. 35

3.1 Critical Taylor number and critical wave number for different η. All the critical modes are axisymmetric ($n_c = 0$). 48

4.1 Values of the threshold slope $\mathrm{Ta}_c(\gamma_a)/\mathrm{Ta}_c(\gamma_a = 0)$ as function of γ_a computed at $\gamma_a = 0$ for different η and Pr. 63

4.2 Variation of dispersion properties of the critical modes with Pr for $\eta = 0.5, \gamma_a = 0.01$. 73

4.3 Critical parameters and coefficients of the Ginzburg-Landau equation against Pr and γ_a ($\eta = 0.8$). 74

6.1 Critical parameters and coefficients of the complex Ginzburg-Landau equation computed by LSA and DNS. 97

8.1 Critical Coriolis number at the codimension-2 point between ONA modes and OC modes in inward heating for different radius ratio. 125

A.1 Properties of silicone oil AK5: $\varepsilon_r = \varepsilon_2/\varepsilon_0$ is the relative electric permittivity, where ε_0 is the permittivity of the vacuum. Properties data are given by the manufacturer and have uncertainties e.g. 10% for the kinematic viscosity. 142

A.2 Critical dimensionless electric potential for the different states of gravity. 160

Chapter 1

Introduction

In geophysics and astrophysics, large scale flows are mainly induced by radial gravitational fields. Coupled with temperature gradients, the gravity field, as well as the centrifugal acceleration and magnetic fields, can generate convective flows in the core of the planets and stars. In this framework, many author have investigated the flow of a fluid confined in a spherical shell [1, 2, 3, 4, 5]. Aiming to have a purely central force field, experiments in weightlessness are of most interest. The application of a radial electric field combined with a temperature gradient is a way to obtain a centripetal effective gravity field. Using this method, experiments have been performed on-board the international space station to obtain long time micro-gravity conditions [6, 7, 8, 9, 10].

The flow of a fluid confined between two concentric cylinders is a model for geophysical flows in the equatorial region of planets and stars, where the direction of gravity and that of the temperature gradient are nearly parallel. It is also a prototype in non-linear physics, since it exhibits a large variety of bifurcation phenomena. In addition, many applications involve the flow induced by centrifugal force together with thermal buoyancy, such as microfluidic systems and heat exchangers [11, 12, 13]. For these reasons, the convective flow induced by centrifugal forces and various thermal buoyancies in a differentially rotating and heated cylindrical annulus has been studied to reinforce existing knowledge.

1.1 Previous work

1.1.1 Taylor-Couette instability

A fluid confined between two concentric cylinders rotating at different rotation rates can undergo instabilities because of the competition of the stabilising effect of the viscous dissipation and the destabilising effect of the centrifugal force. This mechanism is called the Taylor-Couette instability and was first successfully studied theoretically and experimentally by Taylor in 1923 [14] where he considered the small gap approximation. The larger gap problem was then studied by Chandrasekahar in 1958 [15]. Andereck et al. [16] performed in 1986 an exhaustive experimental study, while investigating not only the primary instability, but also regimes of more complex properties observed at higher instability level.

1.1.2 Thermo-hydrodynamic instability

Applying a temperature difference between the two cylinders provides a radial density stratification. The rotation of the cylinders gives rise to the centrifugal acceleration which acts on this stratification and changes the stability conditions. Many authors theoretically investigated this problem through a linear stability analysis while considering a weightless environment. Yih [17] considered steady axisymmetric perturbations and showed in 1961 that if the circulation increases with the radial distance, which is a Rayleigh stable condition, but the density decreases, the flow can be less stable or even unstable. In 1964, Walowit et al. [18] realised a similar analysis for a wide range of gap size, but only for Rayleigh unstable conditions. They found that positive and negative temperature gradients are destabilizing and stabilizing, respectively. Soundalgekar et al. (1981) [19] and Takhar et al. (1985, 1990) [20, 22] confirmed the results of Walowit et al. in the case of a narrow gap with a heated outer cylinder at rest. In 1988, Takhar et al. [21] showed that a constant heat flux at the inner cylinder enhances the stability of the flow and that decreasing the gap-width has a destabilising effect. In 1994, Kong et al. [23] considered the stability of flows in counter-rotating regimes against non-axisymmetric perturbations for different gap widths. They found that oscillatory helical modes can occur in the isothermal case and that the temperature gradient has an impact on the number of modes in the azimuthal direction. Auer et al. [24] added a weakly non-linear study to their linear stability analysis when both cylinders rotate at the same frequency. They found that heating the outer cylinder leads to a convective regime of columnar

modes. Eagles et al. (1997) [25], and Panday et al. (2015) [26] considered a constant heat flux at the outer cylinder for several rotation regimes. They confirmed the destabilising effect of the centrifugal buoyancy and found that the wavenumber of the modes decreases with increasing the temperature difference.

The effect of the Earth's gravity on a vertical differentially heated cylindrical annulus has also been studied theoretically, numerically and experimentally. Choi and Korpela [27] performed in 1980 a linear stability analysis of this problem with positive temperature gradients and compared their theoretical results with experimental ones. The critical modes are axisymmetric and drift upward. The computed thresholds, wavelength and velocities of the modes agreed with those measured experimentally. In 2000, Bahloul et al. [28] highlighted the existence of two different mechanisms for the occurrence of instabilities using a linear stability analysis. Depending on the fluid diffusion properties and on the radius ratio between the two cylinders, the critical modes can have either a hydrodynamic nature or a thermal nature.

In 1964, Snyder and Karlsson [29] performed an experimental study of a fluid confined between an inner rotating cylinder and an outer stationary one. They noticed the occurrence of helical modes when the temperature gradient was applied. Ball and Farouk studied the same problem numerically with a finite volume of fluid [30] and experimentally [31]. They characterised the bifurcation from the quasi-isothermal Taylor-Couette instability to the flow dominated by axial buoyancy through the variation of the ratio between the Grashof number and the square of the inner Reynolds number σ. They found that when $0.01 < \sigma < 10$, the critical modes take the form of helical modes. Ali and Weidman [32] investigated the problem by a linear stability theory for infinite length cylinders of different radius ratios for fluids with different values of the Prandtl number. They found that increasing the Prandtl number destabilises the flow. They compared their results with previous experiments and found a good agreement. In 2013, Yoshikawa et al. [33] also used a linear stability theory for both directions of the temperature gradient. They found that the centrifugal buoyancy can induce an asymmetry between positive and negative temperature gradients on the critical state.

1.1.3 Convection induced by centripetal gravity

In the framework of astrophysical and geophysical research, some authors investigated theoretically the stability of the flow in a cylindrical annulus with an imposed centripetal acceleration

field. In 1981, Economides and Moir [34] performed a linear stability analysis of a fluid confined between a cold rotating inner cylinder and a warm stationary outer one with a narrow gap in an artificial radial gravity field. The gravity field was assumed radially invariant. They found that for sufficiently large values of the Prandtl number, critical modes can be helical. Alonso et al. in 1995 and in 1999 [35, 36] performed a linear stability analysis of a rotating cylindrical annulus with a negative temperature gradient and a constant central gravity field. The annulus has a finite aspect ratio. The authors considered the effect of the boundary conditions imposed at both ends of the annulus. They highlighted the transition from columnar modes to helical ones depending on the radius ratio and the aspect ratio. The columns were found to be stationary in the rotating frame when stress free conditions were used, and oscillatory when no-sleep conditions were used. In the aboved-mentioned investigations [34, 35, 36], the effect of the centrifugal acceleration on the density stratification, i.e. the centrifugal buoyancy, was not taken into account.

1.1.4 Thermo-electro-hydrodynamic instability

A cylindrical annulus of a dielectric fluid subjected to a temperature gradient and an high alternating electric tension undergoes the dielectrophoretic (DEP) force which can be seen as a thermal buoyancy in an effective gravity field of electric nature. In 1972, Chandra and Smylie [38] carried out an experiment with a vertical stationary cylindrical annulus subjected to the DEP force. They also performed a linear stability analysis and compared the experimental results with the theoretical ones. They demonstrated the feasibility of inducing convective flow using the DEP force. The agreement between the stability analysis and the experimental results proved the validity of the simplifications used in the stability analysis. In 1979, Takashima [39] analysed the problem with a narrow gap using linear stability theory. He found that a positive (negative) temperature gradient (de)stabilises the flow as the radius ratio decreases. When the temperature gradient is positive, there exists a value of the radius ratio bellow which no instability occurs. Stiles and Kagan [40] also performed in 1993 a linear stability analysis of the problem with a narrow gap and a rotating inner cylinder. They considered the stability of the flow against stationary axisymmetric modes. When the electric potential is not applied, they found the stabilisation of the circular Couette flow when they decreased the temperature gradient from positive to negative values. With a large electric potential, the critical Taylor number decreases with decreasing the temperature gradient. Malik et al. [41] studied in 2012 the stability of the flow between two

stationary cylinders under microgravity condition against non-axisymmetric oscillatory modes with a negative temperature gradient. The critical mode and the critical Rayleigh number are independent of the Prandtl number, while they depend on the curvature of the cylinders. Critical modes take the form of stationary helical modes. Yoshikawa et al. [33] extended the analysis of Malik et al. one year later with considering positive temperature gradients. The analysis of the different energy transfer mechanisms from the base state to perturbation flows showed that, for strong thermo-electric coupling, the flow is stabilised by the perturbation component of the electric gravity. They also showed that, for positive temperature gradients, instabilities are found for narrow gaps, which is in agreement with the results of Takashima. Travnikov et al. [42, 43] performed a numerical simulation of a cylindrical annulus under microgravity conditions with a negative temperature gradient close to the onset of convective flow. Their results are in good agreement with the previous linear stability analyses [41, 33]. The bifurcation from the conductive state to the convective state was found to be supercritical. The evolution of the heat transfer with the electric Rayleigh number is sensitive to the Prandtl number for low radius ratio. The thermoelectric coupling for small gaps has a stabilising effect and decreases the slope of the Nusselt number as function of the electric Rayleigh number. In 2016, Futterer et al. [44] made experiments consisting on a cylindrical annulus under microgravity conditions during a parabolic flight campaign. They found the increase of the Nusselt number when the electric Rayleigh number is larger than the critical value.

1.2 Thesis organisation

This thesis consists on the study of the bifurcations from a base state to an unstable flow using linear stability analysis (LSA). Such bifurcations are accompanied with heat transfer enhancement and increase of the torque at the cylindrical surfaces. The objective of this thesis is to evaluate the effect of the centrifugal buoyancy and of the dielectrophoretic force on the stability of different flow configurations in order to provide quantitative results on the critical thresholds and on the spatial and temporal nature of the unstable state. The effects of different parameters, such as the geometry, the fluid diffusive properties or the temperature gradient are also investigated. Chapter 2 is dedicated to the formulation of the problem and of the method used to performed the LSA. Then the thesis is divided in two parts.

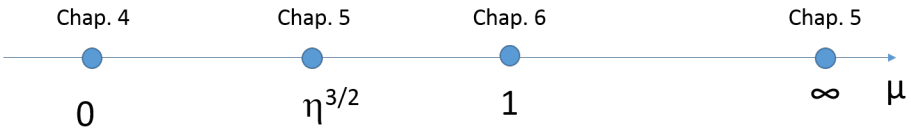

Figure 1.1: Diagram of the different chosen values of μ associated with the chapter where they will be studied.

In the first part, the effect of the centrifugal buoyancy on the circular Couette flow under weightlessness is analysed. As an introduction, the method is applied to the isothermal case for different rotation regimes in Chapter 3. Then the effect of the centrifugal buoyancy is considered on a Rayleigh unstable regime in Chapter 4. In this chapter, we investigated the case $\mu = 0$, where μ is the ratio between the rotation rates of the outer and of the inner cylinders. Chapter 5 is dedicated to the cases where $\mu = \infty$ and $\mu = \eta^{3/2}$, which are two Rayleigh stable regimes. In Chapter 6, the solid body rotation is investigated, i.e. $\mu = 1$. This regime is also Rayleigh stable, but is analysed in a different chapter since solid rotation enable analogies with the Rayleigh-Bénard convection. Figure 1.1 shows the different chosen values of μ in correspondence to the different chapters.

In the second part, the effect of the DEP force on the stability of a fluid confined in a cylindrical annulus is analysed. As an introduction, results based on previous works on the application of the DEP force in a cylindrical annulus are presented in Chapter 7. Chapter 8 is dedicated to the application of the thermoelectric buoyancy to a rigidly rotating annulus of fluid. Then we considered the effect of the DEP force on a stationary annulus of fluid submitted to the Earth's gravity in Chapter 9. General conclusions and outlooks are given in Chapter 10

An additional chapter dealing with experimental results is given in Appendix A. The results obtained in this part come from a collaboration between the University of Le Havre and the Brandenbourgische Technische Universität Cottbus-Senftenberg. This chapter contains experimental results obtained in laboratory, as well as during parabolic flight campaigns. In addition, simulations of shadowgraph method have been performed.

A part of obtained results during the thesis has been published in scientific journals and presented to conferences:

Publications

- H.N. Yoshikawa, A. Meyer, O. Crumeyrolle, and I. Mutabazi, Linear stability of a circular Couette flow under a radial thermoelectric body force, *Phys. Review E* **91**, 033003 (2015).
- A. Meyer, H.N. Yoshikawa and I. Mutabazi, Effect of the radial buoyancy on a circular Couette flow, *Phys. Fluids* **27**, 114104 (2015).
- A. Meyer, M. Jongmanns, M. Meier, C. Egbers, and I. Mutabazi, Thermal convection in a cylindrical annulus under a combined effect of the radial and vertical gravity, *C. R. Mécanique* **345**, 11-20 (2017).
- C. Kang, A. Meyer and I. Mutabazi, Radial buoyancy effects on momentum and heat transfer in a circular Couette flow, *Phys. Review F* **2**, 053901 (2017).

Oral Communications

- A. Meyer, H.N. Yoshikawa, O. Crumeyrolle, and I. Mutabazi, *Instabilities of the Taylor-Couette flow subjected to a radial temperature gradient and a radial electric field*, **ISTROF, Le Havre** (2014).
- A. Meyer, H.N. Yoshikawa and I. Mutabazi, *Effect of the radial buoyancy on the stability of Taylor-Couette flow*, **ICTW-19, Cottbus** (2015).
- A. Meyer, M. Jongmanns, O. Crumeyrolle, M. Meier, C. Egbers and I. Mutabazi, *Résultats de convection thermique induite par champ électrique en vol parabolique*, **GdR-MFA-2798, Belgodere** (2016).
- A. Meyer, C. Kang, H.N. Yoshikawa, and I. Mutabazi, *Convection thermique d'un fluide diélectrique confiné dans un anneau cylindrique en rotation auquel est appliquée une force diélectrophorétique*, **RNL, Paris** (2017).
- A. Meyer, C. Kang, M. Jongmanns, H.N. Yoshikawa, M. Meier, C. Egbers and I. Mutabazi, *Convection thermique dans un anneau cylindrique chauffé de l'intérieur et sous tension électrique alternative*, **CIFQ-13, Saint-Lô** (2017).
- A. Meyer, C. Kang, H.N. Yoshikawa and I. Mutabazi, *Convection thermique d'un fluide diélectrique confiné dans un anneau cylindrique en rotation auquel sont appliqué un gradient de température et une tension électrique alternative*, **CFM-23, Lille** (2017).

- A. Meyer, O. Crumeyrolle, C. Kang, H.N. Yoshikawa, M. Jongmanns, M. Meier, T. Seelig, V. Travnikov, C. Egbers and I. Mutabazi, *Flow pattern and heat transfer in a cylindrical annulus under 1g and low-g conditions: theory and simulation*, **ISPS-7 & ELGRA-25, Juan-les-Pins** (2017).

Chapter 2

Problem formulation

We consider a Newtonian dielectric fluid of density ρ, kinematic viscosity ν, thermal diffusivity κ and permittivity ε confined between two coaxial vertical cylindrical electrodes of infinite length (Fig. 2.1). The inner cylinder, of radius R_1, maintained at a temperature T_1 rotates with an

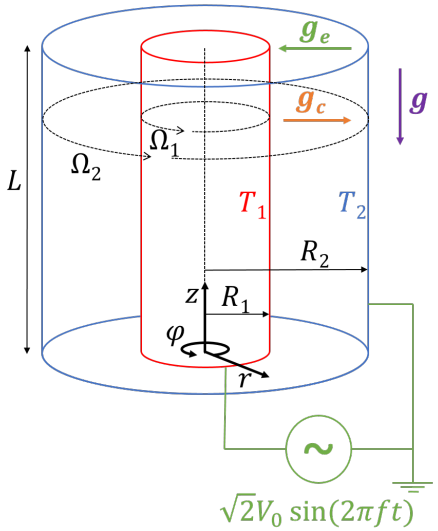

Figure 2.1: Sketch of the flow configuration.

angular velocity Ω_1 while the outer cylinder, of radius $R_2 = R_1 + d$, maintained at another temperature $T_2 \neq T_1$ rotates with an angular velocity Ω_2. In addition, an alternating electric potential is applied between the two electrodes, which gives rise to a radial electric field. The temperature difference $\Delta T = T_1 - T_2$ induces a radial stratification in density and in permittivity, which are, in most cases, both decreasing functions of the temperature. Under these conditions, three thermal buoyancies are present.

- The Earth's gravity acts on the density stratification and gives rise to the Archimedean

buoyancy.

- The centrifugal force also acts on the density stratification and brings about the centrifugal buoyancy.

- The electric field acts on the permittivity gradient to produce the dielectrophoretic force.

These three buoyancies will be considered in various configurations, together or separately, and can be sources of instabilities of different natures.

2.1 The dielectrophoretic force

When an electric field is applied to a dielectric liquid with a permittivity gradient, it undergoes the electrohydrodynamic (EHD) force given per unit volume by [45]:

$$\boldsymbol{F}_{EHD} = \boldsymbol{F}_{EP} + \boldsymbol{F}_{DEP} + \boldsymbol{F}_{ES} \tag{2.1}$$

Figure 2.2 gives a simple representaion of the mechanism of the different terms of Eq. (2.1). The first term $\boldsymbol{F}_{EP}$ is the electrophoretic force. It results from the action of the electric field on free charges and is given by the relation:

$$\boldsymbol{F}_{EP} = \rho_e \boldsymbol{E} \tag{2.2}$$

where $\boldsymbol{E}$ is the electric field and ρ_e is the density of free charges. If the applied tension is alternating with a high frequency compared to the inverse of the charge relaxation time $\tau_e = \varepsilon/\sigma_e$, where σ_e is the electric conductivity, the electrophoretic force can be neglected. In fact, the charge relaxation

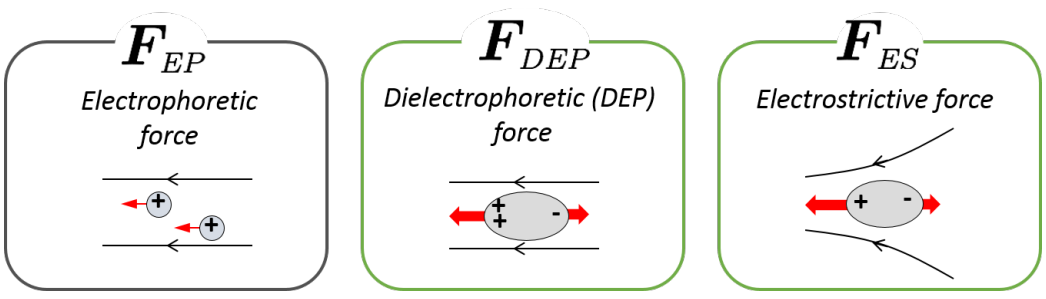

Figure 2.2: Skech of the physical mechanism of the different terms of the electrohydrodynamic force.

time characterises the accumulation process of charges within a fluid. The high frequency of the electric field prevents from this accumulation and makes the fluid electrically neutral [46].

The third term $\boldsymbol{F}_{ES}$ of equation (2.1) is the electrostrictive force and is given by:

$$\boldsymbol{F}_{ES} = \boldsymbol{\nabla}\left[\frac{1}{2}\rho\left(\frac{\partial\varepsilon}{\partial\rho}\right)_T E^2\right] \tag{2.3}$$

As long as the fluid is incompressible or monophasic without any mobile boundary, the electrostrictive force will not play any dynamical role and will be include in the pressure gradient of the momentum equations.

The second term $\boldsymbol{F}_{DEP}$ of Eq. (2.1) is the dielectrophoretic (DEP) force. It arises from the differential polarisation of fluit and is given by:

$$\boldsymbol{F}_{DEP} = -\frac{1}{2}E^2\boldsymbol{\nabla}\varepsilon \tag{2.4}$$

Within the previous assumption, the DEP force is the dominant one and can arise from a temperature difference applied to the fluid. Indeed, the DEP force is proportional to the gradient of the electric permittivity, which is, for most fluids, a decreasing function of the temperature. Its variation will be modelled by the linear relationship $\varepsilon(T) = \varepsilon_{ref}\left[1 - e\left(T - T_{ref}\right)\right]$, where ε_{ref} is the permittivity at the reference temperature T_{ref}. The coefficient e is the coefficient of thermal variation of permittivity and takes positive value of the order of $10^{-3}\ K^{-1}$ to $10^{-1}\ K^{-1}$. Taking into account the linear variation of the permittivity, the DEP force (2.4) can be written:

$$\boldsymbol{F}_{DEP} = -e\left(T - T_{ref}\right)\boldsymbol{\nabla}\frac{\varepsilon_{ref}E^2}{2} + \boldsymbol{\nabla}\left(\frac{e\left(T - T_{ref}\right)E^2}{2}\right) \tag{2.5}$$

The second term in (2.5) is a gradient which can be lumped with the pressure gradient term in the momentum equation. The fist term correspond to the thermoelectric buoyancy and can be written in the form $-\alpha\left(T - T_{ref}\right)\boldsymbol{g}_e$. The choice of this notation highlights the analogy between the thermal Archimedean buoyancy and the thermoelectric buoyancy where the Earth gravity is replaced by an effective gravity $\boldsymbol{g}_e$ of electric nature given by:

$$\boldsymbol{g}_e = \frac{e}{\alpha\rho_{ref}}\boldsymbol{\nabla}\frac{\varepsilon_{ref}E^2}{2} \tag{2.6}$$

where α is the thermal expansion coefficient and ρ_{ref} is the density at the reference temperature. The electric gravity corresponds to the gradient of the electric energy density in the fluid. The analogy implies that thermal convection can be induced by the thermoelectric buoyancy.

2.2 Governing equations

The temperature difference ΔT being sufficiently small, the electrohydrodynamic Boussinesq approximation can be adopted [47]. Thus fluid properties can be considered as constant, except in the terms responsible for the change of stability condition. In these terms, the density is also approximated by the linear functions $\rho(\theta) = \rho_{ref}(1 - \alpha\theta)$, $\theta = T - T_{ref}$ being the temperature deviation from the reference temperature. This Boussinesq approximation remains valid as long as the rotation rates of the two cylinders are low enough to neglect the density variation in the other advection terms than the centrifugal acceleration term [48].

As the frequency of the electric tension is high compared to the inverse viscous time scale $\tau_\nu = d^2/\nu$ and to the inverse thermal time scale $\tau_\kappa = d^2/\kappa$, we can assume that nothing happens during an oscillation of the electric potential. So all the equations can be time-averaged over a period of the electric field and the imposed electric potential $\sqrt{2}V_0 \sin(2\pi f t)$ can be replaced by its effective value V_0. Turnbull and Melcher found that this assumption predicted successfully the onset of the DEP thermal convection [49]. The velocity field $\boldsymbol{u} = (u, v, w)$, the temperature deviation θ, the generalized pressure π and the electric potential ϕ are determined by the continuity equation, the Navier-Stokes equations, the energy equation and the Gauss' law of electricity in the cylindrical polar coordinates (r, φ, z) in the laboratory frame of reference:

$$\boldsymbol{\nabla} \cdot \boldsymbol{u} = 0 \tag{2.7a}$$

$$\frac{\partial \boldsymbol{u}}{\partial t} + (\boldsymbol{u} \cdot \boldsymbol{\nabla})\, \boldsymbol{u} = -\boldsymbol{\nabla}\pi + \nu\Delta\boldsymbol{u} - \alpha\theta\,(\boldsymbol{g} + \boldsymbol{g}_c + \boldsymbol{g}_e) \tag{2.7b}$$

$$\frac{\partial \theta}{\partial t} + (\boldsymbol{u} \cdot \boldsymbol{\nabla})\, \theta = \kappa\Delta\theta \tag{2.7c}$$

$$\boldsymbol{\nabla} \cdot (\varepsilon \boldsymbol{E}) = 0 \quad \text{with} \quad \boldsymbol{E} = -\boldsymbol{\nabla}\phi \tag{2.7d}$$

where the three accelerations $\boldsymbol{g}$, $\boldsymbol{g}_c$ and $\boldsymbol{g}_e$ are given by:

$$\boldsymbol{g} = -g\boldsymbol{e}_z\,, \quad \boldsymbol{g}_c = \frac{v^2}{r}\boldsymbol{e}_r\,, \quad \boldsymbol{g}_e = \frac{e}{\alpha\rho}\boldsymbol{\nabla}\frac{\varepsilon_2 E^2}{2} \tag{2.8}$$

The generalized pressure π includes the conservative term of the DEP force (2.5), the ES force (2.3) and the hydrostatic pressure:

$$\pi = \frac{p}{\rho_2} + gz - \frac{e\theta\varepsilon_2 E^2}{2\rho_2} - \frac{1}{2}\left(\frac{\partial\varepsilon}{\partial\rho}\right)_\theta E^2 \tag{2.9}$$

The flow and electric fields satisfy Dirichlet conditions at the two cylinder surfaces:

$$\begin{cases} \boldsymbol{u} = R_1\Omega_1\boldsymbol{e}_\varphi, & \theta = \Delta T, & \phi = V_0 & \text{at } r = R_1 \\ \boldsymbol{u} = R_2\Omega_2\boldsymbol{e}_\varphi, & \theta = 0, & \phi = 0 & \text{at } r = R_2 \end{cases} \tag{2.10}$$

To make the equations dimensionless, we used the gap width d as the length scale, the characteristic time of viscous dissipation d^2/ν as the time scale, the temperature difference ΔT as the temperature scale, the effective electric potential V_0 as the potential scale and $(\nu/d)^2$ as the pressure scale. From now, unless it is specified, all quantities are dimensionless. The equations (2.7) can then be written in the following forms:

$$\boldsymbol{\nabla}\cdot\boldsymbol{u} = 0 \tag{2.11a}$$

$$\frac{\partial\boldsymbol{u}}{\partial t} + (\boldsymbol{u}\cdot\boldsymbol{\nabla})\,\boldsymbol{u} = -\boldsymbol{\nabla}\pi + \Delta\boldsymbol{u} + \mathrm{Gr}\theta\boldsymbol{e}_z - \gamma_a\theta\frac{v^2}{r}\boldsymbol{e}_r - \frac{\gamma_e V_E^2}{\mathrm{Pr}}\theta\boldsymbol{g}_e \tag{2.11b}$$

$$\frac{\partial\theta}{\partial t} + (\boldsymbol{u}\cdot\boldsymbol{\nabla})\,\theta = \frac{1}{\mathrm{Pr}}\Delta\theta \tag{2.11c}$$

$$\boldsymbol{\nabla}\cdot[(1-\gamma_e\theta)\,\boldsymbol{\nabla}\phi] = 0 \tag{2.11d}$$

where the dimensionless electric gravity $\boldsymbol{g}_e$ is given by:

$$\boldsymbol{g}_e = \frac{1}{2}\boldsymbol{\nabla}\left(\boldsymbol{\nabla}\phi\right)^2 \tag{2.12}$$

In the equations (2.11), dimensionless numbers have been introduced:

$$\text{The Prandtl number:} \qquad \mathrm{Pr} = \frac{\nu}{\kappa} \tag{2.13a}$$

$$\text{The radius ratio:} \qquad \eta = \frac{R_1}{R_2} \tag{2.13b}$$

$$\text{The Grashov number:} \qquad \mathrm{Gr} = \frac{\alpha \Delta T g d^3}{\nu^2} \tag{2.13c}$$

$$\text{The dimensionless electric potential:} \qquad V_E = \frac{V_0}{\sqrt{\rho_2 \nu \kappa / \varepsilon_2}} \tag{2.13d}$$

$$\text{The thermal expansion parameter:} \qquad \gamma_a = \alpha \Delta T \tag{2.13e}$$

$$\text{The thermoelectric parameter:} \qquad \gamma_e = e \Delta T \tag{2.13f}$$

The boundary conditions read:

$$\begin{cases} \boldsymbol{u} = f_1(\mathrm{Ta}, \eta) \boldsymbol{e}_\varphi, \quad \theta = 1, \quad \phi = 1 \quad \text{at } r = \eta/(1-\eta) \\ \boldsymbol{u} = f_2(\mathrm{Ta}, \eta) \boldsymbol{e}_\varphi, \quad \theta = 0, \quad \phi = 0 \quad \text{at } r = 1/(1-\eta) \end{cases} \tag{2.14}$$

Depending on the rotation regime, the condition for the velocity at the cylindrical surfaces will change. We will adopt different definitions of the Taylor number Ta which is the ratio between the characteristic time of viscous dissipation and the characteristic time associated to the centrifugal acceleration, in different rotation regimes. The two functions f_1 and f_2 also depend on the rotation regime. To characterize the buoyancies, we will define the Rayleigh number which is the ratio between the product of the dissipative characteristic times τ_ν and τ_κ and the square of the buoyancy characteristic time, whose definition depends on the considered buoyancy mechanism. The centrifugal Rayleigh number Ra is defined to characterise the centrifugal buoyancy:

$$\mathrm{Ra} = \frac{\alpha \Delta T g_c d^3}{\nu \kappa} \tag{2.15}$$

As g_c depends on the radial position, one has to chose an appropriate position to define the centrifugal Rayleigh number. Another Rayleigh number, called the electric Rayleigh number L is defined to characterise the thermoelectric buoyancy:

$$\mathrm{L} = \frac{\alpha \Delta T g_e d^3}{\nu \kappa} \tag{2.16}$$

where g_e is also computed at a chosen position.

2.3 Base state

For an infinite length annulus, the base state can be assumed to be a stationary, axisymmetric and axially invariant state so that the flow and electric fields depend only on the radial coordinate. The equations (2.11b-2.11d) are reduced for the base state to:

$$\text{Radial momentum equation:} \quad \frac{d\Pi}{dr} = \frac{V^2}{r} - \left(\gamma_a \frac{V^2}{r} - \frac{\gamma_e V_E^2 G_e}{\mathrm{Pr}}\right)\Theta, \tag{2.17a}$$

$$\text{Azimuthal momentum equation:} \quad \frac{d}{dr}\left(r\frac{dV}{dr}\right) - \frac{V}{r} = 0, \tag{2.17b}$$

$$\text{Axial momentum equation:} \quad \frac{1}{r}\frac{d}{dr}\left(r\frac{dW}{dr}\right) + \mathrm{Gr}\Theta = 0, \tag{2.17c}$$

$$\text{Energy equation:} \quad \frac{d}{dr}\left(r\frac{d\Theta}{dr}\right) = 0, \tag{2.17d}$$

$$\text{Gauss' law} \quad \frac{d}{dr}\left(r\varepsilon\frac{d\Phi}{dr}\right) = 0 \tag{2.17e}$$

where Π, V, W, Θ and Φ are the pressure, the azimuthal velocity, the axial velocity, the temperature and the electric potential of the base flows, respectively. G_e is the base electric gravity and has been define as a centripetal gravity so that $\boldsymbol{G}_e = -G_e \boldsymbol{e}_r$. The temperature T_2 of the outer cylinder has been chosen as the reference temperature so that $\theta = (T - T_2)/(T_1 - T_2)$. The base azimuthal velocity, solution of the equation (2.17b), depends on the rotation regime and is given by:

$$V(r) = \frac{\mathrm{Re}_1}{1-\eta^2}\left[\frac{(\mu-\eta^2)(1-\eta)\,r}{\eta} + \frac{\eta(1-\mu)}{r(1-\eta)}\right] \tag{2.18}$$

where $\mathrm{Re}_1 = R_1\Omega_1 d/\nu$ is the Reynold number based on the rotation of the inner cylinder and where $\mu = \Omega_2/\Omega_1$ is the ratio of the cylinder rotation rates. The particular rotation regimes, which are considered in the present thesis, and the base azimuthal velocity of these regimes will be given in section 2.4. Integrating the equations (2.17d - 2.17e), one can find the base temperature and the base electric potential:

$$\Theta = \frac{\ln[r(1-\eta)]}{\ln\eta}, \quad \Phi = \frac{\ln(1-\gamma_e\Theta)}{\ln(1-\gamma_e)} \tag{2.19}$$

The corresponding electric field is given by:

$$\bar{E} = \frac{\gamma_e}{r\ln(\eta)\ln(1-\gamma_e)(1-\gamma_e\theta)} \tag{2.20}$$

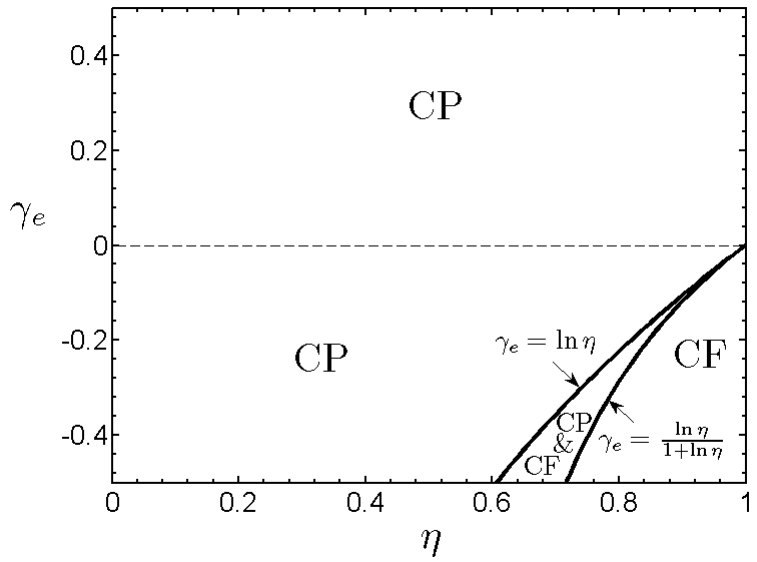

Figure 2.3: Direction of the base electric gravity in the (η, γ_e) plane. CP means centripetal and CF means centrifugal.

Using the base electric potential in the expression of the electric gravity (2.12), one can find:

$$G_e = \frac{1}{(\ln\eta)^2 r^3} \cdot F(r, \gamma_e, \eta) \quad \text{with} \quad F(r, \gamma_e, \eta) = \frac{{\gamma_e}^2 [1 - \gamma_e (\Theta + 1/\ln\eta)]}{[\ln(1-\gamma_e)]^2 (1 - \gamma_e \Theta)^3} \tag{2.21}$$

The electric gravity is oriented toward the region with larger electric field. In the plane geometry, the largest electric field is located at the hot surface [50], but in the cylindrical geometry, the curvature plays an important role. Indeed, in Eq. (2.21), the parameter F can change its sign depending on γ_e and η. Figure 2.3 shows the direction of the base electric gravity in the (η, γ_e) plane. In outward heating ($\gamma_e > 0$), the electric gravity is always centripetal. In inward heating ($\gamma_e < 0$), the electric gravity is centripetal, except in the case of large values of the radius ratio, where the electric gravity can be centrifugal or change its direction inside the gap.

Using the boundary conditions, together with the condition of zero axial volume flux: $\int_{R_1}^{R_2} rW dr = 0$, the base axial velocity, solution of Eq. (2.17c), is given by:

$$W = \mathrm{Gr}\left(C\left[(1-\eta)^2 r^2 - 1 + (1-\eta)^2\Theta\right] - \frac{r^2(1-\eta)^2 - \eta^2}{4(1-\eta)^2}\Theta\right) \tag{2.22}$$

where the coefficient C is:

$$C = \frac{(1-\eta^2)(1-3\eta^2) - 4\eta^4 \ln\eta}{16(1-\eta)^2\left[(1-\eta^2)^2 + (1-\eta^4)\ln\eta\right]}$$

The equation (2.17a) describes the balance between the radial pressure gradient and the radial forces which are the centrifugal force, the centrifugal buoyancy and the thermoelectric buoyancy. The base pressure, solution of Eq. (2.17a), can be written:

$$\Pi(r) = \Pi_{CCF}(r) + \Pi_{CB}(r) + \Pi_{TEB}(r) \tag{2.23}$$

where Π_{CCF} is the pressure profile given by the isothermal circular Couette flow, Π_{CB} is the contribution of the centrifugal buoyancy, and Π_{TEB} is the contribution of the thermoelectric buoyancy. In the general case, these terms are given by:

$$\Pi_{CCF}(r) = \frac{A^2 r^2}{2} + AB\ln(r) - \frac{B^2}{2r^2}, \tag{2.24a}$$

$$\Pi_{CB}(r) = \frac{\gamma_a}{\ln\eta}\left[\left(\frac{A^2 r^2}{4} + AB - \frac{B^2}{4r^2}\right)\ln\left[(1-\eta)\,r\right]^2 - \left(\frac{A^2 r^2}{4} + \frac{B^2}{4r^2}\right)\right], \tag{2.24b}$$

$$\Pi_{TEB}(r) = \frac{\gamma_e V_E^2}{\mathrm{Pr}}\int G_e(r)\Theta(r)dr \tag{2.24c}$$

where:

$$A = \frac{\mathrm{Re}_i}{1-\eta^2}\frac{(\mu-\eta^2)\,(1-\eta)}{\eta}; \quad \text{and} \quad B = \frac{\mathrm{Re}_i}{1-\eta^2}\frac{\eta\,(1-\mu)}{1-\eta} \tag{2.25}$$

The centrifugal buoyancy and the dielectrophoretic force modify the pressure distribution in the radial direction.

The radial profiles of the base state solutions are shown in figure 2.4. When the radius ratio tends to 1, the base state is similar to the one of a plan capacitor, with an anti-symmetric axial velocity profile with respect to the mid-gap and with a linear profile of the temperature. The electric field and electric gravity are sensitive to the curvature of the annulus. Indeed, the electric gravity can be significant in the neighbourhood of the inner cylinder.

2.4 The rotation regimes

Four different rotation regimes have been investigated:

- the case of a steady outer cylinder ($\Omega_2 = 0$).
- the case of a steady inner cylinder ($\Omega_1 = 0$).
- the Keplerian regime ($\Omega_1/\Omega_2 = (R_1/R_2)^{-3/2}$).

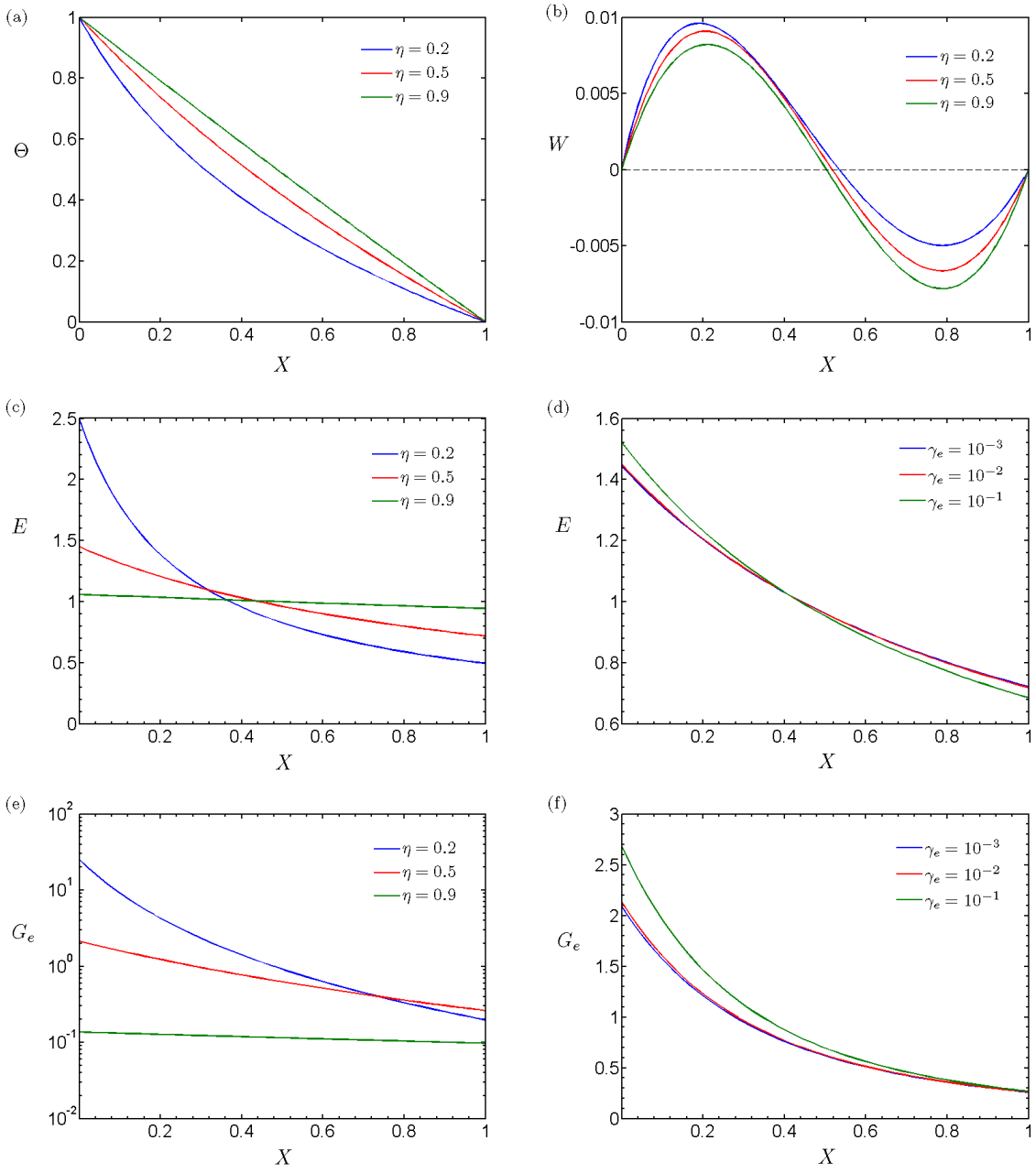

Figure 2.4: Radial profiles of (a) the temperature, (b) the axial velocity, (c-d) the electric field and (e-f) the electric gravity. X is given by $X = (r - R_1)/d$. (c) and (e) are obtained for $\gamma_e = 0.01$. (d) and (f) are obtained for $\eta = 0.5$.

Table 2.1: Expressions of the Taylor number and of the base azimuthal velocity depending on the rotation regime.

	Ta	base axial velocity
$\Omega_2 = 0$	$\mathrm{Ta} = \dfrac{R_1\Omega_1 d}{\nu}\sqrt{\dfrac{d}{R_1}}$	$V(r) = \mathrm{Ta}\dfrac{\eta^{3/2}}{(1-\eta)^{5/2}(1+\eta)}\left[\dfrac{1}{r} - (1-\eta)^2 r\right]$
$\Omega_1 = 0$	$\mathrm{Ta} = \dfrac{R_2\Omega_2 d}{\nu}\sqrt{\dfrac{d}{R_2}}$	$V(r) = \mathrm{Ta}\dfrac{1}{\sqrt{1-\eta}(1+\eta)}\left[r - \dfrac{\eta^2}{(1-\eta)^2 r}\right]$
$\Omega_1/\Omega_2 = \eta^{-3/2}$	$\mathrm{Ta} = \dfrac{2\eta\Omega_1 d^2\left(1-\eta^{3/2}\right)}{\nu(1-\eta^2)}$	$V(r) = \dfrac{\mathrm{Ta}}{2}\left(\dfrac{r\left(\eta^{3/2}-\eta^2\right)}{\eta\left(1-\eta^{3/2}\right)} + \dfrac{\eta}{r(1-\eta)^2}\right)$
$\Omega_1 = \Omega_2 = \Omega$	$\mathrm{Ta} = \dfrac{\bar{R}\Omega_2 d}{\nu}\sqrt{\dfrac{d}{\bar{R}}}$	$V(r) = \mathrm{Ta}\sqrt{\dfrac{2(1-\eta)}{1+\eta}}r$

- the solid rotation regime ($\Omega_1 = \Omega_2$).

In these rotation regimes, only the case where the outer cylinder is stationary can produce instabilities in the isothermal condition (Rayleigh unstable). In the other rotation regimes (Rayleigh stable), a temperature difference has to be applied between the two cylinders in order to make the system potentially unstable (see Sec. 3.3) .

We adopt different definitions of the Taylor number in different rotation regimes in order to better capture the effect of the rotation of one or both cylinders on the flow. The adopted definitions and the base azimuthal velocity profile are given in Table 2.1. If one of the cylinders is steady, the Taylor number is based on the azimuthal velocity of the other cylinder. For solid rotation, the arithmetic mean radius is chosen to define Ta. When the Keplerian regime is considered, the Taylor number is defined through the average shear rate at the geometric mean radius [51]. The base azimuthal velocity profiles are shown on Fig. 2.5 except for the solid body rotation which has a linear velocity profile in r.

2.5 Linearised equations

To perform the linear stability analysis, we add to the base state an infinitesimal perturbation $(u', v', w', \pi', \theta', \phi')$, and linearise the governing equations (2.11) around the base state solution

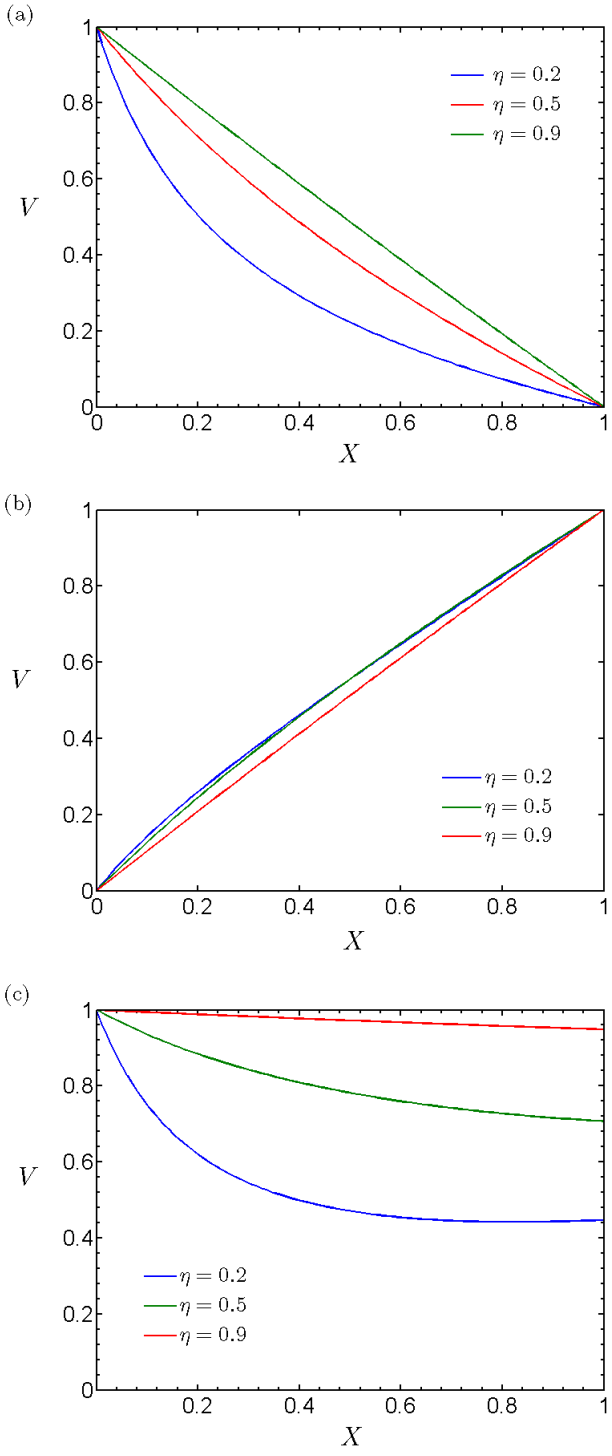

Figure 2.5: Radial profiles of the base azimuthal velocity in the case of (a) the inner cylinder rotation regime, (b) the outer cylinder rotation regime, and (c) the Keplerian regime. X is given by $X = (r - R_1)/d$.

(2.18 - 2.22). We then obtain:

$$\frac{1}{r}\frac{\partial\left(ru'\right)}{\partial r}+\frac{1}{r}\frac{\partial v'}{\partial\varphi}+\frac{\partial w'}{\partial z}=0 \tag{2.26a}$$

$$\frac{\partial u'}{\partial t}+\left(\frac{V}{r}\frac{\partial}{\partial\varphi}+W\frac{\partial}{\partial z}\right)u'=-\frac{\partial\pi'}{\partial r}+\Delta u'-\frac{u'}{r^2}+2\frac{Vv'}{r}-\frac{2}{r^2}\frac{\partial v'}{\partial\varphi}-\gamma_a\left(\theta' G_c+\Theta g_c'\right)-\frac{\gamma_e V_E^2}{\mathrm{Pr}}\left(-\theta' G_e+\Theta g_{e,r}'\right) \tag{2.26b}$$

$$\frac{\partial v'}{\partial t}+\left(\frac{V}{r}\frac{\partial}{\partial\varphi}+W\frac{\partial}{\partial z}\right)v'=-\frac{1}{r}\frac{\partial\pi'}{\partial\varphi}+\Delta v'-\frac{v'}{r^2}-\frac{Vu'}{r}+\frac{2}{r^2}\frac{\partial u'}{\partial\varphi}-u'\frac{dV}{dr}-\frac{\gamma_e V_E^2}{\mathrm{Pr}}\Theta g_{e,\varphi}' \tag{2.26c}$$

$$\frac{\partial w'}{\partial t}+\left(\frac{V}{r}\frac{\partial}{\partial\varphi}+W\frac{\partial}{\partial z}\right)w'=-\frac{\partial\pi'}{\partial z}+\Delta w'-u'\frac{dW}{dr}+\mathrm{Gr}\theta'-\frac{\gamma_e V_E^2}{\mathrm{Pr}}\Theta g_{e,z}' \tag{2.26d}$$

$$\frac{\partial\theta}{\partial t}+\left(\frac{V}{r}\frac{\partial}{\partial\varphi}+W\frac{\partial}{\partial z}\right)\theta'=-u'\frac{d\Theta}{dr}+\frac{1}{\mathrm{Pr}}\Delta\theta' \tag{2.26e}$$

$$\left(1-\gamma_e\Theta\right)\Delta\phi'-\gamma_e\frac{d\Theta}{dr}\frac{\partial\phi'}{\partial r}-\gamma_e\frac{d\Phi}{dr}\frac{1}{r}\frac{\partial\left(r\theta'\right)}{\partial r}-\gamma_e\frac{d^2\Phi}{dr^2}\theta'=0 \tag{2.26f}$$

where $g_{e,r}'$, $g_{e,\varphi}'$ and $g_{e,z}'$ are the r, φ and z components of the perturbation electric gravity vector, respectively:

$$g_{e,r}'=\frac{d\Phi}{dr}\frac{\partial^2\phi'}{\partial r^2}+\frac{d^2\Phi}{dr^2}\frac{\partial\phi'}{\partial r},\quad g_{e,\varphi}'=\frac{d\Phi}{dr}\frac{\partial^2\phi'}{\partial\varphi\partial r},\quad g_{e,z}'=\frac{d\Phi}{dr}\frac{\partial^2\phi'}{\partial z\partial r} \tag{2.27}$$

The centrifugal buoyancy has been separated into two components, the one associated with the base centrifugal acceleration $G_c=V^2/r$ and the other related to the perturbation centrifugal acceleration $g_c'=2Vv'/r$. The Laplacian operator Δ is given by:

$$\Delta=\frac{1}{r}\frac{\partial}{\partial r}\left(r\frac{\partial}{\partial r}\right)+\frac{1}{r^2}\frac{\partial^2}{\partial\varphi^2}+\frac{\partial^2}{\partial z^2} \tag{2.28}$$

The boundary conditions for the perturbation fields are homogeneous:

$$u'=v'=w'=\theta'=\phi'=0\text{ at }r=\frac{\eta}{1-\eta},\ \frac{1}{1-\eta} \tag{2.29}$$

The perturbation fields are developed into normal modes:

$$\chi'=\hat{\chi}\exp\left[st+in\phi+ikz\right]+c.c. \tag{2.30}$$

where $\chi'=(u',v',w',\pi',\theta',\phi')$ and $\hat{\chi}=(\hat{u},\hat{v},\hat{w},\hat{\pi},\hat{\theta},\hat{\phi})$. A hat over a quantity indicates its complex amplitude which depends only on the radial position, and where *c.c.* stands for the complex conjugate. $s=\sigma+i\omega$ is the complex growth rate, where ω is the frequency of perturbation. Note that the sign + implies that a positive frequency corresponds to a perturbation propagating

in direction of negative sign and inversely. k is the axial wavenumber which is real since the cylinders are infinite in the axial direction, and n is the azimuthal mode number which takes only integer values. The total wavenumber q measures the wavenumber of perturbations at the mid-gap in the direction normal to the vortice axes and is given by $q = (k^2 + k_\varphi^2)^{1/2}$, where $k_\varphi = 2n(1-\eta)/(1+\eta)$. Applying this development to the equations (2.26a - 2.26f), one obtains:

$$0 = \left(D + \frac{1}{r}\right)\hat{u} + \frac{in}{r}\hat{v} + ik\hat{w} \tag{2.31a}$$

$$s\hat{u} = -i\left(\frac{nV}{r} + kW\right)\hat{u} - D\hat{\pi} + \Delta\hat{u} - \frac{\hat{u}}{r^2} - \frac{2V}{r}\hat{v} - \frac{2in}{r^2}\hat{v} - \gamma_a\left(\Theta\hat{g}_c + G_c\hat{\theta}\right) - \frac{\gamma_e V_E^2}{\mathrm{Pr}}\left(\Theta\hat{g}_{e,r} - \hat{\theta}G_e\right) \tag{2.31b}$$

$$s\hat{v} = -i\left(\frac{nV}{r} + kW\right)\hat{v} - \frac{in}{r}\hat{\pi} + \Delta\hat{v} - \frac{\hat{v}}{r^2} - \frac{V}{r}\hat{u} + \frac{2in}{r^2}\hat{u} - (DV)\,\hat{u} - \frac{in}{r}\frac{\gamma_e V_E^2}{\mathrm{Pr}}\Theta\hat{g}_{e,\varphi} \tag{2.31c}$$

$$s\hat{w} = -i\left(\frac{nV}{r} + kW\right)\hat{w} - ik\hat{\pi} + \Delta\hat{w} - (DW)\,\hat{u} + \mathrm{Gr}\hat{\theta} - ik\frac{\gamma_e V_E^2}{\mathrm{Pr}}\Theta\hat{g}_{e,z} \tag{2.31d}$$

$$s\hat{\theta} = -i\left(\frac{nV}{r} + kW\right)\hat{\theta} - (D\Theta)\,\hat{u} + \frac{1}{\mathrm{Pr}}\Delta\hat{\theta} \tag{2.31e}$$

$$0 = (1 - \gamma_e\Theta)\,\Delta\hat{\phi} - \gamma_e D\Theta D\hat{\phi} - \gamma_e D\Phi\left(D + \frac{1}{r}\right)\hat{\theta} - \gamma_e\left(D^2\Phi\right)\hat{\theta} \tag{2.31f}$$

where $D = d/dr$ is the radial derivative operator and where $\Delta = D^2 + D/r - n^2/r^2 - k^2$ is the Laplacian operator. The complex amplitudes satisfy homogeneous conditions at the cylindrical surfaces:

$$\hat{u} = \hat{v} = \hat{w} = \hat{\theta} = 0, \quad \text{at} \quad r = \eta/(1-\eta), \quad 1/(1-\eta). \tag{2.32}$$

2.6 Chebyshev collocation method

The eigenvalue problem Eqs. (2.31) is solved by a collocation method. The Chebyshev variable ξ is introduced by associating it with r by:

$$r = \frac{\xi}{2} + \frac{1+\eta}{2\,(1-\eta)} \tag{2.33}$$

By this transformation, the interval $[\eta/(1-\eta)\ ;\ 1/(1-\eta)]$ of r is mapped on $[-1\ ;\ 1]$ of ξ and $D = 2D_\xi$, where $D_\xi = d/d\xi$. The complex amplitudes $\hat{u}$, $\hat{v}$, $\hat{w}$, $\hat{\pi}$, $\hat{\theta}$ and $\hat{\phi}$ are developed into Chebyshev polynomials of order N and the equations (2.31a - 2.31f) are discretized by considering them only at the radial positions $r = r_j$ $(j = 0, 2, \cdots, N)$ which correspond to the Chebyshev-Gauss-Lobbato collocation points $\xi_j = \cos(j\pi/N)$. The eigenvalue problem can be cast into the

following matrix form:

$$\left(2\boldsymbol{K}\boldsymbol{D}_\xi + \left\{\frac{1}{r}\right\}\boldsymbol{K}\right)\boldsymbol{U} + \left\{\frac{in}{r}\right\}\boldsymbol{K}\boldsymbol{V} + ik\boldsymbol{K}\boldsymbol{W} = 0 \tag{2.34a}$$

$$\left[\boldsymbol{L} - \boldsymbol{M} - \left\{\frac{1}{r^2}\right\}\boldsymbol{K}\right]\boldsymbol{U} + 2\left\{\frac{V}{r} - \frac{in}{r^2} - \gamma_a\frac{\Theta V}{r}\right\}\boldsymbol{K}\boldsymbol{V} - 2\boldsymbol{K}\boldsymbol{D}_\xi\boldsymbol{\Pi} + \left\{-\gamma_a\frac{V^2}{r} + \frac{\gamma_e V_E^2}{\mathrm{Pr}}G_e\right\}\boldsymbol{K}\boldsymbol{\Theta} - \frac{\gamma_e V_E^2}{\mathrm{Pr}}\left(4\left\{\Theta D\Phi\right\}\boldsymbol{K}\boldsymbol{D}_\xi^2 + 2\left\{\Theta D^2\Phi\right\}\boldsymbol{K}\boldsymbol{D}_\xi\right)\boldsymbol{\Phi} = s\boldsymbol{K}\boldsymbol{U} \tag{2.34b}$$

$$-\left\{\frac{V}{r} - \frac{2in}{r^2} + DV\right\}\boldsymbol{K}\boldsymbol{U} + \left[\boldsymbol{L} - \boldsymbol{M} - \left\{\frac{1}{r^2}\right\}\boldsymbol{K}\right]\boldsymbol{V} - \left\{\frac{in}{r}\right\}\boldsymbol{K}\boldsymbol{\Pi} - 2in\frac{\gamma_e V_E^2}{\mathrm{Pr}}\left\{\frac{\Theta D\Phi}{r}\right\}\boldsymbol{K}\boldsymbol{D}_\xi\boldsymbol{\Phi} = s\boldsymbol{K}\boldsymbol{W} \tag{2.34c}$$

$$-\left\{DW\right\}\boldsymbol{K}\boldsymbol{U} + \left(\boldsymbol{L} - \boldsymbol{M}\right)\boldsymbol{W} - ik\boldsymbol{K}\boldsymbol{\Pi} + \mathrm{Gr}\boldsymbol{K}\boldsymbol{\Theta} - 2ik\frac{\gamma_e V_E^2}{\mathrm{Pr}}\left\{\Theta D\Phi\right\}\boldsymbol{K}\boldsymbol{D}_\xi\boldsymbol{\Phi} = s\boldsymbol{K}\boldsymbol{W} \tag{2.34d}$$

$$-\left\{D\Theta\right\}\boldsymbol{K}\boldsymbol{U} + \left(\frac{1}{\mathrm{Pr}}\boldsymbol{L} - \boldsymbol{M}\right)\boldsymbol{\Theta} = s\boldsymbol{K}\boldsymbol{\Theta} \tag{2.34e}$$

$$-\gamma_e\left[2\left\{D\Phi\right\}\boldsymbol{K}\boldsymbol{D}_\xi + \left\{\frac{D\Phi}{r} + D^2\Phi\right\}\boldsymbol{K}\right]\boldsymbol{\Theta} + \left[\left\{1 - \gamma_e\Theta\right\}\boldsymbol{L} - 2\gamma_e\left\{D\Theta\right\}\boldsymbol{K}\boldsymbol{D}_\xi\right]\boldsymbol{\Phi} = 0 \tag{2.34f}$$

where $\boldsymbol{K}$ is the transformation matrix that relates Chebyshev spectra to the values of a function at $\xi_0, \xi_1, \cdots, \xi_N$:

$$\boldsymbol{K} = (K_{lm}) \quad \text{with} \quad K_{lm} = \cos\left[\frac{l\,(m-1)\,\pi}{N}\right] \tag{2.35}$$

where $l = 1, 2, \cdots, N+1$ and $m = 1, 2, \cdots, N+1$. The matrix $\boldsymbol{D}_\xi$ is the derivation operator in the Chebyshev space and has a size of $(N+1) \times (N+1)$:

$$\boldsymbol{D}_\xi = \begin{pmatrix} 0 & 1 & 0 & 3 & 0 & 5 & 0 & \cdots & \\ 0 & 0 & 4 & 0 & 8 & 0 & 12 & \cdots & \\ 0 & 0 & 0 & 6 & 0 & 10 & 0 & \cdots & \\ 0 & 0 & 0 & 0 & 8 & 0 & 12 & \cdots & \\ \vdots & \vdots & \vdots & \vdots & \vdots & \vdots & \vdots & \ddots & \\ 0 & 0 & 0 & 0 & 0 & 0 & 0 & \cdots & 2N \\ 0 & 0 & 0 & 0 & 0 & 0 & 0 & \cdots & 0 \end{pmatrix} \tag{2.36}$$

The curly brackets means a diagonal matrix of size $N+1$:

$$\{f(r)\} = \begin{pmatrix} f(r_0) & 0 & 0 & \cdots & 0 \\ 0 & f(r_1) & 0 & \cdots & 0 \\ 0 & 0 & f(r_3) & \cdots & 0 \\ \vdots & \vdots & \vdots & \ddots & \vdots \\ 0 & 0 & 0 & \cdots & f(r_N) \end{pmatrix} \tag{2.37}$$

Note that r_0 and r_N correspond to the positions of the outer and inner cylinder surfaces, respectively. The operator $\boldsymbol{L}$ and $\boldsymbol{M}$ are given by:

$$\boldsymbol{L} = 4\boldsymbol{K}\boldsymbol{D}_\xi^2 + 2\left\{\frac{1}{r}\right\}\boldsymbol{K}\boldsymbol{D}_\xi - \left\{\frac{n^2}{r^2} + k^2\right\}\boldsymbol{K} \tag{2.38}$$

$$\boldsymbol{M} = i\left\{\frac{nV}{r} + kW\right\}\boldsymbol{K} \tag{2.39}$$

At the boundaries, we require the boundary conditions and the continuity equation:

$$\boldsymbol{K}_{BC}\boldsymbol{U} = \boldsymbol{K}_{BC}\boldsymbol{W} = \boldsymbol{K}_{BC}\boldsymbol{D}_\xi\boldsymbol{W} = \boldsymbol{K}_{BC}\boldsymbol{\Theta} = \boldsymbol{0} \tag{2.40}$$

where the transformation matrix $\boldsymbol{K}_{BC}$, that gives the values of a function at $\xi = \xi_0 = 1$ and $\xi = \xi_N = -1$ has been introduced:

$$\boldsymbol{K_{BC}} = \begin{pmatrix} 1 & 1 & 1 & 1 & \cdots & 1 \\ 1 & -1 & 1 & -1 & \cdots & (-1)^N \end{pmatrix} \tag{2.41}$$

The equations (2.34) and the boundary conditions (2.40) is solved using the QZ decomposition. To ensure the convergence of the solutions, the highest order of Chebyshev polynomials is varied from 15 for large values of η to 30 for low values of η.

2.7 Equation for kinetic energy

The equation for the kinetic energy density of the perturbation is derived from the linearized equations. Multiplying Eqs. (2.26b - 2.26d) by u', v', and w', respectively, and summing the

resulting equations, we have:

$$\frac{\partial}{\partial t}\left(\frac{\boldsymbol{u}'^2}{2}\right)+\boldsymbol{u}'\cdot\left[\boldsymbol{\nabla}\cdot(\boldsymbol{u}'\boldsymbol{U})\right]+\boldsymbol{\nabla}\cdot\left[\frac{\boldsymbol{u}'^2}{2}(\boldsymbol{U}+\boldsymbol{u}')\right]=-\boldsymbol{\nabla}\cdot(\pi'\boldsymbol{u}')+\Delta\boldsymbol{u}'^2-\boldsymbol{\nabla}\boldsymbol{u}':(\boldsymbol{\nabla}\boldsymbol{u}')^T$$
$$+\mathrm{Gr}\theta'w'-\gamma_a\left(G_c\theta'+g_c'\Theta\right)u'-\frac{\gamma_e V_E^2}{\mathrm{Pr}}\theta'\boldsymbol{G}_e\cdot\boldsymbol{u}'-\frac{\gamma_e V_E^2}{\mathrm{Pr}}\Theta\boldsymbol{g}_e'\cdot\boldsymbol{u}' \quad (2.42)$$

Integrating over the whole fluid volume and over a period of perturbations propagation with rigid boundary conditions, we have:

$$\frac{dK}{dt}=W_{Sh}+W_{Bu}+W_{Hy}+W_{Th}+W_{BG}+W_{PG}-D_\nu \quad (2.43)$$

where K is the kinetic energy, W_{Sh} is the power performed by the shear stress, W_{Bu} is the power performed by the centrifugal buoyancy, W_{Hy} is the power performed by the axial shear flow, W_{Th} is the power performed by the Archimedean buoyancy, W_{BG} is the power performed by the base electric gravity, W_{PG} is the power performed by the perturbation electric gravity, and D_ν is the rate of viscous energy dissipation. These terms are given by:

$$K=\int\frac{\boldsymbol{u}'}{2}dV, \qquad W_{Sh}=-\int u'v'\left(\frac{dV}{dr}-\frac{V}{r}\right)dV, \quad (2.44a)$$
$$W_{Hy}=-\int u'w'\frac{dW}{dr}dV, \qquad W_{Bu}=-\gamma_a\int\frac{u'\left(V^2\theta'+V\Theta v'\right)}{r}dV, \quad (2.44b)$$
$$W_{Th}=\mathrm{Gr}\int\theta'w'dV, \qquad W_{BG}=\frac{\gamma_e V_E^2}{\mathrm{Pr}}\int\theta'G_e u'dV, \quad (2.44c)$$
$$W_{PG}=-\frac{\gamma_e V_E^2}{\mathrm{Pr}}\int\Theta\boldsymbol{g}_e'\cdot\boldsymbol{u}'dV, \qquad D_\nu=\int\Phi_\nu dV \quad (2.44d)$$

where the viscous dissipation function Φ_ν is given by:

$$\Phi_\nu=2\left[\left|\frac{du'}{dr}\right|^2+\left|\frac{imv'}{r}+\frac{u'}{r}\right|^2+k^2|w'|^2\right]+\left|r\frac{d}{dr}\left(\frac{v'}{r}\right)+\frac{imu'}{r}\right|^2+\left|\frac{imw'}{r}+ikv'\right|^2+\left|iku'+\frac{dw}{dr}\right|^2$$

In one case, the power performed by the centrifugal buoyancy W_{Bu} will be splitted in two contribution: one related to the base centrifugal acceleration W_{BBu} and the other to the perturbation centrifugal acceleration W_{PBu}. These two energy sources are given by:

$$W_{BBu}=-\gamma_a\int\frac{u'V^2\theta'}{r}dV: \quad \text{and} \quad W_{PBu}=-\gamma_a\int\frac{u'V\Theta v'}{r}dV \quad (2.45)$$

The considered case for studying there contribution is the effect of the centrifugal buoyancy in a rigidly rotation cylindrical annulus (Chapter 6), where W_{Bu} and D_ν are the only energy sources.

2.8 Complex Ginzburg-Landau equation

The linear stability analysis provides information about the nature of the transition from the base state to the convective state. Moreover, the evolution of the coefficients of the linear part of the complex Ginzburg-Landau equation (GLE) can be computed and gives information about the variation of the growth rate and frequency of perturbations with the control parameters.

In the following, the GLE is derived using the Taylor number Ta as the control parameter, but it can be changed to the dimensionless electric potential V_E when the DEP force is considered. In the neighbourhood of the instability threshold, the complex linear growth rate $s = \sigma + i\omega$ can be expanded into power series of the axial wavenumber k:

$$s = \sigma_0\epsilon + \sigma_1 Q^2 + i\left[\omega_c + \omega_{\mathrm{Ta}}\epsilon + c_g Q + \omega_2 Q^2\right] + O\left(Q^3\right), \tag{2.46}$$

where $Q = (k - k_c)$, $\epsilon = 1 - \mathrm{Ta}/\mathrm{Ta}_c$ and the coefficients are given by the following partial derivatives evaluated at the critical condition:

$$\begin{aligned} \sigma_0 = \mathrm{Ta}_c\left(\frac{\partial\sigma}{\partial\mathrm{Ta}}\right)_c,\ \sigma_1 = \frac{1}{2}\left(\frac{\partial^2\sigma}{\partial k^2}\right)_c,\ c_g = \left(\frac{\partial\omega}{\partial k}\right)_c, \\ \omega_{\mathrm{Ta}} = \mathrm{Ta}_c\left(\frac{\partial\omega}{\partial\mathrm{Ta}}\right)_c,\ \omega_2 = \frac{1}{2}\left(\frac{\partial^2\omega}{\partial k^2}\right)_c \end{aligned} \tag{2.47}$$

The dispersion relation (2.46) is identical to the linear part of the complex Ginzburg-Landau equation (GLE) describing the amplitude of a Fourier mode e^{ikz}. The GLE, which can describe perturbation flow in its weakly nonlinear regime, is given by:

$$\tau_0\left(\frac{\partial A}{\partial t} - c_g\frac{\partial A}{\partial z}\right) = \epsilon\left(1 + ic_0\right)A + \xi_0^2\left(1 + ic_1\right)\frac{\partial^2 A}{\partial z^2} - l\left(1 + ic_3\right)|A|^2 A + g\left(1 + ic5\right)|A|^4 A \tag{2.48}$$

where

$$\tau_0 = \frac{1}{\sigma_0},\ \xi_0 = \left(-\frac{\sigma_1}{\sigma_0}\right)^{1/2},\ c_0 = \frac{\omega_{\mathrm{Ta}}}{\sigma_0},\ c_1 = \frac{\omega_2}{\sigma_1}$$

The parameters τ_0 and ξ_0 represent the characteristic time and the coherence length of perturbation, respectively. For time-dependent perturbations, c_0 and c_1 are the linear dispersion

coefficients, and c_g is the group velocity. The third and fourth terms at the right-hand-side of Eq. (2.48) concern the nonlinear state of flow. The constants c_3 and c_5 are nonlinear dispersion coefficients. The Landau constant l determines the nature of the bifurcation from the base flow. If $l > 0$, the bifurcation is supercritical. For stationary perturbation flow, the amplitude saturates at the equilibrium value $A_e = \sqrt{\epsilon/l}$ after a large enough time. If $l < 0$, the bifurcation is subcritical and no saturation is expected for the GLE truncated at the third order. Then, the fifth order nonlinearity, i.e., the fourth term at the right-hand-side of Eq. (2.48), is at least needed for saturation.

Part I

Effect of the centrifugal buoyancy on the Couette flow

Chapter 3

Taylor-Couette instability and centrifugal buoyancy

In this part, the effect of the centrifugal buoyancy on the Couette flow is discussed. In order to focus on the effect of the radial buoyancy, the system is assumed to be under microgravity conditions. Two cases are considered: the rotation regime is Rayleigh unstable or it is Rayleigh stable. If the regime is Rayleigh unstable, the centrifugal force destabilises the flow, and the inward and outward heating change the stability conditions of the system. If the regime is Rayleigh stable, the centrifugal force stabilises the flow, and the centrifugal buoyancy has to destabilise the flow in order to get thermal convections.

3.1 The Taylor-Couette instability

Before investigating the effect of the centrifugal buoyancy on the Couette flow, we will first focus on the Taylor-Couette instability in the isothermal case. This instability occurs through the competition of the destabilising effect of the centrifugal force and the stabilising effect of the viscous dissipation, when the former effect overcomes the latter one. The Rayleigh stable and Rayleigh unstable regimes can be defined by deriving the Rayleigh criterion. Considering an inviscid fluid, we can derive the Rayleigh criterion that determines whether the flow is potentially unstable. In the absence of viscous force, the displacement of a fluid particle from an equilibrium position r to $r + dr$ is not accompanied by any change in its angular momentum so that:

$$rV(r) = (r + dr)V'(r + dr) \tag{3.1}$$

Table 3.1: Critical Taylor number and critical wave number for different η. All the critical modes are axisymmetric ($n_c = 0$).

η	0.1	0.2	0.3	0.4	0.5	0.6	0.7	0.8	0.9	0.99	0.995
Ta_c	421.48	176.28	111.85	83.65	68.19	58.56	52.04	47.37	43.87	41.41	41.29
q_c	3.339	3.263	3.215	3.183	3.162	3.148	3.139	3.133	3.129	3.127	3.127

The velocity $V'(r+dr)$ is that of the particle after being displaced to the position $r+dr$, and is thus given by:

$$V'(r+dr) = V(r)\left(1 - \frac{dr}{r}\right) \tag{3.2}$$

A particle at the equilibrium at the position $r+dr$ has the velocity $V(r+dr)$ given by:

$$V(r+dr) = V(r) + \frac{dV}{dr}dr \tag{3.3}$$

The comparison between the centrifugal force sustained by the particle at the equilibrium $F = \rho[V(r+dr)]^2/(r+dr)$ and that of the displaced particle $F' = \rho[V'(r+dr)]^2/(r+dr)$ leads to:

$$dF = F - F' = \rho\bar{\phi}(r)dr \quad \text{where} \quad \bar{\phi}(r) = 2\frac{V}{r}\left(\frac{dV}{dr} + \frac{V}{r}\right) \tag{3.4}$$

where $\bar{\phi}$ is the Rayleigh discriminant. If $\bar{\phi}$ is positive, the displaced particle will return to its initial position, so that the flow is stable. Otherwise, i.e if $\bar{\phi} < 0$ at some radial positions, the flow is potentially unstable. Using the general expression of the base azimuthal velocity in Eq. (2.18), one can find that the condition $\bar{\phi} < 0$ is obtained if $\mu < \eta^2$. The regime defined by $\mu = \eta^2$ corresponds to the boundary between the Rayleigh stable regime and the Rayleigh unstable regime. As a consequence, in counter rotating regimes $\mu < 0$, the flow is always potentially unstable.

3.1.1 Inner rotating cylinder ($\mu = 0$)

Let us apply the linear stability theory to the case where only the inner cylinder rotates. Since we consider the isothermal case, only the continuity and momentum equations are solved. Therefore the Prandtl number is irrelevant, and it is known that critical modes for this regime are axisymmetric. Figure 3.1 shows the eigenvalue spectrum as a function of the axial wavenumber for $\eta = 0.5$. Fig. 3.1 - (a) corresponds to the critical state since the maximum of the growth rate is zero for a certain value k. Table 3.1 gives the critical values of Ta and q for different radius ratio η.

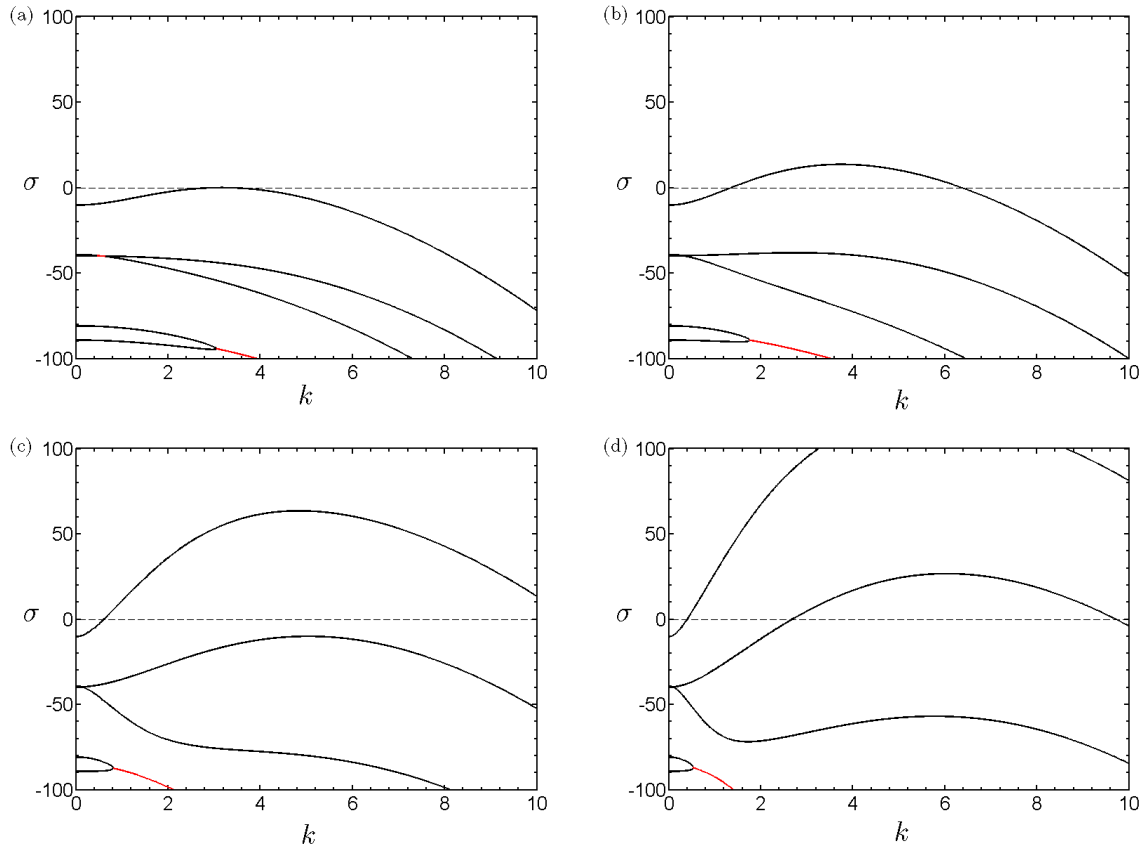

Figure 3.1: Eigenvalue spectrum as function of the axial wavenumber for $\eta = 0.5$ and for (a) Ta = 68, (b) Ta = 100, (c) Ta = 200, (d) Ta = 300. Black and red curves correspond to stationary and oscillatory modes respectively.

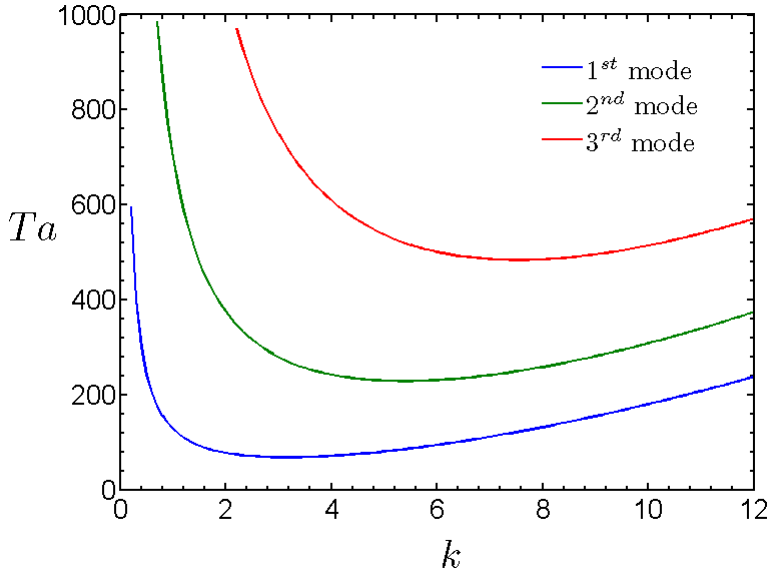

Figure 3.2: Marginal curves for $\eta = 0.5$.

Increasing the Taylor number, the growth rates of all the modes increases so that the radial modes other than the first one can also become unstable ($\sigma > 0$) beyond certain values of Ta (Fig. 3.1 - b-d). For a given k, the value of Ta for which the maximum of the growth rate σ changes its sign indicates the marginal state. Marginal stability curves show the threshold between $\sigma < 0$ and $\sigma > 0$ in the (k, Ta) plane. The marginal curves of the three first modes with the largest values of growth rate for $\eta = 0.5$ are shown in Fig. 3.2. The minimum of a marginal curve gives the critical conditions for given radial modes. The azimuthal vorticity and the amplitudes of the velocity components shown in Fig. 3.3 have been computed for the critical conditions of each radial modes. One can see that the different modes observed in the growth rate spectrum correspond to different number of rolls in the radial direction. The lowest critical Taylor number corresponds to the case where there is only one mode in the radial direction; indeed viscous dissipation favors modes with a small number of convection cells.

3.1.2 Counter-rotation regimes ($\mu < 0$)

As mentioned earlier, the counter-rotation regime is always potentially unstable. Figure 3.4 shows the marginal curves obtained for $\eta = 0.8$ and $\mu = -4$ and for different n. The critical mode is oscillatory non-axisymmetric with $n_c = 5$. For this regime, the vortices have a small wavelength and are concentrated near the inner cylinder (Fig. 3.5). The concentration of convective cells may be explained by the fact that only the flow within a fluid sublayer attached to the inner cylinder

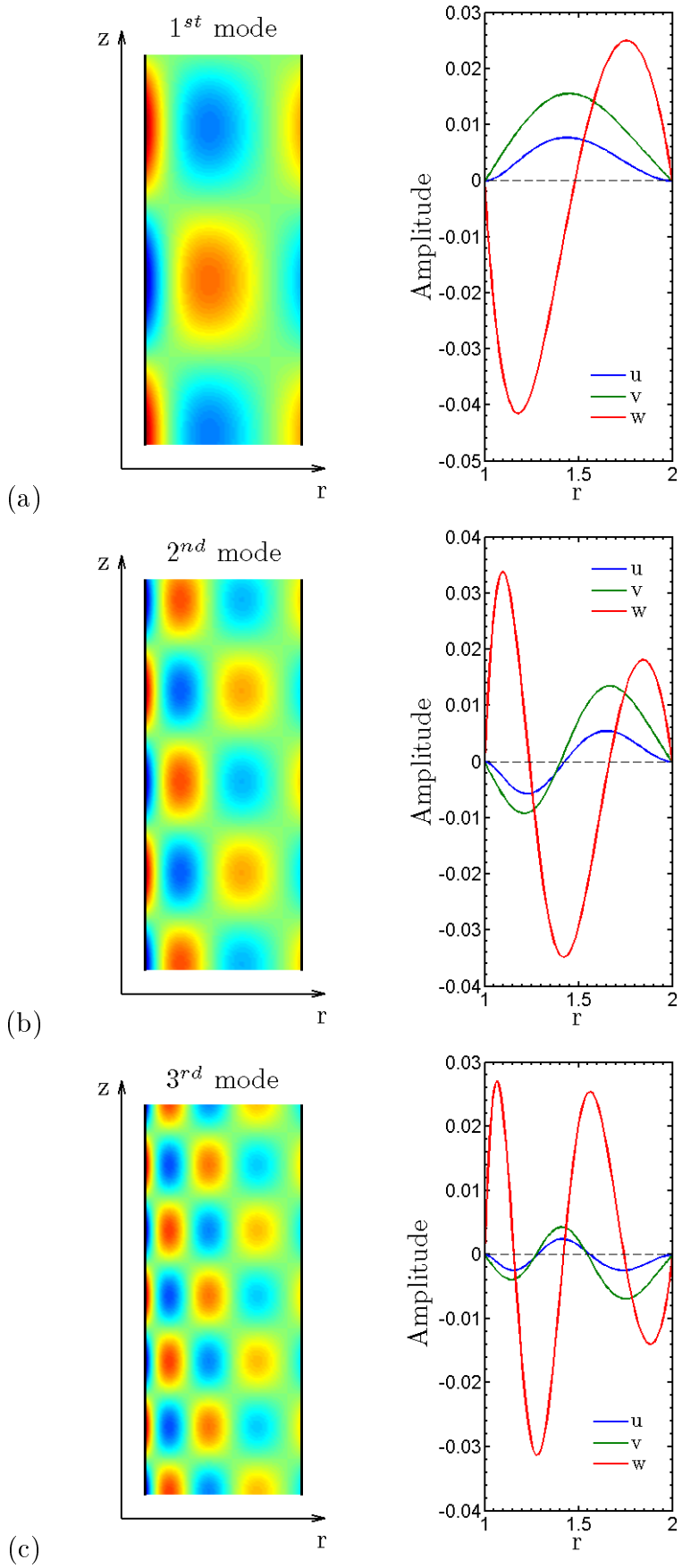

Figure 3.3: Azimuthal vorticity in the (r, z) plane and amplitudes of the velocity components for the three first modes at their respective criticality for $\eta = 0.5$. For the first, second and third modes, the values of (k, Ta) are $(3.2, 68.19)$, $(5.4, 228.75)$ and $(7.5, 483.94)$, respectively.

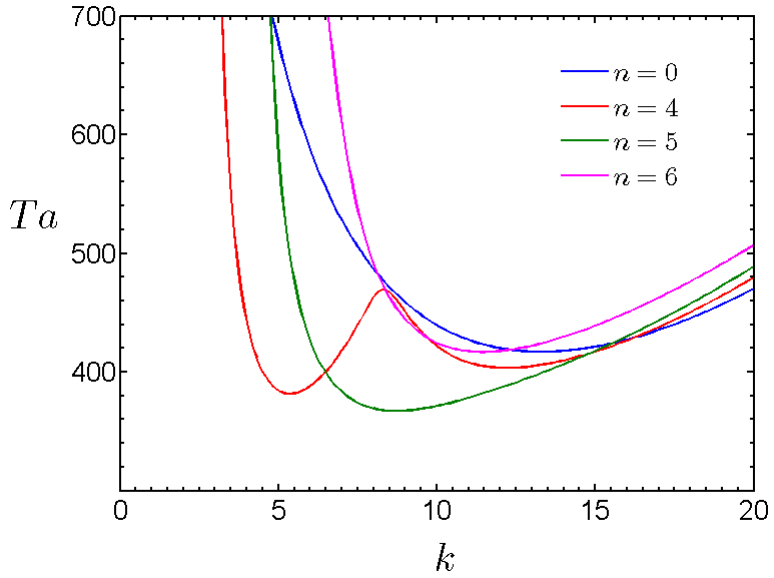

Figure 3.4: Marginal curves for $\eta = 0.8$, $\mu = -4$ and for different values of n.

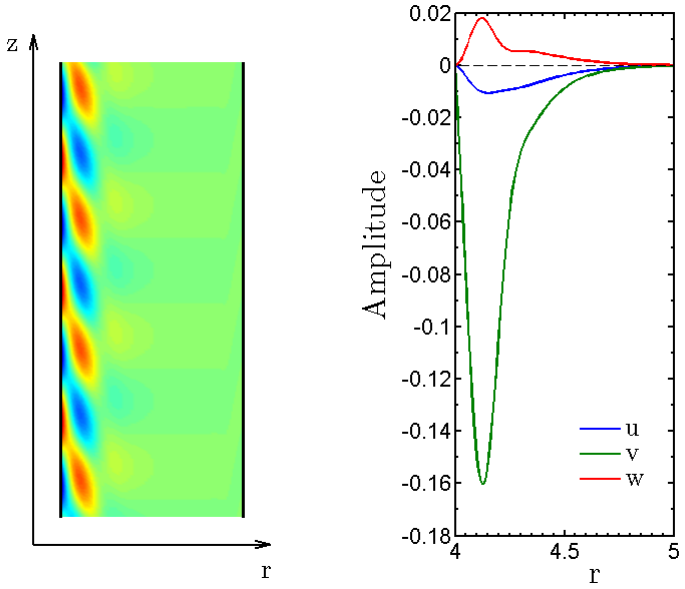

Figure 3.5: Azimuthal vorticity in the (r, z) plane and amplitudes of the velocity components at the criticality for $\eta = 0.8$, $\mu = -4$, Ta $= 364.4$, $k = 8.76$ and $n = 5$.

is potentially unstable according to the Rayleigh criterion. Fig. 3.6 shows the marginal stability curves, as well as the corresponding frequency, for various counter rotating regimes. For $\mu = -0.25$ and $\mu = -0.5$, critical modes are stationary axisymmetric, and for $\mu = -0.8$ the critical mode is oscillatory non-axisymmetric.

3.2 The generalized Rayleigh criterion

In Sec. 3.1, the Rayleigh discriminant of the isothermal case (3.4) has been derived. Using the same method, it is possible to derive the generalized Rayleigh discriminant. The difference resides in the consideration of a linearly decreasing density with the temperature: $\rho = \rho_{ref}\left[1 - \alpha\left(T - T_{ref}\right)\right]$. In the case where only the inner cylinder rotates ($\mu = 0$), the generalized Rayleigh discriminant can be written:

$$\psi(r) = \bar{\Phi} - \gamma_a \left(\Theta\bar{\Phi} + \frac{d\Theta}{dr}\frac{V^2}{r}\right) \quad \text{where} \quad \bar{\Phi} = \left(\frac{2\eta}{1+\eta}\right)^2 \left[1 - \frac{1}{(1-\eta)^2 r^2}\right] \tag{3.5}$$

The Rayleigh discriminant is thus the sum of the isothermal Rayleigh discriminant $\bar{\Phi}$ and a correction due to the centrifugal buoyancy. If $\psi < 0$, the flow is potentially unstable. The figure (3.7) shows the profile of the Rayleigh discriminant in the gap. When the outer cylinder is at rest, the discriminant is always negative, but compared to the isothermal case, we can see that ψ is larger when γ_a is positive, and that it is lower when γ_a is negative. It is hence expected that the circular Couette flow is stabilized when the inner cylinder is hotter than the outer one, and destabilized in the opposite case. The generalized Rayleigh discriminant (3.5) was derived by Mutabazi and Bahloul [28] and by Kirillov and Mutabazi [52] using the short wavelength approximation.

3.3 1-D model for the heated Taylor-Couette system

Another method to derive a criterion which can determine the stability of the system is a 1-dimensional model. One advantage of this method, compared to the derivation of the generalized Rayleigh criterion, is the inclusion of viscosity flow. For the 1-D model of the Taylor-Couette flow with a radial temperature gradient, only the z-dependence of the velocity, the pressure and the temperature perturbations are retained. To make the Reynolds number appear in the set of

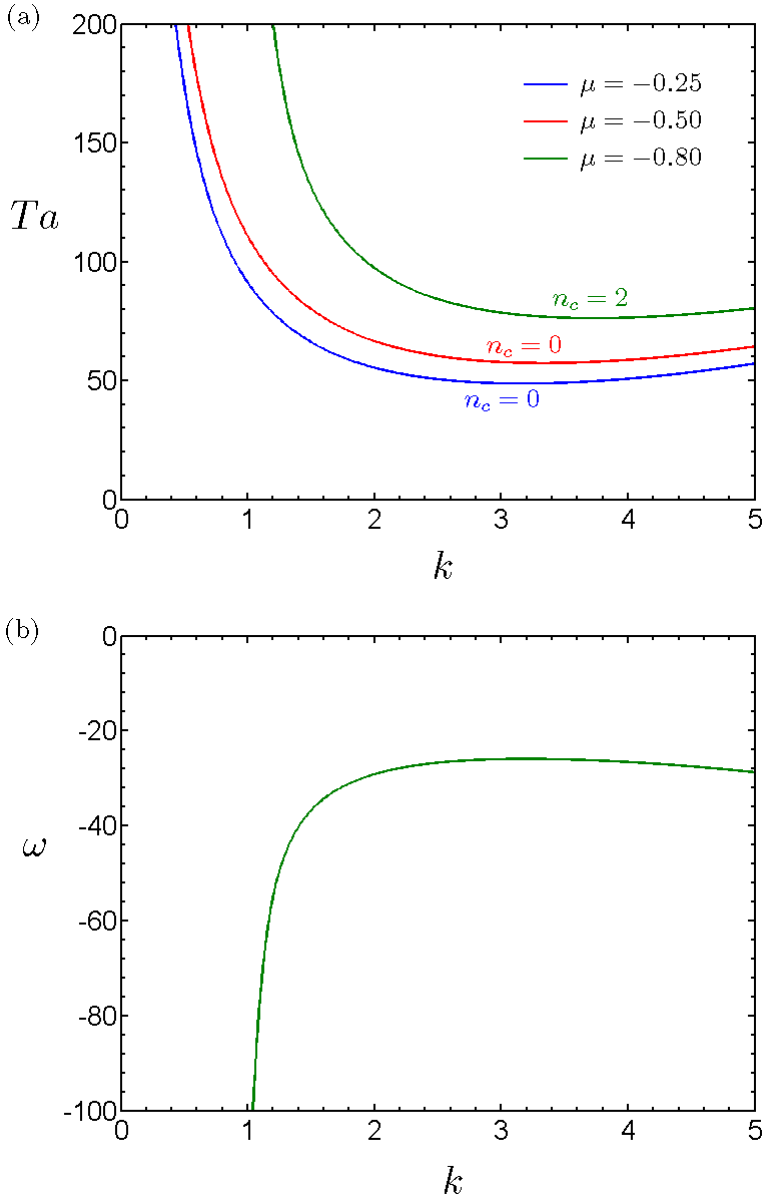

Figure 3.6: Variation of (a) the Taylor number and (b) the frequency at the marginal state for $\eta = 0.8$, and for various μ. At the critical condition, (Ta_c, k_c) is $(48.75, 3.17)$ for $\mu = -0.25$, $(57.37, 3.33)$ for $\mu = -0.5$, and $(76.25, 3.74)$ for $\mu = -0.8$.

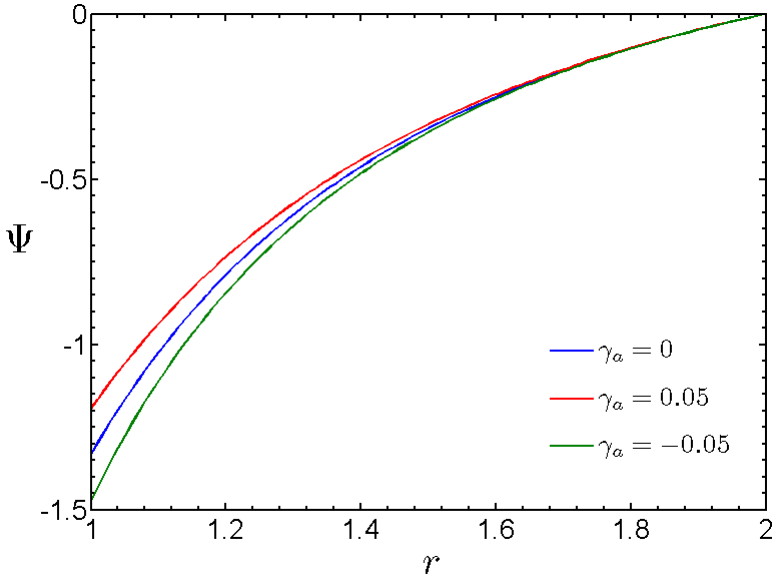

Figure 3.7: Generalised Rayleigh discriminant profile when the outer cylinder is at rest as a function of the dimensionless radial position for different values of γ_a and for $\eta = 0.5$.

linearised equations for perturbations (2.26a - 2.26e), the velocity must be scaled by the velocity of the inner cylinder $R_1\Omega_1$ instead of d^2/ν. This set of equations for perturbations become:

$$\frac{\partial w'}{\partial z} = 0 \tag{3.6a}$$

$$\frac{\partial u'}{\partial t} = \frac{1}{\mathrm{Re}}\left(\frac{\partial^2 u'}{\partial z^2} - \frac{u'}{r^2}\right) + \frac{2Vv'}{r} - \gamma_a \frac{2\Theta V v' + V^2\theta'}{r} \tag{3.6b}$$

$$\frac{\partial v'}{\partial t} = \frac{1}{\mathrm{Re}}\left(\frac{\partial^2 v'}{\partial z^2} - \frac{v'}{r^2}\right) - \frac{Vu'}{r} - \frac{dV}{dr}u' \tag{3.6c}$$

$$\frac{\partial w'}{\partial t} = -\frac{1}{\mathrm{Re}}\frac{\partial \pi'}{\partial z} + \frac{\partial^2 v'}{\partial z^2} \tag{3.6d}$$

$$\frac{\partial \theta'}{\partial t} = -\frac{d\Theta}{dr}u' + \frac{1}{\mathrm{PrRe}}\frac{\partial^2 \theta'}{\partial z^2} \tag{3.6e}$$

Equations (3.6a) and (3.6d) yield $w' = 0$. Considering axisymmetric rolls of the gap size, the solution is sought in the form $e^{st}\cos qz$. Substituting this type of solution into equation (3.6b), (3.6c) and (3.6e), one can find:

$$su' = -\mathrm{Re}^{-1}\left(q^2 u' - \frac{u'}{r^2}\right) + \frac{2Vv'}{r} - \gamma_a \frac{2\Theta V v' + V^2\theta'}{r} \tag{3.7a}$$

$$sv' = -\mathrm{Re}^{-1}\left(q^2 v' - \frac{v'}{r^2}\right) - \frac{Vu'}{r} - \frac{dV}{dr}u' \tag{3.7b}$$

$$s\theta' = -\frac{d\Theta}{dr}u' - \frac{q^2}{\mathrm{PrRe}}\theta' \tag{3.7c}$$

Written in the matrix form, the equations (3.7) read:

$$\begin{pmatrix} s+\mathrm{Re}^{-1}\left(q^2+r^{-2}\right) & -2V(1-\gamma_a\Theta)/r & \gamma_a V^2/r \\ V/r+DV & s+\mathrm{Re}^{-1}\left(q^2+r^{-2}\right) & 0 \\ D\Theta & 0 & s+q^2/(\mathrm{PrRe}) \end{pmatrix} \begin{pmatrix} u' \\ v' \\ \theta' \end{pmatrix} = \begin{pmatrix} 0 \\ 0 \\ 0 \end{pmatrix} \tag{3.8}$$

where $D = d/dr$. The solvability of this system requires that the determinant of the square matrix is zero, which leads to:

$$\left(s+\frac{q^2+r^{-2}}{\mathrm{Re}}\right)^2\left(s+\frac{q^2}{\mathrm{PrRe}}\right)+\frac{2V}{r}\left(\frac{V}{r}+DV\right)(1-\gamma_a\Theta)\left(s+\frac{q^2}{\mathrm{PrRe}}\right) - \gamma_a D\Theta\frac{V^2}{r}\left(s+\frac{q^2+r^{-2}}{\mathrm{Re}}\right)=0 \tag{3.9}$$

Introducing the Rossby number $\mathrm{Ro} = rD\Omega/(2\Omega)$, the thermal Rossby number $\mathrm{Rt} = rD\Theta/(2\Theta)$ and using $\Omega = V/r$, one can find:

$$\left(s+\frac{q^2+r^{-2}}{\mathrm{Re}}\right)^2\left(s+\frac{q^2}{\mathrm{PrRe}}\right)+4\Omega^2(1+\mathrm{Ro})(1-\gamma_a\Theta)\left(s+\frac{q^2}{\mathrm{PrRe}}\right) - 2\gamma_a\Theta\mathrm{Rt}\Omega^2\left(s+\frac{q^2+r^{-2}}{\mathrm{Re}}\right)=0 \tag{3.10}$$

Considering stationary modes at the onset of convection, we have $s = 0$. Moreover, we have $1+\mathrm{Ro} = (\mu-\eta^2)/[(1-\eta)(\mu+\eta)]$, and at the mean geometric radius $\bar{r} = \sqrt{\eta}/(1-\eta)$, we have $\Theta = 1/2$ and $\mathrm{Rt} = 1/\ln\eta$. The equation (3.10) can then be written:

$$\mathrm{Re}^2 = \frac{q^2\left(q^2+\dfrac{(1-\eta)^2}{\eta}\right)^2}{4q^2\left(\dfrac{\gamma_a}{2}\right)\dfrac{\eta^2-\mu}{(1-\eta)(\eta+\mu)}+\dfrac{\gamma_a\mathrm{Pr}}{\ln\eta}\left(q^2+\dfrac{(1-\eta)^2}{\eta}\right)} \tag{3.11}$$

In the isothermal case ($\gamma_a = 0$) the positivity of the expression on the right side of the equality is ensured if $\mu < \eta^2$ which correspond to the Rayleigh unstable flow. In the general case, recalling that $\ln\eta < 0$, positivity is ensured if:

$$\gamma_a\mathrm{Pr} < \gamma_a\mathrm{Pr}^* = 4q^2\left(1-\frac{\gamma_a}{2}\right)\frac{\mu-\eta^2}{(1-\eta)(\mu+\eta)}\times\left(q^2+\frac{(1-\eta)^2}{\eta}\right)^{-1}\ln\eta \tag{3.12}$$

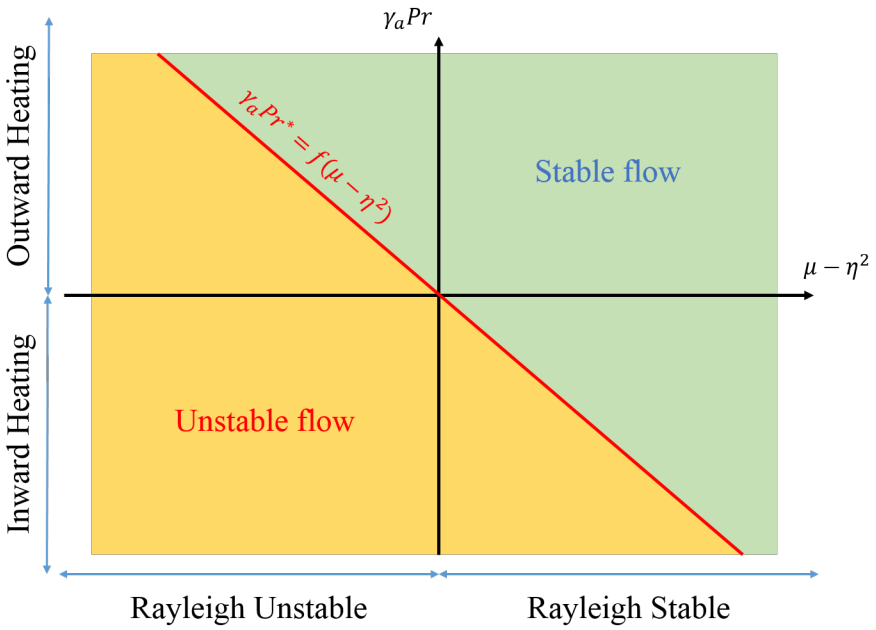

Figure 3.8: Schematic representation of the stability of the flow depending on the value of $\mu - \eta^2$. The condition obtained by the one dimensional model tells that the value $\gamma_a \mathrm{Pr}$ has to be below a certain value $\gamma_a \mathrm{Pr}^*$, which mainly depends on $\mu - \eta^2$.

Let us consider that η, q and γ_a are fixed (γ_a can be positive or negative), then the function $\gamma_a \mathrm{Pr}^*$ is a linearly decreasing function of $\mu - \eta^2$. The condition obtained with the 1-dimensional can thus be summarised as shown in Fig. 3.8. The quantity $\gamma_a \mathrm{Pr}^*$ is positive for Rayleigh unstable flows ($\mu < \eta^2$) and it is negative for Rayleigh stable flows ($\mu > \eta^2$). In outward heating ($\gamma_a > 0$), the condition $\gamma_a \mathrm{Pr} < \gamma_a \mathrm{Pr}^*$ cannot be satisfied for Rayleigh stable flow, while it can be satisfied for Rayleigh unstable flows if $\gamma_a \mathrm{Pr}$ is sufficiently low. In inward heating ($\gamma_a < 0$), the condition $\gamma_a \mathrm{Pr} < \gamma_a \mathrm{Pr}^*$ is always satisfied for Rayleigh unstable flow, while it can be satisfied for Rayleigh stable flows if $-\gamma_a \mathrm{Pr}$ is sufficiently large.

Chapter 4

Centrifugal buoyancy in Taylor-Couette flow with fixed outer cylinder

The effect of the centrifugal buoyancy is investigated in the case where only the inner cylinder rotates with a radial temperature gradient and in weightless environment ($\mathrm{Gr} = 0$). This regime is Rayleigh unstable, which means that the centrifugal force has a destabilising effect. The centrifugal buoyancy induced by the coupling between the centrifugal acceleration and the radial temperature gradient will either stabilise or destabilise the flow, depending on the heating direction.

4.1 Base pressure

The base pressure can provide information about the stability of the system. In this configuration, the base pressure Π, which is the solution of equation (2.17a) with $V_E = 0$, can be written:

$$\Pi = \Pi_{CCF} + \Pi_{BUO} \tag{4.1}$$

The base pressure is defined as that of the isothermal Couette flow Π_{CCF} corrected with the effect of the centrifugal buoyancy Π_{BUO}. These two terms are given by:

$$\Pi_{CCF} = \frac{A^2 r^2}{2} + 2AB \log\left[(1-\eta)\, r\right] - \frac{B^2}{2r^2} + \Pi_0 \tag{4.2}$$

$$\Pi_{BUO} = -\frac{\gamma_a}{\log \eta} \left(AB \left\{ \log\left[(1-\eta)\, r\right] \right\}^2 + C(r) \log\left[(1-\eta)\, r\right]^2 - D(r) \right) \tag{4.3}$$

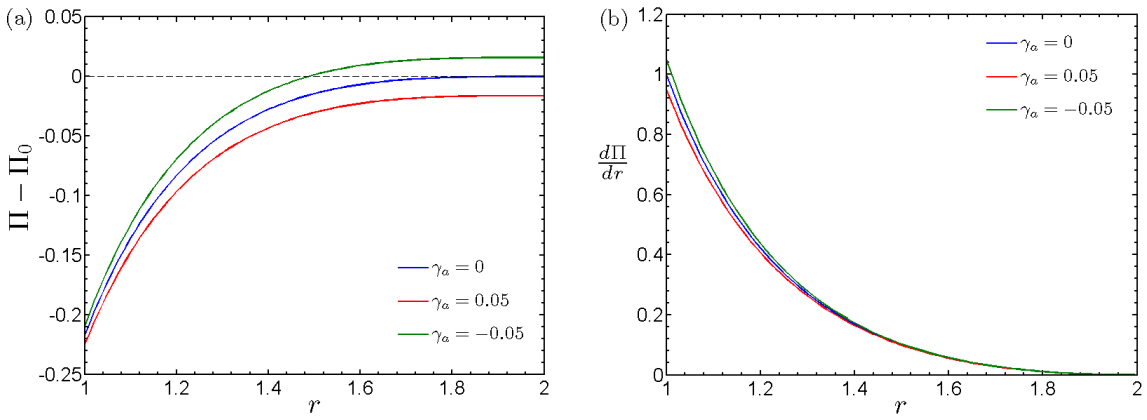

Figure 4.1: Base pressure profile (a) and its derivative (b) as function of the dimensionless position for different values of γ_a with $\eta = 0.5$ and $\Pi_0 = 0$.

where Π_0 is the pressure at the outer cylinder. The functions $C(r)$ and $D(r)$ are given by:

$$C(r) = \frac{A^2 r^2}{4} - \frac{B^2}{4r^2}\,; \quad D(r) = \frac{A^2 r^2}{4} + \frac{B^2}{4r^2}$$

The pressure Π_{BUO} balances the excess or the lack of momentum given by the radial buoyancy, depending on the direction of the heat flux. This pressure couples the base velocity and the base temperature. In view of the balance between the thermal buoyancy and the pressure gradient formulated in (2.17a) with $V_E = 0$, it is possible to identify the role that the temperature has on the flow stability. The figure 4.1-a shows the base pressure profile as function of the dimensionless radial position. The outward heating ($\gamma_a > 0$) diminishes the pressure while the inward heating ($\gamma_a < 0$) increases it with respect to the isothermal case. The profile of the base pressure gradient is shown on figure 4.1-b. As this gradient corresponds to a force balanced by the radial buoyancy, we can conclude that the higher the pressure gradient, the more unstable the flow. Thus, the flow will be more unstable compared to the isothermal case when $\gamma_a < 0$ and will be more stable when $\gamma_a > 0$, which is in agreement with the conclusion of the 1-dimensional model formulated on Sec. 3.3.

4.2 Results

The eigenvalues s are computed for a set of parameters $(\eta, \mathrm{Pr}, \gamma_a, \mathrm{Ta}, k, n)$. A marginal stability curve $\mathrm{Ta} = \mathrm{Ta}\,(k)$ is determined by searching for the condition where the maximum value of the growth rate σ changes its sign. The global minimum of the marginal stability curves

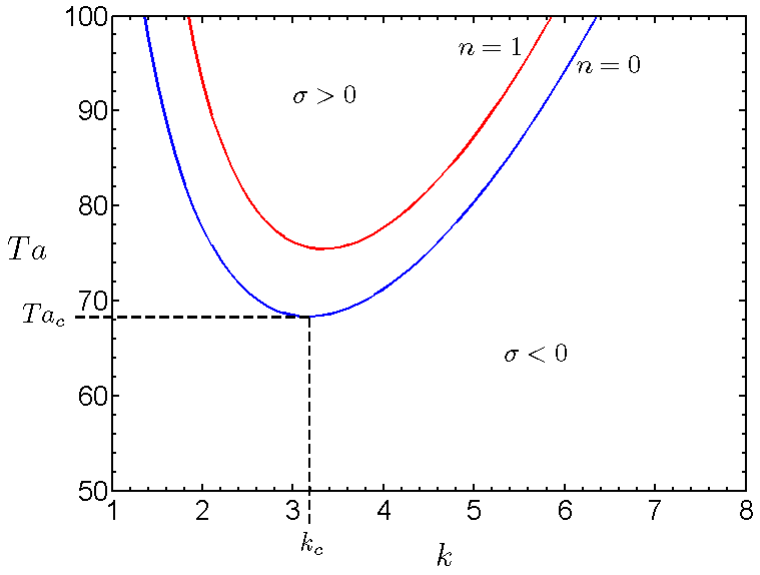

Figure 4.2: Marginal stability curves obtained for Pr = 10, $\eta = 0.5$ and $\gamma_a = 0.001$ and for two values of n. The critical state for this set of parameters is located at the marginal curve for $n = 0$.

(k_n, Ta_n) obtained for different azimuthal mode number n corresponds to the critical state with the corresponding critical parameters $(\mathrm{Ta}_c, k_c, n_c, \omega_c)$ (Fig. 4.2).

4.2.1 Influence of the tenperature difference

The figure 4.3 shows the behaviour of the critical Taylor number normalised by its value for the isothermal case ($\gamma_a = 0$), of the critical wavenumber and of the critical frequency as function of γ_a for Pr = 50 and for different radius ratio η. When the outer cylinder is hotter than the inner one, i.e. inward heating ($\gamma_a < 0$), the threshold decreases with increasing temperature difference between the two cylinders. This highlights the destabilising effect of the centrifugal buoyancy under this condition. The critical modes are axisymmetric ($n_c = 0$) with a critical wavenumber that increases slightly with the temperature difference (Fig. 4.3 - b). These modes are stationary (Fig. 4.3 - c), and therefore we refer to them as SA (stationary axisymmetric) modes.

The SA mode exists also when $\gamma_a > 0$ if γ_a is smaller than a certain value γ_a^*. The critical Taylor number increases with γ_a, highlighting the stabilising effect of the centrifugal buoyancy when the inner cylinder is hotter than the outer one, i.e. outward heating. For a fixed Pr, γ_a^* decreases with increasing the radius ratio. Beyond this particular value of γ_a the critical modes become oscillatory axisymmetric (OA) for small and moderate values of the radius ratio η, or oscillatory non-axisymmetric (ONA) for large η. The critical Taylor number is almost independent of γ_a for

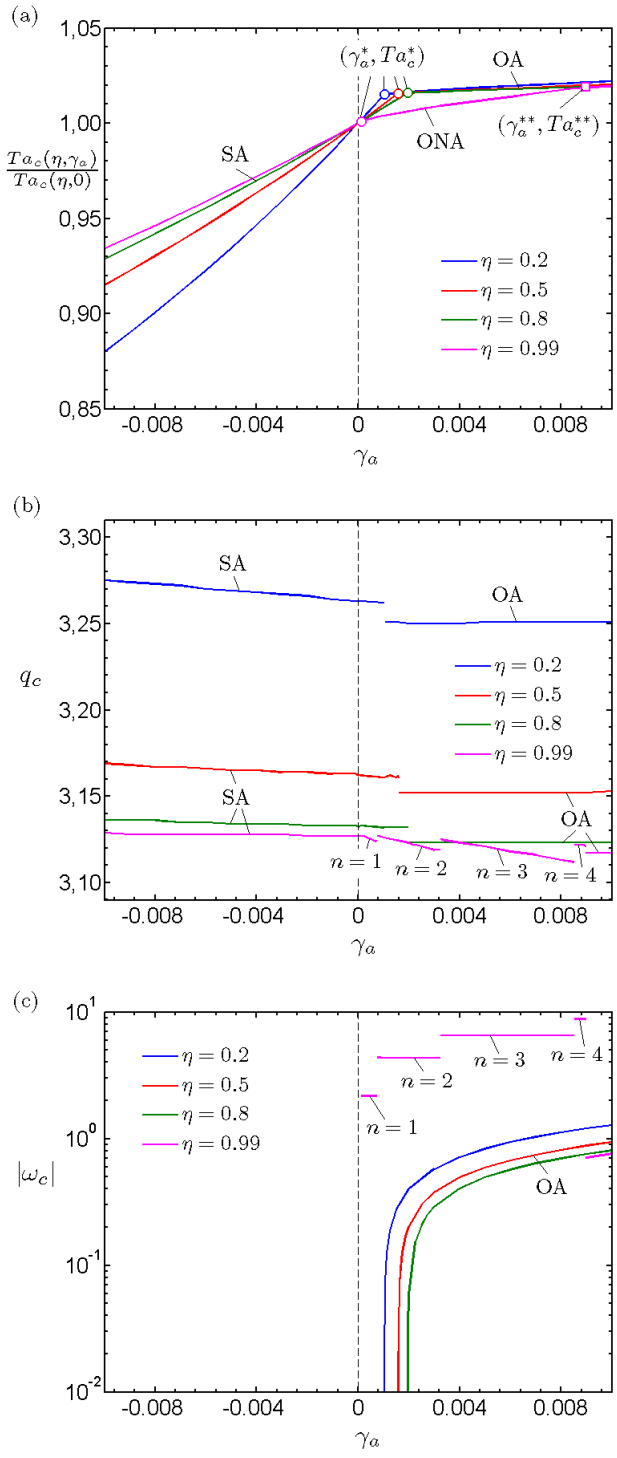

Figure 4.3: Variation of the critical parameters with γ_a for different η and and for Pr = 50: (a) normalized Ta, (b) wavenumber and (c) frequency. SA: stationary axisymmetric mode; OA: oscillatory axisymmetric mode; ONA: oscillatory non-axisymmetric mode.

OA modes while for ONA, it increases with increasing γ_a, until a certain value of γ_a, that we will denote ${\gamma_a}^{**}$. Beyond this value of ${\gamma_a}^{**}$, the ONA modes become OA with an almost constant Ta_c. For OA modes, the critical wavenumber undergoes a discontinuity at (γ_a^*, Ta_c^*). Then, their wavenumber becomes independent of γ_a and their frequency increase with γ_a. For ONA modes, the critical wavenumber undergoes a discontinuity at (γ_a^*, Ta_c^*) and each times the azimuthal mode number changes. Within a value of n, the critical wavenumber decreases and the frequency is almost constant and is approximatively one order of magnitude higher than the frequency of OA modes. The points $({\gamma_a}^*, \mathrm{Ta}_c^*)$ and $({\gamma_a}^{**}, \mathrm{Ta}_c^{**})$ are called *codimension two points* in the literature. These points indicates parametric positions where two modes of different nature are critical at the same time. Their coordinates depend on Pr and η.

The effect of the centrifugal buoyancy on the instability threshold is most apparent for SA modes, in particular for inward heating ($\gamma_a < 0$). The slope of the curve $\mathrm{Ta}_c\,(\eta = cst, \gamma_a)$, computed at $\gamma_a = 0$ is shown on Table 4.1. This slope depends on η and on Pr: for each radius ratio, it increases with the Prandtl number.

4.2.2 Influence of Pr

In the linearised equations (2.31), the Prandtl number is involved in the energy equation, therefore it plays no role for the isothermal Taylor-Couette instability. For $\gamma_a \neq 0$, Pr will modify the stability of the flow through the coupling of temperature and velocity fields. Figure 4.4 shows the behaviour of the threshold, of the critical wavenumber and of the critical frequency as a function of the Prandtl number. When the thermal expansion parameter γ_a is fixed to a positive value, Ta_c increases with Pr until a certain value Pr^*. The critical modes are SA when

Table 4.1: Values of the threshold slope $\mathrm{Ta}_c(\gamma_a)/\mathrm{Ta}_c(\gamma_a = 0)$ as function of γ_a computed at $\gamma_a = 0$ for different η and Pr.

		Pr						
		0.01	0.1	1	10	50	100	1000
η	0.1	0.20	0.24	0.58	3.97	19.03	37.77	359.45
	0.3	0.24	0.26	0.48	2.62	12.11	23.95	230.27
	0.5	0.26	0.28	0.44	2.14	9.68	19.09	184.02
	0.8	0.27	0.29	0.42	1.81	7.94	15.59	150.35
	0.9	0.28	0.29	0.42	1.74	7.57	14.84	143.16
	0.99	0.28	0.29	0.42	1.68	7.29	14.28	137.68

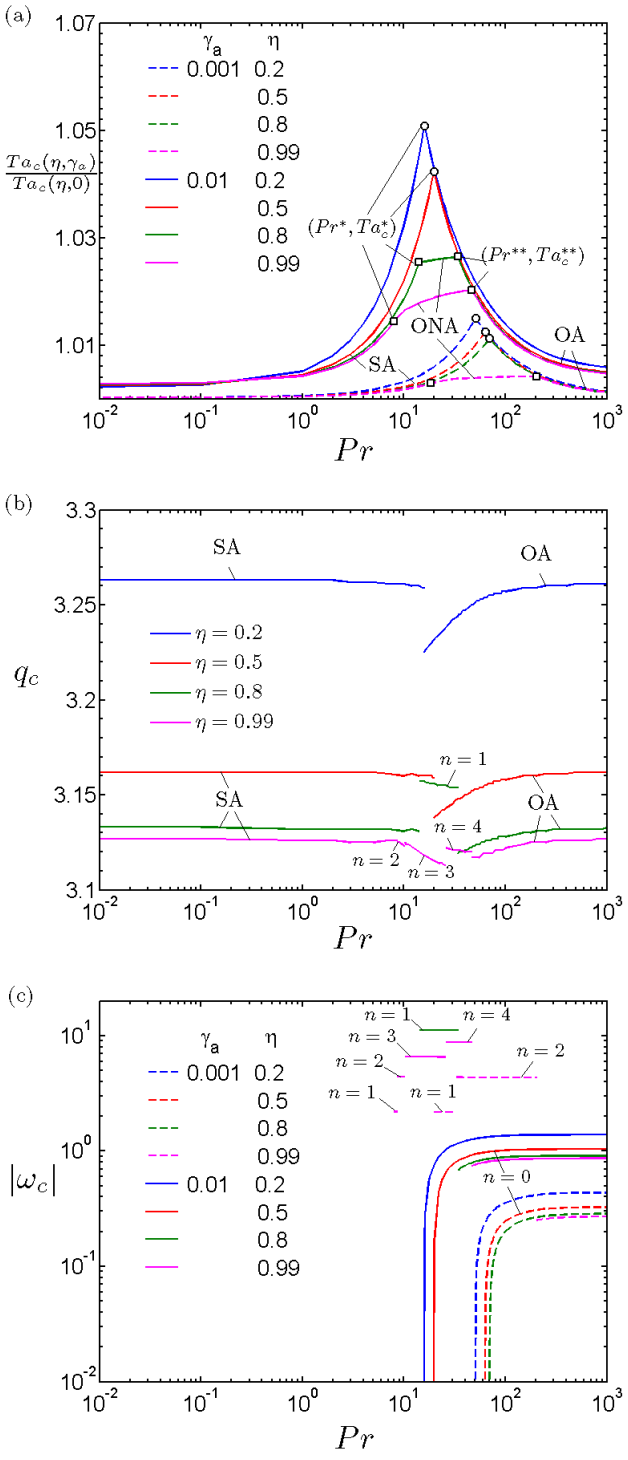

Figure 4.4: Variation of the critical parameters with Pr for different η and γ_a: (a) normalized Taylor number, (b) wavenuber and (c) frequency. For clarity, q_c (b) was plotted only for $\gamma_a = 0.01$. SA: stationary axisymmetric mode; OA: oscillatory axisymmetric mode; ONA: oscillatory non-axisymmetric mode.

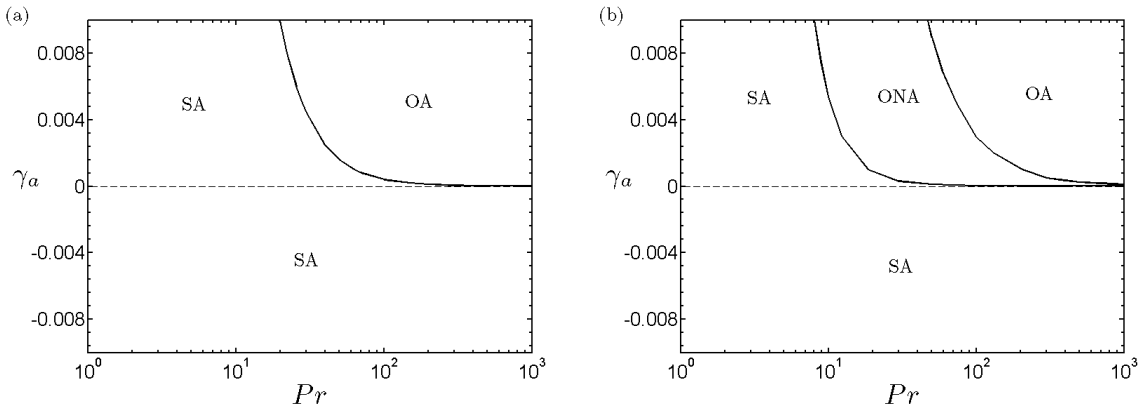

Figure 4.5: Zones of critical states for (a) $\eta = 0.5$ and for (b) $\eta = 0.99$.

$\mathrm{Pr} < \mathrm{Pr}^*$. When the Prandtl number exceeds Pr^*, the critical modes are OA for low and moderate values of η or ONA for large values of η and of γ_a. The ONA modes exists for $\mathrm{Pr}^* < \mathrm{Pr} < \mathrm{Pr}^{**}$ where the critical Taylor number increases with Pr. Above the value Pr^{**}, the OA modes become again critical. The threshold Ta_c of the OA modes decreases with Pr toward its value for the isothermal Taylor-Couette instability. The critical wavenumber of SA and ONA modes decreases with the Prandtl number while for OA modes, it increases with Pr. The wavenumber undergoes discontuinies at the codimension-2 points $(\mathrm{Pr}^*, \mathrm{Ta}^*)$ and $(\mathrm{Pr}^{**}, \mathrm{Ta}^{**})$ and when the azimuthal modes number changes. The critical frequency of OA modes increases with Pr until it becomes Prandtl independent with a constant value which depends on η and γ_a. The frequency of ONA modes remains constant, unless n_c changes.

The values of Pr^* and Pr^{**} depend on both γ_a and η. At $(\mathrm{Pr}^*, \mathrm{Ta}_c^*)$ both SA and OA or ONA modes are critical. At $(\mathrm{Pr}^{**}, \mathrm{Ta}_c^{**})$, the ONA modes as well as the OA modes are critical. The zones of different critical states can be visualized in the plane (Pr, γ_a) in Fig. 4.5 for a moderate and a large value of η.

4.2.3 Eigenvalues behaviour

To have a better insight into the effect of the centrifugal buoyancy, the spectrum of the eigenvalues has been analysed, in particular, that of the axisymmetric modes. In this section, the radius ratio is fixed at $\eta = 0.8$. The behaviour of the growth rate with the wavenumber is shown on Fig. 4.6 - a in the cases of isothermal, inward heating and outward heating Couette flow at a given Pr and Ta ($\mathrm{Ta} = 47.4$ is the critical Taylor number of the isothermal case). When $\gamma_a = 0$, the only visible mode is the centrifugal mode which is critical at $k = 3.132$ for $\mathrm{Ta} = 47.4$. When

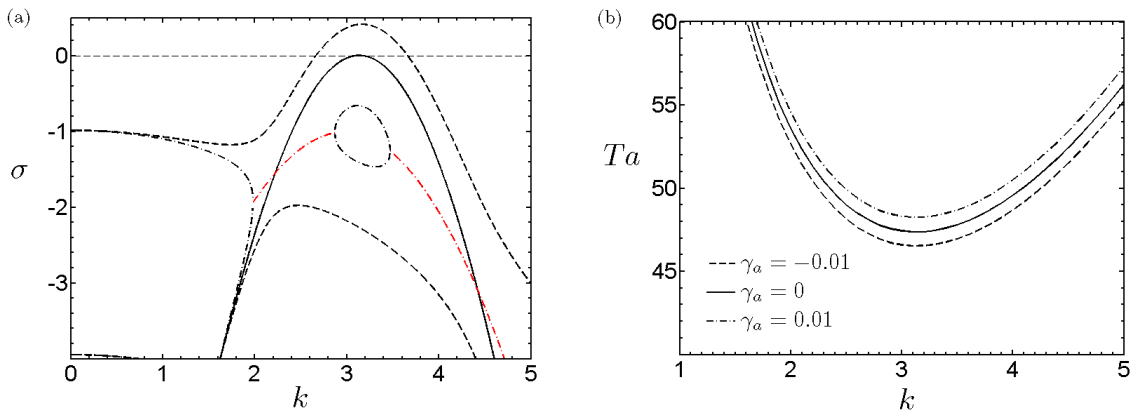

Figure 4.6: (a) Variation of the growth rate with the wavenumber for Ta = 47.4 and (b) marginal stability curves for $\eta = 0.8$ and Pr = 10 for isothermal case ($\gamma_a = 0$), the inward heating ($\gamma_a = -0.01$) and outward heating ($\gamma_a = 0.01$). Black and red curves correspond to stationary and oscillatory modes respectively.

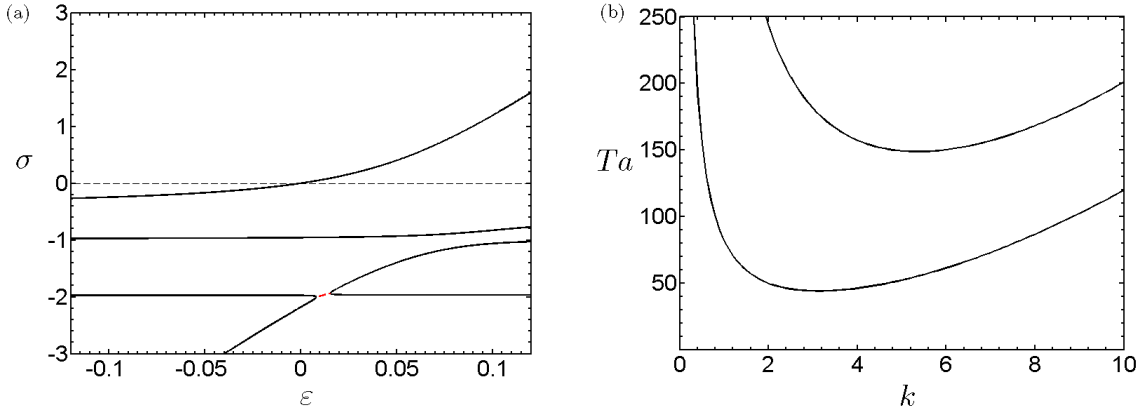

Figure 4.7: (a) Variation of the growth rate with the criticality $\epsilon = \mathrm{Ta}/\mathrm{Ta}_c - 1$ and (b) marginal stability curves for $\eta = 0.8$, Pr = 50 and $\gamma_a = -0.01$. Black and red curves correspond to stationary and oscillatory modes respectively.

$\gamma_a \neq 0$, the centrifugal mode still exists and exhibits the largest growth rate. The growth rate of these modes is modified by the centrifugal buoyancy: the stabilizing or destabilizing effect of the centrifugal buoyancy respectively decreases or increases the growth rate. This can be shown on the marginal stability curves plotted on Fig. 4.6 - b through the decrease of the Taylor number for inward heating and its increase for outward heating compared to the isothermal case. In addition to the centrifugal modes, other modes which are caused by the thermal effects (thermal modes) interact with the centrifugal mode. On figure 4.6 - a, we can see that one of these modes merges with the centrifugal mode for some values of k and gives rise to oscillatory modes. The variation of the growth rate with the criticality parameter $\epsilon = \mathrm{Ta}/\mathrm{Ta}_c - 1$ and corresponding marginal curves show that no oscillatory modes are expected near the criticality (Fig. 4.7).

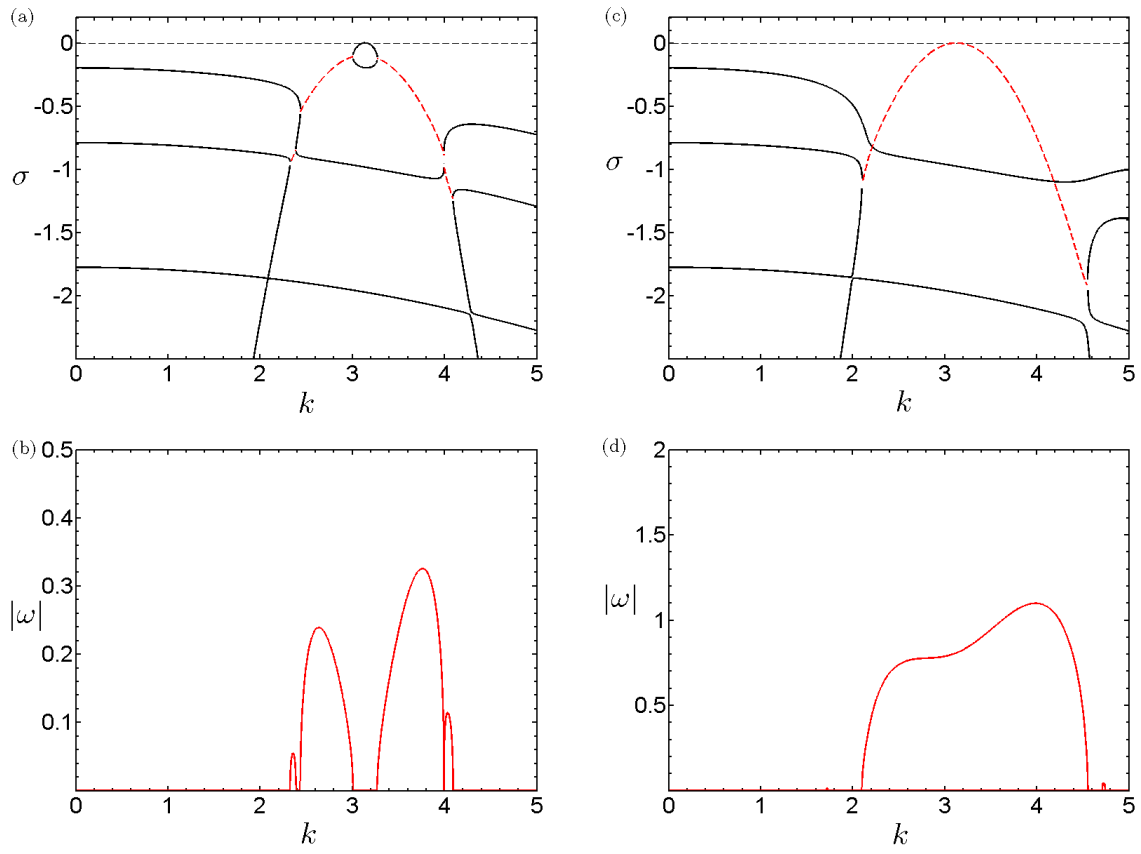

Figure 4.8: Variation of the growth rate and of the frequency with the wave number k for $\eta = 0.8$ and $\mathrm{Pr} = 50$ at $\mathrm{Ta} = \mathrm{Ta}_c$. The thermal expansion parameter $\gamma_a = 0.001 < {\gamma_a}^*$ in (a) and (b) and $\gamma_a = 0.01 > {\gamma_a}^*$ in (c) and (d). Black and red curves correspond to stationary and oscillatory modes respectively.

In outward heating ($\gamma_a > 0$) the centrifugal buoyancy plays a stabilizing effect. In this case, oscillatory axisymmetric modes can become critical when γ_a is larger than ${\gamma_a}^*$ which depends on η and Pr. The dispersion curves $\sigma = \sigma(k)$ and $\omega = \omega(k)$ computed for $\mathrm{Pr} = 50$ at critical conditions ($\mathrm{Ta} = \mathrm{Ta}_c$) are shown on Fig. 4.8 for γ_a values smaller and larger than ${\gamma_a}^*$. When $\gamma_a < {\gamma_a}^*$, the centrifugal mode merges with a thermal mode close to the onset of instability, producing oscillatory modes, but these modes split again close to $k = k_c$ and let a stationary mode become critical (Fig. 4.8 - a,b). When $\gamma_a > {\gamma_a}^*$, the splitting of the centrifugal and thermal modes does not occur, leading to a critical oscillatory axisymmetric mode (Fig. 4.8 - c,d).

Figure 4.9 shows the variation of the growth rate and the frequency with the criticalty parameter together with the marginal stability curves and the frequency dispersion curve when $\gamma_a > {\gamma_a}^*$. The critical condition is obtained for an oscillatory mode.

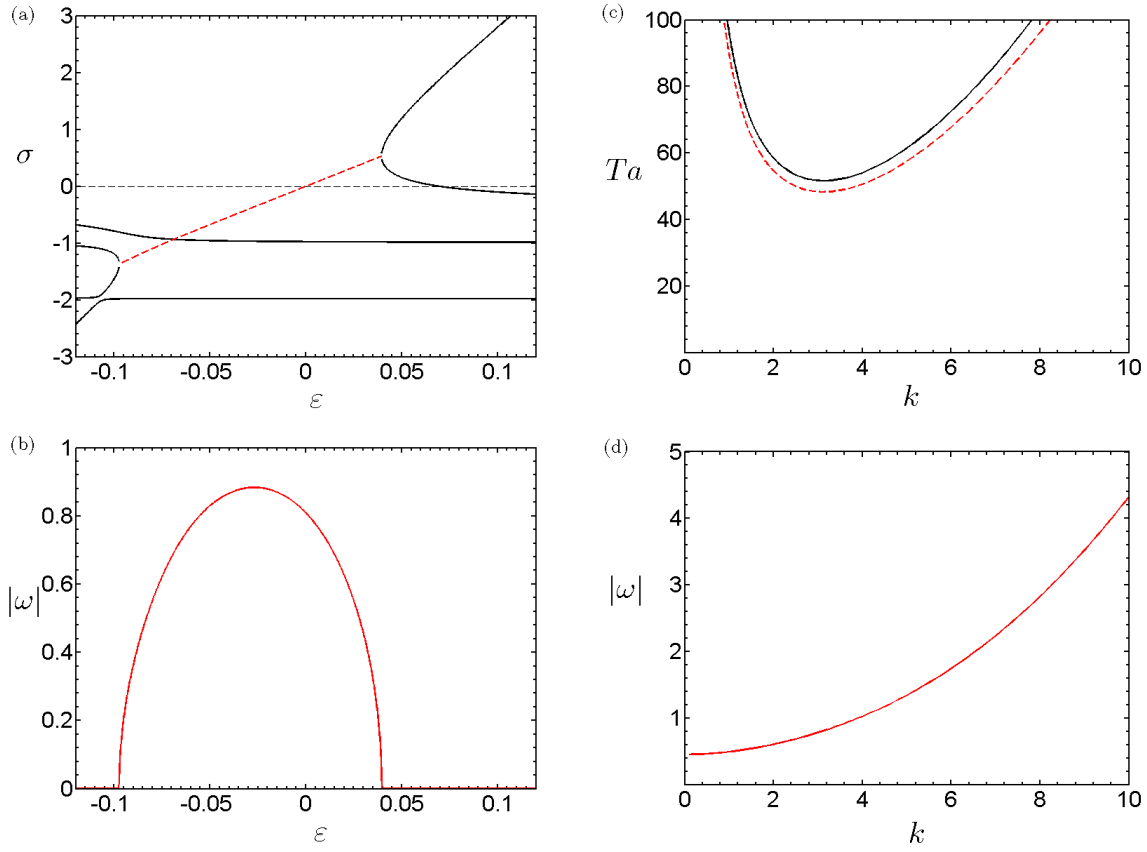

Figure 4.9: Stability analysis for $\eta = 0.8$, Pr $= 50$, and $\gamma_a = 0.01$: Variation of the growth rate (a) and the frequency (b) with the criticality $\epsilon = \mathrm{Ta}/\mathrm{Ta}_c - 1$, marginal curves of the first two unstable modes (c), variation of the frequency of the oscillatory modes with the wave number, i.e., dispersion relation (d). Black and red curves correspond to stationary and oscillatory modes respectively.

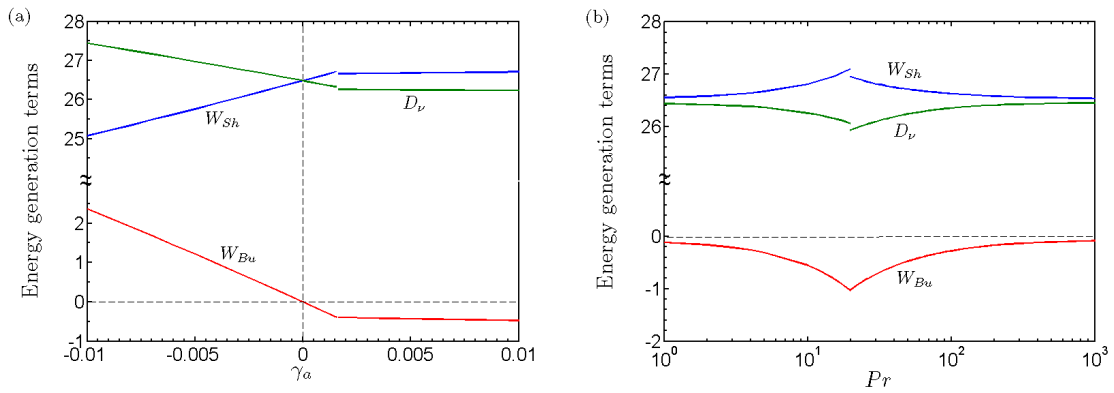

Figure 4.10: Energy generation terms for $\eta = 0.5$ as functions of (a) the thermal expansion parameter γ_a for $Pr = 50$ and (b) as function of the Prandtl number Pr for $\gamma_a = 0.01$.

4.3 Discussion

For inward heating, the imposed temperature gradient has a significant destabilizing effect with no change in the temporal and spatial nature of the critical modes. In contrast, outward heating yields only a slight variation of the instability threshold with γ_a. The most prominent effect of the centrifugal buoyancy is the change of the critical modes in their temporal nature at large Prandtl number.

4.3.1 Energy analysis

In this problem, the equation for kinetic energy (2.43) is reduced to:

$$\frac{dK}{dt} = W_{Sh} + W_{Bu} - D_\nu \tag{4.4}$$

The three terms contributing to the variation rate of perturbation kinetic energy are plotted in figure 4.10 as function of γ_a and Pr for $\eta = 0.5$. These terms vary linearly with γ_a and become constant when $\gamma_a \geq \gamma_a{}^*$ (Fig. 4.10 - a). For inward heating, the power performed by the centrifugal buoyancy W_{Bu} is positive, highlighting the destabilizing effect of the centrifugal buoyancy. When the sign of γ_a changes , W_{Bu} also changes its sign, meaning that the centrifugal buoyancy in inward heating stabilises the flow. When γ_a exceeds the value of $\gamma_a{}^*$, W_{Bu} become constant. So in outward heating, increasing γ_a reinforces the stability of the circular Couette flow, but the stabilizing effect saturates when OA modes occur.

The dependence of W_{Bu} on Pr in outward heating is subtle (Fig. 4.10 - b), but it can be

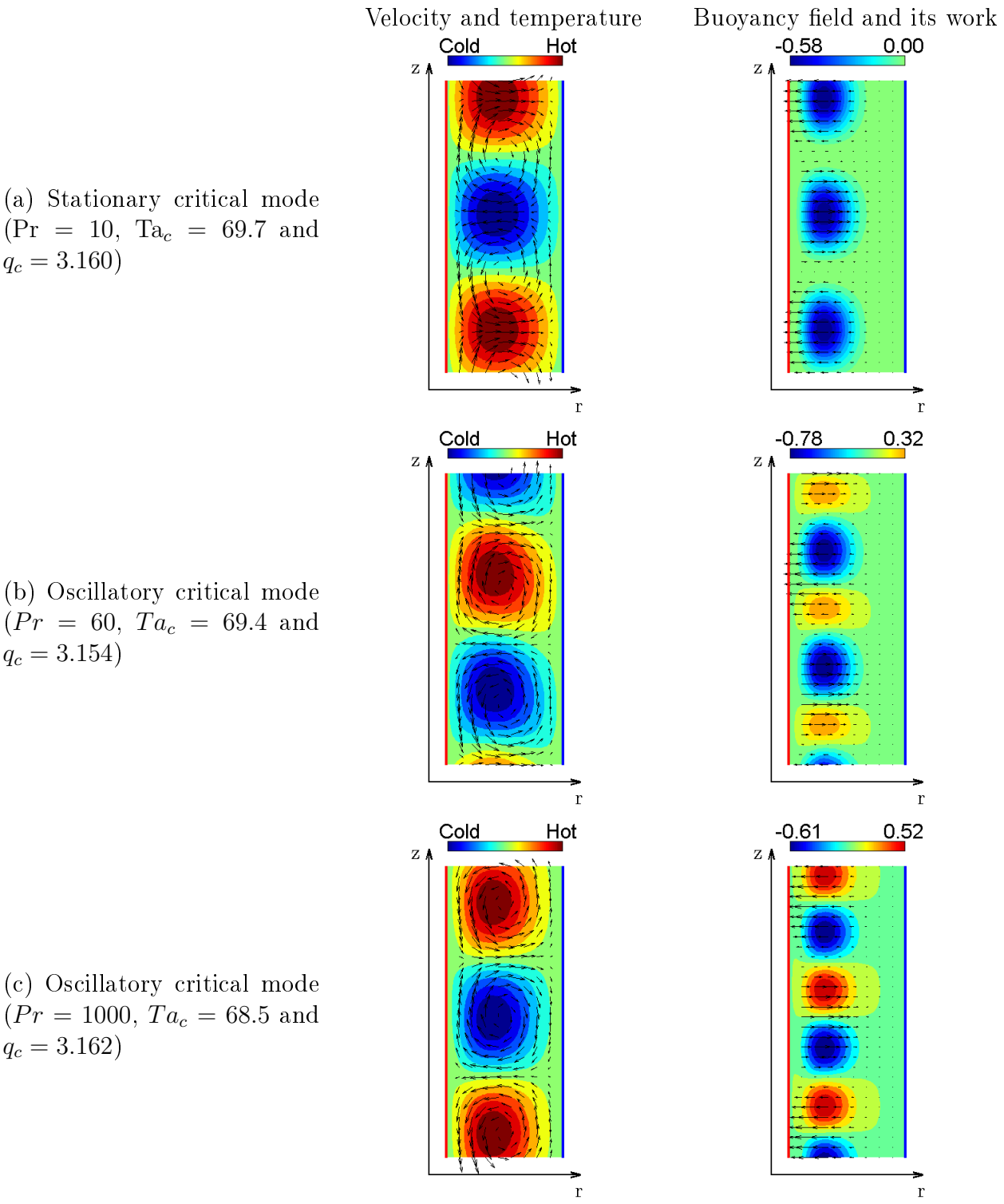

(a) Stationary critical mode (Pr = 10, Ta_c = 69.7 and $q_c = 3.160$)

(b) Oscillatory critical mode (Pr = 60, Ta_c = 69.4 and $q_c = 3.154$)

(c) Oscillatory critical mode (Pr = 1000, Ta_c = 68.5 and $q_c = 3.162$)

Figure 4.11: Eigenfunctions at critical conditions with $\eta = 0.5$ and $\gamma_a = 0.01$.

understood by analysing the density of the radial buoyancy power:

$$w_{Bu} = -\frac{\gamma_a}{r}\left(V^2\theta' + 2\Theta V v'\right)u' \tag{4.5}$$

The figure 4.11 shows some eigenfunctions at the critical condition in the (r, z) plane for $\eta = 0.5$ and for $\gamma_a = 0.01$ (outward heating). We can see from figure 4.11 - a that for stationary modes, the radial velocity perturbation u' and the temperature perturbation θ' are in phase with each other. For fluids with $\mathrm{Pr} < \mathrm{Pr}^*$, the power density w_{Bu} is then negative everywhere inside the gap, leading to a total negative power W_{Bu}. In this condition, if the amplitudes of perturbations increase, the stabilizing effect of the centrifugal buoyancy is reinforced. For fluids with $\mathrm{Pr} > \mathrm{Pr}^*$, the phase of θ' relative to u' increases with Pr (Figs. 4.11 - b,c) and will attains $-\pi/2$ at large Pr. The increase of the phase delay increases the total power W_{Bu} (Fig.4.10 - b) because of the appearance of a zone of positive w_{Bu} inside the gap. For large enough values of Pr, the zones of positive w_{Bu} balance the zones of negative w_{Bu} so that $W_{Bu} = 0$. We then have no effect of the centrifugal buoyancy and the threshold is thus the one for the isothermal case.

This mechanism can be observed from the equation of energy (2.31e). When OA modes are critical, we have:

$$\mathrm{Pr} D\Theta \hat{u} = \left[\frac{1}{r}\frac{d}{dr}\left(r\frac{d}{dr}\right) - k_c^2\right]\hat{\theta} \tag{4.6}$$

Because of the sign of $D\Theta$, the radial velocity perturbation and the temperature perturbation are in phase in inward and in antiphase in outward heating. In both cases, the flow goes from the hot wall to the cold one, passing through the zones of positive temperature disturbances. This mechanism is similar to what observed in the Rayleigh-Bénard thermal convection. However, in the limit of infinite values of Pr, OA modes are critical and Eq. (2.31e) leads to the relation:

$$\hat{\theta} \to \frac{1}{\omega}\left|D\Theta\right|\hat{u}e^{-i\pi/2} \tag{4.7}$$

which exhibits a phase delay of $\pi/2$ between $\hat{\theta}$ and $\hat{u}$ and produces the zone of positive w_{Bu}.

4.3.2 Frequency analysis

The flow system under consideration can be analysed by analogy with Rayleigh-Bénard convection. In fact, for $\gamma_a < 0$, the gravity is oriented towards the hot wall and therefore, there is a

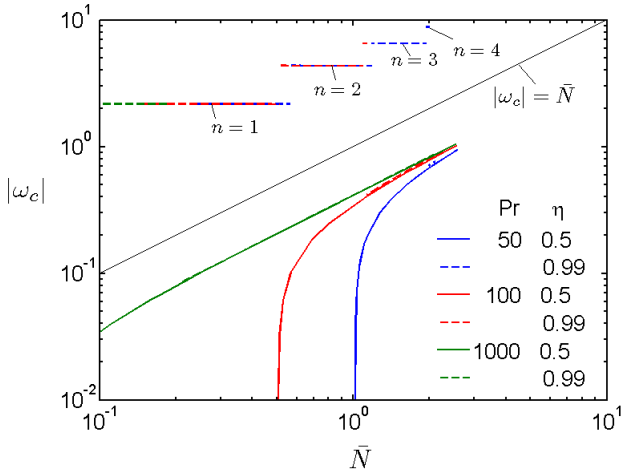

Figure 4.12: Critical frequencies as a function of Brunt-Väisälä frequency.

thermal convection instability which reinforces the centrifugal instability and decreases the threshold compared to the isothermal case. In opposite case of $\gamma_a > 0$, the radial density stratification is associated with internal waves which have the Brunt-Väisälä frequency $[-(1/\rho_2)(d\rho/dr)g_c]$ due to the stable stratification of the density regarding the centrifugal acceleration and given by its dimensionless expression:

$$\bar{N}^2 = \frac{\gamma_a \mathrm{Ta}^2}{\ln \eta} \frac{\eta V^2}{(1-\eta)\, r} \tag{4.8}$$

with the azimuthal velocity $V(r)$ estimated at the position $r_\eta = -1/\ln \eta$. At this particular position, the heat flux is equal to the one coresponding to the plane geometry, which has a constant heat flux between the two plates. Thus, the use of r_η weakens the effect of curvature. The Brunt-Väisälä frequency thus reads:

$$\bar{N} = \frac{\eta^{3/2} \left[(\ln \eta)^2 - (1-\eta)^2\right]}{(1-\eta^2)\,(1-\eta)^{3/2}} \sqrt{\frac{-\gamma_a \mathrm{Ta}^2}{\ln \eta}} \tag{4.9}$$

Figure 4.12 shows that the critical frequency of OA modes is proportional to $\bar{N}$ for large $|\omega_c|$ where viscous damping during an oscillation period is not significant (the time has been scaled with the characteristic time of viscous dissipation). This upper bound of the critical frequency suggests that the oscillations of critical modes originate from internal waves arising from the radial buoyancy effect on stable density stratification.

The dispersion of the OA modes can be developed about the critical condition $q = q_c$ as follows

$$\omega(q) \simeq c\, q_c + v_g\,(q - q_c) + P\,(q - q_c)^2\,, \tag{4.10}$$

Table 4.2: Variation of dispersion properties of the critical modes with Pr for $\eta = 0.5, \gamma_a = 0.01$.

Pr	c	v_g	P
50	0.297	0.256	0.045
100	0.321	0.281	0.048
1000	0.329	0.290	0.050

where

$$c = \frac{\omega_c}{q_c}, \qquad v_g = \frac{d\omega}{dq}, \qquad P = \frac{1}{2}\frac{d^2\omega}{dq^2}, \tag{4.11}$$

represent the phase velocity, the group velocity and the dispersion coefficient, respectively. Their values (Table 4.2) depend weakly on Pr. The OA modes induced by the radial buoyancy in the Taylor-Couette flow exhibit a normal dispersion.

Using the short wavelength approximation, Kirillov and Mutabazi [52] were able to give analytic expressions of the threshold of oscillatory modes and for the frequency of these modes:

$$\frac{\mathrm{Ta}_c^*}{\mathrm{Ta}_0} = \frac{\mathrm{Pr}+1}{\mathrm{Pr}}\left[1 - \frac{\gamma_a}{2} + \frac{\gamma_a}{2\ln\eta}\frac{\mathrm{Pr}+1}{\mathrm{Pr}}\left(\mathrm{Ta}_0\right)^2\right]^{-1/2} \tag{4.12a}$$

$$\frac{\omega_c}{\Omega} = \frac{\beta}{\mathrm{Pr}+1}\frac{1}{\mathrm{Ta}_0}\sqrt{-1 + \frac{\gamma_a}{2} - \frac{\gamma_a \mathrm{Pr}\,(\mathrm{Pr}+1)}{2\ln\eta}\left(\mathrm{Ta}_0\right)^2} \tag{4.12b}$$

where $\beta = k_z/|\boldsymbol{k}|$ and Ta_0 is the Taylor number of the isothermal case. They found that the threshold and the critical frequency depend on both γ_a and Pr. Figure 4.13 shows the results of Kirillov and Mutabazi concerning the critical frequency. There is a good agreement between our results and those of Kirillov. Indeed, they reproduced the saturation of the frequency at large Pr

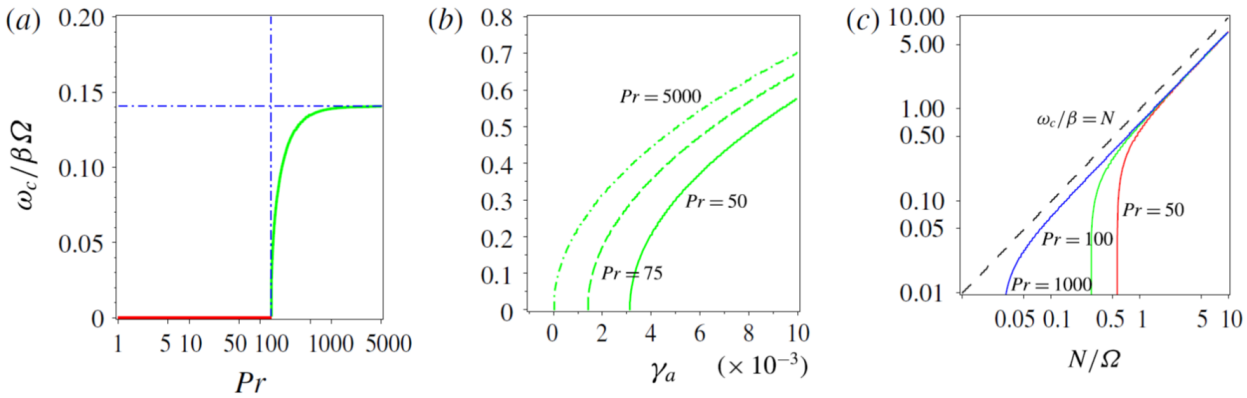

Figure 4.13: Critical frequencies in units of $\beta\Omega$ (a) as function of the Prandtl number for $\gamma_a = 0.0004$, (b) as function of γ_a and (c) as function of the Brunt-Väisälä frequency. All these results have been obtained for $\eta = 0.99$. [52]

Table 4.3: Critical parameters and coefficients of the Ginzburg-Landau equation against Pr and γ_a ($\eta = 0.8$).

Pr	γ_a	Ta_c (LSA)	Ta_c (DNS)	τ_0 (LSA)	τ_0 (DNS)	ξ_0	c_0	c_g	c_1	l (DNS)
10	-10^{-2}	46.533	46.594	4.16	4.791	0.269	0	0	0	60.82
	-10^{-3}	47.281	47.231	3.66	3.559	0.270				29.31
	10^{-3}	47.452	47.380	3.54	3.475	0.270				25.69
	10^{-2}	48.246	48.209	2.98	3.288	0.270				17.84
50	-10^{-2}	43.996	44.343	17.6	9.59	0.269	0	0	0	1157.24
	10^{-2}	48.292	49.020	7.19	3.294	0.271	−0.469	0.002	−0.469	−60.04
100	-10^{-2}	41.337	41.509	51.0	36.326	0.268	0	0	0	2485.11
	-10^{-3}	46.643	47.160	10.5	3.801	0.269				1499.98
	10^{-3}	47.748	47.595	7.17	3.527	0.270	−0.951	0.001	−0.951	−53.62
	10^{-2}	47.932	48.905	7.21	3.097	0.270	−0.181	0.003	−0.218	−431.22

and the permanent increase of ω_c with γ_a. They also recovered the proportionality between the critical frequency and the Brunt-Väisälä frequency for large enough frequency ($\omega > 1$).

4.3.3 Comparison with numerical simulations

For the present problem, direct numerical simulations (DNS) have been performed by C. Kang. The linear coefficients of the Ginzburg-Landau equation (Eq. (2.48)) were computed by LSA and the nonlinear coefficient l was extracted from DNS results. For validation of the numerical code, the time constant τ_0 has also been computed by DNS. The results of both LSA and DNS agree quite well with each other. The computed values of the coefficients are given in Table 4.3 for some values of γ_a and Pr. We found that all the stationary modes appear through supercritical bifurcation (i.e., with $l > 0$) while oscillatory modes appear through subcritical transition. Indeed, for Pr = 50 and 100, the bifurcation to oscillatory axisymmetric modes is subcritical for $\gamma_a = 0.001$ and 0.01 while the transition to stationary axisymmetric modes is supercritical for all values of Pr. The coherence length ξ_0 is almost independent of Pr for inward and outward heating. The characteristic time τ_0 weakly varies with Pr for $\gamma_a > 0$ while it strongly increases with Pr for $\gamma_a < 0$. For a given fluid, the perturbations grow faster in outward heating than in inward heating.

The friction coefficient C_M has been computed by numerical simulation and measures the torque that the fluid exerts on the inner cylinder. Fig. 4.14 shows the variation of C_M with the Taylor number. When the Taylor number is below the critical value, C_M is equal to its laminar flow value. When $Ta > Ta_c$, the friction coefficient has higher values than for the base state. The

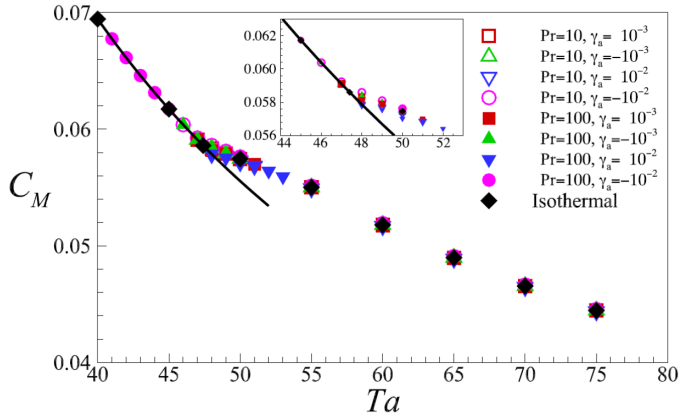

Figure 4.14: Total friction coefficient as function of Ta for different values of Pr and γ_a. The solid line corresponds to the isothermal laminar flow.

centrifugal buoyancy plays no significant role since Pr and γ_a do not bring difference compared to the isothermal case. The measure of the heat transfer is done through the computation of the Nusselt number Nu_i at the inner cylinder. In contrast to the friction coefficient, Nu_i is very sensitive to Pr: for a given Ta, increasing Pr increases the Nusselt number. For Pr = 10 (Fig. 4.15 - a) critical modes in inward and outward heating are SA, and γ_a plays no role on the variation of Nu_i. For Pr = 100 (Fig. 4.15 - b,c), the sign of γ_a plays a role on the slope of the curves at the onset of convective flow. But for sufficiently large Ta, this difference vanishes. The decrease of Nu_i observed for Pr = 100 is due to the occurrence of wavy vortex flow.

4.4 Conclusion

The Taylor-Couette flow with the inner cylinder rotating and a steady outer cylinder is Rayleigh unstable: the angular momentum decreases with the radial coordinate. The application of a temperature gradient produces the centrifugal buoyancy which changes the stability condition of the Taylor-Couette flow. In outward heating ($\gamma_a < 0$), the centrifugal buoyancy has a destabilising effect, and the critical modes are stationary axisymmetric. In inward heating ($\gamma_a > 0$), it has a stabilising effect. In this case, critical modes can be stationary axisymmetric, oscillatory axisymmetric or oscillatory non-axisymmetric, depending on η, Pr and γ_a. The oscillatory nature of the axisymmetric modes comes from the generation of internal waves due to the stable stratification of the density regarding the centrifugal acceleration. The Prandtl number plays a unexpected role in inward heating: it reinforces the stability of the flow for SA modes and diminishes the sta-

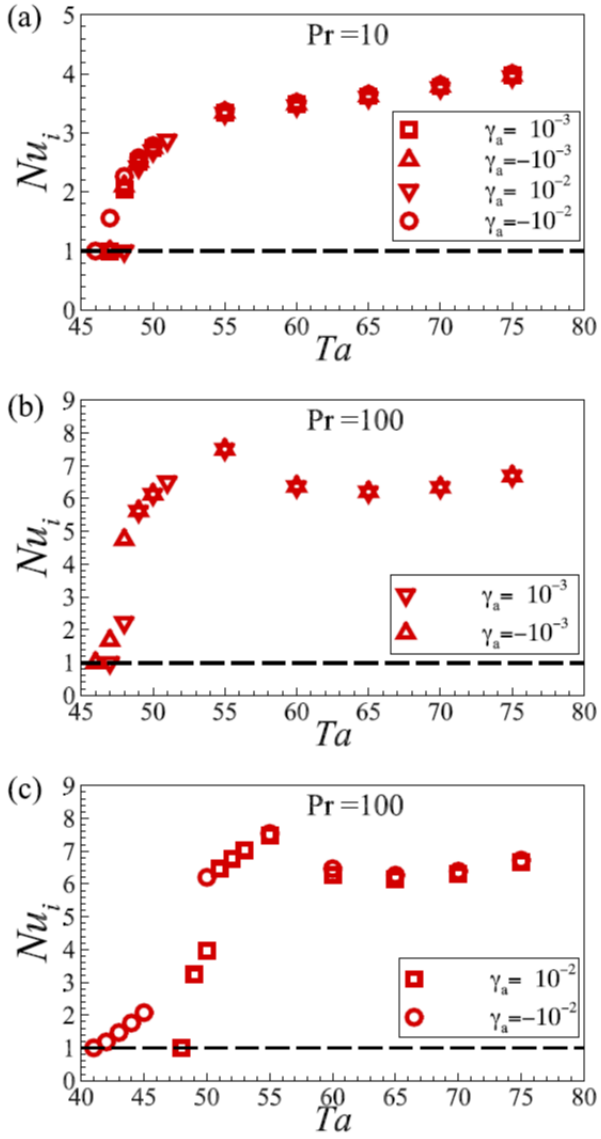

Figure 4.15: Variation of the heat transfer coefficients at the inner cylinder with Ta for different values of Pr and γ_a. (a) Pr = 10 and different values of $|\gamma_a|$, (b) Pr = 100 and $|\gamma_a| = 0.001$ and (c) Pr = 100 and $|\gamma_a| = 0.01$.

bilisation for OA modes. This effect is related the phase shift between the perturbation velocity and the perturbation temperature fields. The numerical simulation of this problem validated the results from the linear stability analysis, but showed that the OA modes are subcritical. In fact, the oscillation of the vortices only occurs during the linear growth of the modes. The vortices become stationary during the non-linear state, where the amplitude of the modes stop growing. Increasing the Prandtl number enhances the heat transfer, but has not much influence on the friction coefficient.

Chapter 5

Centrifugal buoyancy in Rayleigh stable Taylor-Couette flows

In the previous chapter, we investigated the effect of the centrifugal buoyancy on a Rayleigh unstable rotation regime. We will now focus on two Rayleigh stable flows. In the isothermal case, when only the outer cylinder rotates or when both cylinders rotate in the Keplerian regime, i.e. following the law $\Omega_2/\Omega_1 = (R_1/R_2)^{3/2}$, the flow is always stable. The application of a temperature difference between the two cylinders produces the centrifugal acceleration which is able to change the stability conditions. To have a destabilising effect of the centrifugal acceleration, the outer cylinder has to be hotter than the inner one, i.e. $\gamma_a < 0$. The two rotation regimes are investigated under weightless environment ($\mathrm{Gr} = 0$). The eigenvalues s are computed in the same way as in the previous chapter. The determination of the global minimum of marginal curves gives the critical state of the system, with the corresponding critical parameters $(\mathrm{Ta}_c, k_c, n_c, \omega_c)$.

5.1 Outer rotating cylinder

When the outer cylinder rotates and is heated, the centrifugal buoyancy has a destabilizing effect on the flow and convection rolls can appear. In fact, the gravity is oriented towards the hot surface and there is a negative stratification of the density and therefore the centrifugal buoyancy can induce thermo-convective instability. The critical modes are axisymmetric and stationary. The figure 5.1 shows marginal stability curves obtained for different n. The marginal curve obtained for $n = 0$ has the lowest value of Ta.

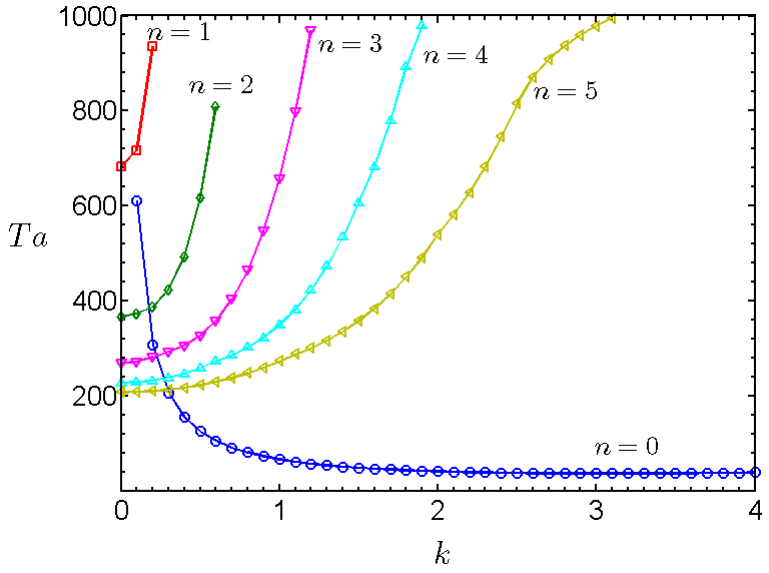

Figure 5.1: Marginal stability curves obtained for $\eta = 0.5$, $\mathrm{Pr} = 1000$ and for $\gamma_a = -0.008$. The critical modes are axisymmetric.

5.1.1 Critical parameters

The critical parameters depend both on γ_a and Pr, but we found that they depend on the combination $\gamma_a \mathrm{Pr}$. In other words, for a fixed value of η, two systems with different γ_a and Pr but identical $\gamma_a \mathrm{Pr}$ will have instabilities of the same nature and at the same threshold. Figure 5.2 shows the behaviour of the critical Taylor number and the critical axial wavenumber as functions of $-\gamma_a \mathrm{Pr}$ for different radius ratios. The critical Taylor number decreases with $-\gamma_a \mathrm{Pr}$ and asymptotically tents to zero. For a given $\gamma_a \mathrm{Pr}$, increasing the radius ratio destabilises the flow. The lower the value of $-\gamma_a \mathrm{Pr}$, the larger the slope of the threshold, so that decreasing further the parameter $-\gamma_a \mathrm{Pr}$ makes the critical Taylor number tend to the infinite. The axial wavenumber decreases with increasing $-\gamma_a \mathrm{Pr}$, except for low values of the radius ratio for which q_c decreases with $-\gamma_a \mathrm{Pr}$.

Figure 5.3 shows the behaviour of the growth rate of critical modes in the (k, Ta) plane and highlights how the critical wavenumber increases with $-\gamma_a \mathrm{Pr}$ for low radius ratio and how it decreases otherwise. For $\eta = 0.2$ and low $-\gamma_a \mathrm{Pr}$, the zone of positive growth rate is concentrated at small wavenumbers. At larger $-\gamma_a \mathrm{Pr}$, a zone of positive growth rates becomes positive at larger axial wavenumbers and increases the critical wavenumber. For larger radius ratios, the zone where $\sigma > 0$ is located at larger wavenumbers for small $-\gamma_a \mathrm{Pr}$. This zone is shifted to lower values of k when $-\gamma_a \mathrm{Pr}$ increases.

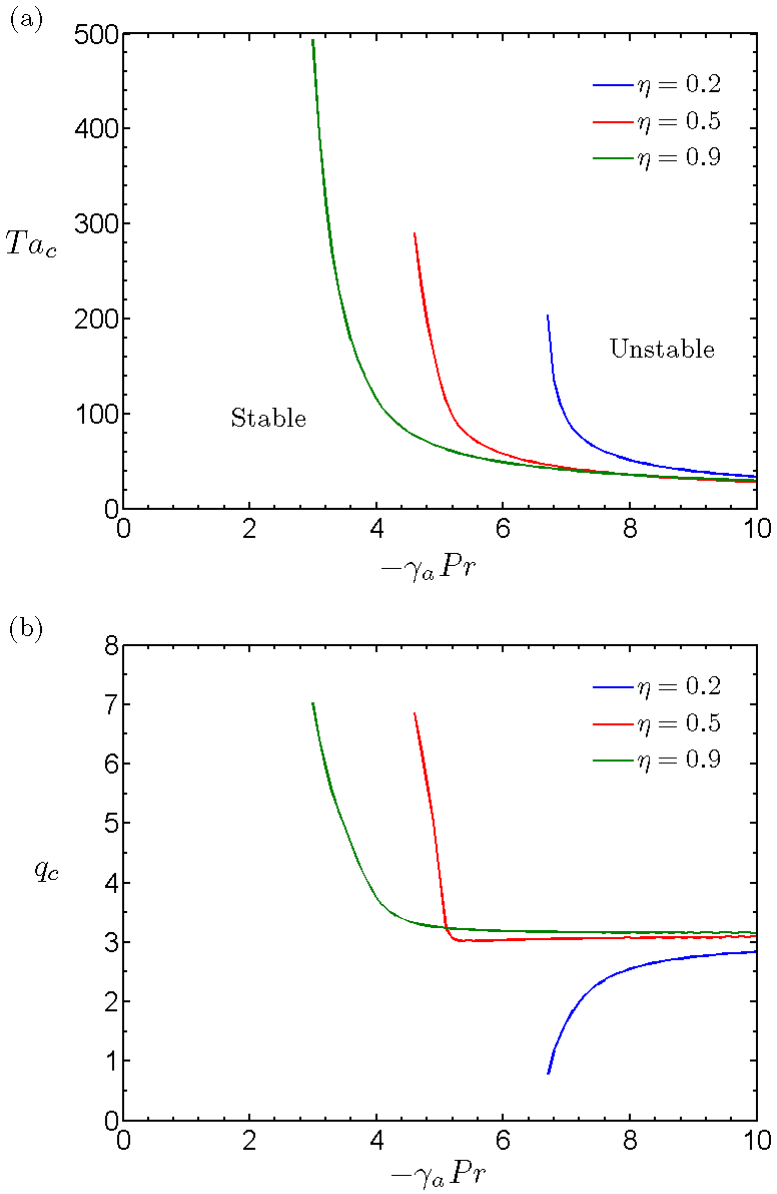

Figure 5.2: Variation of the critical parameters with $-\gamma_a$Pr for different η: (a) Taylor number and (b) wavenumber.

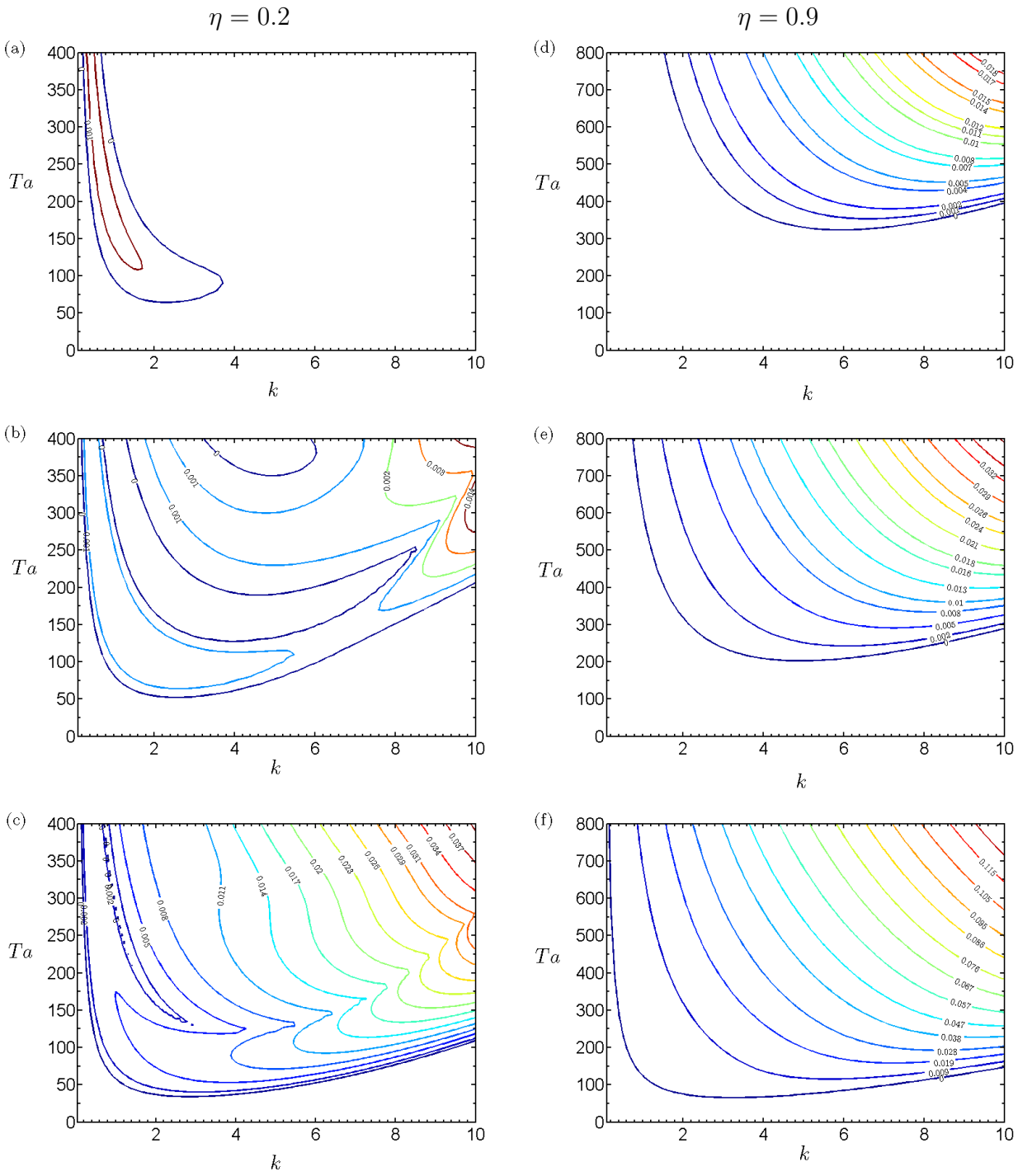

Figure 5.3: Isovalues of the growth rate σ in the (k, Ta) plane for different radius ratio and different $\gamma_a \mathrm{Pr}$. Diagrams (a - c) are obtained for $\eta = 0.2$ and diagrams (d - f) are obtained for $\eta = 0.9$. The values of $-\gamma_a \mathrm{Pr}$ are: (a) 7.5, (b) 8, (c) 10, (d) 3.2, (e) 3.5 and (f) 5.

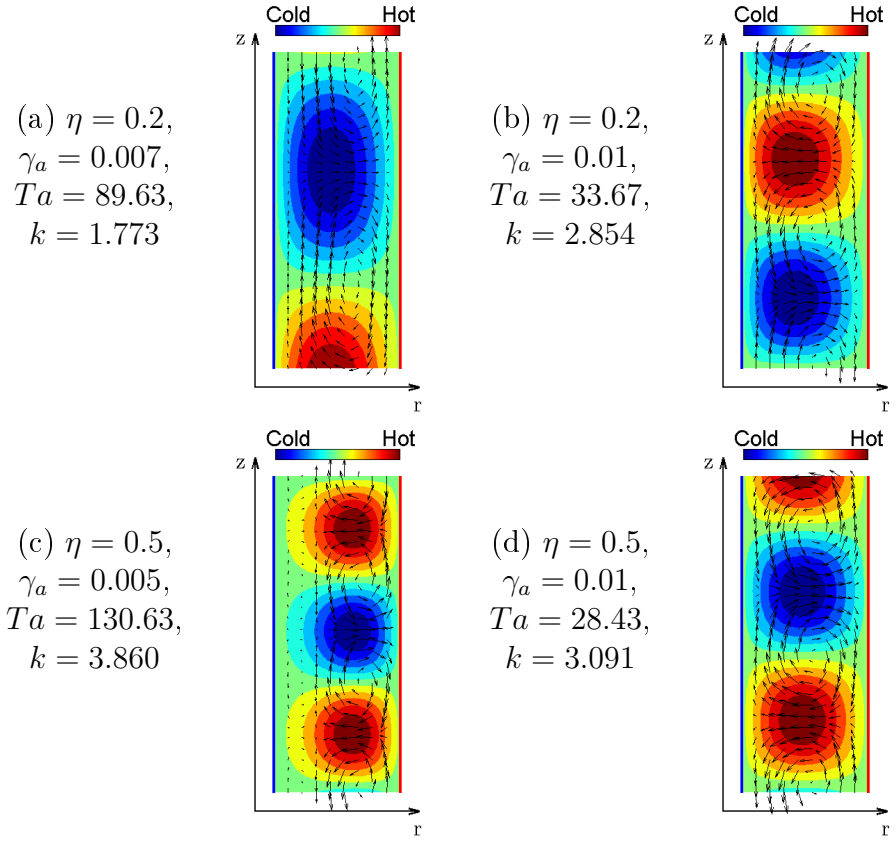

Figure 5.4: Eigenfunctions at critical conditions for Pr = 1000 and for different values of η and γ_a.

5.1.2 Eigenfunctions

The eigenfunctions for the perturbation velocity field and for the perturbation temperature at critical states are illustrated in Fig. 5.4. The radial velocity perturbation and the temperature perturbation are in antiphase, which means that a fluid particle will travel from the hot cylinder to the cold one by passing through the high temperature. In Fig. 5.4(c), the axial wavenumber is large and we can observe that the vortices are concentrated in the outer part of the cylindrical annulus.

5.2 Keplerian regime

As in the case where the outer cylinder rotates, it is found that for the Keplerian regime the critical parameters depend on the combination γ_aPr. Moreover, critical modes are also found to be stationary axisymmetric.

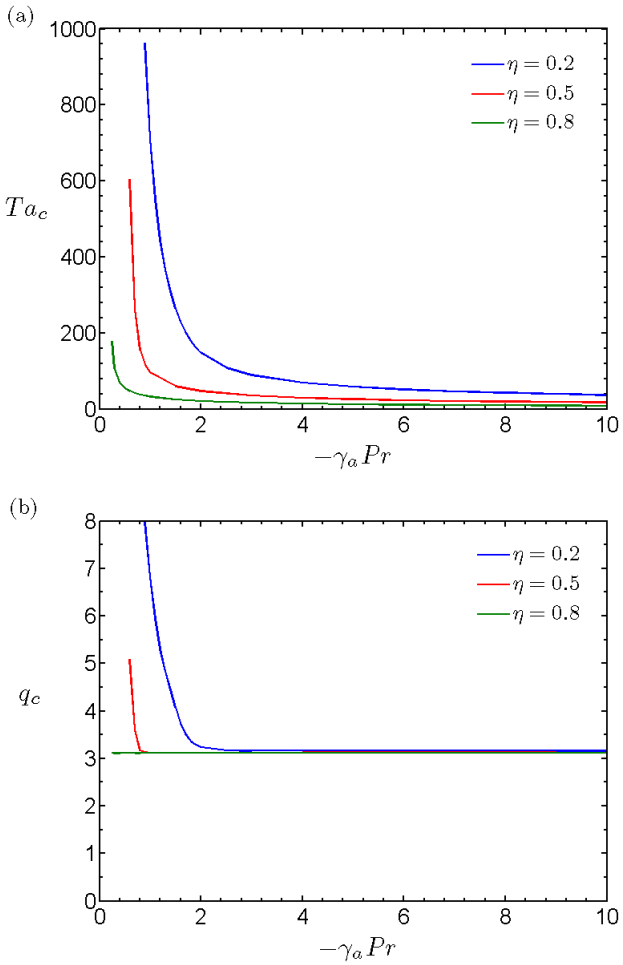

Figure 5.5: Variation of the critical parameters with $-\gamma_a$Pr for different η: (a) Taylor number and (b) wavenumber.

5.2.1 Critical parameter

Figure 5.5 shows the critical parameters behaviour as function of $-\gamma_a$Pr. The critical Taylor number decreases with increasing $-\gamma_a$Pr and asymptotically tends to zero. The larger the curvature, the more stable the flow. The critical axial wavenumber decreases with $-\gamma_a$Pr and asymptotically tents to a constant value around $q_c = 3.15$.

5.3 Discussion

5.3.1 Energy analysis

For these systems, the equation of kinetic energy is the same as for the previous chapter (Eq. (4.4)). Three mechanisms intervene in the process of energy transfer from the base state to the perturbation: the shear stress, the centrifugal buoyancy and the viscous dissipation. Fig. 5.6

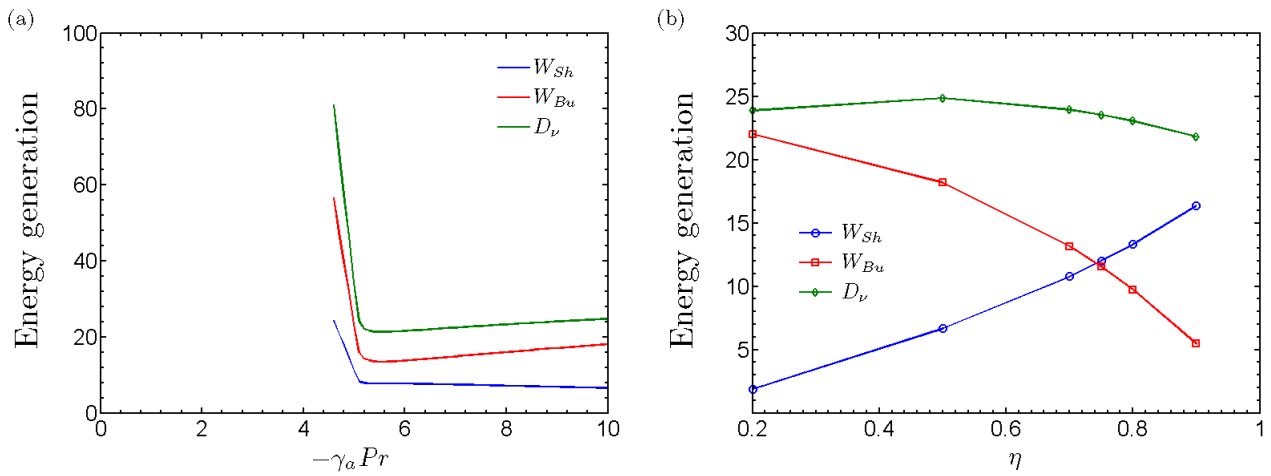

Figure 5.6: Power terms of the outer rotation regime (a) as function of $-\gamma_a \mathrm{Pr}$ for $\eta = 0.5$, and (b) as function of η for $\gamma_a \mathrm{Pr} = -10$.

represents the evolution of the power given by these three mechanisms with the parameter $\gamma_a \mathrm{Pr}$ and with η in the outer rotation regime. The power given by the centrifugal buoyancy and by the shear rate are always positive, which means that in inward heating, these two mechanisms contribute to the destabilisation of the system. In Fig. 5.6 - b, obtained for $\gamma_a \mathrm{Pr} = -10$, we can see that there exists a certain value of η bellow which $W_{Bu} > W_{Sh}$, and above which $W_{Bu} < W_{Sh}$. This latest case is counter intuitive because the instability is produced by thermal effects, and the power given by the shear is only a consequence of the presence of vortices in the annulus. The shear rate is given by:

$$r \frac{d}{dr}\left(\frac{V}{r}\right) = \frac{2\eta^2}{(1+\eta)(1-\eta)^{5/2}} \frac{\mathrm{Ta}}{r^2} \tag{5.1}$$

The critical Taylor number decreases with increasing the radius ratio, making the power given by the centrifugal buoyancy decrease. But in counterpart, the shear rate (5.1) increases with η, making the power given by the shear stress increase.

Fig. 5.7 shows the behaviour of the different power source against the parameter $\gamma_a \mathrm{Pr}$ and against η in the Keplerian regime. The power given by the centrifugal buoyancy is positive as for the outer rotation regime. But this time, the shear stress always contributes to stabilise the flow, since W_{Sh} is negative. For large enough values of $-\gamma_a \mathrm{Pr}$ and large enough η, the shear stress does not transfer energy to the perturbations, i.e. $W_{Sh} = 0$, and the power given by the centrifugal buoyancy becomes constant.

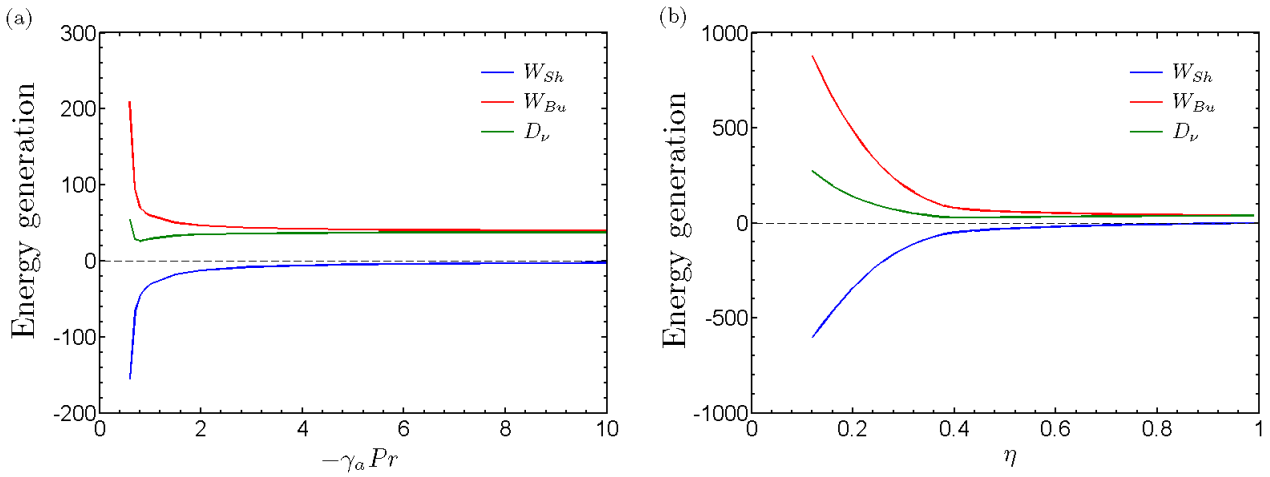

Figure 5.7: Power terms in the Keplerian regime (a) as function of $-\gamma_a$Pr for $\eta = 0.5$, and (b) as function of η for γ_aPr $= -10$.

5.3.2 Small gap approximation

Kirillov and Mutabazi [52] analysed the problem both in the case where the outer cylinder rotates and in the Keplerian regime while considering the small gap approximation, in the limit of short wavelength of vortices. There method allows them only to consider axisymmetric perturbation, which is convenient since the linear stability theory predicted axisymmetric modes. They found that OA modes can be critical at low Prandtl number, for both rotation regimes. When only the outer cylinder rotates, the OA modes have not been captured by the LSA, because the values of Ta larger than 1000 have not been admitted in the linear stability theory. But in the Keplerian regime, for $\eta = 0.99$ and $\gamma_a = -0.01$, the OA modes have been found as critical modes. Fig. 5.8 shows the threshold, the critical wavenumber and the critical frequency for these conditions. The transition from OA modes and SA modes is at about Pr $= 1$ which is pretty close to what Kirillov and Mutabazi calculated (for them, the OA modes stop at Pr $= 0.98$ and the SA modes start at Pr $= 1.01$). The critical wavenumber is constant for SA modes but varies with Pr for OA modes. In fact, increasing the Prandtl number first decreases the wavenumber, and then increases it until the SA modes become critical. The frequency of OA modes decreases with Pr and undergoes a discontinuity when the temporal nature of the modes changes.

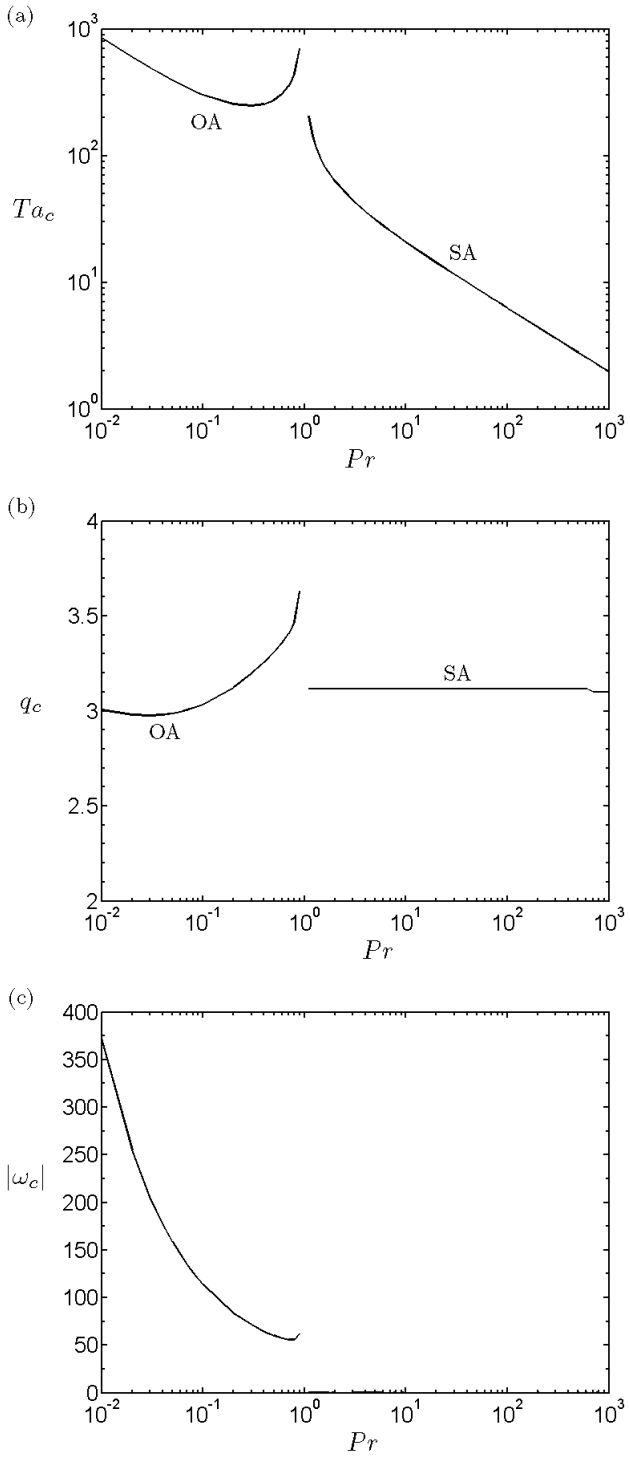

Figure 5.8: Variation of the critical parameters as functions of Pr for $\eta = 0.99$ and $\gamma_a = -0.01$ in the Keplerian regime: (a) Taylor number, (b) wavenumber and (c) frequency.

5.4 Conclusion

The regimes where the outer cylinder rotates and the Keplerian regime are Rayleigh stable. To destabilise there flow, a positive temperature gradient has to be applied.

The Keplerian regime and the regime where only the inner cylinder rotates in inward heating show some similarities. For both regimes, the critical parameters depend on both the Prandtl number and the thermal expansion parameter, through the combination γ_aPr. Indeed, the parameter γ_aPr makes the critical parameters only dependent on the radius ratio. This parameter has been found in the 1-dimensional model derived in Sec. 3.3. In both cases, critical modes take the form of axisymmetric modes. When only the outer cylinder rotates, the radial shear plays a subtle role. It destabilises the flow and, depending on the radius ratio, can transfer more energy to the perturbation than the centrifugal buoyancy. This result is counter intuitive since the centrifugal buoyancy is the motor for the onset of convections. In contrast, in the Keplerian regime, for large values of γ_aPr and of η, the shear rate plays no role on the stability and the centrifugal buoyancy becomes the only source of energy transfer from the base state to the perturbations.

For large radius ratios and small Prandtl number, oscillatory axisymmetric modes are found, which confirm the results obtained by Kirillov et all [52].

Chapter 6

Centrifugal buoyancy in fluids with solid-body rotation

A rigidly rotating cylindrical annulus is a model for geophysical and astrophysical flows. According to the Rayleigh criterion derived in (3.4), the isothermal case is stable against centrifugally-driven perturbations. The centrifugal force cannot brings instability, but in inward heating ($\gamma_a < 0$), the centrifugal buoyancy has a destabilizing effect and can lead to thermal convection. In fact, the centrifugal gravity is oriented toward the hot surface and this configuration resembles the Rayleigh-Bénard convection of a fluid layer heated from below (Fig. 6.1).

6.1 Flow equation in the rotating frame of reference

The linear stability analysis has been performed using the set of equations (2.11) which describes the system in the laboratory frame. But for convenience, the rotating frame should be

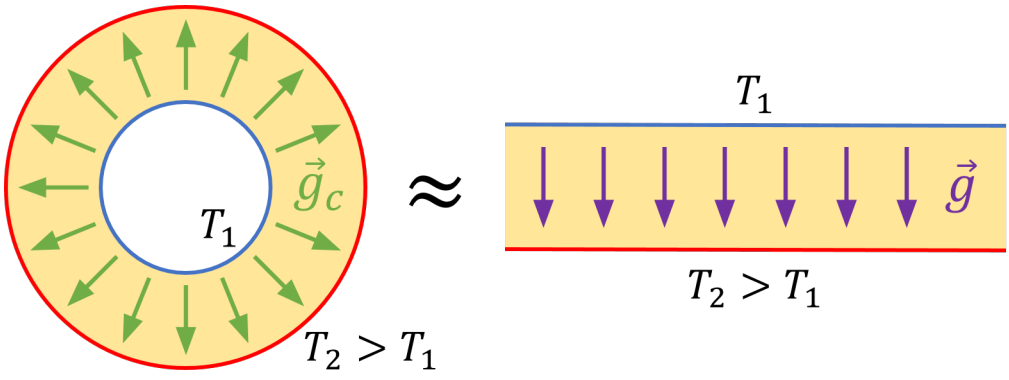

Figure 6.1: Sketch showing the analogy between the rigidly rotating cylindrical annulus with heated outer cylinder and the Rayleigh-Bénard problem.

used instead of the static frame. In a frame rotating at the angular velocity Ω of the cylindrical annulus, there is no base flow and we have to consider the Coriolis force $\boldsymbol{f}_C$ and the Coriolis buoyancy which is the action of $\boldsymbol{f}_C$ on the density stratification. The governing flow equations in the rotating frame read:

$$\boldsymbol{\nabla}\cdot\boldsymbol{u}=0 \tag{6.1a}$$

$$\frac{\partial \boldsymbol{u}}{\partial t}+\boldsymbol{u}\cdot\boldsymbol{\nabla}\boldsymbol{u}=-\boldsymbol{\nabla}\pi+\Delta\boldsymbol{u}-2\tau\left(\boldsymbol{e}_z\times\boldsymbol{u}\right)+2\gamma_a\tau\theta\left(\boldsymbol{e}_z\times\boldsymbol{u}\right)-\frac{\gamma_a\tau^2}{2}\theta r\boldsymbol{e}_r \tag{6.1b}$$

$$\frac{\partial \theta}{\partial t}+\left(\boldsymbol{u}\cdot\boldsymbol{\nabla}\right)\theta=\kappa\Delta\theta \tag{6.1c}$$

where $\tau=\Omega d^2/\nu$ is the Coriolis number. Using the definitions:

$$\mathrm{Ra}=\gamma_a\mathrm{PrTa}^2,\quad \tau=\mathrm{Ta}\sqrt{f(\eta)}\quad\text{where}\quad f(\eta)=\frac{2(1-\eta)}{1+\eta} \tag{6.2}$$

where Ta is the Taylor number defined at the arithmetic mean of the two cylinder radii, the equation (6.1b) can be written:

$$\frac{\partial \boldsymbol{u}}{\partial t}+\boldsymbol{u}\cdot\boldsymbol{\nabla}\boldsymbol{u}=-\boldsymbol{\nabla}\pi+\Delta\boldsymbol{u}-2\tau\left(\boldsymbol{e}_z\times\boldsymbol{u}\right)+2\sqrt{f(\eta)\mathrm{Ra}\frac{\gamma_a}{\mathrm{Pr}}}\theta\left(\boldsymbol{e}_z\times\boldsymbol{u}\right)-f(\eta)\frac{\mathrm{Ra}}{\mathrm{Pr}}\theta r\boldsymbol{e}_r \tag{6.3}$$

In the rotating frame of reference, there is no base flow, therefore the no-slip conditions at the boundaries leads to $\boldsymbol{u}=\boldsymbol{0}$. The basic velocity and temperature are given by:

$$U=V=W=0\,;\quad \Theta=\frac{\ln\left[r\left(1-\eta\right)\right]}{\ln\eta} \tag{6.4}$$

Adding a small perturbation to the base state and developing these perturbations into normal modes, the set of equations (6.1) becomes:

$$0=\left(D+\frac{1}{r}\right)\hat{u}+\frac{in}{r}\hat{v}+ik\hat{w} \tag{6.5a}$$

$$s\hat{u}=-D\hat{\pi}+\Delta\hat{u}-\frac{\hat{u}}{r^2}-\frac{2in\hat{v}}{r^2}+\tau\hat{v}-2\sqrt{f(\eta)\mathrm{Ra}\frac{\gamma_a}{\mathrm{Pr}}}\Theta\hat{v}-f(\eta)\frac{\mathrm{Ra}}{\mathrm{Pr}}\hat{\theta}r \tag{6.5b}$$

$$s\hat{v}=-\frac{in}{r}\hat{\pi}+\Delta\hat{v}-\frac{\hat{v}}{r^2}+\frac{2in\hat{u}}{r^2}-\tau\hat{u}+2\sqrt{f(\eta)\mathrm{Ra}\frac{\gamma_a}{\mathrm{Pr}}}\Theta\hat{u} \tag{6.5c}$$

$$s\hat{w}=-ik\hat{\pi}+\Delta\hat{v} \tag{6.5d}$$

$$s\hat{\theta}=-D\Theta\hat{u}+\frac{1}{\mathrm{Pr}}\Delta\hat{\theta} \tag{6.5e}$$

6.2 Critical parameters

In inward heating, when both cylinders rotate at the same angular velocity, for most sets of parameters, the critical modes take the form of columnar vortices, i.e. $k_c = 0$ and $n_c \neq 0$. Due to the analogy with the Rayleigh Bénard problem, the convenient parameter for this rotation regime is the Rayleigh number. Indeed Ra_c depends only on the radius ratio (Fig. 6.2 - a). The azimuthal mode number increases with η and corresponds to the maximum number of convection roll pairs of the gap size: $n_c \simeq [\pi(1+\eta)/2(1-\eta)]$. Each time the value of n_c changes, the slope of Ra_c with respect to η also changes. For large values of the radius ratio, the critical Rayleigh number tends to $\mathrm{Ra} = 1708$ which is the threshold for onset of convection in the Rayleigh-Bénard problem. The critical wavenumber depends only on η (Fig. 6.2 - b). It decreases with η and undergoes ascendant discontinuities each time the value of n_c changes, so that q_c oscillates around $q = 3.116$, and tends to this value when η tends to 1, which is the critical wavenumber in the Rayleigh Bénard problem. The threshold $\mathrm{Ra} = 1708$ together with the wavenumber $q = 3.116$ were also predicted by Auer et al. [24] in the framework of the small gap approximation. In figure 6.2 - c) the critical frequency measured in the rotating frame is normalized with the Coriolis number τ, defined on Eq. (6.2). The frequency undergoes discontinuities each time the azimuthal mode number changes. Unlike the threshold and the wavenumber, the critical frequency depends on γ_a and Pr. Indeed, for a fixed value of γ_a, the frequency decreases with increasing Prandtl number, and for a fixed value of Pr, ω_c/τ increases with increasing γ_a. The frequency is positive which indicates retrograde propagation (remind that $s = \sigma + i\omega$) .

For low values of the radius ratio, the axial wavenumber can be different from zero (helical modes) when the parameter $\gamma_a\mathrm{Pr}$ is sufficiently large (Fig. 6.3). Columnar modes have an angle of 90° with respect to the azimuthal direction. When helical modes become critical, this angle decreases to about 80° with increasing η until columnar modes become critical again(Fig. 6.3 - c). The critical frequency of these helical modes quickly increases with η (Fig. 6.2 - c). Figure 6.4 shows the parameters for which helical modes are critical. The change of azimuthal modes number occurs at a constant η. Just before this change, at small values of η and large values of $\gamma_a\mathrm{Pr}$, helical modes can be critical.

The perturbation temperature and perturbation velocity fields of an oscillatory columnar mode are shown on figure 6.5. The flow goes from the hot wall to the cold one passing through hot cells. The spatio-temporal profile of the perturbation temperature (Fig. 6.5 - c) shows how the columns

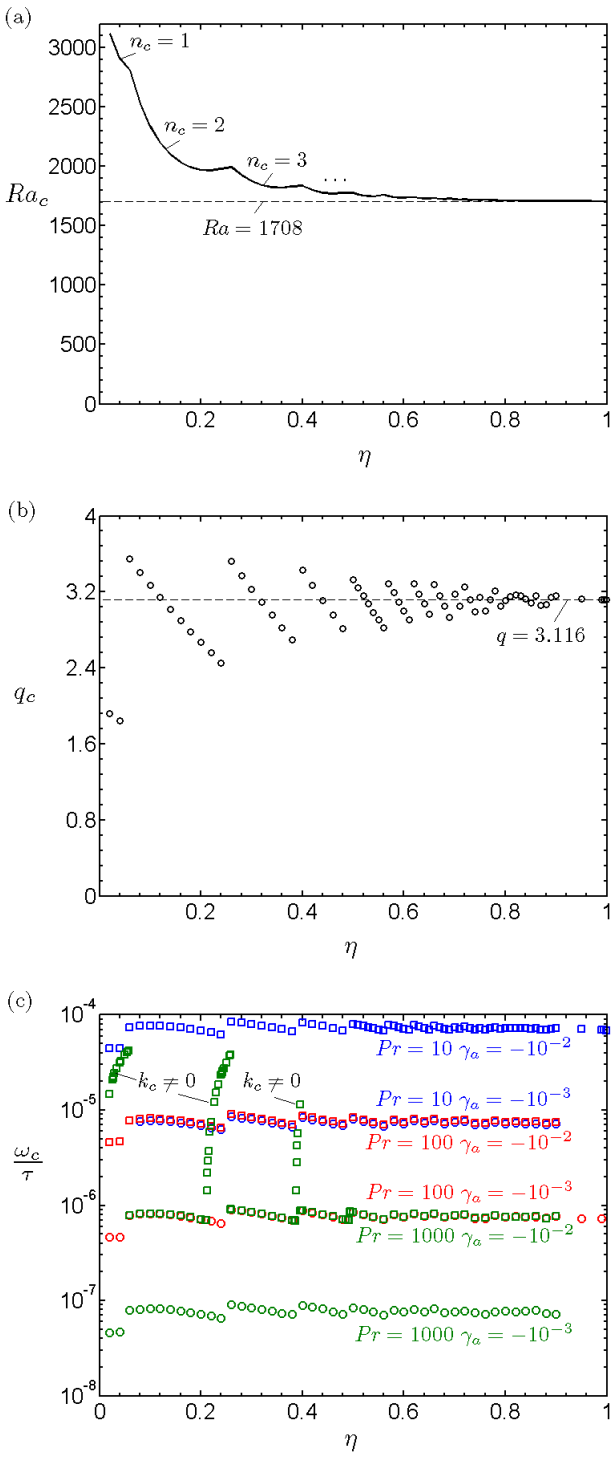

Figure 6.2: Variation of the critical parameters as fonctions of the radius ratio for different Pr and different γ_a: (a) Rayleigh number, (b) wavenumber and (c) normalized frequency.

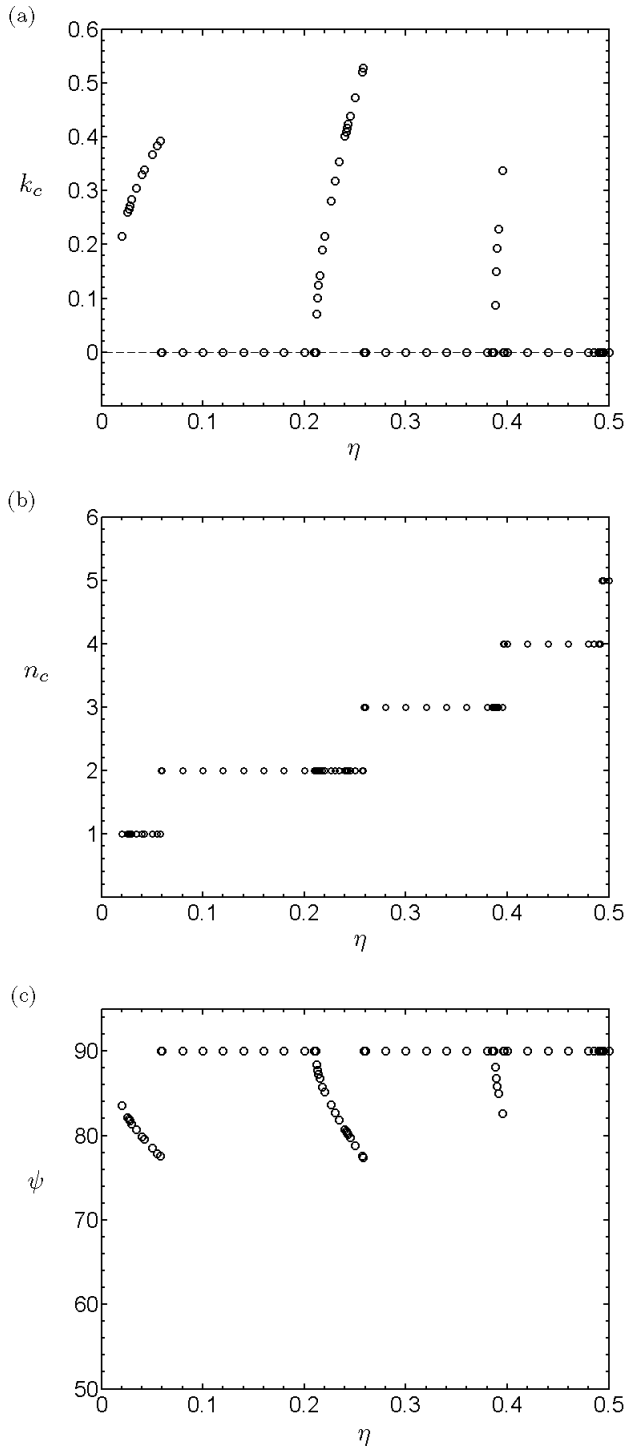

Figure 6.3: Variation of (a) the critical axial wavenumber, (b) the critical azimuthal mode number and (c) the angle of vortices with respect to the azimuthal direction as function of the radius ratio for $\gamma_a \mathrm{Pr} = -10$.

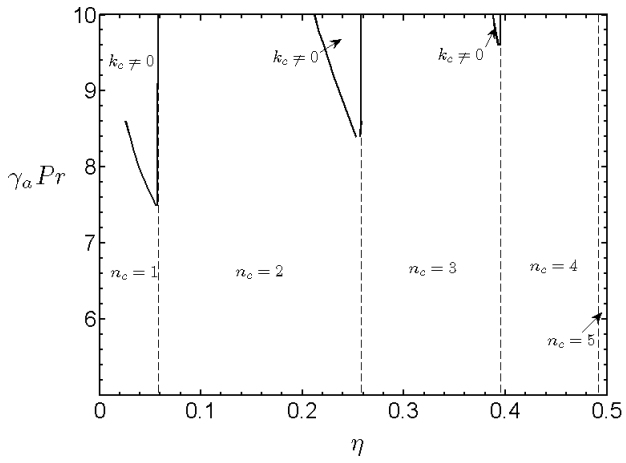

Figure 6.4: Zones of critical states. Columnar modes are critical below the solid line, otherwise helical modes are critical.

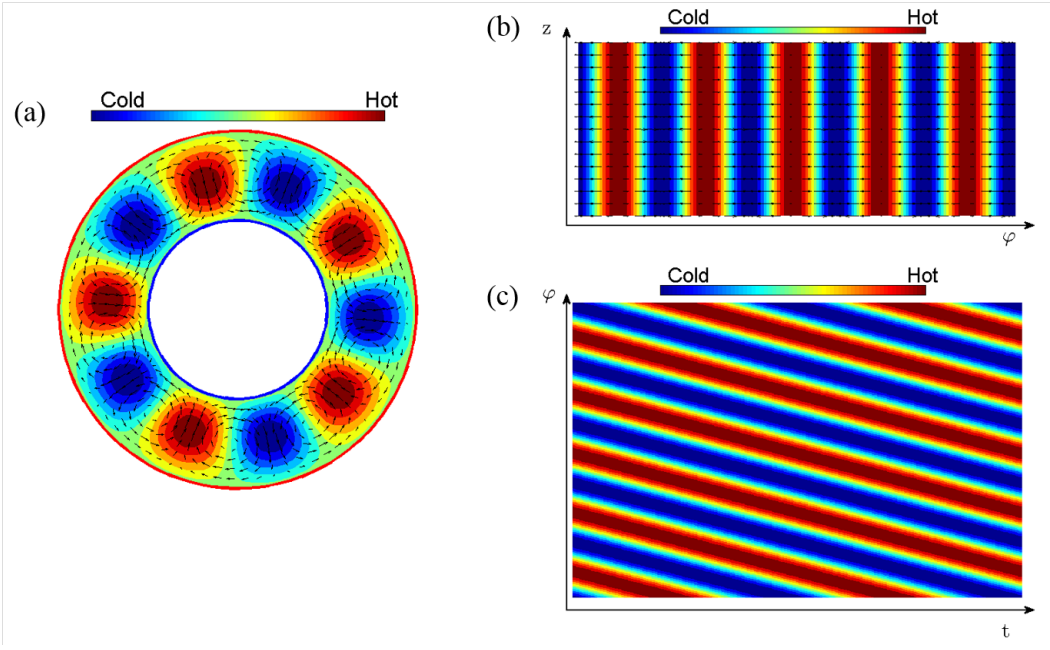

Figure 6.5: Perturbation temperature profile and perturbation velocity field at the critical condition (a) in the (r, φ) plane (b) in the (φ, z) plane, and (c) in the (t, φ) plane for $\eta = 0.5$, $\mathrm{Pr} = 10$ and $\gamma_a = -0.01$.

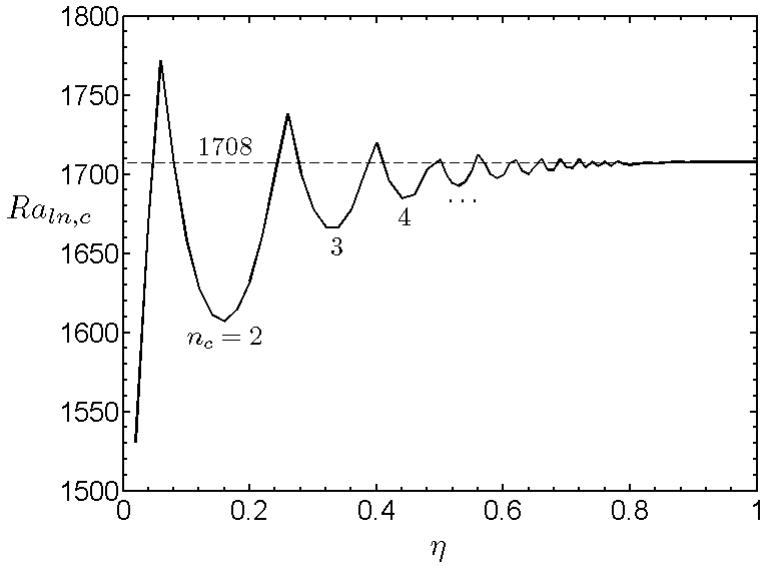

Figure 6.6: Critical centrifugal Rayleigh number defined at the logarithmic radial position $R_{\ln,c}$ as a function of the radius ratio

drift in the retrograde direction.

6.3 Discussion

6.3.1 Centrifugal Rayleigh at the logarithmic radius

The centrifugal Rayleigh number is the convenient parameter to discuss the stability of the rotating annulus in inward heating. As the Taylor number is defined at the arithmetic mean of the two cylinder radii, the Rayleigh number $\mathrm{Ra} = \gamma_a \mathrm{PrTa}^2$ has the same definition as the one of Auer et al. [24]. An other way to define the Rayleigh number is to chose the logarithmic radius: $R_{\ln} = -d/\ln\eta$ in its dimensional form, as Walowit et al. did [18]. At this particular radial position, the heat flux through the cylindrical surface is equivalent to the one through two plane surfaces separated by d. The centrifugal Rayleigh number defined at $R_{\ln}$ is given by:

$$Ra_{\ln} = \gamma_a \mathrm{PrTa}^2 \frac{2(1-\eta)}{\ln\eta(1+\eta)} \tag{6.6}$$

When the centrifugal Rayleigh number defined in Eq. (6.6) is used to plot the threshold as function of the radius ratio, we see that the influence of the curvature on the threshold is very weakened and remains sensitive to η for $\eta < 0.7$ (Fig. 6.6). The values of $Ra_{\ln,c}$ oscillate around 1707.7 with an amplitude which decreases with the radius ratio until η has no influence on the threshold.

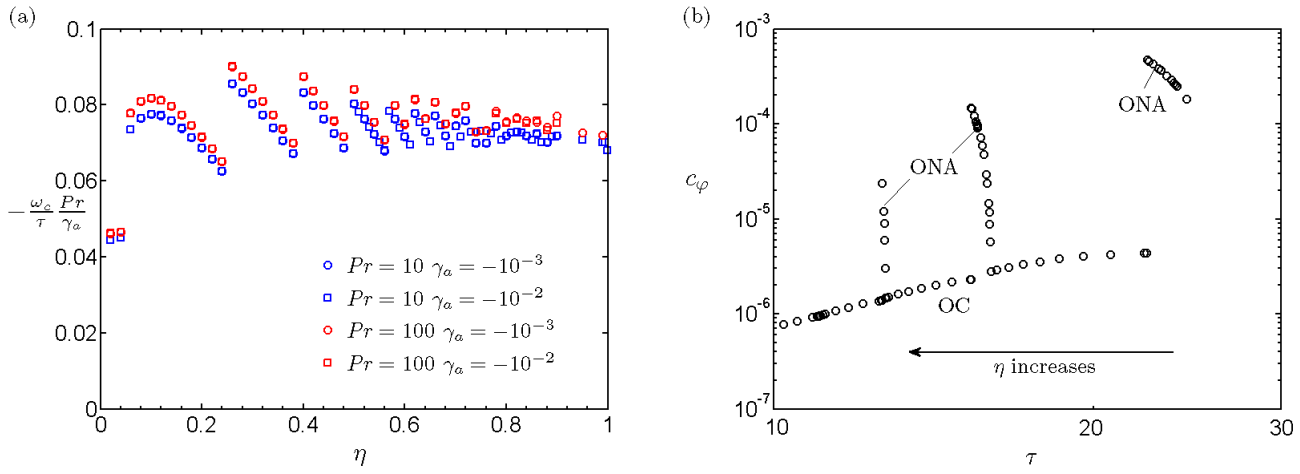

Figure 6.7: (a) Critical normalized frequency ω_c/τ of columnar modes scaled with the parameter $-\gamma_a/\mathrm{Pr}$ as a function of the radius ratio, and (b) azimuthal phase velocity as a function of τ for $\gamma_a \mathrm{Pr} = -10$.

6.3.2 Nature of the frequency

The normalised critical frequency ω_c/τ can be scaled using the parameter γ_a/Pr which involves in the term of the Coriolis buoyancy of equation (6.3). By doing this, unless for the non axisymmetric modes, the scaled critical frequency becomes independent from the Prandtl number and the thermal expansion parameter (Fig. 6.7 - a). The success of this scaling indicates that the Coriolis buoyancy is the source of the propagation of vortices. The scaled frequency of the columnar modes is almost constant with $\frac{\omega_c}{\tau}\frac{\mathrm{Pr}}{\gamma_a} \approx -0.008$. It indicates that the normalized frequency ω_c/τ is a linear function of the parameter γ_a/Pr with a slope of -0.008 which is nearly independent from η.

The variation of the azimuthal phase velocity c_φ with the Coriolis parameter τ is shown in Fig. 6.7 - b. For small values of τ, the phase velocity of columnar modes is almost proportional to τ, which could indicate that the OC modes are advected by the rotation of the cylindrical walls. However, the phase velocity of ONA modes show no particular links with the Coriolis parameter.

6.3.3 Energy analysis

In this problem, the centrifugal buoyancy is the only mechanism which gives energy to perturbations. At the critical condition, the energy rate of viscous dissipation D_ν balances W_{Bu} so that there is no time variation of the averaged kinetic energy. In this case, the power performed by the base centrifugal buoyancy W_{BBu} and the one performed by the perturbation centrifugal buoyancy

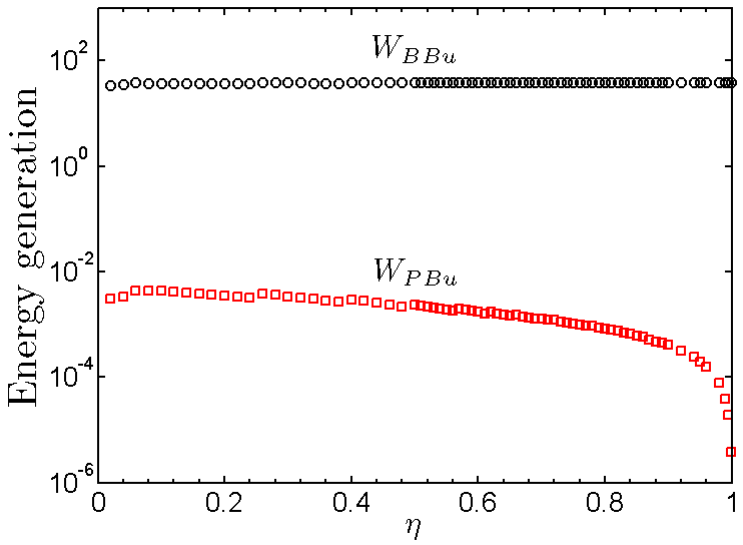

Figure 6.8: Variation of the power performed by the base centrifugal buoyancy W_{BBu} and of the power performed by the perturbation centrifugal buoyancy W_{PBu} with η for Pr = 10 and $\gamma_a = -0.01$.

W_{PBu} are distinguished in order to have an insight on the effect of the latest power source.

Figure 6.8 shows the evolution of W_{BBu} and W_{PBu} with the radius ratio. Most of the energy transfer from the base state to perturbations is done through the effect of the base centrifugal buoyancy. The perturbation centrifugal buoyancy has a positive contribution which means that it destabilises the flow, however its contribution is negligible compared to that of the base centrifugal buoyancy.

6.3.4 Comparison with numerical simulations

Numerical simulation of this problem has been performed by Changwoo Kang for two different values of η and different Pr and γ_a. The Table 6.1 shows a good agreement between LSA and

Table 6.1: Critical parameters and coefficients of the complex Ginzburg-Landau equation computed by LSA and DNS.

η	Pr	γ_a	τ_c		τ_0		ξ_0	l
			LSA	DNS	LSA	DNS	LSA	DNS
0.5	1	10^{-2}	688.24	689.07	0.0364	0.0364	0.2679	28229
	10	10^{-3}	688.37	689.04	0.2476	0.2444	0.2703	411852
	100	10^{-3}	217.68	218.16	2.3600	2.2328	0.2703	451353
0.8	1	10^{-2}	390.19	390.90	0.0385	0.0389	0.2736	8973
	10	10^{-3}	390.20	390.91	0.2676	0.2678	0.2726	128357
	100	10^{-3}	123.40	124.13	2.5589	2.2978	0.2722	143532

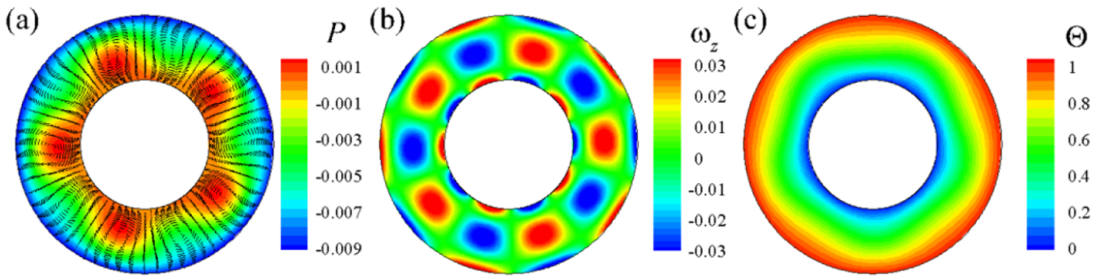

Figure 6.9: Flow and temperature fields in the (r, z) plane for $\eta = 0.5$, Ra $= 1811$, Pr $= 1$ and $\gamma_a = -0.01$: (a) velocity fields and pressure, (b) avial vorticity, and (c) temperature.

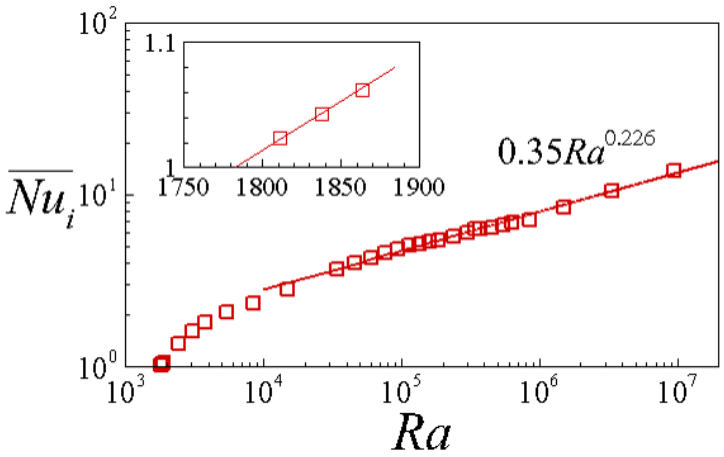

Figure 6.10: Variation of the Nusselt number with Ra for $\eta = 0.5$, Ra $= 1811$, Pr $= 1$ and $\gamma_a = -0.01$.

DNS regarding the critical thresholds of τ and the characteristic times τ_0. The characteristic time depends on γ_a and Pr in contrast to the coherence length of perturbation ξ_0 which only depends on the geometry. The Landau constant l is always positive, indicating supercritical bifurcations from the base flow.

Figure 6.9 shows the flow fields close to the onset of convection. The counter rotating vortices are columnar and are retrograde with a frequency close to that found with the LSA. The vortices which rotate in the same sense than the cylindrical annulus (cyclonic vortices) create low pressure regions while thus which rotate in the other sense (anticyclonic) create high pressure regions. The number of modes in the azimuthal direction is in agreement with that found with LSA. Increasing further the rotation rate of the annular cavity may make the number of modes varying, as well as their size. The temporal behaviour of the vortices also changes with additional low frequency oscillations of the modes. Finally, for large enough rotation rate, a chaotic behaviour of the flow occurs.

The time averaged Nusselt number is measured at the inner cylindrical surface and is ploted

against the centrifugal Rayleigh number on Fig. 6.10. For $\mathrm{Ra} < \mathrm{Ra}_c$, $\mathrm{Nu} = 1$ since the heat transfer is only done through diffusion. For $\mathrm{Ra} > \mathrm{Ra}_c$, the columnar vortices enhance the heat transfer and the Nusselt number growths. In the vicinity of Ra_c, the growth of the Nusselt can be represented as a linear function of Ra with a slope which depends on η and on the parameter $\gamma_a \mathrm{Pr}$. Indeed, the larger the parameter $\gamma_a \mathrm{Pr}$, the lower the value of the slope, which takes values of about 1 to 1.3. For large values of Ra, the growth of Nu can be fitted with a power-law scaling, and for $\eta = 0.5$ and $\mathrm{Pr} = 1$, the scaling exponent is equal to 0.226. Such value of the scaling exponent was found in many experiments on Rayleigh-Bénard convection [53, 54, 55].

6.4 Conclusion

As the regime where only the outer cylinder rotates or the Keplerian regime, the solid body rotation regime is Rayleigh stable, and a positive temperature gradient has to be applied to get instabilities. The stability can be characterised using the centrifugal Rayleigh number because the centrifugal acceleration plays the role of the gravity, in analogy with the Rayleigh-Bénard problem. The threshold only depends on the radius ratio. In most cases, the critical modes are oscillatory columnar, with a propagation frequency slightly lower than the rotation rate of the annulus. The oscillation of the columnar modes are due to the Coriolis buoyancy. For large values of the parameter $\gamma_a \mathrm{Pr}$ and low values of the radius ratio, critical modes can take the form of oscillatory helical modes. The numerical simulation showed that the onset of convection occurs through supercritical bifurcations.

Part II

Thermoelectric convection in cylindrical annular geometry

Chapter 7

Thermoelectric convection in stationary cylindrical annulus

As an introduction to this part dealing with the effect of the DEP force in different fluid systems, the results of previous works will first be introduced. Yoshikawa et al. [33] performed the linear stability analysis of a stationary cylindrical annulus submitted to the DEP force under microgravity condition. Then Travnikov et al. [42, 43] provided results of numerical simulation for the same case.

7.1 Threshold of the thermoelectric convection

We saw in Sec. 2.1 that the electric gravity is centripetal, except in the case of small gap where the electric gravity can be centrifugal or can change its sign inside the gap. When the electric gravity is centripetal (centrifugal), thermoelectric convection can occur in outward (inward) heating, and the instability mechanism is analogue to the Rayleigh instability in horizontal plane. This analogy is of main interest since in a cylindrical annulus of dielectric fluid under microgravity condition, the dieletrophoretic force can be seen as a purely central gravity force field.

Figure 7.1 shows the critical parameters as functions of the radius ratio η. Critical modes are Prandtl independent and are stationary. The electric Rayleigh number L used to plot the threshold (Fig. 7.1 - a) has been defined at the logarithmic radius $R_{ln} = -1/\ln\eta$ as we did in Sec. 6.3.1. We remind that at this position, the radial heat flux in a cylindrical annulus is equivalent to the one on the plate cavity. The threshold L_c slightly depends on η in outward heating, but its value stays close to $L = 1708$, which is the critical value for the classical Rayleigh problem. For relatively

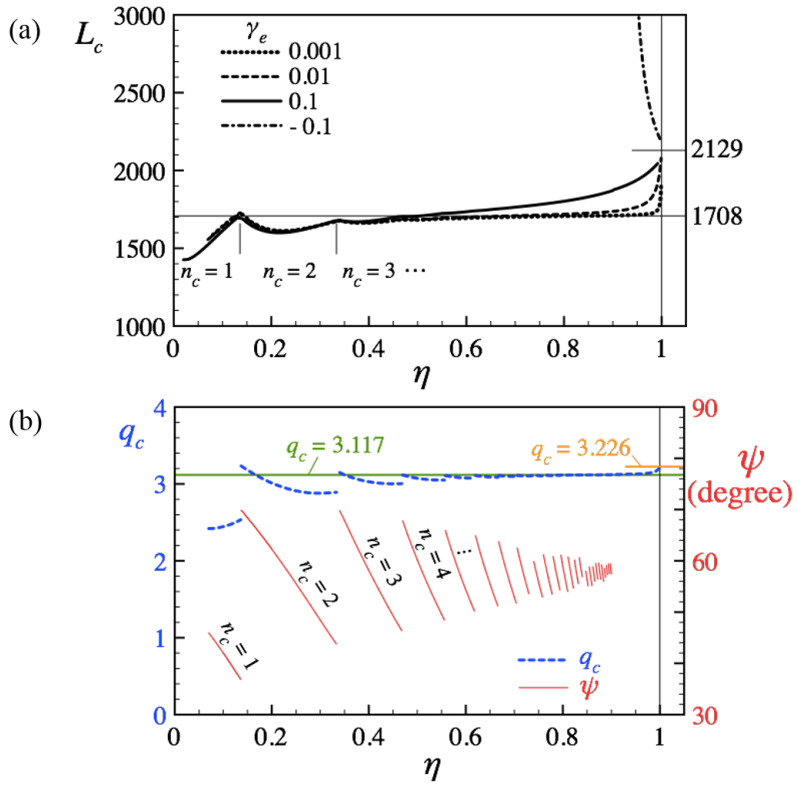

Figure 7.1: Variation of the critical parameters with the radius ratio: (a) electric Rayleigh number for different γ_e and (b) wavenumber and angle of the vortices with respect to the azimuthal direction for $\gamma_e = 0.01$. [33]

large values of η, L_c increases and tends to $L = 2129$ when η tends to one. This stabilisation starts at lower radius ratio when the thermoelectric parameter γ_e is increased. Indeed, for large γ_e and large η, there is a feedback effect of the perturbation electric gravity, which makes the threshold higher than that for the classical Rayleigh problem. This was first found in the plate cavity of dielectric fluid feeling the dielectrophoretic force [56]. In this case, there is always a non-negligible energy dissipation done by the perturbation electric gravity. Note that, in the energy analysis of Chapter 6, the perturbation centrifugal gravity has a different effect than the perturbation electric gravity since the perturbation centrifugal gravity destabilises the flow.

In inward heating, for large values of the thermo-electric parameter γ_e and large values of η the electric gravity is centrifugal. Thermal convection can thus occur and the threshold decreases with the radius ratio and also tends to the value $L = 2129$ when η tends to one.

Critical modes obtained in inward heating are axisymmetric, but they are helical in outward heating. The number of modes in the azimuthal direction n_c increases with the radius ratio and the wavenumber q_c undergoes discontinuities each times n_c changes (Fig. 7.1 - b). The feedback effect of the perturbation electric gravity is at the origin of the slight increase of q_c for low curvature

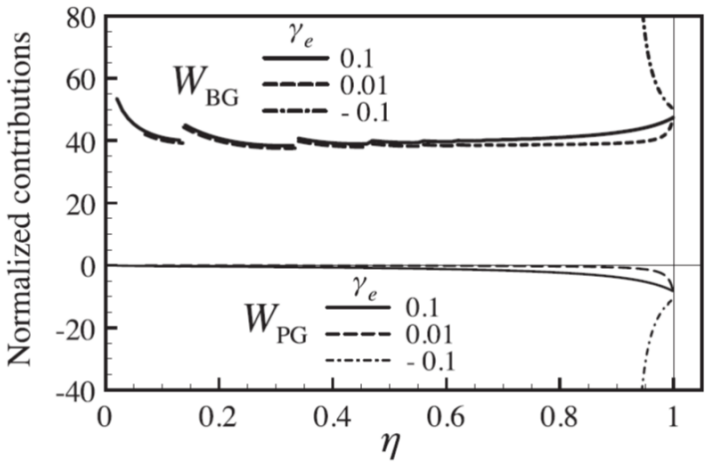

Figure 7.2: Power given by the base and perturbation electric gravity (W_{BG} and W_{PG} respectively) as function of the radius ratio for different γ_e. [33]

compared the its value for the classical Rayleigh problem. The angle of the helical modes with respect to the azimuthal direction ψ is sensitive to η and tends to $\psi \approx 60°$ for large values of η.

The conservation of kinetic energy involves three mechanisms of energy transfer from the base state to perturbations: the power performed by the base electric gravity W_{BG}, the power performed by the perturbation electric gravity W_{PG}, and the energy rate of viscous dissipation D_ν. The latest balances the other term since at the onset of convective flow, there is no time variation of the kinetic energy. Figure 7.2 shows the variations of W_{BG} and W_{PG} with η for different γ_e. The power performed by the base electric gravity is positive in inward heating and in outward heating when the base electric gravity is centrifugal, i.e. for large values of η and γ_e. In these cases, the base electric gravity is the source of thermal convection and the value of W_{BG} is large compared to that of W_{PG}, meaning that the base gravity is the predominant contribution for the energy transfer. In counterpart, the power performed by the perturbation electric gravity is negative, and therefore stabilises the flow in inward and outward heating when the gravity is centrifugal. For low to moderate values of η, depending on γ_e, the contribution of W_{PG} is negligible such as in the classical Rayleigh-Bénard problem in an horizontal plate cavity where there is no analogue contribution of a perturbation gravity. This explains why the the thresholds of both cases are comparable. However for large radius radio, the feedback through the perturbation electric gravity is no longer negligible, making the threshold increase compared to its value for the Rayleigh-Bénard problem. The value of W_{PG} decreases with η in outward heating and increases with η in inward heating, but its value when $\eta \to 1$ is a constant independently of

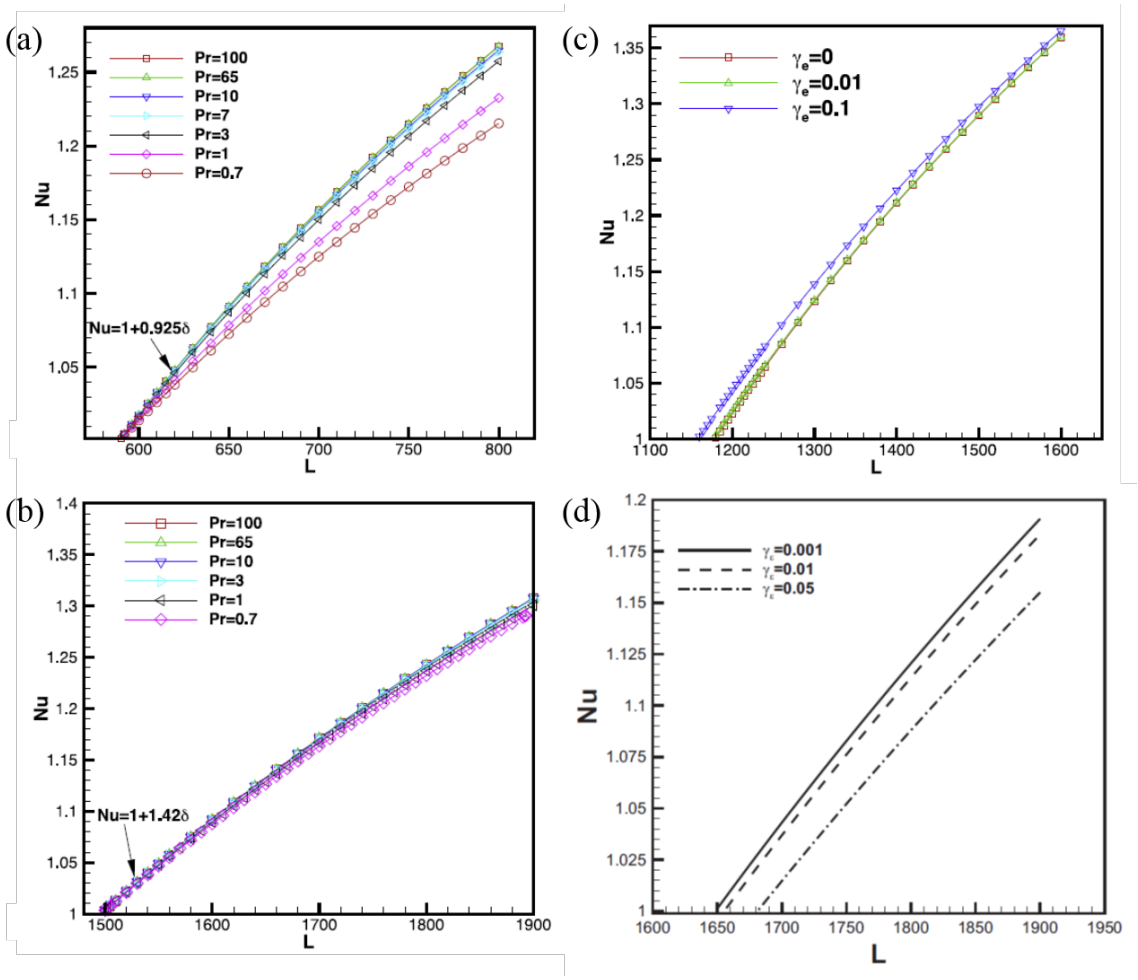

Figure 7.3: Variation of the Nusselt number with the electric Rayleigh number: (a) for $\eta = 0.1$, $\gamma_e = 0.01$ and for different Pr, (b) for $\eta = 0.5$, $\gamma_e = 0.01$ and for different Pr, (c) for $\eta = 0.3$, Pr = 10 and for different γ_e, and (d) for $\eta = 0.7$, Pr = 100 and for different γ_e. [42, 43]

the value of γ_e, explaining the uniqueness of the threshold when there is no curvature.

7.2 Heat transfer

The numerical simulations performed by Travikov et al. were done with periodic boundary conditions in the axial direction and close to the onset of convection. For L larger than the critical value, stationary helical modes were also found with thresholds and number of modes in the azimuthal direction in agreement with thus of the linear stability theory. The averaged radial heat flux was measured at the inner cylinder for an established flow in order to provide values of the Nusselt number. Figure 7.3 shows the evolution of the Nusselt number Nu with the electric Rayleigh number. When $L < L_c$, Nu = 1 since the base state is conductive. For $L > L_c$, the Nusselt number growths, highlighting the increase of the heat transfer by the thermoelectric

buoyancy. At the onset of convection the slope of Nu(L) mainly depends on the radius ratio and is equal to 0.925 for $\eta = 0.1$ and 1.42 for $\eta = 0.5$. We recall that, in the case of a cylindrical annulus of fluid rigidly rotating around its axis and heated from the outside, the slope of Nu(Ra) for $\eta = 0.5$ is about 1 to 1.3 depending on γ_aPr. This means that the heat transfer enhancement induced by thermoelectric convection is more efficient than that induced by centrifugal buoyancy (at least close to the onset of convection). For weak values of the radius ratio, the Nusselt number increases with increasing Prandtl number (Fig. 7.3 - a) while the thermoelectric parameter has no significant influence on the heat transfer (Fig. 7.3 - c). For larger values of η, the effect of the Prandtl number on the Nusselt number is weak (Fig. 7.3 - b) while increasing γ_e enhance the feedback effect of the perturbation electric gravity and decreases the Nusselt number.

Chapter 8

Thermo-electric convection in a fluid system in solid-body rotation

We consider now a dielectric fluid confined in a rigidly rotating cylindrical annulus with an alternative electric potential between the two cylinders under microgravity conditions (Gr = 0). The momentum equation (6.3) now includes the dielectrophoretic force and reads:

$$\frac{\partial \boldsymbol{u}}{\partial t} + \boldsymbol{u}\cdot\boldsymbol{\nabla}\boldsymbol{u} = -\boldsymbol{\nabla}\pi + \Delta\boldsymbol{u} - 2\tau\left(\boldsymbol{e}_z \times \boldsymbol{u}\right) + 4\sqrt{f(\eta)\mathrm{Ra}\frac{\gamma_a}{\mathrm{Pr}}}\theta\left(\boldsymbol{e}_z \times \boldsymbol{u}\right) - \left(f(\eta)\frac{\mathrm{Ra}}{\mathrm{Pr}} + \frac{\mathrm{L}}{\mathrm{Pr}}\right)\theta\boldsymbol{e}_r \quad (8.1)$$

In this chapter, we will only consider the case where the electric gravity is centripetal. Due to the different orientations of the centrifugal acceleration and of the electric gravity, we will separate the cases of inward and outward heating. Indeed, the destabilisation mechanism will be different in both cases.

8.1 Effect of the DEP force on the centrifugally-induced thermal convection

When the outer cylinder is hotter than the inner one (inward heating), the electric gravity is oriented toward the cold cylinder while the centrifugal gravity is oriented toward the hot cylinder (Fig. 8.1). The centrifugal buoyancy will thus be the destabilising mechanism which can induce thermo-convective instabilities even without electric field. The temperature stratification has a stable profile regarding the electric gravity, implying a stabilizing effect of the thermoelectric

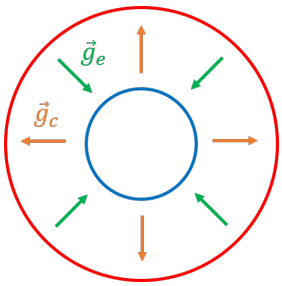

Figure 8.1: Sketch of the directions of the gravity fields with respect to the temperature gradient.

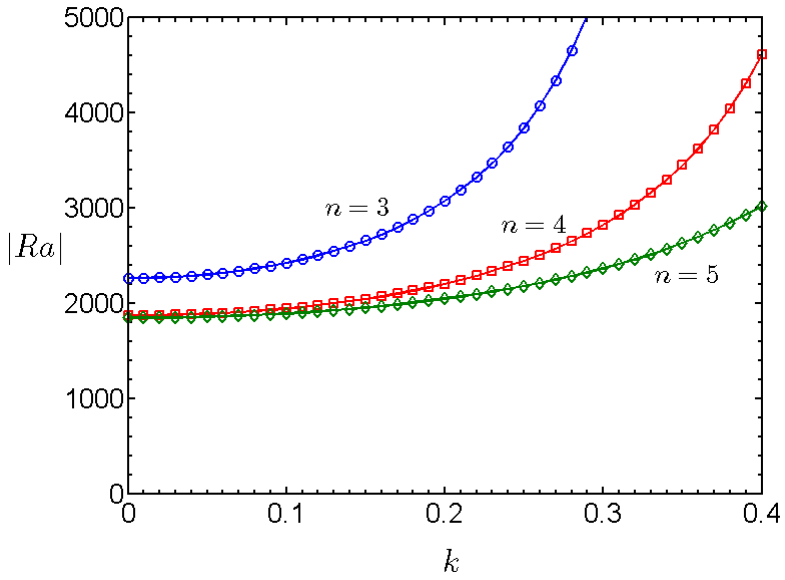

Figure 8.2: Marginal stability curves in the (k, Ra) plane for $\eta = 0.5$, $\mathrm{Pr} = 10$, $\gamma_a = \gamma_e = -0.01$, $V_E = 100$ and for different azimuthal mode number.

buoyancy. When the electric field is not active, we saw that the critical modes take the form of oscillatory columns (OC). We would like to investigate the effect of the DEP force on this instability.

8.1.1 Influence of the Prandtl number

Since in inward heating ($\gamma_a < 0$), the centrifugal Rayleigh number Ra and the electric Rayleigh number L are negative, the absolute values of these parameters will be considered. The global minimum of the marginal curves obtained with an active electric field is associated with the OC modes (Fig. 8.2). The critical centrifugal Rayleigh number is independent from the Prandtl number. It increases with increasing V_E (Fig. 8.3 - a), which underlines the stabilising effect of the thermoelectric buoyancy under this configuration. In fact, the electric gravity and the centrifugal acceleration are oriented in opposite direction, so the resulting buoyancy force is weakened. There

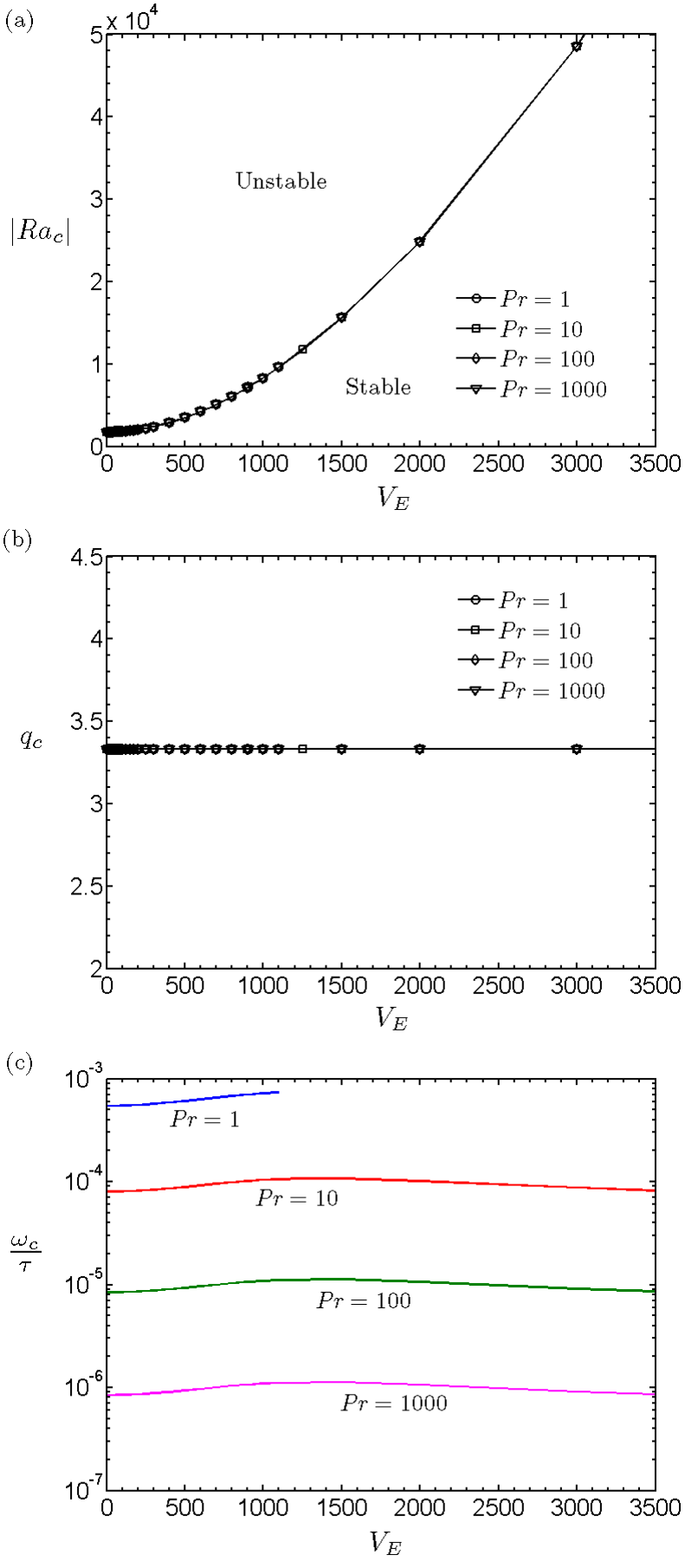

Figure 8.3: Variation of the critical values with V_E for $\eta = 0.5$, $\gamma_a = \gamma_e = -0.01$, and for different Prandtl number. (a) centrifugal Rayleigh number, (b) wavenumber, and (c) frequency.

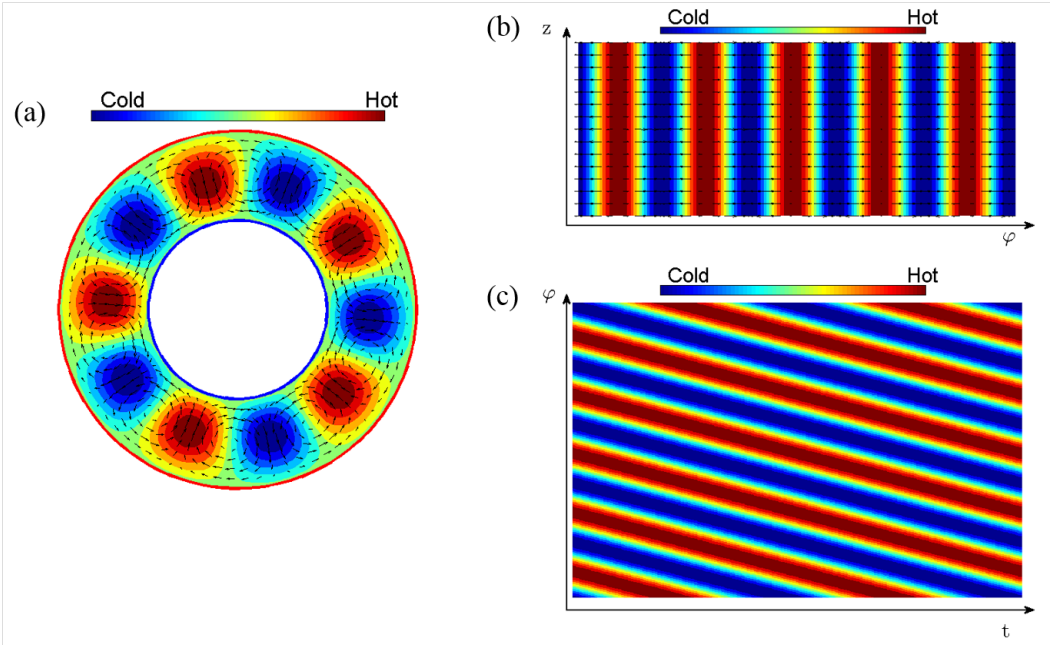

Figure 8.4: Perturbation temperature and perturbation velocity fields: (a) in the (r, φ) plane (b) in the (φ, z) plane, and (c) in the (t, φ) plane for $\eta = 0.5$, $\mathrm{Pr} = 10$ and $\gamma_a = \gamma_e = -0.01$ and $V_E = 600$ at the critical condition ($\mathrm{Ra}_c = -211.6$).

is a need of a large rotation rate, i.e. large centrifugal gravity, to overcome the stabilizing effect of the DEP force. The critical modes are columns with an azimuthal mode number n_c that is independent of the electric potential. For $\eta = 0.5$, the azimuthal mode number is $n_c = 5$ and $k_c = 0$ which gives a constant critical wavenumber $q_c = 3.333$ (Fig. 8.3 -b). The critical frequency is, as in the case without electric field, normalised with the Coriolis number (Fig. 8.3 - c). The frequency of the OC modes is positive which indicates retrograde vortices. The temporal behaviour of these convection rolls depends on the Prandtl number. For a fixed V_E, fluids with large values of Pr have a smaller critical frequency than those with small values of Pr. Figure 8.4 shows the perturbation temperature and the perturbation velocity fields of a OC mode in different spatial and spatio-temporal planes. In the spatio temporal profile of the perturbation temperature (Fig. 8.4 - c), one can see the retrograde propagation of the vortices.

8.1.2 Influence of the thermal parameters

In inward heating, the temperature difference has no influence on the threshold of the columnar modes (Fig. 8.5 - a). This affirmation is true if we consider the effect of the DEP force through the use of L, and not through the use of V_E. The thermoelectric parameter γ_e plays no role on the frequency of vortices propagation (Fig. 8.5 - b). Indeed, the feedback effect of the perturbation

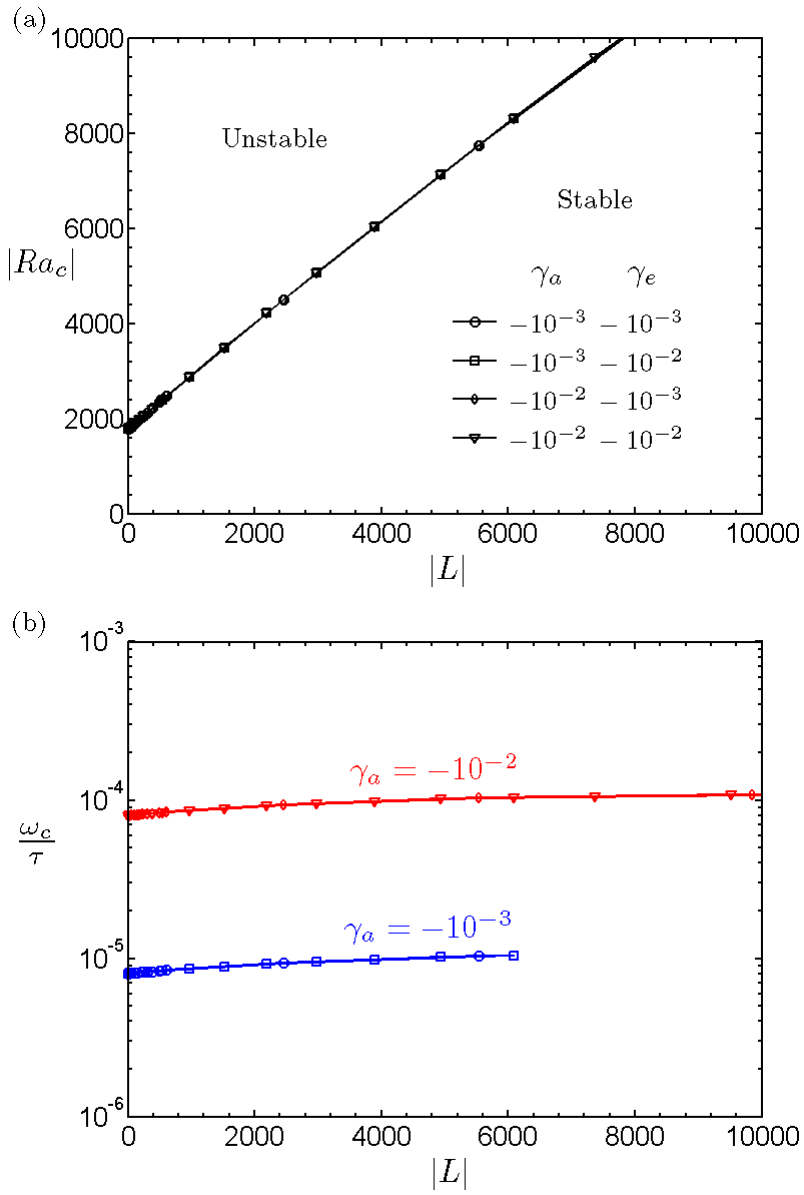

Figure 8.5: Critical values of (a) the electric Rayleigh number, and (b) the normalised frequency for $\eta = 0.5$ and $\mathrm{Pr} = 10$ in inward heating.

electric gravity is negligible for the considered set of parameters. In contrast with the thermal expansion parameter which plays an important role on the temporal behaviour of the critical modes. For a fixed electric Rayleigh nummber, increasing the temperature difference between the two cylinders increases the critical normalised frequency.

8.1.3 Influence of the radius ratio

For a given value of the electric potential, flows in annulus with large radius ratio (small curvature) are more unstable than those with small radius ratio (large curvature) (Fig. 8.6 - a). For some values of η, the number of columns can change when V_E increases (Fig. 8.6 - b). For $\eta = 0.2$, n_c jumps from 2 to 3, and for $\eta = 0.8$, it jumps from 14 to 15. This discontinuity is also observed for the frequency (Fig. 8.6 - c). So besides the delay of the onset of thermal convection, the electric potential has an effect on the spatial and temporal properties for some radius ratios.

8.2 Effect of the rotation on thermoelectric convection

When the inner cylinder is hotter than the outer one (outward heating), the thermoelectric buoyancy is the destabilising mechanism, leading to thermoelectric convection while the centrifugal buoyancy stabilises the flow (Fig. 8.7). Indeed, as the direction of the electric gravity field is dominated by the curvature of the system, it does not change with the direction of the temperature gradient (within the chosen set of parameters). We investigate the effect of the rotation on the critical parameters of the thermoelectric convection. We remind that when the cylinders are not rotating, the critical modes are stationary helical vortices.

8.2.1 Influence of the Prandtl number

For low values of Coriolis number τ (Fig. 8.8 - a), the global minimum corresponds to oscillatory non axisymmetric (ONA) modes, while for larger τ (Fig. 8.8 - b), the global minimum corresponds to oscillatory columnar (OC) modes. Figure 8.9 shows the behaviour of the critical electric Rayleigh number with τ. The threshold increases with increasing the rotation rate of the cylindrical annulus, which highlight the stabilising effect of the centrifugal buoyancy in this configuration. The value of τ for which both ONA and OC modes are critical does not depend on the Prandtl number. For a given τ, increasing the Prandtl number increases the threshold

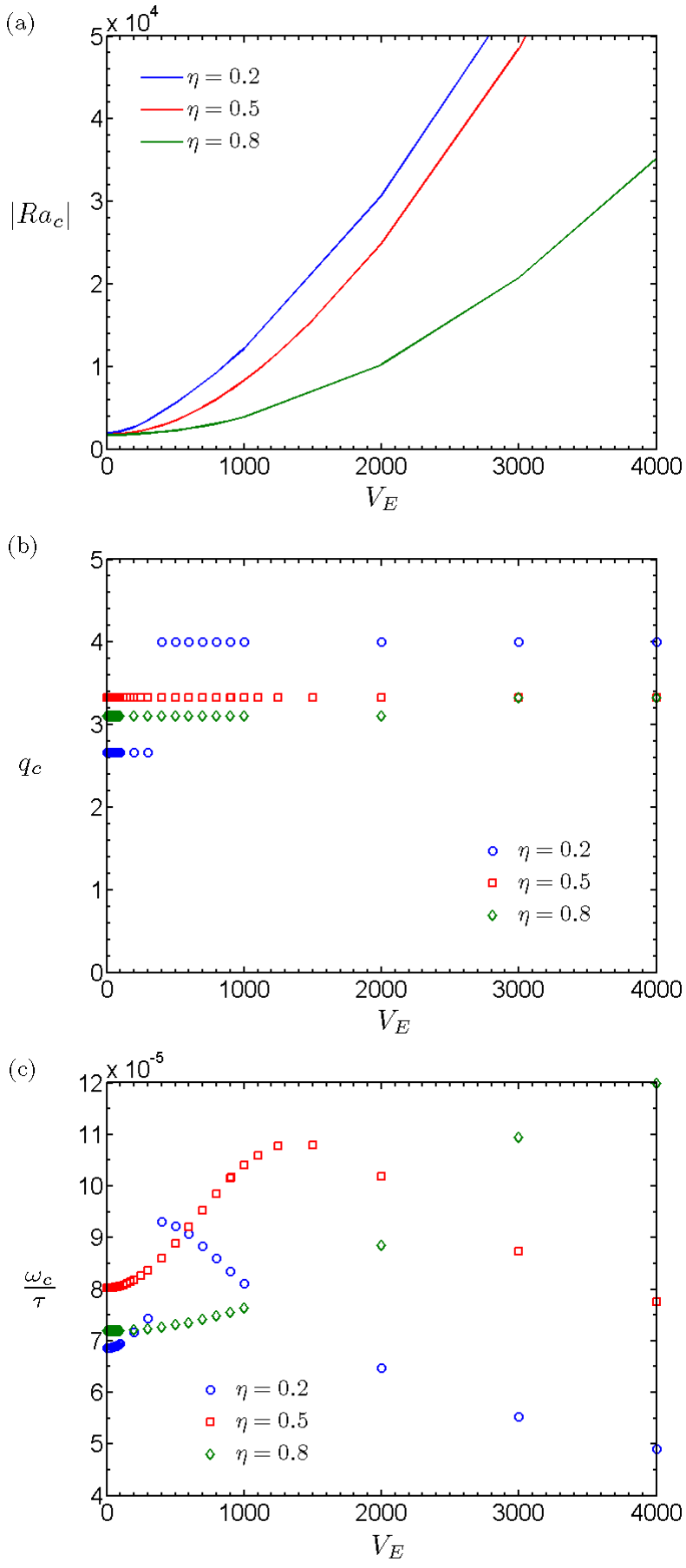

Figure 8.6: Variation of the critical parameters with V_E for Pr = 10, $\gamma_a = \gamma_e = -0.01$ and for different η: (a) centrifugal Rayleigh number, (b) wavenumber, and (c) normalised frequency.

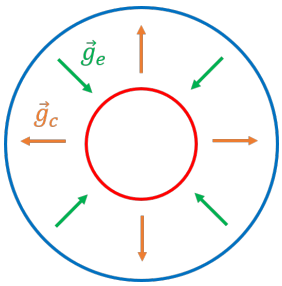

Figure 8.7: Sketch of the directions of the gravity fields with respect to the temperature gradient.

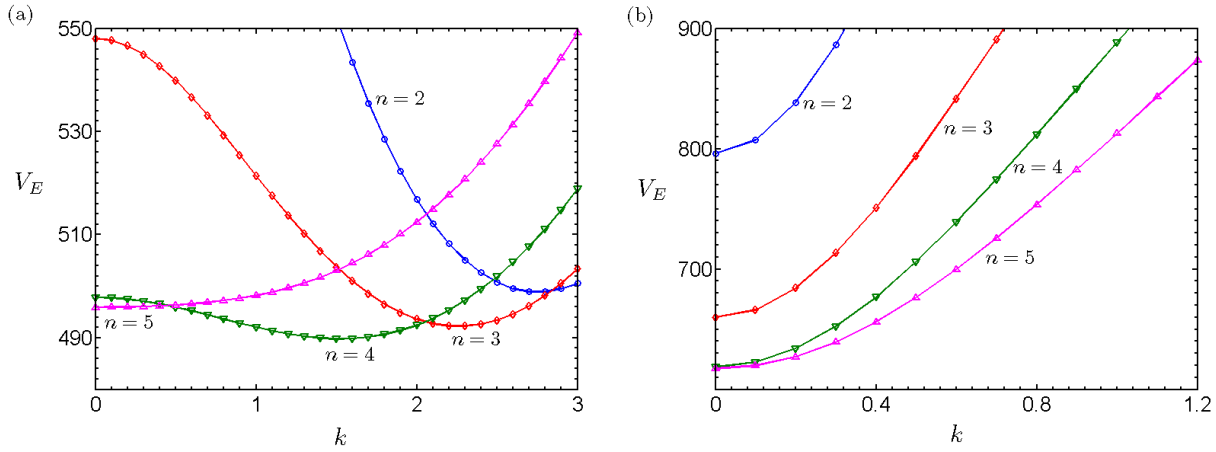

Figure 8.8: Marginal stability diagram in the (k, V_E) plane for $\eta = 0.5$, Pr $= 10$, $\gamma_a = \gamma_e = 0.01$, $\tau = 1.63$ (a) and $\tau = 163.30$ (b) and for different azimuthal mode number.

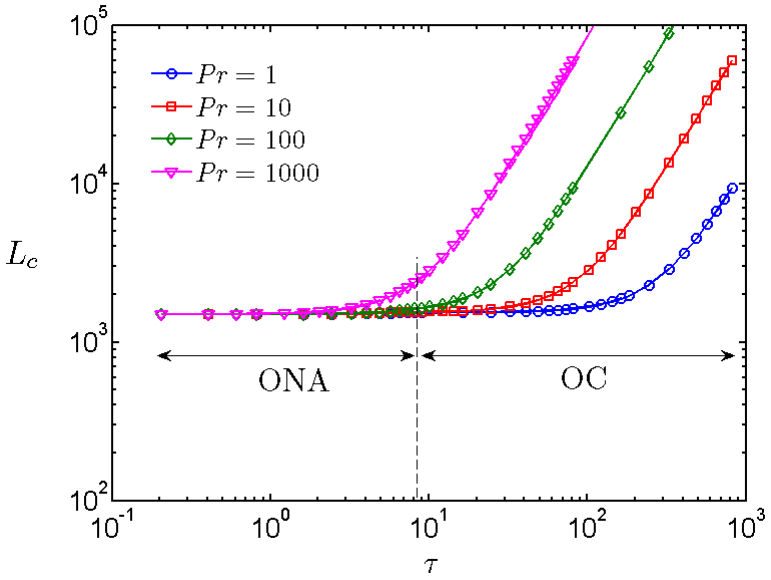

Figure 8.9: Variation of the critical electric Rayleigh number with τ for $\eta = 0.5$, $\gamma_a = \gamma_e = 0.01$, and for different Prandtl number.

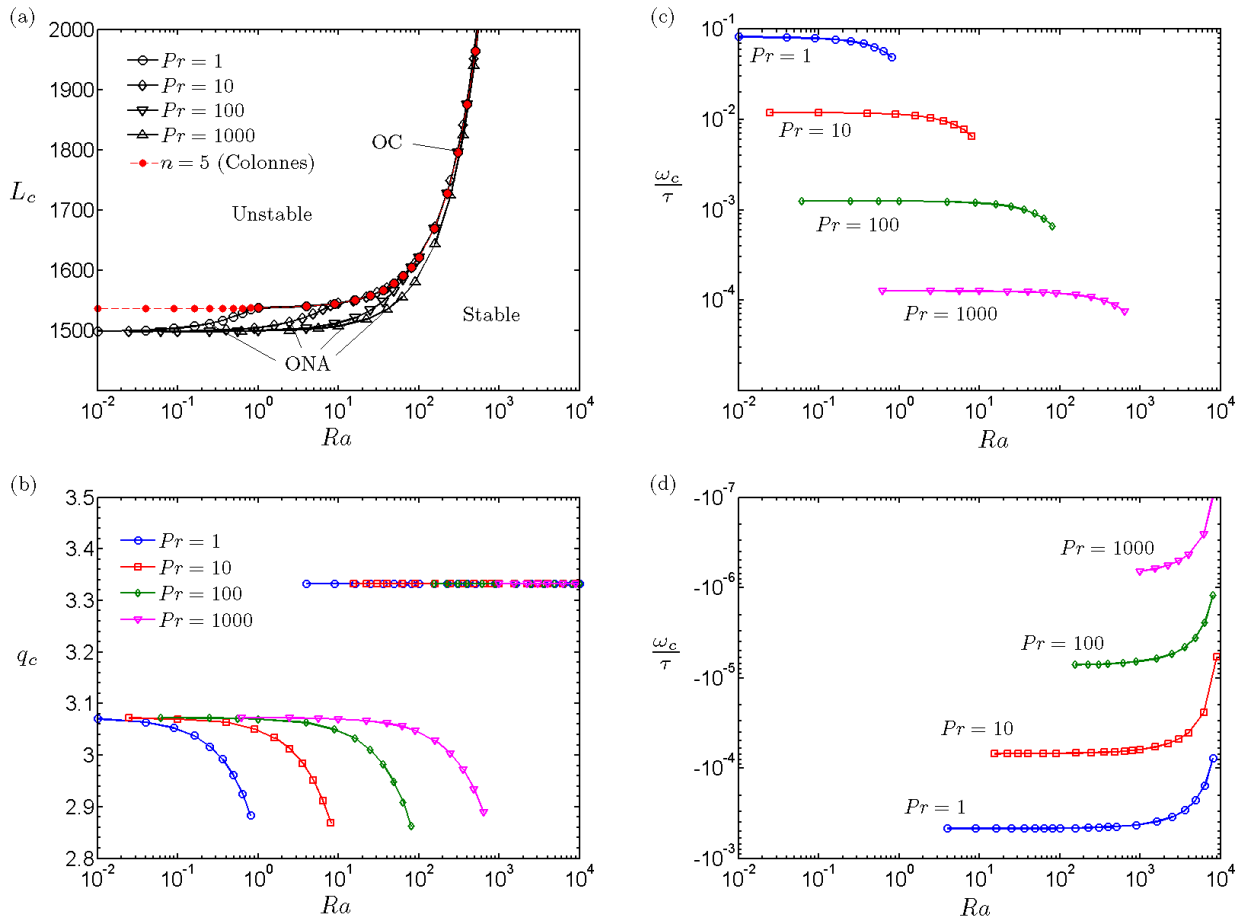

Figure 8.10: Variation of the critical values with the centrifugal Rayleigh number for $\eta = 0.5$, $\gamma_a = \gamma_e = 0.01$, and for different Prandtl number: (a) electric Rayleigh number (b) wavenumber and normalized frequency (c) of ONA modes and (d) of OC modes.

of OC modes with a certain scaling law. In fact, the threshold of columnar modes (with $n = 5$ when $\eta = 0.5$) against the centrifugal Rayleigh number is independent from the Prandtl number, and its behaviour corresponds to the red dotted curve on Fig. 8.10 - a. At low rotation rates, the threshold of ONA modes is lower than the one of OC modes. The threshold of ONA modes increases with the Coriolis number until the codimension-2 point for which both ONA and OC modes are critical. Beyond this value, the OC modes become critical. The Coriolis number at this codimension-2 point does not depend on Pr, therefore the centrifugal Rayleigh number at this codimension-2 point depends on Pr. For weak Pr, the domain of existence of ONA modes is short while for large Pr the ONA modes exists within a wide range of Ra. The threshold of OC modes also increases with the Rayleigh number. The critical wavenumber q_c of ONA modes is constant for small values of Ra and then decreases with Ra near the codimension two point. Beyond the codimension two point, q_c remains constant (Fig. 8.10 - b) since the number of columns does not vary with Ra for $\eta = 0.5$. The critical normalized frequency of ONA modes as function of Ra is

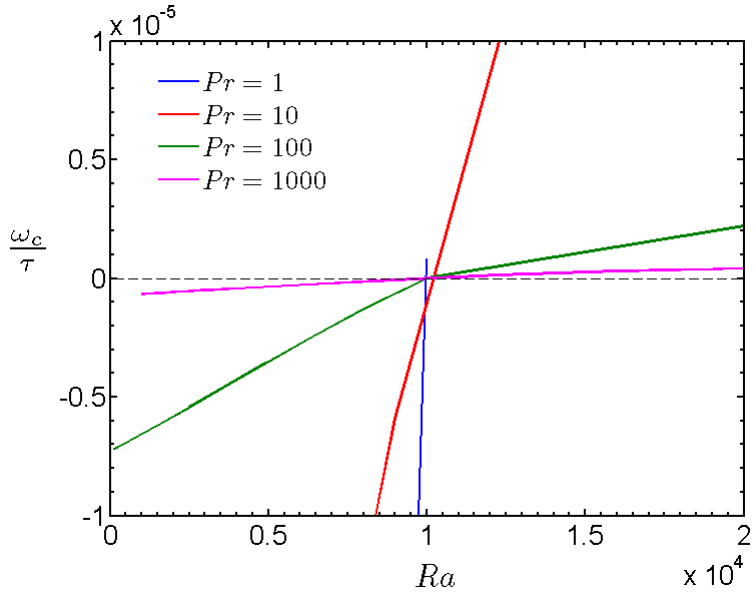

Figure 8.11: Critical normalised frequency of OC modes as a function of Ra for different Prandtl numbers close to $\omega_c/\tau = 0$. The critical frequency changes its sign at a constant value of Ra.

shown on Fig. 8.10 - c, while the one of OC modes is shown on Fig. 8.10 - d. The critical frequency of ONA modes is positive, i.e. the ONA modes propagate in the retrograde sense in the azimuthal direction, and decreases with increasing the rotation rate. Fluids with large values of Pr have a lower frequency of ONA modes. The critical normalized frequency of OC is negative, indicating prograde columnar vortices. Increasing the Prandtl number increases the frequency of OC modes.

The critical frequency of OC modes increases with the centrifugal Rayleigh number and reaches $\omega = 0$ at a certain value Ra_s which does not depend on the Prandtl number (Fig. 8.11). When $\mathrm{Ra} > \mathrm{Ra}_s$, the critical frequency become positive indicating retrograde columnar vortices. The perturbation temperature and perturbation velocity fields of an ONA mode and an OC mode with $\mathrm{Ra} < \mathrm{Ra}_s$ in outward heating and in different spatial or spatio-temporal planes are shown on Fig. 8.12. The spatio-temporal profile of perturbation temperature shows the retrograde propartion of the ONA mode and the prograde propagation of the OC mode.

8.2.2 Influence of the thermal parameters

The thermoelectric parameter has almost no influence on the threshold due to the negligible feedback effect, but the thermal expansion parameter has an impact on the position of the codimension-2 point where both ONA and OC modes are critical (Fig. 8.13 - a). Indeed, the larger γ_a, the larger the value of Ra at the codimension-2 point. The critical wavenumber of ONA

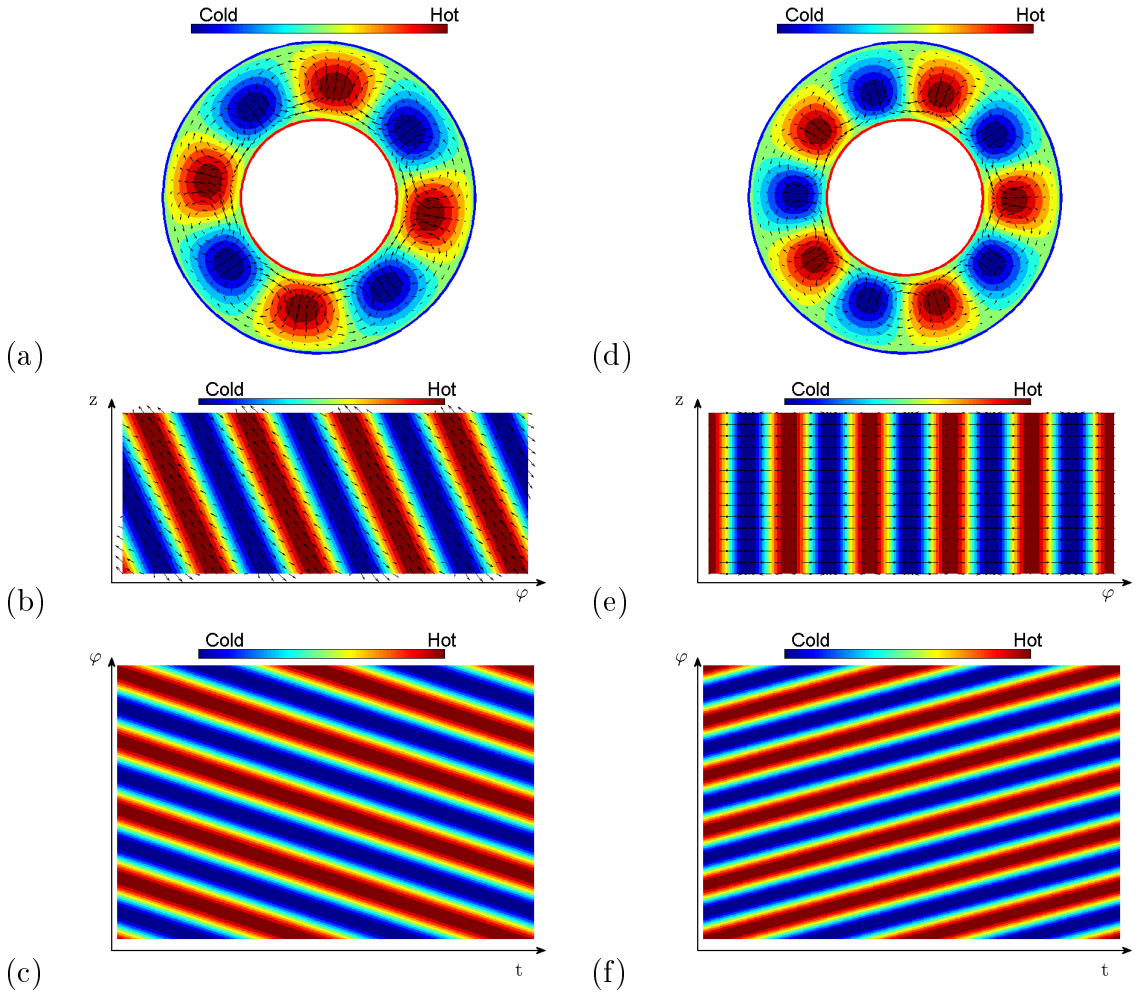

Figure 8.12: Perturbation temperature and perturbation velocity fields of an ONA mode (Ra = 5) in (a) the (r, φ) plane, (b) in the (φ, z) plane and (c) in the (t, φ) plane, and of an OC mode (Ra = 4000) in (d) the (r, φ) plane, (e) in the (φ, z) plane and (f) in the (t, φ) plane at the critical condition for $\eta = 0.5$, $\gamma_a = \gamma_e = 0.01$ and Pr = 10.

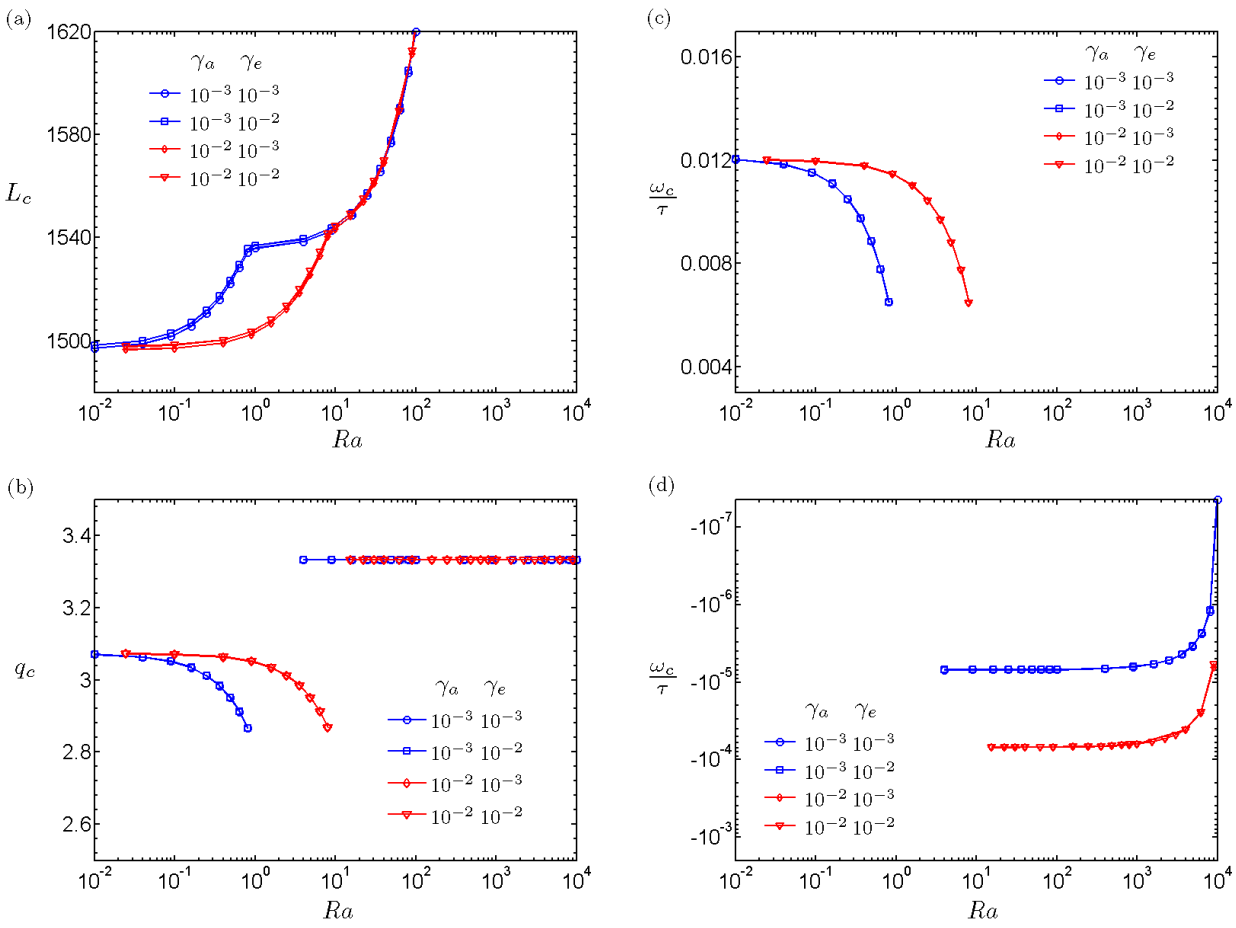

Figure 8.13: Variation of the critical parameters with Ra for $\eta = 0.5$, Pr = 10 and for different γ_a and γ_e: (a) electric Rayleigh number, (b) wavenumber, (c) normalised frequency of ONA modes and (d) normalised frequency of OC modes.

modes depends on γ_a in the sense that γ_a changes the codimension-2 point position (Fig. 8.13 - b). For OC modes the critical wavenumber is constant since, for $\eta = 0.5$, $n_c = 5$ and is constant. The critical normalised frequency of ONA modes (Fig. 8.13 - c) and OC modes(Fig. 8.13 - d) have been separated in two different diagrams in order to have a better insight on there different behaviours. The thermo-electric parameter plays no role on the frequency of vortices propagation, both for ONA and OC modes. In contrast, the thermal expansion parameter plays an important role on the temporal behaviour of the critical modes. For ONA modes, the critical normalised frequency is affected by γ_a through the change of Ra at the codimension-2 point. For OC modes, increasing the absolute value of γ_a increases the absolute value of the critical frequency.

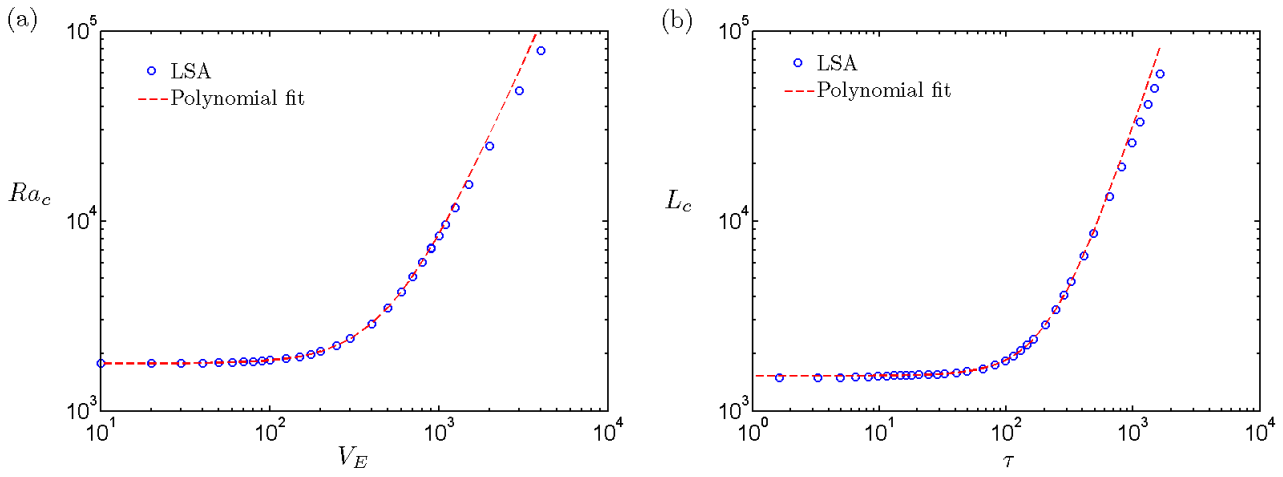

Figure 8.14: Threshold fitted with a polynomial function of second order for $\eta = 0.5$, Pr = 10: (a) Ra_c against V_E in inward heating with $\gamma_a = \gamma_e = -0.01$ ($P_1^i = 0.0067; P_2^i = 0.0638; P_3^i = 1774.4$) and (b) L_c against τ in outward heating with $\gamma_a = \gamma_e = 0.01$ ($P_1^o = 0.0300; P_2^o = 0.3058; P_3^o = 1527.9$).

8.3 Discussion

8.3.1 Parabolic behaviour of the threshold

The variation of the threshold with V_E in inward heating and with τ in outward heating seems to have the behaviour of a polynomial function of second order. Figure 8.14 shows the thresholds fitted with the following functions:

$$\mathrm{Ra}_c = P_1^i V_E^2 + P_2^i V_E + P_3^i \quad \text{and} \quad \mathrm{L}_c = P_1^o \tau^2 + P_2^o \tau + P_3^o \tag{8.2}$$

where i and o refer to inward heating and outward heating, respectively. In outward heating, the fitting has been performed only for the threshold of columnar modes. There is a good agreement between the parabolic functions (8.2) and the thresholds until $V_E \approx 10^3$ in inward heating and until $\tau \approx 400$ in outward heating. We retrieve the same results as for the Rayleigh-Bénard convection in the horizontal layer of fluid heated from below and rotating around its vertical axis [57].

8.3.2 Energy analysis

In this problem, the equation for kinetic energy is given by:

$$\frac{dK}{dt} = W_{Bu} + W_{BG} + W_{PG} - D_\nu \tag{8.3}$$

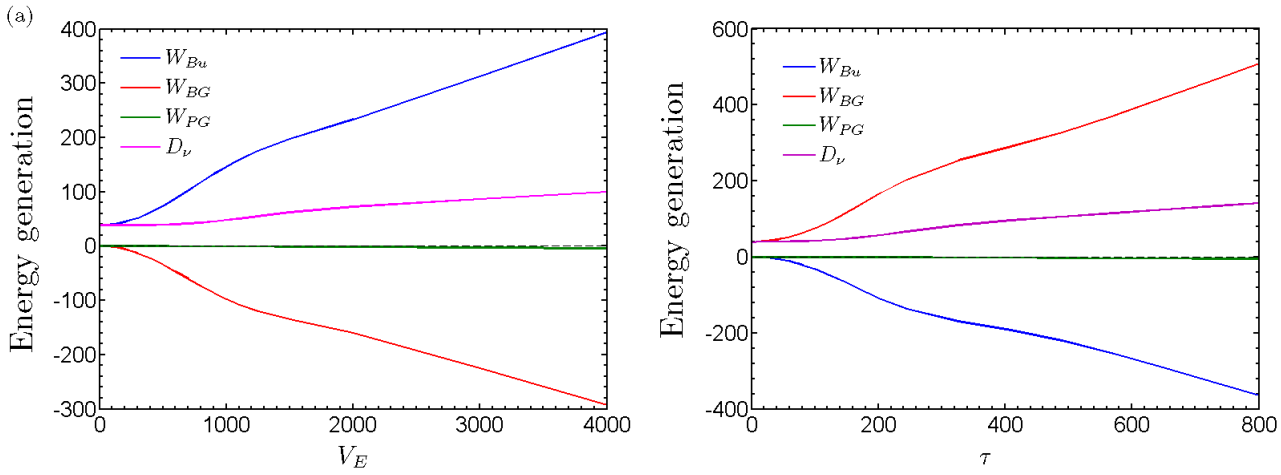

Figure 8.15: Power given by the different mechanisms for $\eta = 0.5$, $\mathrm{Pr} = 10$ (a) in inward heating against V_E with $\gamma_a = \gamma_e = -0.01$ and (b) in outward heating against τ with $\gamma_a = \gamma_e = 0.01$.

The energy transfer from the base state to perturbations is done by the centrifugal buoyancy W_{Bu}, the base thermoelectric buoyancy related to the base electric gravity W_{BG}, the perturbation thermoelectric buoyancy related to the perturbation electric gravity W_{PG}, and the viscous dissipation D_ν. Even if the destabilising mechanisms in inward and outward heating are different, the variation of the different power terms with either V_E or τ shows very similar behaviours. In inward heating (Fig. 8.15 - a), the power performed by the centrifugal buoyancy is always positive and increases with increasing V_E, while the power performed by the base electric gravity is always negative and decreases with V_E. In outward heating (Fig. 8.15 - b), it is now W_{BG} which is always positive and increases with increasing τ, and W_{Bu} is always negative and decreases with τ. In both cases, the viscous dissipation slightly increases with V_E in inward heating, or with τ in outward heating, and the power performed by the perturbation electric gravity is negligible, considering the chosen values of η and γ_e [33].

8.3.3 Frequency analysis

In the corotating regime in the absence of electric field (Chapter 6), we saw that scaling the normalised frequency with the parameter γ_a/Pr, which involves in the Coriolis buoyancy terms, unified the results obtained for different γ_a and Pr. The same scaling is tested on the frequency of OC modes obtained in inward and outward heating.

In inward heating, the scaled critical normalised frequency is independent from the Prandtl number when Pr is sufficiently large (Fig. 8.16 - a). Otherwise the larger the Prandtl number,

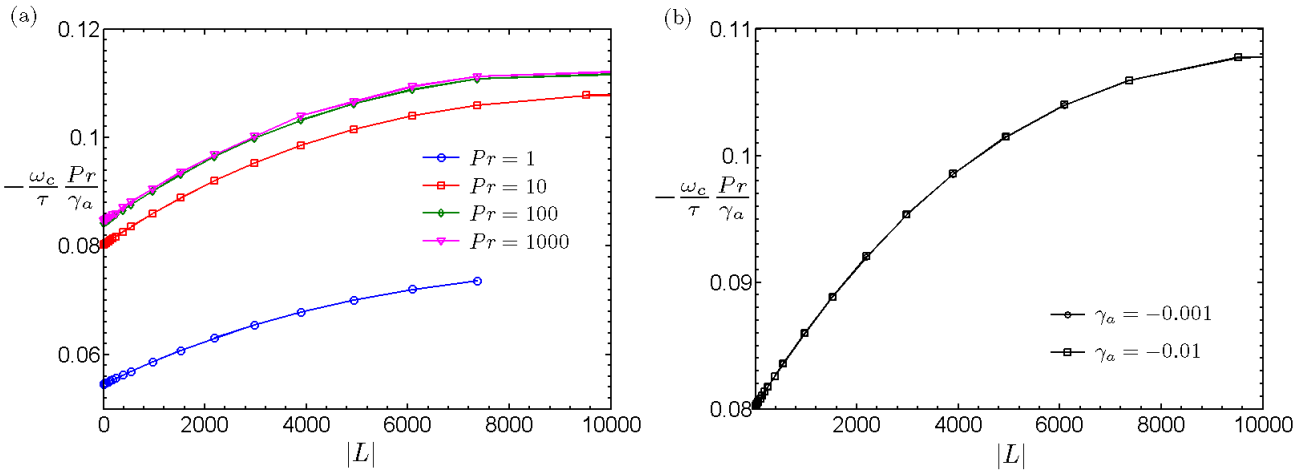

Figure 8.16: Critical normalised frequency scaled with the parameter γ_a/Pr in outward heating for (a) different Pr with $\gamma_a = \gamma_e = -0.01$ and (b) for different γ_a with $\gamma_e = -0.01$ and $\mathrm{Pr} = 10$.

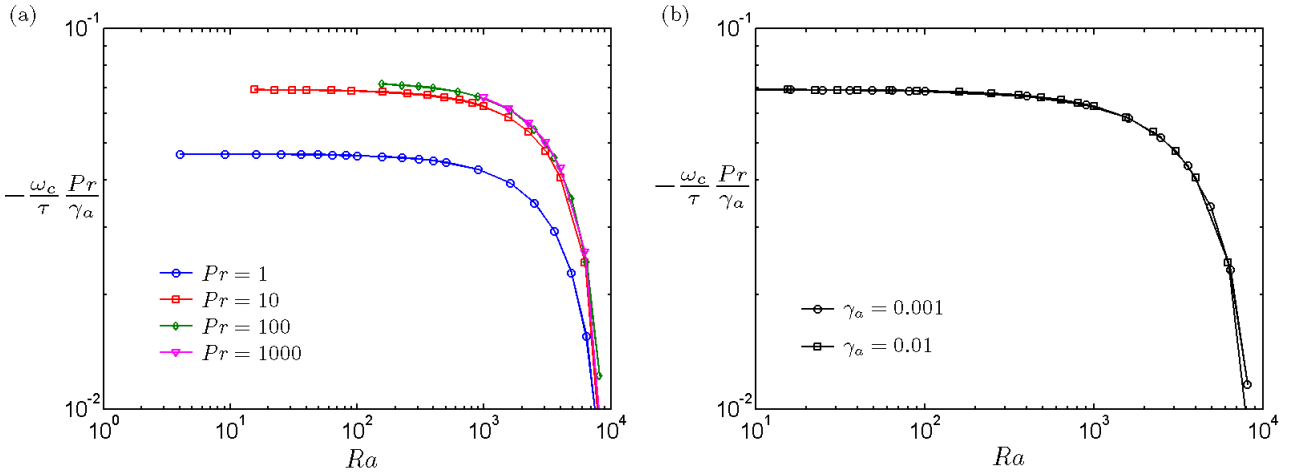

Figure 8.17: Critical normalised frequency of OC modes scaled with the parameter γ_a/Pr in outward heating for (a) different Pr with $\gamma_a = \gamma_e = 0.01$ and (b) for different γ_a with $\gamma_e = 0.01$ and $\mathrm{Pr} = 10$.

the larger the scaled frequency. In another hand, the scaling of the normalised frequency makes it independent from γ_a (Fig. 8.16 - b).

In outward heating, for the OC modes, the same observation is made concerning the behaviour of the scaled frequency. For fixed thermal parameters, increasing the Prandtl number increases the scaled frequency, and for sufficiently large Pr, the scaled frequency become independent from Pr (Fig. 8.17 - a). For a fixed Pr, the thermal expansion parameter has no influence on the scaled frequency (Fig. 8.17 - b).

These results indicate that the oscillation of columns takes its origin in the effect of the Corilis buoyancy since the parameter γ_a/Pr involves in this term in the momentum equation written in the rotating frame of reference (Eq. (8.1))

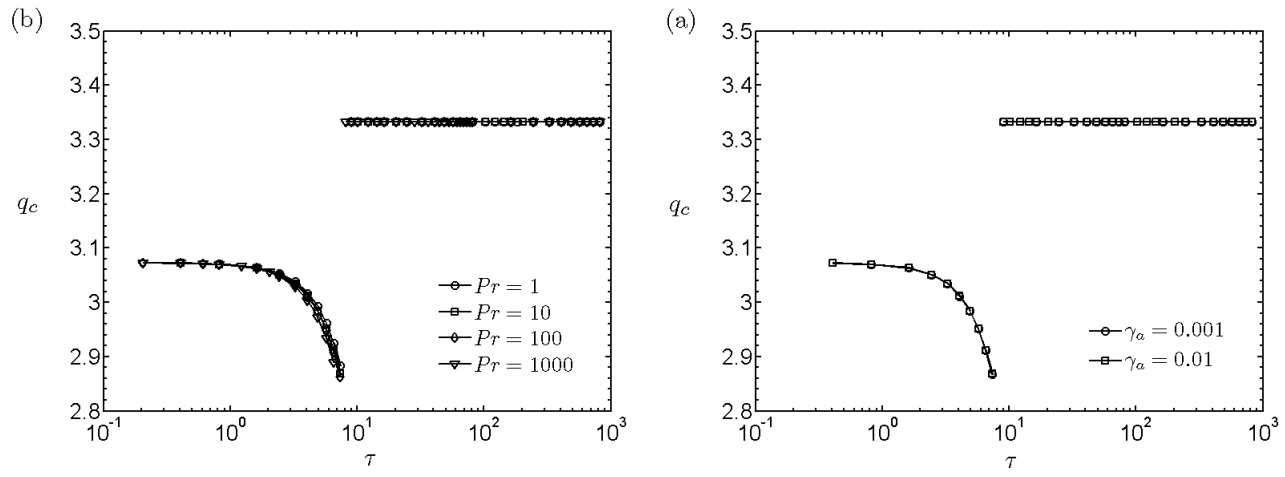

Figure 8.18: Critical wavenumber in outward heating for (a) different Pr with $\gamma_a = \gamma_e = 0.01$ and (b) for different γ_a with $\gamma_e = 0.01$ and Pr $= 10$.

8.3.4 Columnar modes in outward heating

In outward heating, the critical Rayleigh number at the codimension-2 point between the ONA modes and the OC modes depends on the Prandtl number and on the thermal expansion parameter. But the critical Coriolis number at this codimension-2 point is independent from Pr and γ_a (Fig. 8.18). This result could be related to the Taylor-Proudman theorem.

Lets consider a rotating inviscid and incompressible fluid in the inertial frame. A volume conservative force $\boldsymbol{F} = \boldsymbol{\nabla}\Phi$ is applied to this fluid, and the advection terms are neglected. For a steady state, the Navier-Stokes equation reads:

$$2\rho\boldsymbol{\Omega} \times \boldsymbol{u} = \boldsymbol{\nabla}\Phi - \boldsymbol{\nabla}p \tag{8.4}$$

Applying the rotational operator to the equation, one can obtain the Taylor-Proudman theorem:

$$(\boldsymbol{\Omega} \cdot \boldsymbol{\nabla})\,\boldsymbol{u} = 0 \tag{8.5}$$

Developing the scalar product, we obtain a more convenient form of the theorem:

$$\Omega_x \frac{\partial \boldsymbol{u}}{\partial x} + \Omega_y \frac{\partial \boldsymbol{u}}{\partial y} + \Omega_z \frac{\partial \boldsymbol{u}}{\partial z} = 0 \tag{8.6}$$

Choosing the coordinates system where $\Omega_x = \Omega_y = 0$, Eq. (8.6) is reduced to $\partial \boldsymbol{u}/\partial z = 0$. It implies that the three components of the velocity are axially invariant.

Table 8.1: Critical Coriolis number at the codimension-2 point between ONA modes and OC modes in inward heating for different radius ratio.

η	0.2	0.5	0.8
$\tau*$	17.3	8.2	1.9

Considering a viscous fluid, Eq. (8.6) reads:

$$\Omega_x \frac{\partial \boldsymbol{u}}{\partial x} + \Omega_y \frac{\partial \boldsymbol{u}}{\partial y} + \Omega_z \frac{\partial \boldsymbol{u}}{\partial z} = \frac{\nu}{2} \boldsymbol{\nabla} \times \left(\boldsymbol{\nabla}^2 \boldsymbol{u} \right) \tag{8.7}$$

Written in its dimensionless form with $\boldsymbol{\Omega} = \Omega_z \boldsymbol{e}_z$, we have:

$$\frac{\partial \boldsymbol{u}}{\partial z} = \frac{1}{\tau} \boldsymbol{\nabla} \times \left(\boldsymbol{\nabla}^2 \boldsymbol{u} \right) \tag{8.8}$$

The Taylor-Proudman theorem is recovered if the Coriolis number τ tends to the infinite.

The linear stability analysis showed that for a given radius ratio, the Coriolis number at the codimension-2 point has a finite constant value which is at least larger than unity (Table 8.1).

8.4 Conclusion

In this problem, two radial thermal buoyancies are active: the centrifugal buoyancy and the thermoelectric buoyancy. Since the electric gravity is centripetal, these two buoyancies have opposite effects. It is thus crucial to consider separately the inward heating and the outward heating cases.

In inward heating, the centrifugal buoyancy is the source of instabilities while the thermoelectric buoyancy stabilises the flow. The critical modes are then oscillatory columnar modes. The Prandtl number and the thermal expansion parameter have an influence only on the temporal behaviour of the vortices, which can be scaled by the parameter γ_a/Pr, showing that the frequency of these modes is related to the Coriolis buoyancy.

In outward heating, the thermoelectric buoyancy is the source of instabilities while the centrifugal buoyancy stabilises the flow. For low rotation rate of the annulus, critical modes are oscillatory helical modes with a threshold, a wavenumber and a frequency that depends on Pr, and γ_a. At a certain Coriolis number which only depends on the radius ratio, both ONA and OC modes

are critical. For this value of the Coriolis number, the viscous dissipation effects are negligible compared to the inertial effects, making the Taylor-Proudman theorem valid. The threshold and the wavenumber of OC modes are independent from Pr and γ_a, when considered at a given value of the centrifugal Rayleigh number, but there frequency depend on these two parameters, and exhibit the same mechanism as for the OC modes in inward heating, i.e. the temporal behaviour is related to the Coriolis buoyancy.

In both inward and outward heating, the thresholds variation with V_E and τ respectively, behave like a polynomial function of second order, until a certain value of V_E or τ. Behind this certain value, the threshold and the polynomial function diverge.

Chapter 9

Thermo-electric convection in a vertical fluid system on the Earth

The stability of a vertical stationary cylindrical annulus with a heated inner cylinder and with the combined effect of the radial electric gravity and of the Earth gravity is investigated. This study has been carried out in order to give information about the critical parameters and the nature of the critical modes in the framework of laboratory experiments or of parabolic flight campaigns. Indeed, parabolic flight experiments are performed to reach microgravity conditions in order to investigate the effect of a purely radial gravity field. But the duration of the low-gravity phase is small and the base flow provided by the previous gravity phase has to be taken into account.

9.1 Dimensionless control parameters

For this study, the Galileo number $\mathrm{Ga} = \sqrt{gd^3}/\nu$ has been introduced to fix the flow system in the axial gravity. The Grashof number can be written $\mathrm{Gr} = \gamma_a \mathrm{Ga}^2$ and only depends on the temperature difference between the two cylinders when Ga is fixed. The parameter $\delta = \gamma_a/\gamma_e$, which is a fluid property, is also introduced and thermally links the Archimedean and thermoelectric buoyancies. In this chapter, the dimensionless electric potential V_E will be preferred to the electric Rayleigh number L to keep independent parameters (both Gr and L depend on ΔT). These parameters will facilitate the physical interpretation of the results and the comparison to the experimental results obtained from laboratory and parabolic flight experiments.

9.2 Thermal convection in a stationary annulus due to the Archimedean buoyancy

In the absence of electric field, the Prandtl number has an important influence on the flow stability. Indeed, for low Prandtl number, the critical parameters are independent of the value of the Prandtl number. This mode is commonly called hydrodynamic mode (HM). But beyond a certain value of Pr, the critical Grashof number decreases with Pr and tends to a constant which is nearly independent of the radius ratio. This mode is commonly called thermal mode (TM). These two modes are axisymmetric and oscillatory and differ by there origins [28]. The wavenumber and the frequency of vortices undergo a discontinuity at the codimension-2 point between HM and TM and then increase with increasing the Prandtl number. The HM take their origin in the shear produced by the base axial flow while TM are related to the Archimedes' buoyancy mechanism.

For low values of the radius ratio and of the Prandtl number, the critical modes can also be oscillatory non-axisymmetric. Figure 9.1 obtained for Pr = 0.72 shows that from $\eta = 0$ to $\eta = 0.44$, critical modes are helical with the azimuthal mode number $n_c = 1$. For small values of η, the threshold increases with increasing η, but beyond the value $\eta = 0.18$, the threshold decreases with increasing η. The frequency of non-axisymmetric modes decreases with η for small values of η, and from $\eta = 0.22$, the frequency increases with η. For axisymmetric modes, the frequency increases with η. The axial wavenumber of non-axisymmetric modes increases with the radius ratio. At the codimension-2 point between non-axisymmetric and axisymmetric modes, the frequency and the wavenumber undergo discontinuity.

9.3 Coupled effect of Archimedean and dielectrophoretic buoyancies

We remind that, in weightless environment, the thermoelectric buoyancy produces stationary helical modes called electric modes (EM). Hence, we are interested in the investigation of resulting modes when both the Archimedean and the dielectrophoretic buoyancies are acting on the fluid.

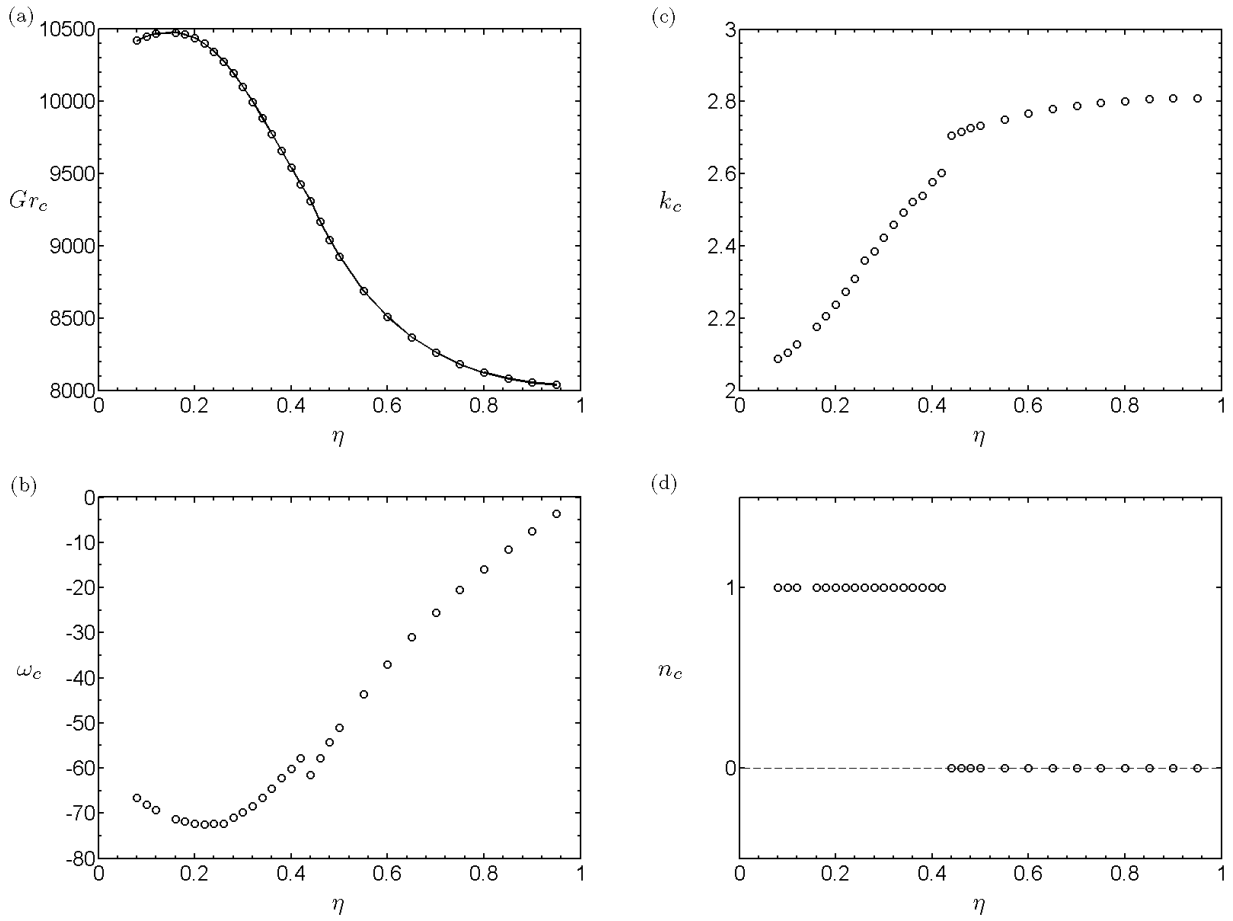

Figure 9.1: Variation of the critical parameters with η for Pr = 0.72 and $V_E = 0$: (a) Grashof number (b) frequency, (c) axial wavenumber and (d) azimuthal mode number.

9.3.1 Influence of the radius ratio

Figure 9.2 shows the variation of the critical parameters with V_E for Ga = 1370, Pr = 10, $\delta = 0.1$ and for different η. In the absence of electric potential, we recover the critical values for the classical thermal instability in a vertical cylindrical annulus. And when the Grashof number tends to zero, we obtain the critical parameters of the problem in microgravity condition. For weak electric potential, the stability threshold weakly decreases with increasing the electric potential (Fig. 9.2 - a). These critical modes are oscillatory (Fig. 9.2 - e) and axisymmetric (Fig. 9.2-c) for Pr = 10. In fact they correspond to TM. The axial and total wavenumber (Fig. 9.2 - b,d) are nearly independent from V_E. In this range of electric potential, for a fixed value of V_E, increasing the radius ratio will decrease the axial wavelength of vortices. The frequency of the critical modes is independent from V_E, but depends on η.

Over a certain value of V_E called V_E^*, the threshold strongly decreases with the electric potential. This regime is stationary and exhibits columnar vortices. Indeed, the azimuthal mode number is

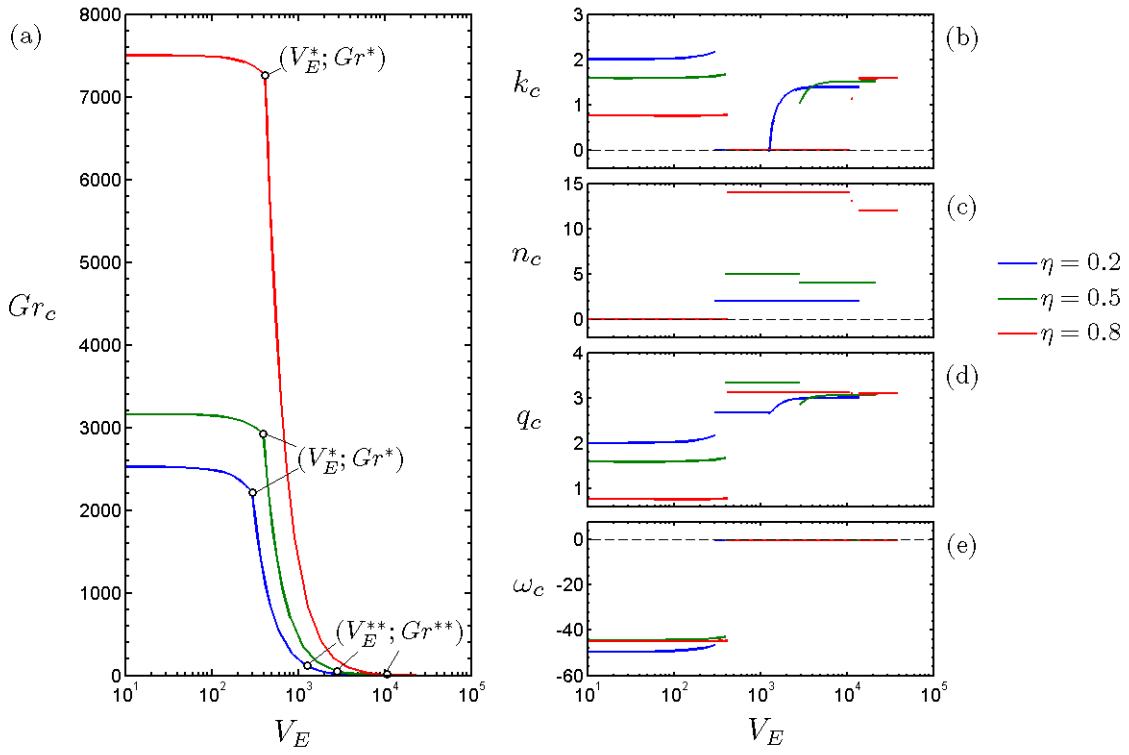

Figure 9.2: Variation of the critical parameters with V_E for $Pr = 10$, $Ga = 1370$, $\delta = 0.1$ and for different values of η: (a) Grashof number, (b) axial wavenumber, (c) azimuthal mode number, (d) total wavenumber and (e) frequency.

different from zero and depends on the radius ratio while the axial wavenumber is equal to zero.

For large values of V_E, there is another transition from the columnar regime to a steady non-axisymmetric mode at the codimension-2 point V_E^{**}, corresponding to the electric mode predicted by Yoshikawa et al. [33] Above V_E^{**}, k_c increases and tends to a constant. Depending on the radius ratio, n_c can gradually decrease from its value for the columnar regime to its value for the microgravity case which is equivalent to a so large applied electric potential that the thermoelectric buoyancy is the dominant mechanism for inducing instabilities. Note that for $\eta = 0.2$, there is no change in n_c at the codimension-2 point V_E^{**}. For all these regimes, the curvature of the annulus has a destabilising effect.

9.3.2 Influence of the Prandtl number

Figures 9.3 shows the behaviours of the critical parameters with the dimensionless electric voltage for different values of Pr and with $\eta = 0.5$. We can see from figure (Fig. 9.3 - a) that, as expected, the thresholds for hydrodynamic or thermal modes depend on the Prandtl number, and the thresholds for electric modes are independent of Pr. However, the Prandtl number has

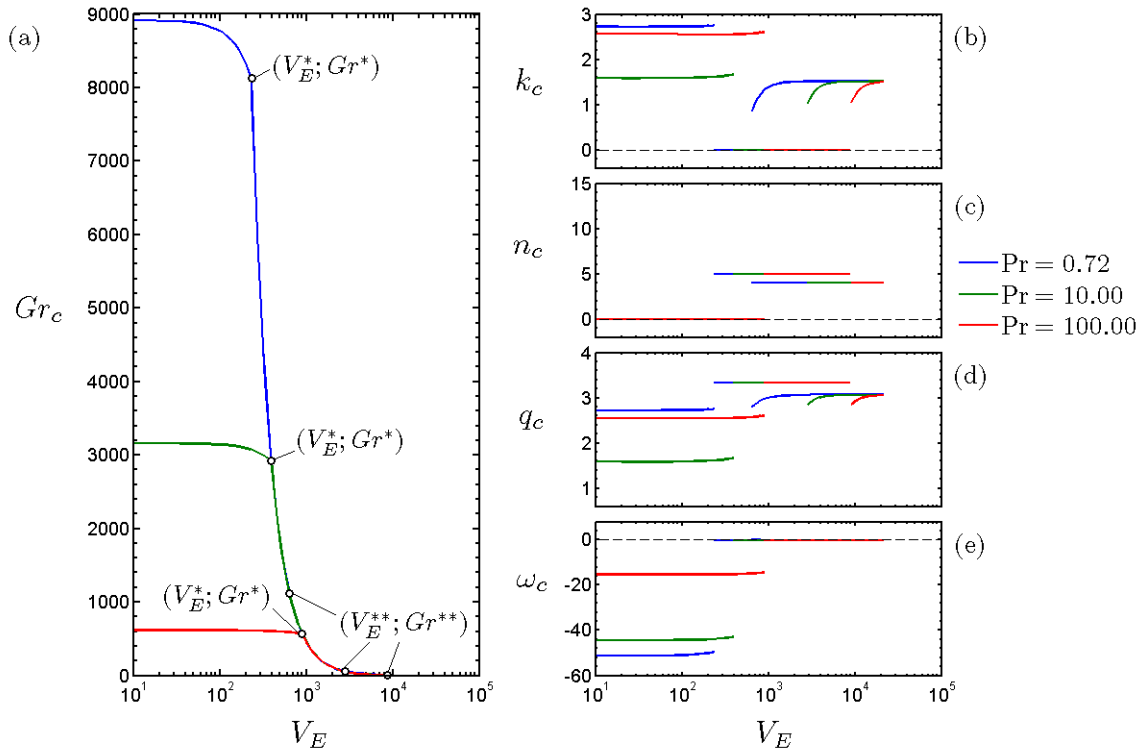

Figure 9.3: Variation of the critical parameters with V_E for $\eta = 0.5$, $Ga = 1370$, $\delta = 0.1$ and for different values of Pr: (a) Grashof number, (b) axial wavenumber, (c) azimuthal mode number, (d) total wavenumber and (e) frequency.

an influence on the position of the codimension-2 points (V_E^*, Gr^*) and $(V_E^{**}, \mathrm{Gr}^{**})$. The larger the Prandtl number, the lower the critical Grashof number at the codimension-2 points. The axial and total wavenumber (Fig. 9.3 - b,c) depend on Pr for hydrodynamic or thermal modes. For column vortices, the azimuthal wavenumber q_c is a constant and we can see the shift of the codimension-2 points depending on the value of Pr. For electric modes, the wavenumber increases until its value encountered in weightlessness which does not depend on Pr. The critical frequency depends on Pr for thermal modes.

9.3.3 Influence of the ratio of the two thermal expansion coefficients

The ratio between the thermal expansion parameter and the thermoelectric parameter $\delta = \alpha/e$ is a fluid property and it influence on the critical parameter is investigated (Fig. 9.4). Using the electric Rayleigh number instead of the dimensionless electric voltage makes the critical parameters independent on δ. If the critical parameters were plotted against V_E, we would have seen a shift of all the parameters to larger values of V_E for lower values of δ, and inversely. This fluid property may have an impact on the time needed for convection cells to be established. It could also affect

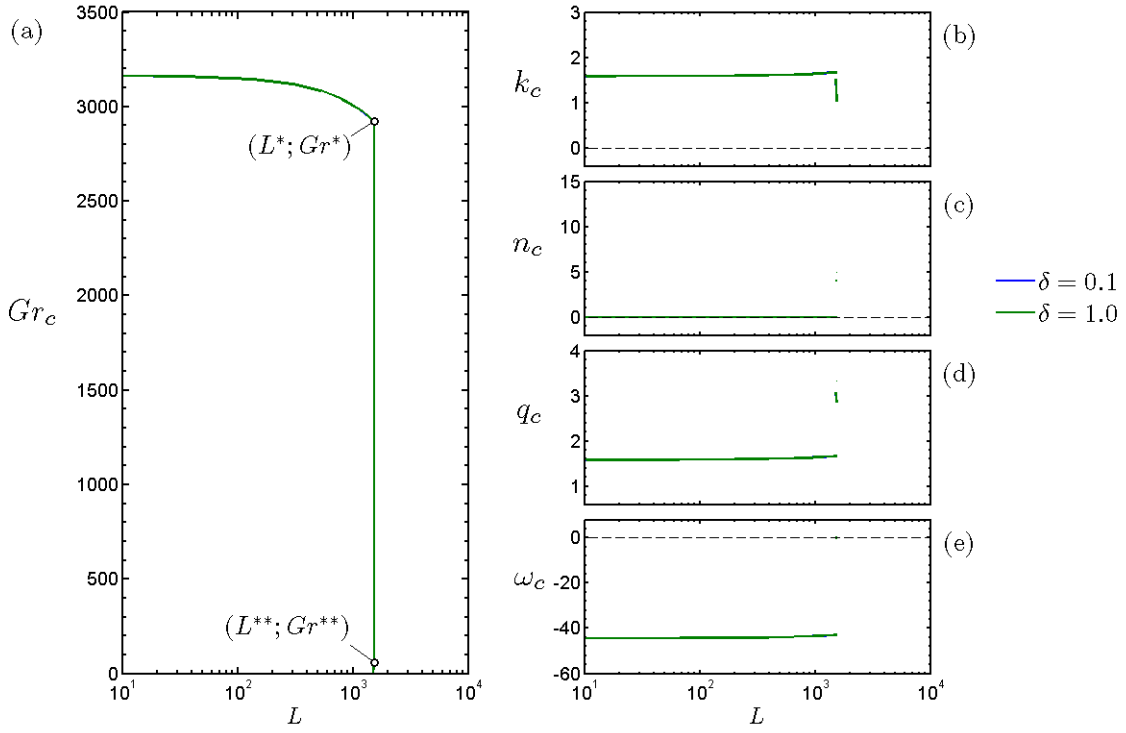

Figure 9.4: Variation of the critical parameters with the electric Rayleigh number for Ga = 1370, $\eta = 0.5$, Pr = 10 and for different δ: (a) Grashof number, (b) axial wavenumber, (c) azimuthal mode number, (d) total wavenumber and (e) frequency.

the non-linear behaviour of the system, but it plays no role on its stability.

9.3.4 Eigenfunctions

Figure 9.5 shows the perturbation temperature and the perturbation velocity fields of the four different flow regimes found in this problem. The hydrodynamic mode (Fig. 9.5 - a) have a larger axial wavenumber than the thermal mode (Fig. 9.5 - b). In both modes, the base axial flow twists the vortices by pushing them upward near the hot wall and downward near the cold one. These vortices propagate upward. The columnar modes (Fig. 9.5 - c) are similar to those observed in the cylindrical annulus in solid body rotation under microgravity conditions (Chapter 6, 8) except that they are stationary. The helical modes (Fig. 9.5 - d) are the electric modes encountered in convections only induced by the thermoelectric buoyancy (Chapter 7).

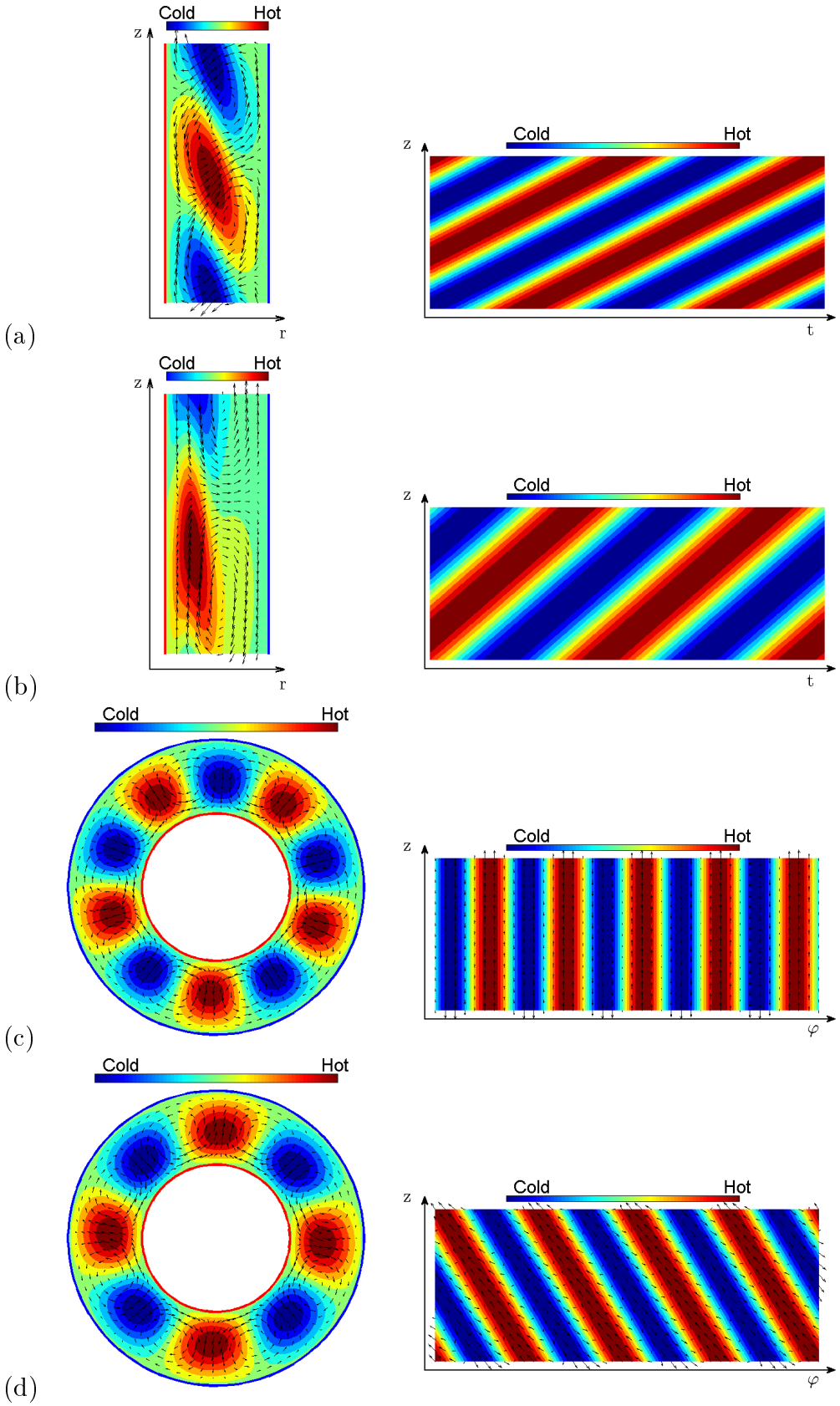

Figure 9.5: Temperature and velocity fields at the critical condition for Ga = 1370, $\delta = 0.1$, $\eta = 0.5$ and for (a) a hydrodynamic mode (Pr = 0.72, $V_{E,c} = 200$, $\mathrm{Gr}_c = 8342$, $k_c = 2.747$ and $n_c = 0$), (b) a thermal mode (Pr = 10, $V_{E,c} = 113$, $\mathrm{Gr}_c = 3150$, $k_c = 1.604$ and $n_c = 0$), (c) a stationary columnar mode (Pr = 10, $V_{E,c} = 512$, $\mathrm{Gr}_c = 1760$, $k_c = 0$ and $n_c = 5$) and (d) a stationary helical mode (Pr = 10, $V_{E,c} = 4780$, $\mathrm{Gr}_c = 20$, $k_c = 1.674$ and $n_c = 4$).

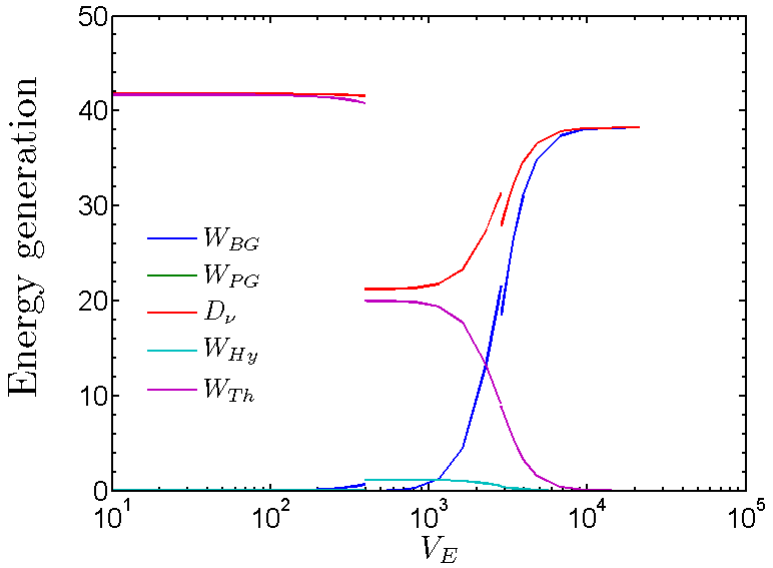

Figure 9.6: Variation of the energy generation terms with the dimensionless electric potential V_E. These curves has been obtain for $Ga = 1370$, $\delta = 0.1$, $Pr = 10$ and $\eta = 0.5$.

9.4 Energy analysis

For this situation, the energy transfer from the base state to the perturbations is gouverned by the equation:

$$\frac{dK}{dt} = W_{Hy} + W_{Th} + W_{BG} + W_{PG} - D_\nu = 0 \tag{9.1}$$

The figure 9.6 shows the behaviours of the different power terms with the variation of V_E. For low values of V_E, for the considered Prandtl number and radius ratio, the critical modes are thermal modes, and the term W_{Th} is the dominant one. For large values of V_E, the power W_{BG} is the main contribution to the energy transfer from the base state to perturbations. In the intermediate case, i.e. for columnar modes, both W_{Th} and W_{BG} are important. In an order of magnitude lower, W_{Hy} also contributes to the energy transfer. In the hole diagram, the power input by the perturbation electric gravity W_{PG} is negligible compared to the other terms.

9.5 Conclusion

The effect of the natural convection on the thermoelectric buoyancy in a cylindrical annulus has been studied. Indeed the prediction of the threshold and of the spatial and temporal behaviour of the unstable state is important in the framework of laboratory experiments and experiments in parabolic flight campaigns, where the effect of the Earth gravity cannot be neglected. In the

absence of electric potential, the critical modes are oscillatory axisymmetric, and can have two different origins: the shear produced by the base state (hydrodynamic mode), or the Archimedean buoyancy (thermal mode). Under weightlessness, the critical modes are steady helical (electric mode). When both axial and radial gravity are active, stationary columnar modes become critical. These modes have a threshold which is strongly dependant on the electric potential. There columnar nature are not very well understand, but the energy analysis showed that the effect of the thermoelectric buoyancy and of the Archimedean buoyancy are coupled for these modes.

Chapter 10

General conclusions and outlook

The effect of the centrifugal buoyancy and of the thermoelectric buoyancy on a dielectric fluid confined in a cylindrical annulus has been investigated by a linear stability theory and through some numerical simulations. These two buoyancies are radially oriented and are of most interest for astrophysical and geophysical applications, as well as for technical applications.

The effect of the centrifugal buoyancy has been studied for different rotation regimes of the cylinders under weightlessness. These regimes can be cast in two categories: Rayleigh unstable regimes which can sustain instabilities in the isothermal case, and Rayleigh stable regimes which cannot. For the Rayleigh unstable regime, the case where the outer cylinder is at rest has been chosen for its simplicity and its large amount of possible applications. We found an antisymmetric effect of the centrifugal buoyancy with respect to the direction of the temperature gradient. Indeed, the centrifugal buoyancy destabilises the flow in inward heating and stabilises it in outward heating. Critical modes are axisymmetric and may be oscillatory in outward heating, due to the stable stratification of the density regarding the centrifugal acceleration. For the Rayleigh stable flow systems, the regime where the inner cylinder is at rest and the Keplerian regime were investigated. These regimes become unstable to axisymmetric perturbations in the case of inward heating. For large values of Pr, the critical modes are stationary while for low values of Pr and in the case of small gap systems, critical modes are oscillatory. The parameter $\gamma_a \mathrm{Pr}$ is an important parameter for studying the centrifugal buoyancy in Rayleigh stable flows, in agreement with results from short-wavelength approximation. The solid body rotation regime is also Rayleigh stable and is particular in the sense that it brings no azimuthal shear stress in the laminar flow. Therefore this system is an analogue of the Rayleigh-Bénard system when the outer cylinder is heated. The

centrifugal Rayleigh number is the important parameter for studying thermal convection since the only mechanism is the centrifugal buoyancy. The critical convective flow takes the form of oscillatory columnar vortices, except for large values of γ_aPr and low radius ratios, where critical modes can be oscillatory helical ones. The oscillation of the columnar modes may be related to the effect of the Coriolis buoyancy.

The effect of the dielectrophoretic force has been investigated in two different systems: the rigidly rotating cylindrical annulus system, and the vertical stationary cylindrical annulus considering the Archimedean buoyancy in the axial direction. For the solid body rotation regime, the centrifugal, and thermoelectric buoyancies plays antagonist roles. Therefore, it was important to separate the case of inward and outward heating since the respective effects of the two buoyancies are not symmetric. In inward heating, the thermoelectric buoyancy increases the threshold of the occurrence of thermal convection induced by the centrifugal buoyancy. Critical modes are then always oscillatory columns. In outward heating, the centrifugal buoyancy increases the threshold of the occurrence of thermal convection induced by the thermoelectric buoyancy. For low rotation rates, critical modes are electrical and appear in form of oscillatory helical modes. At a certain value of the Coriolis number, the critical modes become oscillatory columnar ones. The Coriolis number at the codimension-2 point does not depend on the diffusive properties of the fluid, neither on the imposed temperature difference between the two cylinders.

In the case of a vertical cylindrical annulus with Earth gravity, four different regimes can be critical. For low applied electric tension, critical modes are oscillatory axisymmetric either thermal or hydrodynamic, depending on the Prandtl number and on the radius ratio. For large applied electric tension, critical modes are stationary helical, which indicate there electric nature. For moderate applied electric tension, stationary columnar modes have been predicted to be critical. This is due to the superposition of the vertical Earth gravity and of the radial electric gravity which gives a certain angle of the resulting gravity in the (r, z) plane. Depending on the value of this angle, critical modes may be either columnar or helical vortices.

Experiments on the effect of the thermoelectric convection on a stationary cylindrical annulus have been performed in laboratory, as well as during parabolic flight. Some of these results are in Appendix A. This work has been done in collaboration with the Technical University of Brandenbourg, and more details on these experiment will be provided in the thesis of Marcel Joungmanns. More experiments with improved measurement techniques are necessary to make

the comparison between theoretical, numerical and experimental results possible. In particular, the shadowgraph measurement technique performed in the axial direction of containment seems to be suitable for the determination of the convective flow structure. In that sense, simulation of this technique has been performed with a simple model (Appendix A). A more accurate model could provide quantitative results and should be done in the future.

Appendix A

Experiments and simulation of shadowgraph method

The laboratory experiments have been carried in the Department of Aerodynamics and Fluid Mechanics, in Cottbus (Germany), and the parabolic flight experiments took place in the Bordeaux Airport in the premises of Novespace which is a subsidiary company of the CNES (Centre National d'Etudes Spatiales). Two parabolic flight campaigns (PFC) have been performed in October 2015 and in October 2016. In 2015, the experiment consisted of two identical cells, in different orientations, and filled with the same working fluid. One experiment cell was horizontal and the other one was vertical oriented with respect to the direction of the Earth gravity. To visualise the density variation inside the gap, a shadowgraph method was used in the axial direction. In 2016, two different working fluids were considered in two identical vertical cells. During this second PFC, shorter cells were used in order to use the BOS (Background Oriented Schlieren) method to visualise the density variations.

Usually, shadowgraph and Schlieren techniques are used to visualise the density profile within a thin layer of liquid, which allows to consider that the density is invariant in the direction of observation. In our cases, the observation is done in the axial direction, along the height of the cylinders. It is therefore not possible to get information about the axial structure of the vortices. Thus, the shadowgraph method is numerically simulated using simple profile of unstable flows to have a better understanding of the experimental shadowgraph picture.

In this work, we will focus on results obtained for the vertical cells with the density variations captured by the shadowgraph method. And to make comparisons between the experimental results

and the linear stability analysis possible, the largest cells have to be considered. Indeed, for small cells, the end effect due to the finite height of the cylinders will have too much impact on the flow stability.

A.1 Experimental setup

The experiment cell consists of two concentric cylinders. The radius of the inner cylinder is $R_1 = 5.1$ mm and that of the outer one is $R_2 = 10.2$ mm which gives a gap size of $d = 5.1$ mm and a radius ratio of $\eta = 0.5$. The length of the two cylinders is $L = 100$ mm which gives an aspect ratio of $\Gamma = L/d = 19.6$. The properties of the working fluid (silicone oil Wacker AK5) inside the cylindrical annulus are given in Table A.1. The viscous diffusion time is $\tau_\nu = 5.2$ s and the thermal diffusion time is $\tau_\kappa = \mathrm{Pr}\tau_\nu = 336$ s.

The inner cylinder is made of aluminium oxide (Al_2O_3) and coated with Titanium Nitride (TiN) to create a conductive layer. The applied alternative peak voltage $V_{peak} = \sqrt{2}V_0$ has a frequency of 200 Hz corresponding to a period of $T = 5 \times 10^{-3}$ s that is very small compared to τ_ν and τ_κ. This is in agreement with the assumption made in the linear stability analysis, which states that the alternative electric tension can be replaced by its effective potential when the electric field period is small enough compared to the characteristic times of the fluid flow. To heat the inner cylinder, two different methods were used: for the PFC 2015, a heating cartridge with a temperature sensor was located inside the inner cylinder, while the PFC 2016 and for laboratory experiments, a heating fluid loop was used with AK5 used as cooling fluid. The outer cylinder, made of Aluminum (AlMgSi0.5) is connected to ground potential and is cooled by a cooling fluid loop, which also uses AK5. The thermal conductivity of silicone oil AK5 is lower than that of water, but during the experiments, it happened that some fluid from the heating or cooling loop came inside the cylindrical annulus, and we had to ensure that this would not compromise the results or the non-electrical conductivity of the working fluid. Indeed we had to ensure that there

Table A.1: Properties of silicone oil AK5: $\varepsilon_r = \varepsilon_2/\varepsilon_0$ is the relative electric permittivity, where ε_0 is the permittivity of the vacuum. Properties data are given by the manufacturer and have uncertainties e.g. 10% for the kinematic viscosity.

$\nu(10^{-6}m^2/s)$	$\rho(kg/m^3)$	$\alpha(10^{-3}K^{-1})$	ϵ_r	$e(10^{-3}K^{-1})$	Pr	α/e
5.0	920	1.08	2.70	1.07	64.6	1.01

would be no breakdowns, and silicone oil has very high breakdown values. The top and bottom lids are made of polymethylmethacrylate (PMMA) to ensure thermal and electrical insulation. Since the inner cylinder is thin (1.85 mm) and has a high thermal conductivity, we considered that the temperature measured by the heating cartridge, or by the thermo-couples which measure the temperature of the heating fluid loop, corresponds to the temperature of the inner cylinder. With this heating and cooling system it is possible to generate a temperature difference between the inner and outer cylinder of up to $12K$.

A.2 Parabolic flight campaign

Parabolic flight is an easy way to obtain a microgravity condition. Moreover, it gives the opportunity to investigate the fluid behaviour in three different gravity conditions. Indeed, the plane initially stays at a constant altitude and leads to a vertical gravity intensity of $1g$ which is the natural gravity of the Earth .

After about a minute, the plane increases its speed upward to give a hyper-gravity phase (Fig. A.1). During this 20 seconds phase, the vertical gravity intensity is $1.8g$. At the end of this phase, the plane nose is about 45^o to the horizon and the engines are cut back. The plane follows a parabolic trajectory to induce the microgravity phase which lasts about 22 seconds. A second hyper-gravity phase is obtained when the downward velocity of the plane is decreased to recover the first natural gravity phase. There exist several other ways to reach the microgravity condition (i.e. drop tower or suborbital Rocket Flight), but the main advantage of the parabolic flight is the good balance between the duration of the microgravity phase, the quite large allowable size of the experiment module, and the opportunity for investigators to be onboard the aircraft during the flight.

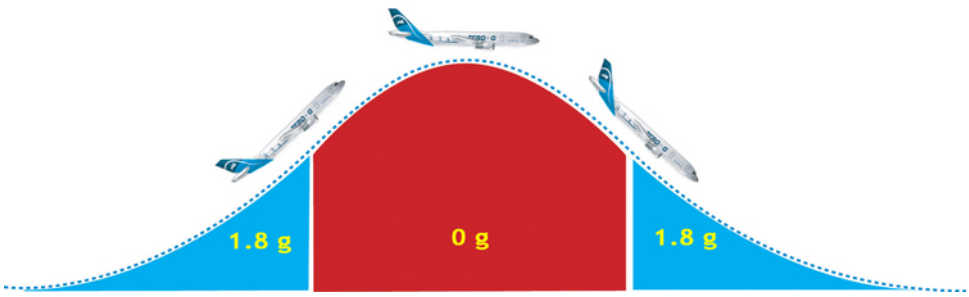

Figure A.1: Sketch showing the different gravity phases encountered during one parabola. Courtesy of Novespace.

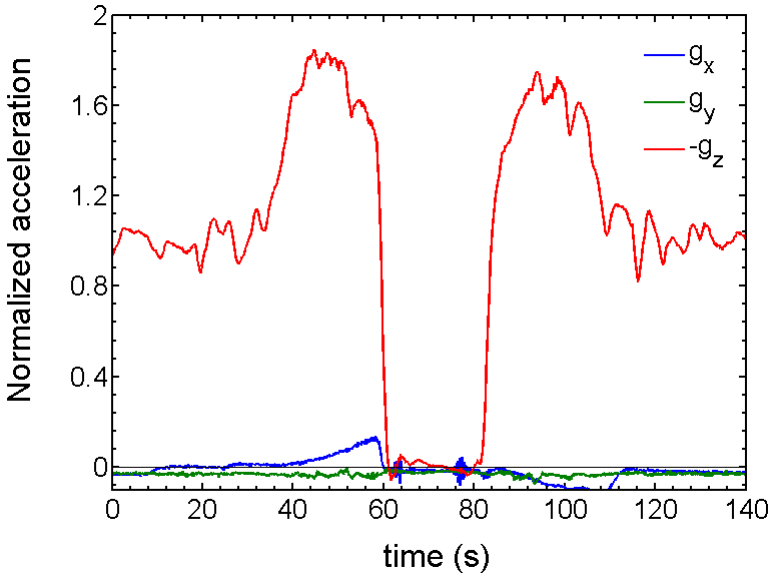

Figure A.2: Time variation of the different components of the acceleration during a parabolic flight. The acceleration values are normalized by the earth gravity intensity.

Figure A.2 shows the intensity of the different components of the acceleration during a parabola. The quality of the microgravity phase is about $10^{-2}g$ which is largely sufficient for the assumption of a purely radial gravity in the experiment when the electric field is applied.

Figure A.3: Participants of the parabolic flight campaign of October 2016 in front of the ZERO G aircraft. From the left to the right: R. Stöbel, V. Ruoff, M. Jongmanns, M. Meier, A. Meyer, I. Mutabazi, C. Egbers.

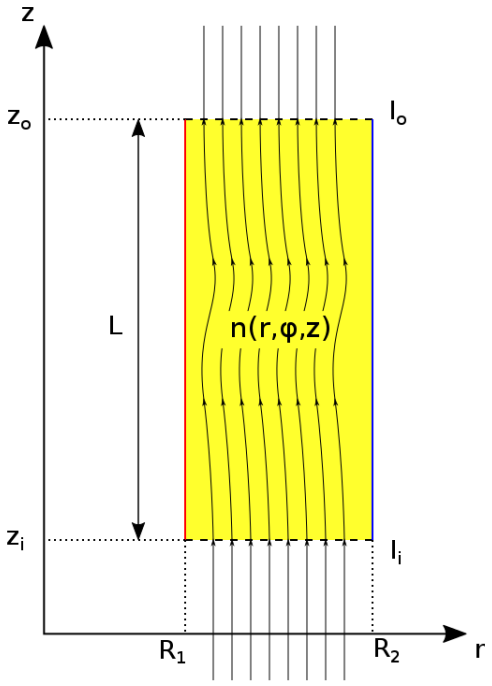

Figure A.4: Schematic representation of the light beam trajectories inside the cells. The light beams are refracted due to the inhomogeneity of the fluid optical index n_f which is a function of the temperature.

A.3 The shadowgraph method

The shadowgraph method is a common technique to visualise the density variation in a fluid. In supersonic fluid flows, the density field can be reconstructed using this method which can be combined with other techniques such as BOS or interferometry [58]. The shadowgraph method is also widely used in the process of solidification to observe flows due to buoyancies [59] or to measure the solutal density during the growing process [60].

A.3.1 Principle

The cell is illuminated from the bottom by a LED with homogeneous light intensity profile $I_i(r, \varphi, z_i)$ and telecentric lighting obtained using light control films. The light goes through the liquid in the cell and is refracted because of density gradients which are produced by the base temperature profile and the perturbation temperatures generated by the onset of instabilities. At the outlet of the working fluid, the initially homogeneous light intensity exhibits a new profile $I_o(r, \varphi, z_o)$ which depends on the 3-dimensional profile of the fluid optical index n_f (see Fig. A.4). A camera focused on the top of the cell captures the light intensity profile.

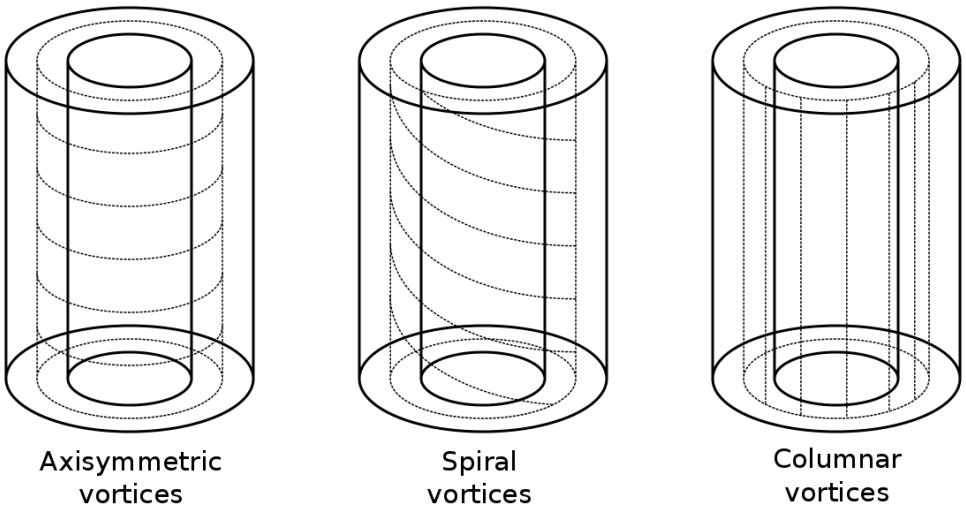

Figure A.5: Schematic representation of the different instability modes that can appear in a cylindrical gap.

A.3.2 Theoretical modeling

A fluid confined between two coaxial vertical cylinders is considered. The height of these cylinders is L and the top and bottom horizontal lids are assumed to be thermally insulating. In weightless environment, the base temperature only depends on the radial coordinate, while in the Earth's gravity field, the top and bottom lids induce thermal boundary layers which make the base temperature also depend on the axial position. In addition, the consideration of a radial gravity field can affect the flow stability, as in the Rayleigh-Bénard problem. If the temperature difference between the two cylinders exceeds a critical value, counter-rotating vortices occur with spacial periodicity, resulting in a temperature profile with the same periodicity. The shape of these modes can differ depending on the nature and the direction of the total gravity field. In general, one can observe axisymmetric vortices [28], helical vortices [33] or columnar vortices [61] (Fig. A.5).

The cylindrical gap is illuminated from the bottom plate with a telecentric light in the direction parallel to the cylinders common axis. The refractive index of the fluid n_f is proportional to the temperature which can be a general function of all three spatial cylindrical coordinates (r, φ, z). The light beams are refracted inside the gap while following Fermat's principal which states that the length of the optical light path in the system has to be minimum. When parametrizing the

light path by z, the Fermat's condition can be written:

$$\partial \left(\int_{z_i}^{z_o} n_f(r,\varphi,z) \sqrt{r'^2 + (r\varphi')^2 + 1}\, dz \right) = 0 \tag{A.1}$$

where $r' = dr/dz$ and $\varphi' = d\varphi/dz$. z_i and z_o are the axial position of the bottom and the top lids, respectively. To verify Fermat's principle (A.1), the function $f = n_f(r'^2 + (r\varphi')^2 + 1)^{1/2}$ must satisfy the Euler-Lagrange equation for both the radial and azimuthal directions. Developing the two Euler-Lagrange equations using the function f leads to:

$$r'' = \frac{1}{n_f} \left[\left(r'^2 + (r\varphi')^2 + 1 \right) \frac{\partial n_f}{\partial r} + n_f r \varphi'^2 - r' \frac{\partial n_f}{\partial z} \right] \tag{A.2a}$$

$$\varphi'' = \frac{1}{n_f} \left[\frac{\left(r'^2 + (r\varphi')^2 + 1 \right)}{r^2} \frac{\partial n_f}{\partial \varphi} - \frac{2 n_f r' \varphi'}{r} - \varphi' \frac{\partial n_f}{\partial z} \right] \tag{A.2b}$$

To obtain this set of equations, the terms in third order of r',r'',φ' and φ'' have been neglected. The problem is discretized by dividing the height into P steps of length Dz. Eqs. (A.2) read in the discrete, explicit form:

$${r'}_{k+1} = {r'}_k + \frac{Dz}{n_{f,k}} \left[\left(1 + {r'}_k^2 + ({r}_k {\varphi'}_k)^2 \right) \left. \frac{\partial n_f}{\partial r} \right|_k + r_k {\varphi'}_k^2 n_{f,k} - {r'}_k \left. \frac{\partial n_f}{\partial z} \right|_k \right] \tag{A.3a}$$

$${\varphi'}_{k+1} = {\varphi'}_k + \frac{Dz}{n_{f,k}} \left[\frac{\left(1 + {r'}_k^2 + ({r}_k {\phi'}_k)^2 \right)}{r^2} \left. \frac{\partial n_f}{\partial r} \right|_k + \frac{2 {r'}_k {\varphi'}_k n_{f,k}}{r_k} - {\varphi'}_k \left. \frac{\partial n_f}{\partial z} \right|_k \right] \tag{A.3b}$$

$$r_{k+1} = r_k + Dz {r'}_{k+1} \tag{A.3c}$$

$$\varphi_{k+1} = \varphi_k + Dz {\varphi'}_{k+1} \tag{A.3d}$$

where $k = (0, 1, 2, \cdots, P)$. A centred second-order approximation is used for the second derivatives, with a first-order explicit approximation for the non linear terms [62]. For each light beam, the initial position and angle with respect to the z axis has to be defined. At the height $z = z_i$, we have:

$$r_{k=0} = r_i \ ; \ \varphi_{k=0} = \varphi_i \ ; \ {r'}_{k=0} = {\varphi'}_{k=0} = 0 \tag{A.4}$$

which corresponds to telecentric illumination parallel to the axial direction. The choice of $r_{k=0}$ and $\varphi_{k=0}$ for all the light rays has to verify a homogeneous light intensity profile at $z = z_i$. The inlet positions of the light beams have thus been defined in the Cartesian coordinate system, and then transformed into their corresponding polar coordinates. Due to refraction of the light

when passing through the gap, the intensity distribution may change depending on the height. To measure this quantity, the top surface at $z = z_o$ is divided into small square cells. The relative intensity I is computed by dividing the number of light beams which hit each cells by the one for the case of homogeneous refractive index. Thus we have $I = 1$ if there is no local change in light intensity between the top and the bottom surfaces, and we have $I > 0$ ($I < 0$) if the local density of light at $z = z_o$ is higher (lower) than the density of light at the same location at $z = z_i$.

The refractive index of a fluid is proportional to the density of the fluid. For a small temperature difference between the two cylinders, the dependency of the density with the temperature can be considered as linear. The refractive index is then modelled by:

$$n_f(r, \varphi, z) = n_{f,0} \left(1 + \frac{1}{n_{f,0}} \frac{dn_f}{dT} \theta(r, \varphi, z) \right) \tag{A.5}$$

where $\theta = T - T_2$ is the temperature deviation from the reference temperature T_2 and where $n_{f,0} = n_f(T_2)$. The derivative dn/dT is negative and can be set as constant. For silicon oils, its value is $dn/dT = -3.8 \times 10^{-4} K^{-1}$.

A.3.3 Weightless environment

In weightlessness, the gravity field is radially oriented, the base state is then purely conductive and is only dependant on the radial position. It is thus possible to model the complete temperature profile using a simple analytic function. Using the simplest model for the thermal instability modes, the temperature can be defined by:

$$\theta(r, \varphi, z) = \Theta(r) + \tilde{\theta}(r, \varphi, z) \tag{A.6}$$

where Θ is the base temperature defined in Eq. (2.19), and where $\tilde{\theta}$ is the temperature for the instability mode and is given by:

$$\tilde{\theta}(r, \varphi, z) = T_{amp} \sin \left(\frac{\pi(r - R_1)}{d} \right) \cos \left(\frac{2\pi p z}{L} + n\varphi \right) \tag{A.7}$$

where T_{amp} is the amplitude of the perturbation temperature. p and n are the number of modes in the axial and azimuthal direction respectively.

As a first step, we can pay attention to temperature profiles which are axisymmetric, i.e. the

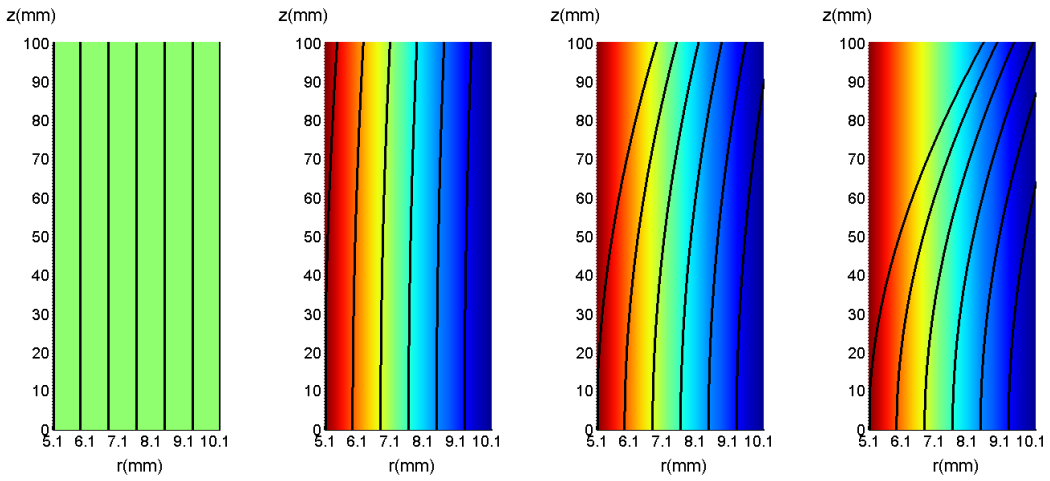

Figure A.6: Temperature profile (color) and trajectories of a selection of light beams (black) in the (r, z) plan for different ΔT.

base temperature profile without instability modes or with axisymmetric modes ($n = 0; p \neq 0$). For symmetry reason, the light beams trajectories for these regimes are confined in the $(r; z)$ plan. Therefore, the equation system (A.3) can be reduced to the system (A.3a , A.3c), with $\varphi' = 0$ and using the initial condition concerned by the radial position and angle with respect to z. Fig. A.6 shows in the (r, z) plane the temperature profile and the light beam trajectories for the stable state for different ΔT. In the isothermal case, the light rays stay parallel to the vertical axis. But when a temperature difference is applied between the two cylinders, the light rays are deviated in the direction of lower temperature, i.e. larger density. Moreover, the larger the temperature difference, the larger the deviation.

To compute the relative intensity as function of the radial position, the top is divided into one dimensional cells of size 0.2 mm and the number of light beams is 5000. Fig. A.7 shows the relative intensity as function of the radial position for different ΔT. The radial deviation of the light rays brings about an area around the inner cylinder where $I = 0$. Indeed, a light beam initially located at the inner cylinder reaches the top surface at the position $r^* > R_1$. The radial position r^* increases with ΔT. The intensity for $r > r^*$ is larger than unity and decreases with r. The maximum value of the intensity increases with the temperature difference between the two cylinders.

Axisymmetric modes are characterized by there amplitude and there wavelength. It is possible to focus on the effect of these kind of modes by setting the temperature difference between the two cylinder at $\Delta T = 0$ K. But this case has no physical meaning since there can not be thermal

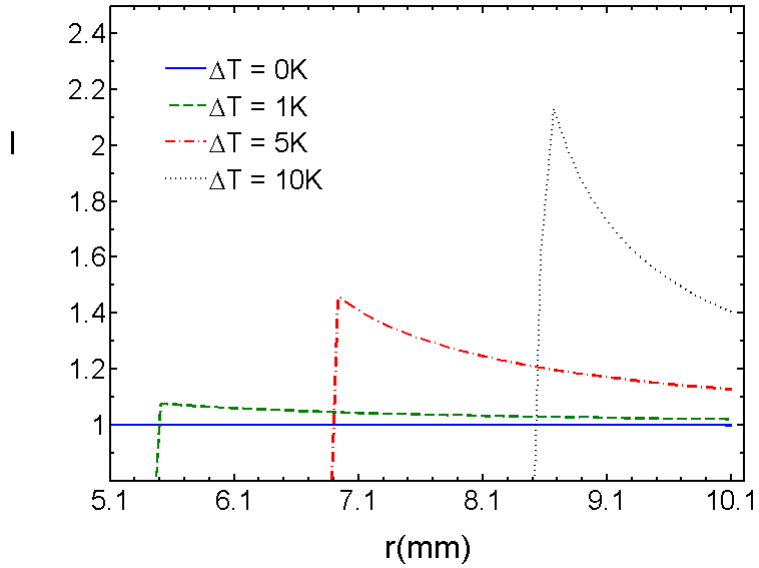

Figure A.7: Relative intensity as function of the radial position for stable states.

instability in the isothermal case. Fig. A.8 - a shows the influence of the number of waves on the relative intensity at the mid-gap I_0 for the special case of $\Delta T = 0$ K. When $p = 0$, the model chosen for temperature perturbations leads to the presence of a hot temperature cell with an infinite wavelength. Therefore the resulting intensity is always minimum for this case. The relative intensity at the mid-gap increases with p and reach $I_0 = 1$ when $p = 1$. Then I_0 undergoes modulations so that it is equal to unity when p takes an integer value, and it is below unity in between two integer values. Indeed, when p takes integer values, there is a complete balance between the hot perturbation temperature cells, which make the light beams diverge, and the cold ones, which make the light beams converge. Finally, a light beam returns to its initial radial position when p is an integer. Otherwise, if p is not an integer, there is always a part of a hot cell which is not balanced with a cold one, and thus brings about a divergence of the light beams which decreases the intensity. Increasing the amplitude of the perturbation temperature increases the amplitude of the modulations of intensity, but these modulations vanish for sufficiently large wavenumbers so that p has no more influence on the intensity. Fig. A.8 - b shows the relative intensity profile for different ΔT and T_{amp} when $p = 10$ which corresponds to the closest integer value of p that satisfies $\lambda_z/2 = d$. There is no differences between the shadowgraph image for the base temperature profile and the one for the perturbed temperature profile.

To focus on the effect of non-axisymmetric modes, it is possible to consider a radially homogeneous temperature profile. By doing that, the equation system (A.3) can be reduced to the system

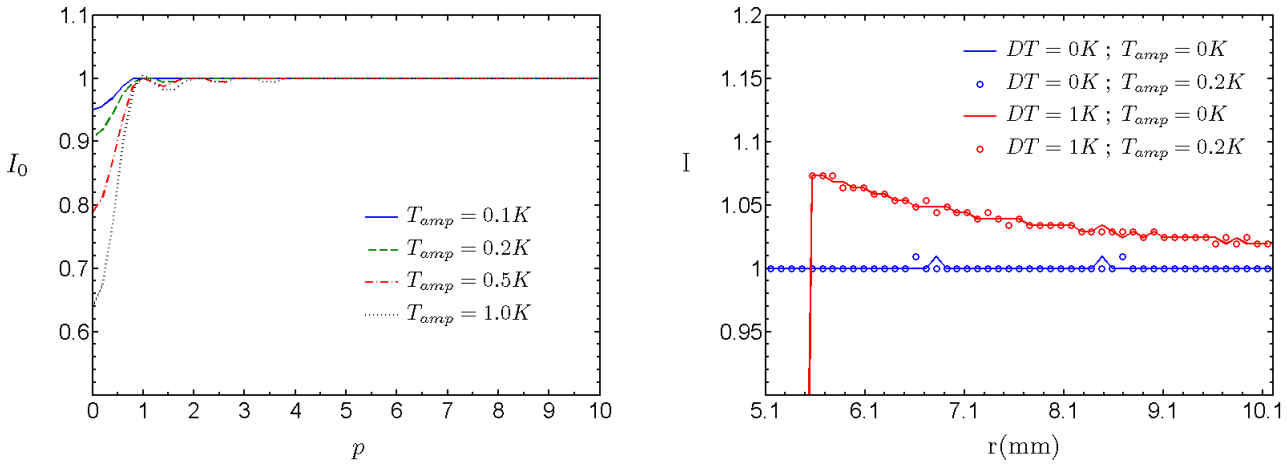

(a) (b)

Figure A.8: (a): relative intensity as function of the radial position for different ΔT and T_{amp} with $p = 10$ and (b): relative intensity at the mid-gap as function of the axial modes number for different T_{amp}.

(A.3b , A.3d), with $r' = 0$. The radial position is thus axially invariant and is chosen at the median surface between the two cylinders, where the radial derivative of the perturbation temperature is effectively equal to zero. To compute the relative light intensity profile in the azimuthal direction, the azimuthal angle at the top plate is divided into 60 parts equally sized. At the mid-gap, this corresponds to cells of length $r_0 d\varphi = 0.8$ mm where r_0 is the radial position of the mid-gap and $d\varphi$ is the difference between two consecutive azimuthal angle.

The pairs of parameters (p, n) are now restricted to integer values in such a way that the total wavelength of the modes is the closest to the double of the gap wide. For a given axial mode number p, the azimuthal mode number n and the inclination angle of the modes with respect to the azimuthal direction Ψ are given by:

$$n = round\left[\frac{r_0\pi}{d}\sqrt{1-\left(\frac{2p}{\Gamma}\right)^2}\right] \quad ; \quad \Psi = \tan^{-1}\left(\frac{n\Gamma d}{2\pi p r_0}\right) \tag{A.8}$$

Fig. A.9 - a shows the relative light intensity with respect to the azimuthal angle for an axisymmetric mode $(n = 0; p = 10)$, a helical mode $(m = 4; p = 5)$ and a columnar mode $(m = 5; p = 0)$. The spiral modes with $n = 4$ has been observed both theoretically and numerically by Yoshikawa & al. [33] and by Travnikov & al. [43] in the case of a steady cylindrical annulus subjected to a radial dielectrophoretic force under microgravity conditions. As seen before, the axisymmetric modes has no influence on the resulting shadowgraph image. However for helical modes and

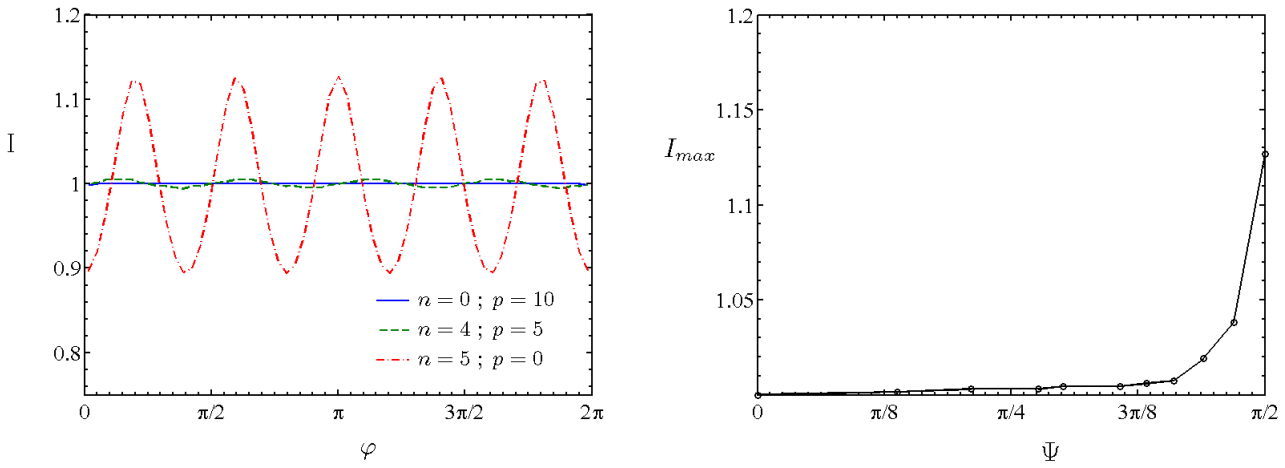

Figure A.9: (a): relative intensity as function of the azimuthal angle for different shape of modes with $T_{amp} = 0.2K$ and (b): maximum of the relative intensity at as function of the deviation angle of the modes with respect to the azimuthal direction with $T_{amp} = 0.2K$.

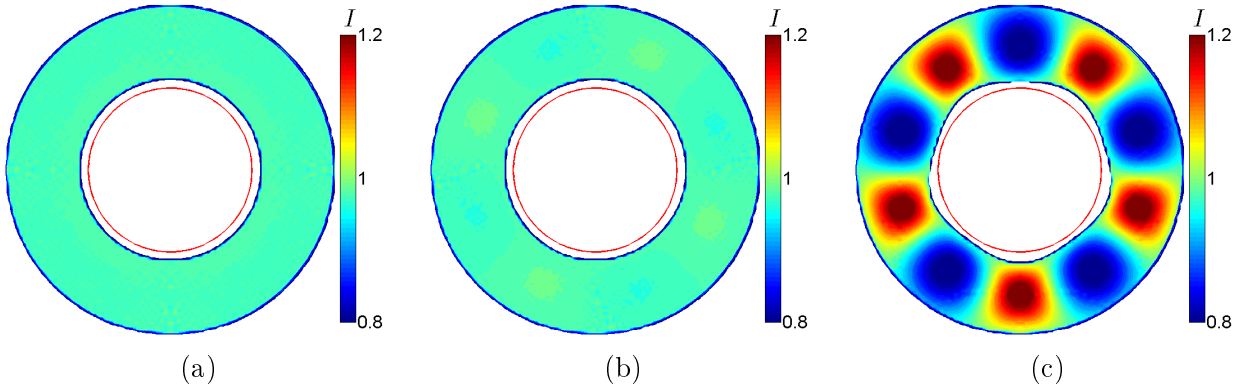

Figure A.10: Shadowgraph images for (a) axisymmetric mode ($m = 0; p = 10$), (b) spiral mode ($m = 4; p = 5$) and (c) collumnar mode ($m = 5; p = 0$) both for $DT = 1K$ and $T_{amp} = 0.2K$.

columnar modes, there is a modulation of the relative intensity with a number of modes equal to the one of perturbation temperature in the azimuthal direction. The amplitude of these modulations is small for spiral modes whereas it is much larger for columnar modes. Fig. A.9 - b shows the maximum value of the relative intensity profile with respect to the inclination angle of the modes for $T_{amp} = 0.2$ K. The modulation of the relative intensity become significant when the inclination angle of the modes approach the value $\Psi = \pi/2$.

Resolving the full set of equations (A.3) gives the simulated 2D shadowgraph image. Fig. A.10 shows these shadowgraph images for different expected instability modes, that is to say the axisymmetric mode (Fig. A.10 - a), the helical mode (Fig. A.10 - b) and the columnar mode (Fig.A.10 - c). The axisymmetric mode has no impact on the image. The shadowgraph images of the helical

and the columnar modes are plotted using the same color map. Columnar modes have a much larger impact on shadowgraph images than helical modes.

A.3.4 Earth gravity environment

On Earth, the gravity acts on the density gradient and leads to a large recirculation flow where the fluid flows upward near the hot cylinder and downward near the cold one. The top and bottom thermal boundary layers bring about an axial positive temperature gradient than can not be considered using a simple analytic function. Therefore, a two-dimensional steady numerical simulation is used to extract the base temperature profile in the (r, z) plane. The velocity field $\vec{u} = u\vec{e_r} + w\vec{e_z}$, the temperature deviation $\theta = T - T_2$ and the reduced pressure π are solved by the continuity equation, the Navier-Stokes equations and the energy equation in the polar coordinates.

$$\frac{u}{r} + \frac{\partial u}{\partial r} + \frac{\partial w}{\partial z} = 0 \tag{A.9a}$$

$$u\frac{\partial u}{\partial r} + w\frac{\partial u}{\partial z} + \frac{\partial \pi}{\partial r} - \nu\left(\frac{\partial^2 u}{\partial r^2} + \frac{1}{r}\frac{\partial u}{\partial r} + \frac{\partial^2 u}{\partial z^2} - \frac{u}{r^2}\right) = 0 \tag{A.9b}$$

$$u\frac{\partial w}{\partial r} + w\frac{\partial w}{\partial z} + \frac{\partial \pi}{\partial z} - \nu\left(\frac{\partial^2 w}{\partial r^2} + \frac{1}{r}\frac{\partial w}{\partial r} + \frac{\partial^2 w}{\partial z^2}\right) - \alpha\theta|g| = 0 \tag{A.9c}$$

$$u\frac{\partial \theta}{\partial r} + w\frac{\partial \theta}{\partial z} + \kappa\left(\frac{\partial^2 \theta}{\partial r^2} + \frac{1}{r}\frac{\partial \theta}{\partial r} + \frac{\partial^2 \theta}{\partial z^2}\right) = 0 \tag{A.9d}$$

The Boussinesq approximation has been adopted with taking the density as a linearly decreasing function of the temperature, i.e. $\rho = \rho_0(1 - \alpha\theta)$, which is valid if the temperature differences are small. The boundary conditions are no slip condition for the velocity, fixed temperature at the cylindrical surfaces and adiabatic condition at the top and bottom caps:

$$\begin{cases} u = 0 & w = 0 & \theta = \Delta T & \text{at } r = R_1 \\ u = 0 & w = 0 & \theta = 0 & \text{at } r = R_2 \\ u = 0 & w = 0 & \partial\theta/\partial z = 0 & \text{at } z = 0 \\ u = 0 & w = 0 & \partial\theta/\partial z = 0 & \text{at } z = L \end{cases} \tag{A.10}$$

A finite difference scheme is used to solve the problem, with a centred approximation for the first and second derivatives. The non-linear terms are computed by iterations until the Nusselt number measured at the outer cylinder tends to a constant. A non-homogeneous rectangular grid is used

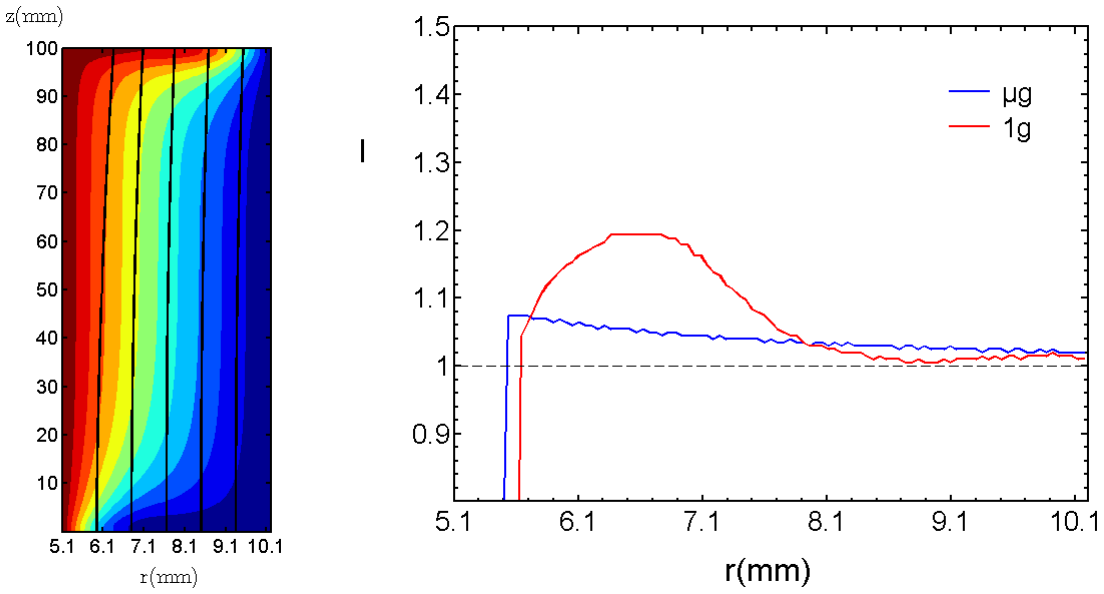

(a) (b)

Figure A.11: Results for the base flow of (a) temperature distribution and trajectories of some light beams shown by the black lines and (b) resulting 1D shadowgraph images. The temperature difference is $DT = 1K$

with thinner steps at the surfaces of the problem. The rectangular grid consists of 12 steps for the radial direction and 100 steps for the axial direction.

Fig. A.11 - a shows the temperature profile of the base state in the $(r; z)$ plane for $\Delta T = 1$ K and with an axial downward gravity field corresponding to the Earth gravity field. Thermal boundary layers involve at the top and bottom plates, leading to a hotter zone near the top and a cooler zone near the bottom with respect to the base state in microgravity condition. The resulting intensity profile at the top plate for both the case of microgravity and the case of Earth condition are shown in Fig. A.11 - b. The existence of the thermal boundary layers completely changes the shadowgraph images through the appearance of two maximums and one minimum in between. The first largest maximum is related to the bottom thermal boundary layer while the second lower maximum is due to the top thermal boundary layer.

A.4 Experimental results

A.4.1 Laboratory experiments

The light homogeneity is characterised by using a shadowgraph image in the isothermal case with no applied electric field. At this condition, the light intensity should be homogeneous because

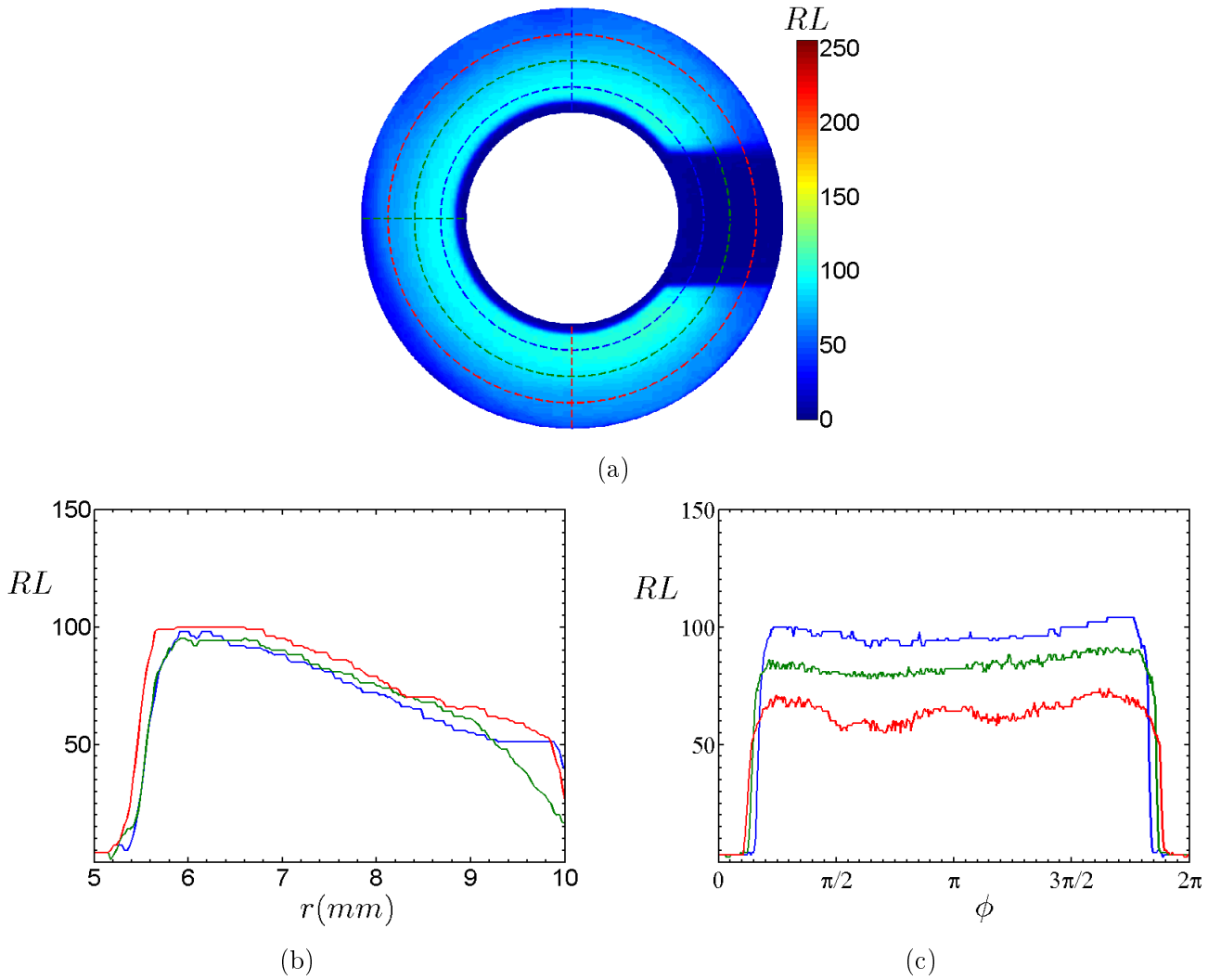

Figure A.12: (a) Contour, (b) radial distribution and (c) azimuthal distribution of the shadowgraph red level (RL) with $\Delta T = 0$ K and V_{peak})0 kV.

of the absence of density gradient. As the LED panel produces a red light, the treatment of the experimental shadowgraph images are done using only the red part of the RGB color vector. The figure A.12 shows that the light red level (RL) is nearly homogeous in the azimuthal direction. However, a RL gradient exists in the radial direction, i.e. the red level decreases with the radius. In the following, the light intensity profile is computed by normalising the RL profile of a given image by the one of the isothermal case (Fig. A.12 - a).

Fig. A.13 shows the effect of the temperature difference between the two cylinders on the radial light intensity profile. These profiles have been obtained by averaging the intensity along a hundred different radii distributed over the entire circumference of the cylindrical ring. As the isothermal case is used as the reference picture, $\Delta T = 0$ K gives a constant intensity profile equal to unity. Increasing ΔT has a large impact on the shadowgraph images. There is a minimum of

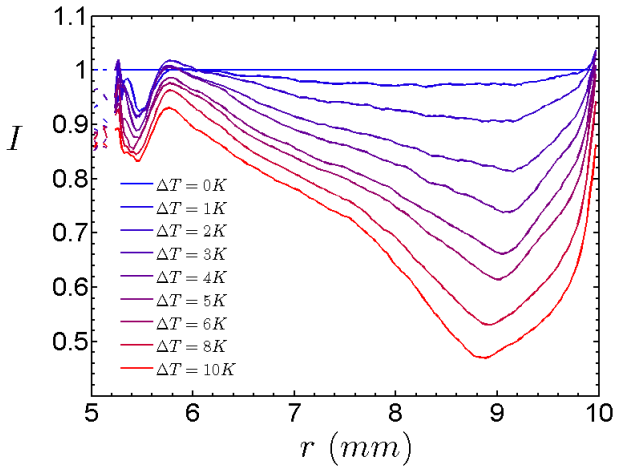

Figure A.13: Radial profile of the light intensity for different temperature differences between the two cylinders.

intensity close to the inner cylinder and a maximum at the outer cylinder which could be related to reflections of the light at the cylindrical surfaces. Just after the first minimum, there is a maximum of the intensity, followed by a decrease of the intensity with the radial position. After reaching a minimum, the intensity increases until the maximum of intensity located at the outer cylinder. Increasing the temperature difference decreases the overall light intensity profile.

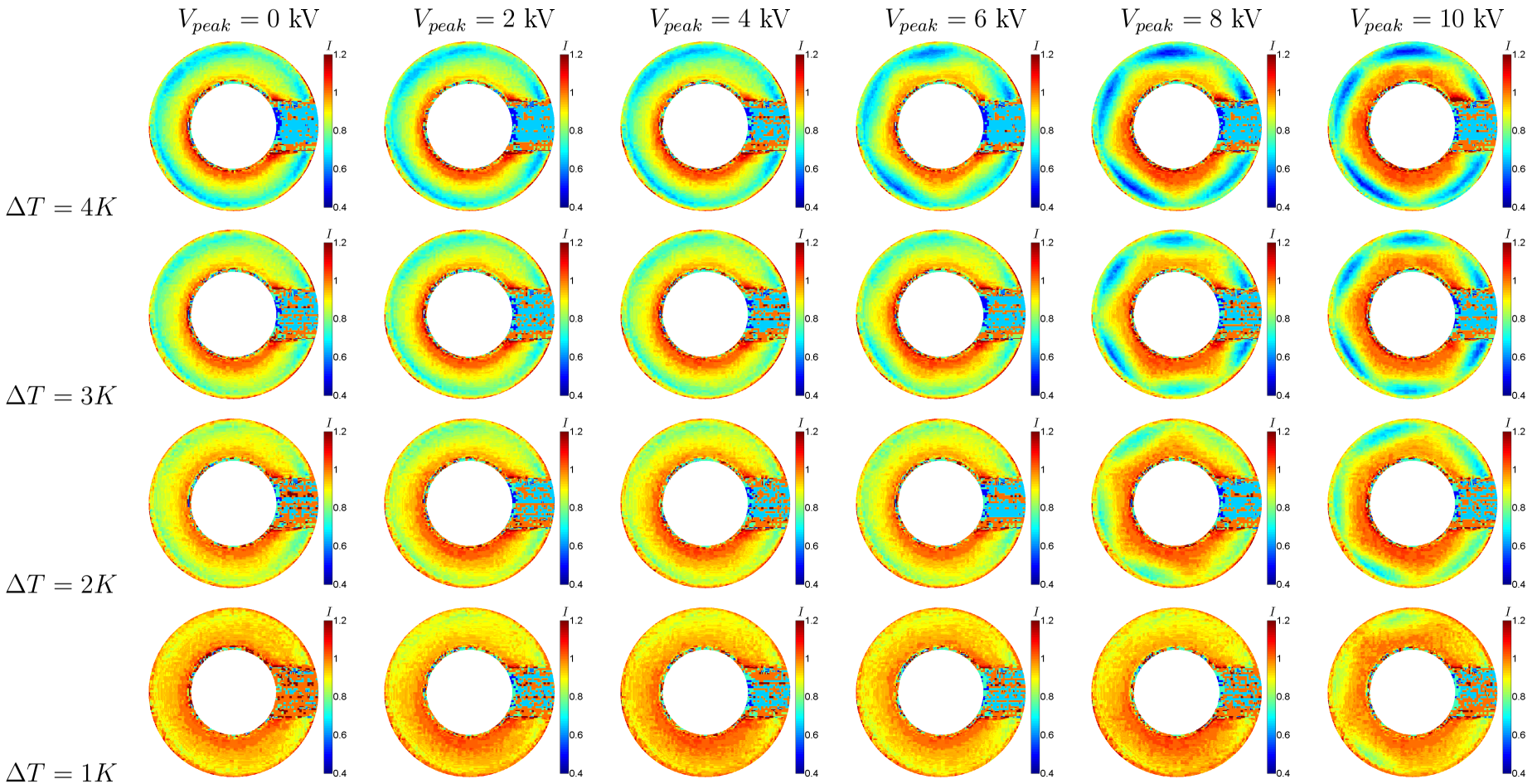

Figure A.14: Shadowgraph images obtained for different temperature differences and different applied electric potential.

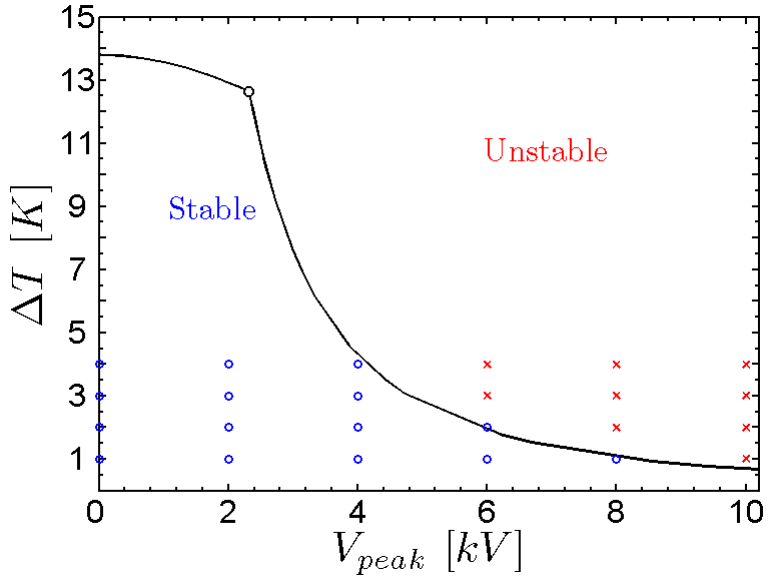

Figure A.15: Comparison between the linear stability diagram obtained for the silicone oil AK5 under earth gravity conditions (black curve) and the experimental results in the dimensional plan $(V_{peak}, \Delta T)$. The blue circles correspond to axisymmetric intensity profiles while the red crosses exhibit non-axisymmetric patterns.

As it is shown in the Chapter 9, the application of the electric field destabilises the convective base flow and produces non-axisymmetric vortices, i.e. columnar modes or helical modes. Figure A.14 summaries the laboratory experiments for a temperature difference of 1K to 4K and an alternative peak tension of 0kV to 10kV. From 0kV to 4kV, the pattern observed on the shadowgraph pictures are axisymmetric. Accordingly to the simulations of the shadowgraph method, this pattern is the one for the base convective state, or the one involving axisymmetric vortices, which have no impacts on the shadowgraph images. For sufficiently large values of the temperature difference and of the electric tension, a non-axisymmetric pattern appears on the shadowgraph images. This pattern is the signature of the presence of vortices with an azimuthal structure. For most cases, the pattern is pentagonal, which corresponds to an azimuthal mode number of $n = 5$, but for $\Delta T = 3$K, the number of modes in the azimuthal direction is $n = 6$.

The presence or not of the non-axisymmetric pattern gives an information about the stability of the flow. The experimental results can thus be confronted to the results from the linear stability analysis. In the figure A.15, the stability diagram for AK5 under earth gravity conditions is plotted in the dimensional plan $(V_{peak}, \Delta T)$. The experimental results are added to this curve through the indications of blue circles or red crosses, depending on the symmetry of the intensity pattern. For ΔT up to 4K, there is a good agreement between the linear stability analysis and the results

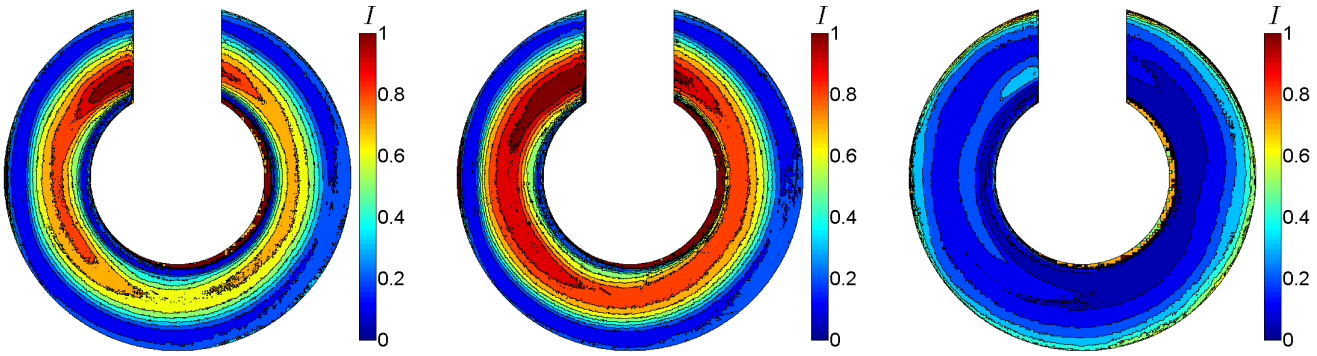

(a) 1g (b) 1.8g (c) 0g

Figure A.16: Shadowgraph images obtained at the end of the three different gravity phases with $\Delta T \approx 10$K and without applied electric tension.

from shadowgraph measurements.

A.4.2 Parabolic flight experiments

The reference picture we choose for the calculation of the light intensity is the first picture we have after we were allowed to switch the experiment on. But one has to note that the global temperature inside the experiment box increased during the flight because of the heating and electrical devices. Close to the experiment cell, the temperature started at about 18°C and was at about 25°C at the end of the flight. This temperature variation could affect the relevance of the reference picture. An other difference between the laboratory experiments and the PFC experiments is the way the inner cylinder is heated. The heating cartridge used during the PFC is able to fix the temperature difference by switching it on and off depending on the measurement made by the cartridge temperature sensor. But during this PFC, a defection of temperature measurement of the outer cylinder made this technique impossible to use. Thus the heating power of the heating cartridge was fixed and provided a constant heat flux at the inner cylinder. Anyway, in the following, we will consider that the temperature difference between the two cylinders was of about 10K.

Fig. A.16 shows the shadowgraph picture obtained at the end of the three different gravity phases which are the normal gravity (1g), the hypergravity (1.8g) and the microgravity (0g) phases without applied electric tension. The thermal boundary layers responsible for the axisymmetric pattern observed for the two gravity phases, is reinforced for the 1.8g phase compared to the 1g phase, inducing a more marked pattern for the hypergravity phase. At the end of the microgravity

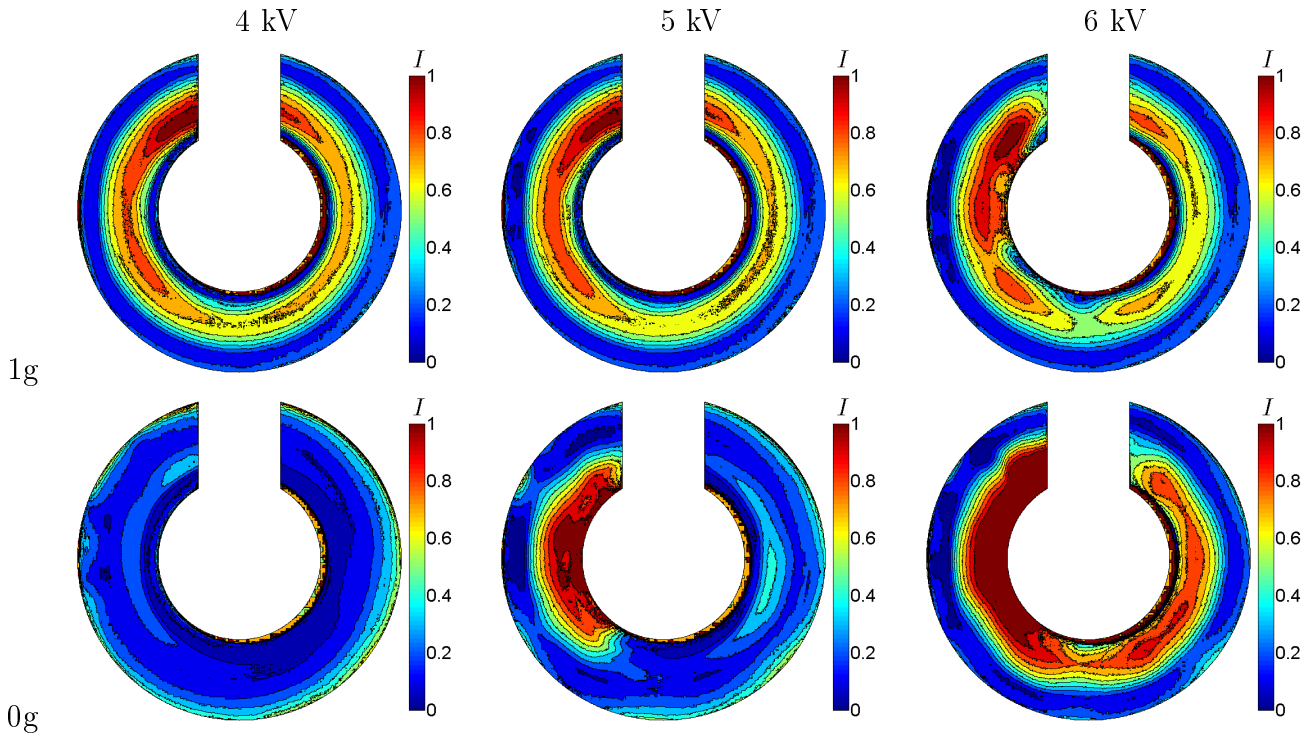

Figure A.17: Shadowgraph images obtained at the end of the normal gravity phase and of the microgravity phase with $\Delta T \approx 10$K and for different applied electric tensions.

phase, the light intensity is close to zero.

Figure A.17 shows the shadowgraph pictures obtained at the end of the 1g and 0g phases for different applied electric tensions. For the normal gravity phase, an non-axisymmetric pattern seems to appear at $V_{peak} \approx 6$kV while under microgravity conditions, a pattern is growing for $V_{peak} \approx 5$kV. As seen in Table A.2, these values of the electric potential are much larger than the ones predicted by the linear stability analysis. This difference can be due to the Boussinesq approximation which is no more valid when the temperature difference is too large.

On figure A.18, the azimuthal distribution of light intensity is measured at a given radius close to the mid-gap all along a parabola to give the space-time diagram of the light intensity. During the selected parabola, the electric potential was always active with $V_0 = 6.36$kV. During the 1g phase, a non-axisymmetric pattern was observed. The corresponding shadowgraph image taken at the end of this phase is shown on Fig. A.19 - a. When the hypergravity phase starts,

Table A.2: Critical dimensionless electric potential for the different states of gravity.

		μg	1g
V_{Ec}	Theory	473	479
	Experiment	$732 < V_{Ec} < 916$	$916 < V_{Ec} < 1099$

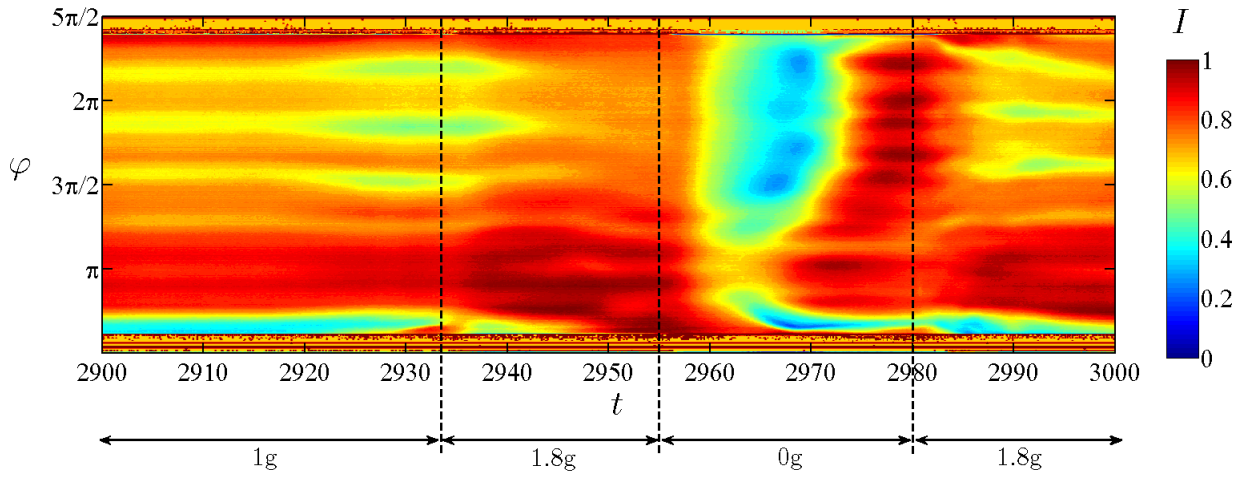

Figure A.18: Time variation of the light intensity measured in the azimuthal direction at $r = 5/7R_2$ during a parabola. The electric potential is always active with $V_0 = 6.36kV$ and $\Delta T \approx 10K$.

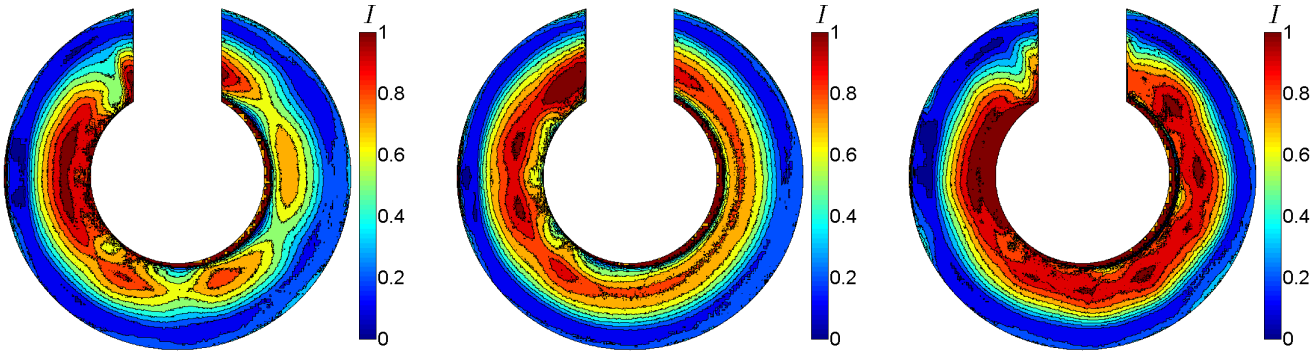

(a) $1g$ phase (b) $1.8g$ phase (c) $0g$ phase

Figure A.19: Patterns of the light intensity distribution. All images are captured at $V_0 = 6.36kV$ and $\Delta T \approx 10$K. The images (a), (b) and (c) are taken at the end of the $1g$, $1.8g$ and $0g$ phases respectively.

the non-axisymmetric pattern vanishes because of the reinforcement of the base convective flow. Fig. A.19 - b shows the shadowgraph image taken at the end of this 1.8g phase. During the first half of the microgravity phase, the brightness strongly decreases inside the gap. Then, a new non-axisymmetric pattern growths until the end of the microgravity phase, which was too short to get a steady state of this pattern. Fig. A.19 - c shows the shadowgraph image taken at the end of the 0g phase. This pattern is the signature of a convective state only generated by the thermoelectric buoyancy.

A.5 Discussion

A.5.1 Comparison between the simulation of the shadowgraph method and the experimental results

The shadowgraph technique can not give information about the structure of the vortices in the axial direction because the resulting picture consists of an integration over the entire optical path. Therefore, the columnar and helical modes can not be distinguished. An idea behind the simulation of the shadowgraph technique was to search for a mode that can make the resulting simulated shadowgraph image and an experimental one match. The success of the matching between the two shadowgraph images would mean that the shape and the amplitude of the experimental instability mode is similar to the simulated one. This comparison did not conclude because of the many hypotheses and simplifications that have been made concerning the simulation. Besides the fact that, in the experiments, the LED panel does not produce perfectly parallel illumination, or the fact that the camera is not located directly at the top of the cylindrical gap, but a dozen centimetres away from the top PMMA lid, one of the largest simplification is that the camera used to capture the shadowgraph images has optics to focus the image, where in the simulations, the camera is in fact a CCD panel, which is more relevant to capture parallel lights.

A.5.2 Comparison between the linear stability analysis and the experimental results

The aspect ratio used in the experiment is relatively small in order to neglect the boundary layers from the end plates and to ensure the conduction regime of the base state which was assumed in the linear stability analysis. In fact, according de Vahl Davis and Thomas [63], the conduction regime is realized if $Gr < 400\Gamma/Pr$ and the transition regime occurs when $400\Gamma/Pr < Gr < 3000\Gamma/Pr$; for $Gr > 3000\Gamma/Pr$, the flow is in the boundary layer regime. For our experimental conditions, the conduction regime exists for $Gr < 121.4$, the transition regime exists for $121.4 < Gr < 910.2$, and the boundary regime for $Gr > 910.2$. Therefore, the comparison with the linear stability results is realistic only in the microgravity phase. Moreover, the temporal variation of the axial gravity during the PFC experiments was neglected.

In other hand, the application of a temperature difference of 10K between the two cylinders

invalidates the Boussinesq approximation and can lead to differences between the experimental results and the predictions of the linear stability analysis.

A.6 Conclusion

The simulation of the shadowgraph method showed that the base state has already a large influence on the light intensity distribution. Under microgravity conditions, the axially invariant temperature profile has a weak effect on the images, while the axial gravity produces thermal boundary layers which change the light intensity distribution of the images. Axisymmetric vortices have no impact on the shadowgraph images, while non-axisymmetric modes produce an azimuthal light intensity pattern with a maximum efficiency for columnar modes, which were predicted by the linear stability analysis. The experiments in the laboratory and during the PFC showed the presence of non-axisymmetric patterns when the electric potential is applied. The laboratory experiments showed a good agreement with LSA, at least for small temperature differences between the two cylinders. The PFC experiments showed that convection rolls appear during the microgravity phases, which can only be caused by the thermoelectric buoyancy. But the 22 s of microgravity remains too short to get a steady flow, even though the growth rate is maximized by choosing parameters far from the onset of convection.

Bibliography

[1] I.M. Yavorskaya, N.I. Fomina, and Y.N. Belyaev, A simulation of central-symmetry convection in microgravity conditions, *Acta Astronautica* **11**, 179-183 (1984).

[2] R. Hollerbach, A spectral solution of the magneto-convection equations in spherical geometry, *Int. J. Numer. Meth. Fluids* **32**, 773-797 (2000).

[3] V. Travnikov, H.J. Rath, and C. Egbers, Stability of natural convection between spherical shells: energy theory, *Int. J. Heat Mass Transf.* **45**, 4227-4235 (2002).

[4] V. Travnikov, K. Eckert, and S. Odenbach, Influence of an axial magnetic field on the stability of convective flows between non-isothermal concentric spheres, *Int. J. Heat Mass Transf.* **55**, 7520-7531 (2012).

[5] V. Travnikov, K. Eckert, and S. Odenbach, Influence of the Prandtl number on the stability of convective flows between non-isothermal concentric spheres, *Int. J. Heat Mass Transf.* **66**, 154-163 (2013).

[6] J.E. Hart, G.A. Glatzmaier, and J. Toomre, Space-laboratory and numerical simulations of thermal convection in a rotating hemispherical shell with radial gravity, *J. Fluid Mech.* **173**, 519-544 (1986).

[7] B. Futterer, M. Gellert, T. von Larcher and C. Egbers, Thermal convection in rotating spherical shells: an experimental and numerical approach within GeoFlow, *Acta Astronautica* **62**, 300-307 (2008).

[8] B. Futterer, C. Egbers, N. Dahley, S. Koch and L. Jehring, First identification of sub- and supercritical convection patterns from 'GeoFlow', the geophysical flow simulation experiment integrated in Fluid Science Laboratory, *Acta Astronautica* **66**, 193-200 (2010).

[9] B. Futterer, N. Dahley, S. Koch, N. Scurtu and C. Egbers, From isoviscous convective experiment 'GeoFlow I' to temperature-dependent viscosity in 'GeoFlow II' - Fluid physics experiments on-board ISS for capture of convection phenomena in Earth's outer core and mantle, *Acta Astronautica* **71**, 11-19 (2012).

[10] B. Futterer, A. Krebs, A.C. Plesa, F. Zaussinger, R. Hollerbach, D. Breuer and C. Egbers, Sheet-like and plume-like thermal flow in a spherical convection experiment performed under microgravity, *J. Fluid Mech.* **735**, 647-683 (2013).

[11] D.C. Wadsworth and I. Mudawar, Cooling of a multichip electronic module by means of confined two-dimensional jets of dielectric liquid, *J. Heat Transfer* **112**, 891-898 (1990).

[12] Y. Joshi, M.D. Kelleher, M. Powell and E.I. Torres, Natural convection heat transfer from an array of rectangular protrusions in an enclosure filled with dielectric liquid, *J. Electron. Packag.* **116**, 138-147 (1994).

[13] M. Barbic, J.J. Mock, A.P. Cray and S. Schultz, Electromagnetic micromotor for microfluidics applications, *Appl. Phys. Lett.* **79**, 1399 (2001).

[14] G.I. Taylor, Stability of a viscous liquid contained between two rotating cylinders, *Phil. Trans. A* **223**, 289-343 (1923).

[15] S. Chandrasekhar, The stability of viscous flow between rotating cylinders, *Proc. Roy. Soc. Lond. A* **246**, 301-311 (1958).

[16] C.D. Andereck, S.S. Liu and H.L. Swinney, Flow regimes in a circular Couette system with independently rotating cylinders, *J. Fluid Mech.* **164**, 155-183 (1986).

[17] C. Yih, Dual role of viscosity in the instability of revolving fluids of variable density, *Phys. Fluids* **4**, 806-811 (1961).

[18] J. Walowit, S. Tsao and R.C. Diprima, Stability of flow between arbitrarily spaced concentric cylindrical surfaces including the effect of a radial temperature gradient, *J. Appl. Mech.* **31**, 585-593 (1964).

[19] V.M. Soundalgekar, H.S. Takhar and T.J. Smith, Effect of radial temperature gradient on the stability of viscous flow in an annulus with a rotating inner cylinder, *Warme und Stoffubertragung* **15**, 233-238 (1981).

[20] H.S. Takhar, T.J. Smith and V.M. Soundalgekar, Effects of radial temperature gradient on the stability of flow of a viscous incompressible fluid between two rotating cylinders, *Math. Analysis App.* **111**, 349-352 (1985).

[21] H.S. Takhar, M.A. Ali and V.M. Soundalgekar, Effects of radial temperature gradient on the stability of flow in an annulus with constant heat flux at the inner cylinder: wide-gap problem, *J. Franklin Institute* **325**, 609-619 (1988).

[22] H.S. Takhar, V.M. Soundalgekar and M.A. Ali, Effects of radial temperature gradient on the stability of a narrow-gap annulus flow, *Math. Analysis App.* **152**, 156-175 (1990).

[23] C. Kong and I. Liu, The stability of nonaxisymmetric circular Couette flow with a radial temperature gradient, *Phys. Fluids* **6**, 2617-2622 (1994).

[24] M. Auer, F.H. Busse and R.M. Clever, Three-dimensional convection driven by centrifugal buoyancy, *J. Fluid Mech.* **301**, 371-382 (1995).

[25] P.M. Eagles and V.M. Soundalgekar, Stability of flow between two rotating cylinders in the presence of a constant heat flux at the outer cylinder and radial temperature gradient - wide gap problem, *Heat Mass Transfer* **33**, 257-260 (1997).

[26] S. Pandey, A.K. Singh and R. Prasad, Effect of a constant heat flux at outer cylinder on stability of viscous flow in a narrow-gap annulus with radial temperature gradient, *Int. J. Eng. Science Tech.* **7**, 1-10 (2015).

[27] I. Choi and S. Korpela, Stability of the conduction regime of natural convection in a tall vertical annulus, *J. Fluid Mech.* **99**, 725-738 (1980).

[28] A. Bahloul, I. Mutabazi and A. Ambari, Codimension 2 points in the flow inside a cylindrical annulus with a radial temperature gradient, *Eur. Phys. J.* **9**, 253-264 (2000).

[29] H.A. Snyder, S.K.F. Karlsson, Experiments on the stability of Couette motion with a radial thermal gradient, *Phys. Fluids* **7**, 1696-1706 (1964).

[30] K.S. Ball and B. Farouk, Bifurcation phenomena in Taylor-Couette flow with buoyancy effects, *J. Fluid Mech.* **197**, 479-501 (1988).

[31] K.S. Ball, B. Farouk and V.C. Dixit, An experimental study of heat transfer in a vertical annulus with rotating inner cylinder, *J. Heat Mass Transfer* **32**, 1517-1527 (1989).

[32] M. Ali and P.D. Weidman, On the stability of circular Couette flow with radial heating, *J. Fluid Mech.* **220**, 53-84 (1990).

[33] H.N. Yoshikawa, O. Crumeyrolle and I. Mutabazi, Dielectrophoretic force-driven thermal convection in annular geometry, *Phys. Fluids* **25**, 024106 (2013).

[34] D.G. Economides and G. Moir, Taylor vortices and the Goldreich-Schubert instability, *Geophys. Astrophys. Fluid Dynamics* **16**, 299-317 (1981).

[35] A. Alonso, M. Net and E. Knobloch, On the transition to columnar convection, *Phys. Fluids* **7**, 935-940 (1995).

[36] A. Alonso, M. Net, I. Mercader and E. Knobloch, Onset of convection in a rotating annulus with radial gravity and heating, *Fluid Dynamics Research* **24**, 133-145 (1999).

[37] R. Tagg and P. Weidman, Linear stability of radially-heated circular Couette flow with simulated radial gravity, *Z. anqew. Math. Phys.* **58**, 431-456 (2007).

[38] B. Chandra and D.E. Smylie, A laboratory model of thermal convection under a central force field, *Geophys. Fluid Dynamics* **3**, 211-224 (1972).

[39] M. Takashima, Electrohydrodynamic instability in a dielectric fluid between two coaxial cylinders, *Mech. Appl. Math.* **33**, 93-103 (1980).

[40] P.J. Stiles and M. Kagan, Stability of cylindrical Couette flow of a radially polarised dielectric liquid in a radial temperature gradient, *Physica A* **197**, 583-592 (1993).

[41] S.V. Malik, H.N. Yoshikawa, O. Crumeyrolle and I. Mutabazi, Thermo-electro-hydrodynamic instabilities in a dielectric liquid under microgravity, *Acta Astronautica* **81**, 563-569 (2012).

[42] V. Travnikov, O. Crumeyrolle and I. Mutabazi, Numerical investigation of the heat transfer in cylindrical annulus with a dielectric fluid under microgravity, *Phys. Fluids* **27**, 054103 (2015).

[43] V. Travnikov, O. Crumeyrolle and I. Mutabazi, Influence of the thermo-electric coupling on the heat transfer in cylindrical annulus with a dielectric fluid under microgravity, *Acta Astronaut.* **129**, 88-94 (2016).

[44] B. Futterer, N. Dahley and C. Egbers, Thermal electro-hydrodynamic heat transfer augmentation in vertical annuli by the use of dielectrophoretic forces through a.c. electric field, *Int. J. Heat Mass Transfer* **93**, 144-154 (2016).

[45] L.D. Landau and E.M. Lifshitz, *Electrodynamics of Continuous media*, 2nd ed., Landau and Lifshitz Course of Theoretical Physics Vol. 8 (Elsevier Butterworth-Heinemann, Burlington, MA, 1984).

[46] T.B. Jones, Electrohydrodynamically enhanced heat transfer in liquids: A review, *Appl. Sci. Res.* **2**, 235-244 (1979).

[47] R.J. Turnbull, Effect of dielectrophoretic forces on the Bénard instability, *Phys. Fluids* **12**, 1809-1815 (1969).

[48] J.M. Lopez, F. Marques and M. Avila, The Boussinesq approximation in rapidly rotating flow, *J. Fluid Mech.* **737**, 56-77 (2013).

[49] R.J. Turnbull and J.R. Melcher, Electrohydrodynamic Rayleigh-Taylor bulk instability, *Phys. Fluids* **12**, 1160-1166 (1969).

[50] P.H. Roberts, Electrohydrodynamic convection, *Q. J. Mechanics Appl. Math.* **22**, 211-220 (1969).

[51] Y. Bai, Study of the viscoelastic instability in Taylor-Couette system as an analog of the magnetorotational instability, *Thesis, Université du Havre* (2015).

[52] O.N. Kirillov and I. Mutabazi, Short-wavelength local instabilities of a circular Couette flow with radial temperature gradient, *J. Fluid Mech.* **818**, 319-343 (2017).

[53] A.H. Davis, Natural convection cooling in fluids, *Phil. Mag.* **44**, 920-940 (1922).

[54] E.D. Siggia, High Rayleigh number convection, *Ann. Rev. Fluid Mech.* **26**, 137-168 (1994).

[55] S. Grossmann and D. Lohse, Scaling in thermal convection: a unifying theory, *J. Fluid Mech.* **407**, 27-56 (2000).

[56] H.N. Yoshikawa, M. Tadie Fogaing, O. Crumeyrolle and I. Mutabazi, Dielectrophoretic Rayleigh-Bénard convection under microgravity conditions, *Phys. Rev. E* **87**, 043003 (2013).

[57] S. Chandrasekhar and F. R. S., The instability of a layer of fluid heated below and subject to Coriolis forces, *Royal Society journal* **217**, 306-327 (1953).

[58] H. Kleine, H. Grönig and K. Takayama, Simultaneous shadow, Schlieren and interferometric visualisation of compressible flows, *Optics Lasers Eng.* **44**, 170-189 (2006).

[59] B. Robert, O. Johnston and M.H. Johnston, Laser shadowgraph and Schlieren studies of gravity-related flow during solidification, *Optics Lasers Eng.* **2**, 129-146 (1981).

[60] S. Verma, A. Srivastava, V. Prabhakar, K. Muralidhar and V.K. Wadhawan, Simulation and experimental verification of solutal convection in the initial stages of crystal growth from an aqueous solution, *Indian J. Pure Ap. Phys.* **43**, 24-33 (2005).

[61] F.H. Busse, and C.R. Carrigan, Convection induced by centrifugal buoyancy, *J. Fluid Mech.* **62**, 579-592 (1974).

[62] W. Schöpf, J.C. Patterson, and A.M.H. Brooker, Evaluation of the shadowgraph method for the convective flow in a side-heated cavity, *Exp. Fluids* **21**, 331-340 (1996).

[63] G. de Vahl Davis, and R.W. Thomas, Natural convection between concentric vertical cylinders, *Phys. Fluids* **12**, 198-207 (1969).